Coherent Spin Dynamics of Radical Pairs in Weak Magnetic Fields

by

Hannah J. Hogben

A thesis submitted in partial fulfillment of the requirements

for the degree of

Doctor of Philosophy

Trinity Term 2011

University of Oxford

Department of Chemistry

Physical and Theoretical Chemistry Laboratory

Oriel College

Abstract

Coherent Spin Dynamics of Radical Pairs in Weak Magnetic Fields

Hannah J. Hogben

Department of Chemistry

Physical and Theoretical Chemistry Laboratory and Oriel College

Abstract of a thesis submitted for the degree of Doctor of Philosophy

Trinity Term 2011

The outcome of chemical reactions proceeding via radical pair (RP) intermediates can be influenced by the magnitude and direction of applied magnetic fields, even for interaction strengths far smaller than the thermal energy. Sensitivity to Earth-strength magnetic fields has been suggested as a biophysical mechanism of animal magnetoreception and this thesis is concerned with simulations of the effects of such weak magnetic fields on RP reaction yields.

State-space restriction techniques previously used in the simulation of NMR spectra are here applied to RPs. Methods for improving the efficiency of Liouville-space spin dynamics calculations are presented along with a procedure to form operators directly into a reduced state-space. These are implemented in the spin dynamics software *Spinach*.

Entanglement is shown to be a crucial ingredient for the observation of a low field effect on RP reaction yields in some cases. It is also observed that many chemically plausible initial states possess an inherent directionality which may be a useful source of anisotropy in RP reactions.

The nature of the radical species involved in magnetoreception is investigated theoretically. It has been shown that European Robins are disorientated by weak radio-frequency (RF) fields at the frequency corresponding to the Zeeman splitting of a free electron. The potential role of superoxide and dioxygen is investigated and the anisotropic reaction yield in the presence of a RF-field, without a static field, is calculated. Magnetic field effect data for *Escherichia coli* photolyase and *Arabidopsis thaliana* cryptochrome 1, both expected to be magnetically sensitive, are satisfactorily modelled only when singlet-triplet dephasing is included.

With a view to increasing the reaction yield anisotropy of a RP magnetoreceptor, a brief study of the amplification of the magnetic field experienced by a RP from nearby magnetite particles is presented.

Finally in a digression from RPs, *Spinach* is used to determine the states expected to be immune from relaxation and therefore long-lived in NMR experiments on multi-spin systems.

Acknowledgments

I must begin by thanking Prof. Peter Hore for allowing me to come and join his group for my DPhil, especially considering my previous organic tendencies, and for suggesting such interesting projects over the last three years. I am deeply grateful for all of his help when I was stuck and for always allowing me time to get to grips with each new idea at my own pace. I could not have asked for a kinder and more patient supervisor.

Secondly I must thank Dr Ilya Kuprov for introducing me to state space restriction techniques and subsequently letting me loose with *Spinach*. I appreciate his help, suggestions and encouragement throughout the last three years. I am grateful to Dr. Chris Rodgers for not only giving me his γ-COMPUTE codes but also for teaching me how to use them and then for letting me modify them. I thank Prof. Blundell for helping me to understand the dynamics of magnetite nanoparticles.

On a technical note thanks are due to Dr Pete Biggs for keeping my linux machine running. He has tirelessly fixed software and hardware problems for this, often rather inept, linux user.

I am extremely grateful to the other members of the Hore group. The part II's of the last three years, Ian, Mikey and Dave, have been great fun to work with. Alice Bowen was delightful to have in the office, and was a source of lots of useful information about cryptochromes. Special thanks to Jason "Top Cat" Lau for helpful discussions about theory and computation, as well as being excellent company at tea time. Finally, I would like to thank Dr Till Biskup for teaching me more than a theoretical chemist really ought to know about cryptochromes and photolyases, for help with the technical aspects of writing in LaTeXand for putting up with my thesis-related rants. Thanks also go to members of the Timmel group for keeping me in touch with the real world. Drs Kiminori Maeda, Kevin Henbest and Alex Robinson were invaluable for discussions about the data fitting in Chapter Five, and for showing me the experimental set-up. Kelly-Anne Ferguson kindly showed me her rotary-RYDMR experiments and has always patiently answered my questions about her experiments.

Thanks are also due to Prof. Harry Anderson, Prof. Stephen Faulkner and Dr Brid Cronin for letting me teach physical chemistry at Keble over the last three years, I have thoroughly enjoyed it. They have provided interesting conversation and encouragement over the course of many SCR lunches.

I must acknowledge my home for the past seven years, Oriel. I am very grateful to the college for awarding me a graduate scholarship for the last two years and for in general providing an extremely supportive academic and social environment. I must thank my undergraduate tutors, Prof. David Hodgson and Dr. Hugh Cartwright, both of whom are excellent teachers and have been sources of support and guidance, as well as being founts of knowledge, over the years.

I would like to thank the (mostly) chemists whose company over soup at lunch time never failed to amuse me and from whom I have learnt many things about experimental magnetic field effects, electron paramagnetic resonance, neutron scattering and rocks. My house-mate and fellow part-II back in the day, Nicola Davis, I thank for lots of cups of tea.

I am grateful to my marvelous friends from Oriel: Pete, Georgie, Liz, Stu, James, Katie, Mark, Tessa, Sarah and Nick who despite growing up and joining the real world still have time for their student chum and without whose friendship I would not have made it through seven years in Oxford.

I would like to thank the members of Headcorn Baptist Church for their support and prayers, especially over the last few months.

My final acknowledgment must be to my parents. Thanks for the unwavering love and support! I really do love you both hugely.

"The heavens display the glory of God, and the firmament shows His handiwork" Psalm 19v1

Contents

Chapter 1

Introduction

This thesis is concerned with understanding how magnetic fields, particularly weak ones, can influence the outcome and rates of chemical reactions. Such effects have been observed experimentally since the 1970s in a myriad of different reactions, and a large body of complementary theoretical work has also accumulated [1]. In all cases magnetic fields affect the kinetic, not thermodynamic, aspects of chemical reactions [2]. Radical pair reactions are almost exclusively responsible for the observed influence of magnetic fields on chemical reactions [3, 4].

This chapter seeks to concisely introduce the aspects of the field of spin chemistry relevant to this research. We begin with a description of the property of spin and its quantum mechanical formalism. The radical pair mechanism is then described in detail along with some examples of its experimental manifestations. A discussion of the theoretical treatment of spin chemical systems is provided, in particular summarising the various contributors to radical pair spin state evolution and finally an outline of the remainder of this thesis is given.

1.1 Spin

That electrons and some nuclei possess an intrinsic angular momentum has long been known. The Stern-Gerlach experiment of 1922 first demonstrated the property in electrons [5, 6] and Pauli was the first to invoke nuclear spin in an attempt to explain the hyperfine structure of hydrogen spectra [7]. However, the phenomenon was not given a name until 1925 when Goudsmit and Uhlenbeck published the theory of the observed magnetic moment of electrons arising from a rotation about its own axis and subsequently the term “spin” was adopted. Pauli had already predicted the need for a fourth quantum number to describe the electronic structure of atoms in work on his exclusion principle and went on to develop a formal description of spin within

quantum mechanics by adding a new coordinate to the wavefunction to describe it [8]. Finally, the concept of half-integral angular momenta was confirmed theoretically by Dirac as a natural consequence of combining quantum mechanics and special relativity [9].

Since the 1920s a huge body of work seeking to understand the behaviour of spins in magnetic fields has accumulated. Most notably, though by no means exhaustively, in the fields of nuclear magnetic resonance (NMR), electron paramagnetic resonance (EPR) and spin chemistry. Despite the manifold differences in application of these three areas their underlying theoretical description is identical. It is fundamental to the practical application of spin dynamics to assume that the time evolution of the electronic spatial and spin parts of the total wavefunction are very different.[1] Thus it is possible to consider the spin part of the Hamiltonian and wavefunction only and drastically reduce the complexity of the problems to be addressed.

1.1.1 Properties of Spin

Electrons and magnetic nuclei have quantised intrinsic angular momentum described by a spin quantum number, S, which can take positive half-integer values or zero, and a projection along an arbitrary z-axis, S_z, which takes values $M_S\hbar$ with $M_S = S, S-1, \cdots, -S+1, -S$ [10]. States defined by these two properties are eigenstates of the total spin angular momentum operator, $\hat{S}^2 = \hat{S}_x^2 + \hat{S}_y^2 + \hat{S}_z^2$ and $\hat{S}_z$:

$$\hat{S}^2 \left|S, M_S\right\rangle = S(S+1)\hbar^2 \left|S, M_S\right\rangle \tag{1.1}$$

$$\hat{S}_z \left|S, M_S\right\rangle = M_S\hbar \left|S, M_S\right\rangle \tag{1.2}$$

There are $2S+1$ eigenstates of $\hat{S}_z$ for a given value of S, which in the familiar vector model can be viewed as different orientations relative to the z-axis, for example any single arrow in Fig 1.1. In this model $\sqrt{S(S+1)}\hbar$ defines the length of the angular momentum vector, $\boldsymbol{S}$.[2] Electrons, and ^{1}H nuclei amongst others, have $S = \frac{1}{2}$ and $M_S = \pm\frac{1}{2}$ for which the states are commonly known as $|\alpha\rangle$ and $|\beta\rangle$ respectively. In the absence of an applied electromagnetic field these states are degenerate, but are separated into $2S+1$ energy levels in the presence of a magnetic field (hence the M_S quantum number is the 'magnetic spin' quantum number). When two spin-$\frac{1}{2}$ species couple strongly their spins combine according to the Clebsch-Gordon series

[1] Analogous to the Born-Oppenheimer approximation which states that motions occurring on vastly different time scales are isolated from each other such that the two (or more) parts so the wavefunction may be dealt with independently.

[2] Hereafter $\hbar$ is dropped for convenience; subsequent Hamiltonians will be given in angular frequency units.

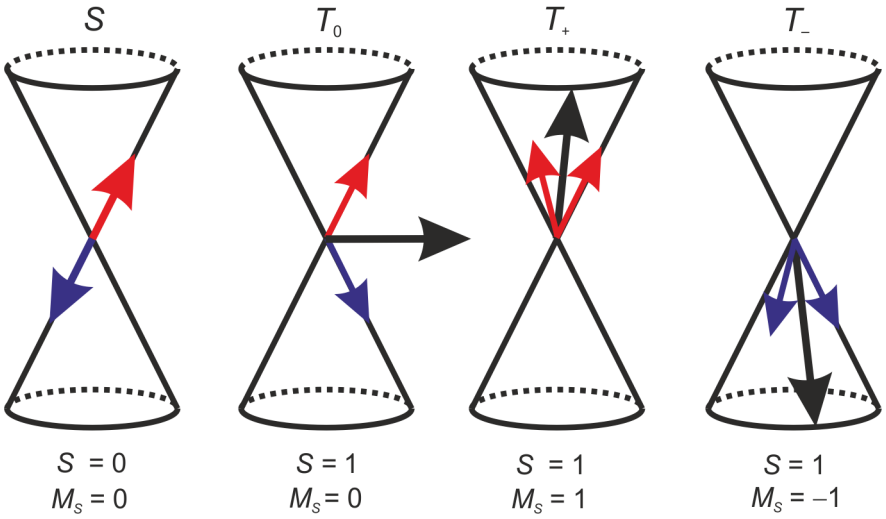

Figure 1.1. Vector model representation of the singlet (left) and triplet (right) spin states. Short arrows represent single spin states and the long bold arrow their resultant.

in one of four ways. There are three symmetric combinations, the triplets, $S = 1, M_S = 0, \pm 1$:

$$\begin{aligned} |T_+\rangle &= |\alpha\rangle \otimes |\alpha\rangle = |\alpha\alpha\rangle \\ |T_0\rangle &= \frac{1}{\sqrt{2}}\left(|\alpha\rangle \otimes |\beta\rangle + |\beta\rangle \otimes |\alpha\rangle\right) = \frac{1}{\sqrt{2}}\left(|\alpha\beta\rangle + |\beta\alpha\rangle\right) \\ |T_-\rangle &= |\beta\rangle \otimes |\beta\rangle = |\beta\beta\rangle \end{aligned} \tag{1.3}$$

and one anti-symmetric combination, the singlet, $(S = 0, M_S = 0)$:

$$|S\rangle = \frac{1}{\sqrt{2}}\left(|\alpha\rangle \otimes |\beta\rangle - |\beta\rangle \otimes |\alpha\rangle\right) = \frac{1}{\sqrt{2}}\left(|\alpha\beta\rangle - |\beta\alpha\rangle\right) \tag{1.4}$$

The singlet and triplet states are often represented in the vector model Fig 1.1 as the resultant (bold arrow) of two single-spin vectors added in different relative orientations. The cones in this figure represent the path swept out by the tip of the arrows as the spins precess about the resultant field direction - often provided by a large applied static field.

1.1.2 Single-Spin Operators

The eigenstates of $\hat{S}_z$ are commonly used as the basis for the matrix representation of angular momentum operators and the Pauli matrices in this basis are shown below for a spin-$\frac{1}{2}$ particle

[8]:

$$\sigma_x = \begin{pmatrix} 0 & 1 \\ 1 & 0 \end{pmatrix} \tag{1.5}$$

$$\sigma_y = \begin{pmatrix} 0 & -\mathrm{i} \\ \mathrm{i} & 0 \end{pmatrix} \tag{1.6}$$

$$\sigma_z = \begin{pmatrix} 1 & 0 \\ 0 & -1 \end{pmatrix} \tag{1.7}$$

These are used to form the spin operators; $\hat{S}_i = \frac{1}{2}\sigma_i$. Inclusion of the unit operator completes a set of generating operators. However, it is sometimes more convenient to use the raising and lowering operators which are defined as:

$$\hat{S}_\pm = \hat{S}_x \pm \mathrm{i}\hat{S}_y \tag{1.8}$$

in place of the Cartesian x and y operators. This leads to two alternative generating sets:

$$\left\{\hat{\mathbb{1}}, \hat{S}_z, \hat{S}_x, \hat{S}_y\right\} \tag{1.9}$$

$$\left\{\hat{\mathbb{1}}, \hat{S}_z, \hat{S}_+, \hat{S}_-\right\} \tag{1.10}$$

from which any single- or multi- spin operator can be formed. Similar generating operators may be derived for higher spin orders using the properties of the angular momentum operators [10]. All operators derived from these generator sets will be defined in the α, β basis in the laboratory frame (LF).

1.1.3 Irreducible Spherical Tensors

The generating set chosen should be appropriate to the particular problem at hand and it often proves most convenient to work with the normalised irreducible spherical tensors (nISTs), $\hat{T}_{l,m}$,

where l is the rank and $m = -l, -l+1, \cdots, l-1, l$, is the order. These are defined for spin-$\frac{1}{2}$ as:

$$\begin{aligned}
\hat{T}_{0,0} &= \frac{\hat{\mathbb{1}}}{\sqrt{2}} \\
\hat{T}_{1,+1} &= -\hat{S}_+ \\
\hat{T}_{1,0} &= \sqrt{2}\hat{S}_z \\
\hat{T}_{1,-1} &= \hat{S}_-
\end{aligned} \tag{1.11}$$

and thus form a third possible generating set for spins-$\frac{1}{2}$. Higher rank nISTs are invoked when spins with $S > \frac{1}{2}$ are present to increase the size of the generating set. The irreducible spherical tensors (ISTs) (normalised or otherwise) are irreducible representations of the 3D rotation group SO(3) which proves particularly convenient as their properties under 3D rotations are well-defined. A rotation, $\hat{R}$, acting on $\hat{T}_{l,m}$ results in a linear combination over all the ISTs of that rank, such that [11]:

$$\hat{R}\left(\alpha,\beta,\gamma\right)\hat{T}_{l,m} = \sum_{m'=-l}^{l} \mathcal{D}^{(l)}_{m',m}\left(\alpha,\beta,\gamma\right)\hat{T}_{l,m'} \tag{1.12}$$

where $\mathcal{D}^{(l)}_{m',m}\left(\alpha,\beta,\gamma\right)$ are the Wigner coefficients of the Euler angles (α,β,γ). In the zyz-convention the rotation, $\hat{R}_{zyz}$, is defined as:

$$\hat{R}_{zyz}\left(\alpha,\beta,\gamma\right) = \mathrm{e}^{\mathrm{i}\alpha\hat{S}_z}\mathrm{e}^{\mathrm{i}\beta\hat{S}_y}\mathrm{e}^{\mathrm{i}\gamma\hat{S}_z} \tag{1.13}$$

where $\hat{S}_i$ are the angular momentum operators. The ISTs, $\hat{T}_{l,m}$, have a further advantageous property that they have well-defined commutation relations with the $\hat{S}_z$ operator such that: $\left[\hat{S}_z, \hat{T}_{l,m}\right] = m\hat{T}_{l,m}$ [11].

1.1.4 Multi-spin Operators

For a system with N spin-$\frac{1}{2}$ species there are 4^N potential product operators formed from all direct product combinations, in the order of the spin labels, of the generating operators, $\hat{B}_i$, within a set above, such that:

$$\hat{O}_k = M\bigotimes_{i=1}^{N}\hat{B}_i \tag{1.14}$$

where M is a scaling factor required in the case of nISTs to convert them back to the spin operators. Any Hamiltonian can be formed as a linear combination of these operators with real coefficients, c_k:

$$\hat{H} = \sum_k c_k \hat{O}_k \tag{1.15}$$

Higher rank ISTs can be used to describe coupled spin systems (*i.e.* those operators with more than one non-$\hat{\mathbb{1}}$ generator operator in (1.14)). They are derived by taking linear combinations of products of the lower rank tensors with either Clebsch-Gordan coefficients or $3j$-symbols defining the coefficients [11, 12]:

$$\hat{T}'_{k,q}(k_1,k_2) = \sum_{q_1,q_2} (-1)^{-k_1+k_2-q} \sqrt{2k+1} \begin{pmatrix} k_1 & k_2 & k \\ q_1 & q_2 & -q \end{pmatrix} \hat{T}'_{k_1,q_1} \hat{T}'_{k_2,q_2} \tag{1.16}$$

where the indices are restricted such that $q_1+q_2 = q$ and $k = |k_1 - k_2|, |k_1 - k_2|+1, \cdots, |k_1 + k_2|$ and the prime indicates that the ISTs are not necessarily normalised. Using Equations (1.16) and (1.11) it is possible to express the rank-2 tensors in terms of the operators for two coupled spins-$\frac{1}{2}$, I and S:

$$\begin{aligned} \hat{T}'_{2,0} &= -\sqrt{\frac{2}{3}} \left(\hat{S}_z \hat{I}_z - \frac{1}{4} \left(\hat{S}_+ \hat{I}_- + \hat{S}_- \hat{I}_+ \right) \right) \\ \hat{T}'_{2,\pm 1} &= \mp \frac{1}{2} \left(\hat{S}_z \hat{I}_\pm + \hat{S}_\pm \hat{I}_z \right) \\ \hat{T}'_{2,\pm 2} &= \frac{1}{2} \hat{S}_\pm \hat{I}_\pm \end{aligned} \tag{1.17}$$

Any spin Hamiltonian can be built from the operators described already along with appropriate interaction constants. The nature of common interactions will be returned to in Section 1.3.3.

1.2 Spin Chemistry

The outcomes of certain chemical reactions are affected by magnetic fields, though for many years such an effect was disputed. It was argued that magnetic fields could affect chemical reactions thermodynamically or kinetically, by altering the relative Gibbs energies of products, transition states and reactants, or kinetically by affecting reactant orientation [13]. However,

even extremely high fields (> 10 T) interact with electrons with an energy much less than thermal energy at room temperature (and even more weakly with magnetic nuclei) hence could not be expected to affect the thermodynamic control of any reaction, or the Boltzmann distribution of initial orientations [2]. Nevertheless, it has been shown experimentally even for fields as weak as that of the Earth ($\approx 50\ \mu$T), that the outcome of some chemical reactions are strongly dependent on the magnetic field [1]. Such reactions cannot be under thermodynamic control, but are instead determined by the spin selection rules. To explain this phenomenon, first as it appeared in the polarisation of NMR signals and later more generally, the radical pair mechanism, RPM, was proposed [3, 4].

1.2.1 Radical Pair Mechanism

Any two electrons may be described as an electron pair. To be a radical pair (RP) the two electrons must be spatially separated, either on two distinct radical species or on separate regions of a biradical. Furthermore to be of use in the RPM the electrons must have correlated spins, *i.e.* there must be some phase relation between the two electron states [14].

A general reaction scheme for the RPM is shown in Fig 1.2 [15]. In this case the spin correlated RP is initially formed as a singlet (S) by photoexcitation of the ground state (though more generally an initial triplet state is also possible). In the scheme shown only the singlet state can undergo reaction to return to the diamagnetic ground state, but either state can follow a path that is not spin-selective, for example diffusion apart to form free radicals which are subsequently quenched [14], and eventually are returned to the ground state at a much slower rate than direct recombination along the singlet path. The simplest scheme possible has $k_S^F = 0\ \mathrm{s}^{-1}$ and thus only triplet state RPs follow the second pathway. Some RP reactions have much more complicated kinetic schemes, for example those that occur as part of feedback loops in oscillating reactions [16].

The fate of a triplet RP is irrelevant if the RP is born as a singlet and remains so until reaction. Such reactions are not interesting from a spin dynamics standpoint but luckily in many cases a radical pair undergoes coherent evolution between the singlet and triplet states and thus the spin chemistry becomes much more interesting.

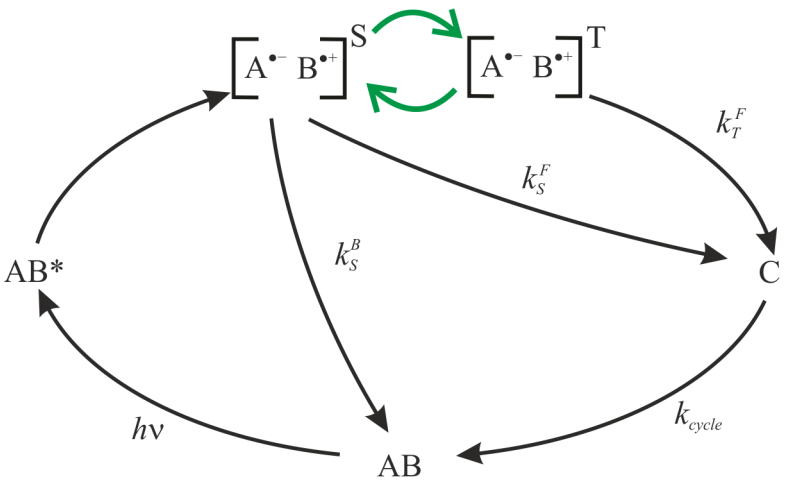

Figure 1.2. Radical pair mechanism [15]. k_S^F and k_T^F are the rates of forwards reaction from the singlet and triplet RPs respectively, k_S^B is the rate of spin selective reaction back to the ground state, AB. The product C reforms the starting material on a timescale ($\frac{1}{k_{cycle}}$) which does not influence the radical pair dynamics. The curved green arrows indicate coherent spin-state evolution.

Radical Pair Formation

In the majority of cases a molecule, A, is irradiated with light and is excited to an electronically excited level, A*. Light-induced electronic transitions which involve spin flips are not allowed and so the excited state is formed in the same spin state as its ground state precursor. Most species are diamagnetic in the ground state (though molecular oxygen provides a famous example of a triplet ground state species) and so form excited singlet state species. The excited state can either undergo intersystem crossing (ISC) to a different multiplicity spin state, internal conversion to an excited state of the same multiplicity, fluorescence to the ground state or undergo reaction to form a radical pair [17]. Such reactions may for example be hydrogen abstraction, homolytic bond cleavage or electron transfer [1], all of which conserve spin angular momentum and so produce a geminate RP in the same spin state and with correlated electron spins.

It is also possible that a RP may arise when two electrons meet in a solvent cage via diffusion. A RP born in this manner, a so-called F-pair, is not initially spin correlated. Spin correlation can only arise in this situation in the case of different singlet and triplet reaction rates. The rapid selective reaction of one spin state changes the proportion of spin states in the remaining ensemble – it is no longer completely mixed – and the unreacted RPs have gained coherence.

Coherent Evolution

Coherent evolution between the different spin multiplicities occurs only when the magnetic environments of the two electrons are distinct. In the well-known vector model this can be viewed as the radicals having different Larmor frequencies and so precessing around the eigenaxis at different rates *i.e.* the arrows of Fig 1.1 travel around their cones at different rates. This unsynchronised precession leads the electrons of the RP to move in and out of phase with one another, thus converting from T_0 to S and back again. The process may be driven by, for example, unequal g-values [18], interactions with nuclei via hyperfine interactions (HFI) [19] or spin-orbit coupling [20]. In order for the radicals to evolve it is necessary that there is no strong interaction between the two electrons. Exchange (J), and dipolar couplings suppress interconversion as the singlet and triplet spin states are their eigenstates and thus exist as stationary (non-evolving) states when these interactions dominate [21].

Reaction

The singlet RP state may undergo spin-allowed recombination to reform the diamagnetic ground state. This often progresses through either direct electron transfer (ET) or via the formation of an exciplex which subsequently undergoes fluorescent relaxation [22]. The Pauli exclusion principle prevents the same reactions occurring directly from the triplet state. Electron transfer processes preserve spin multiplicity and, as evidenced by the slow rate of phosphorescence in comparison with fluorescence following photoexcitation of a molecule, radiative transitions likewise have strong spin selection rules, $\Delta S = 0$ [17]. The triplet may instead simply diffuse apart to form free radicals which are subsequently quenched or may participate in a triplet selective reaction. Alternatively a non-spin-selective reaction path, for example a proton transfer, may be accessible to both spin states. In order to see a magnetic field effect it is necessary to have at least one spin-selective reaction step – otherwise the spin state of the intermediate RP has no bearing on the outcome of the reaction and changing the ratio of singlet and triplet species has no observable manifestation.

Effect of Static Field on Reaction Yield

Applying an additional static (or oscillating *e.g.* Ref [23]) magnetic field to the system, or changing the intrinsic interactions (for example through magnetic isotope effects on the hyperfine interaction [24]) affects the rate of coherent interconversion and hence the populations of singlet

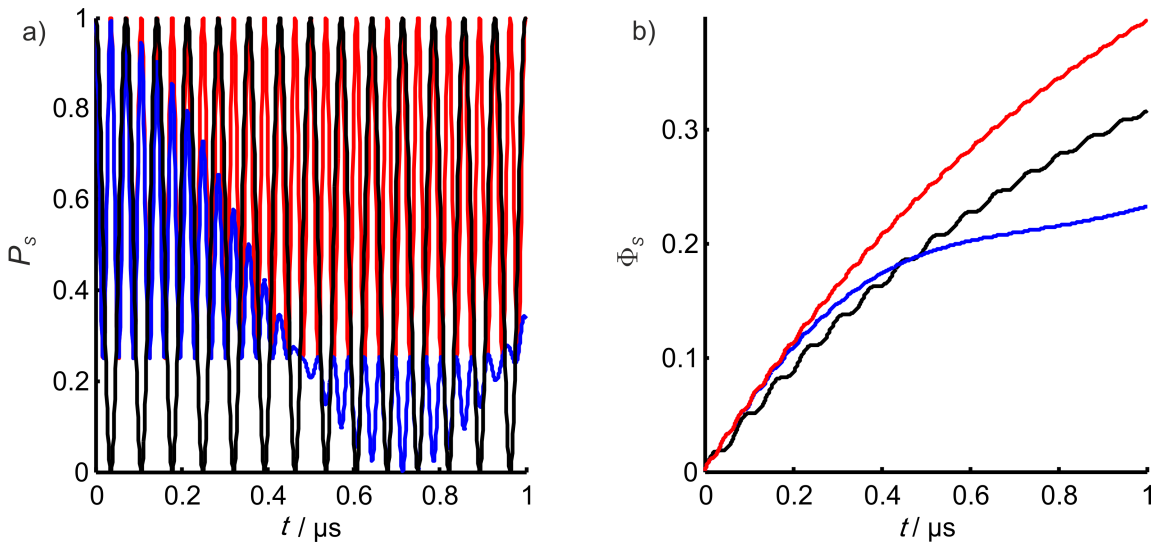

Figure 1.3. a) The singlet probability, P_S, and b) the singlet yield Φ_S, for a singlet-born RP with a single hyperfine interaction, $a = 1$ mT and $k_S = k_T = 10^6$ s^{-1}, in the absence (red) and presence of a weak (blue, 50 μT) and strong (black, 1 T) applied static field. Based on Figure 2 in Ref [15].

and triplet states in the RP intermediate which in turn directly affects the proportions of the product yields. The effects of a strong (1 T) and weak (50 μT) static field on the simplest possible RP reaction (one isotropic hyperfine interaction with a spin-$\frac{1}{2}$ nucleus and exponential decay of the singlet and triplet states with equal rate constants) are shown in Fig 1.3. In the absence of a field the hyperfine interaction causes an oscillation between the singlet and triplet spin states which share the same total spin angular momentum and the same projection of the spin angular momentum on the z-axis. Though an applied field does not cause spin state evolution, it does remove the need to conserve the total spin angular momentum allowing more triplet states to become populated, this is evidenced by the minimum singlet probability falling to 0% when the field is turned on. The field causes a modulation, at a frequency corresponding to the strength of the field, of the singlet probability in addition to the hyperfine-driven evolution which results in an altered reaction yield from the singlet state in the presence of the applied field.

1.2.2 Evidence for the Radical Pair Mechanism from Magnetic Resonance

Magnetic resonance spectroscopy makes use of the interaction of nuclear and electron spins with an applied magnetic field to probe the local magnetic environment, which in turn reflects the local structure, of the spin [25, 26].

The sensitivity of magnetic resonance techniques is limited by the weak polarisation of electron and nuclear spins, even at low temperature and high field, at Boltzmann equilibrium. Chemically induced dynamic nuclear polarisation (CIDNP) and chemically induced dynamic

electron polarisation (CIDEP) are phenomena which produce a non-Boltzmann distribution of spin states following a thermal or photochemical reaction. This was observed in NMR and EPR as enhanced signal amplitudes which can be either absorptive or emissive depending on the nature of the polarisation [27, 28].

As aforementioned the RPM was proposed to explain the phenomenon of CIDNP. When coherent evolution of the RP is driven by hyperfine interactions the states of nuclear spins affect the rate of interconversion between singlet and triplet spin-states [29]. For example, for a triplet-born RP nuclear spin states which accelerate S-T mixing will favour formation of the singlet state and thus are more likely to populate the singlet product. Conversely those nuclear spin states which do not favour interconversion will dominate the population of nuclear spin states in the triplet product. Overall there is no net polarisation of the nuclear spins (beyond that of the Boltzmann distribution) but the spin states have been sorted into different products. The signal enhancement due to the polarisation within each product is usually observed as the difference between the so-called light spectrum (when a laser flash initiates a RP reaction) and the dark spectrum where only normal polarisation leads to the signal.

CIDEP is somewhat more complex as there are two mechanisms which can lead to distortions in the signal intensity in EPR spectra [28]. The first is the triplet mechanism (TM) [30]. The radical precursor must be a molecular triplet which is formed following anisotropic intersystem crossing from the initial singlet excited state and leads to non-equal populations of the triplet sub-levels. The RPM also provides a route to electron polarisation [31]. At high field the $T_{\pm}$ states are far removed in energy from T_0 and S so that coherent evolution to the $M_S \neq 0$ states is strongly suppressed. This is not so for the interconversion between T_0 and S, thus an initial singlet state selectively populates only T_0 over time or analogously an initial triplet state has only T_0 emptied out. The TM–RPM by which a polarised triplet state is the initial state for interconversion in the normal RPM also causes CIDEP [32]. However it is achieved, the non-Boltzmann population differences between $T_{\pm}$ and T_0 are then observed by enhanced absorptive or emissive (or mixed multiplet) peaks in the EPR spectrum.

1.2.3 Experimentally Observed Magnetic Fields Effects

The most common observation of magnetic field effects (MFE) on chemical reaction has been from chemical reactions proceeding via a radical pair intermediate in solution, although some MFEs have been observed in the gas phase [33] and in the solid state [1]. In order to observe a

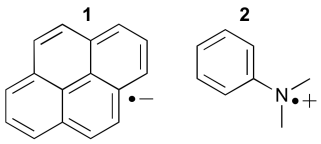

Figure 1.4 Radical pair comprising pyrene, **1**, and dimethylaniline, **2**.

MFE the reaction rates along singlet and triplet channels must be competitive. The existence of solvent cages limits the rate at which radical pairs can diffuse apart, hence the rate at which triplet RPs separate is comparable to the rate of singlet recombination. There are myriad published examples of observed MFEs, Ref [1] provides a comprehensive review of experiments prior to 1989 and is still extremely relevant.

The radical pair formed from pyrene (Py) and dimethylaniline (DMA) is shown in Fig 1.4. This pairing exhibits a strong field-dependent response and the synthetic pathways to the molecules are well established allowing for relatively easy isotopic labelling. It is thus often used as a test system in a range of MFE experiments [24, 34–36]. Pyrene undergoes efficient excitation to an excited singlet state upon irradiation with light and subsequently accepts an electron from its partner, most often an aromatic amine such as DMA. The radical ion pair (RIP) can then either form a singlet exciplex and fluoresce to the ground state (fluorescence intensity provides a measure of singlet yield) or undergo coherent interconversion to and from the triplet which itself cannot undergo reverse ET and diffuses apart to form escape products. The initial excitation may be performed with a laser flash to allow time-resolved singlet yields to be measured or by continuous illumination such that only the total yield is observed. The effect of a static magnetic field on the reaction yield is termed MARY – **M**agnetically **A**ltered **R**eaction **Y**ield.

When anisotropic HFIs are present, and the RPs are at a fixed orientation, it is possible to detect not just the effect of field magnitude on reaction yield but also the the effect of varying field direction. The first example of a system showing sensitivity to the the field direction was reported in Ref [37] for a carotenoid-porphyrin-fullerene (CPF) triad molecule, Fig 1.5. This type of magnetic sensitivity is sometimes termed MARYAN (MARY ANisotropic).[3]

Oscillating fields applied in addition to static fields allow for the observation of magnetic resonances in the RP system through **R**eaction **Y**ield **D**etected **M**agnetic **R**esonance, RYDMR [38, 39]. As already mentioned in the context of CIDEP in a strong magnetic field the $T_{\pm}$ states are energetically removed from T_0 and S which inhibits interconversion. An appropriate

[3]The name MARYAN is also often used for MARY experiments with an added radio-frequency field.

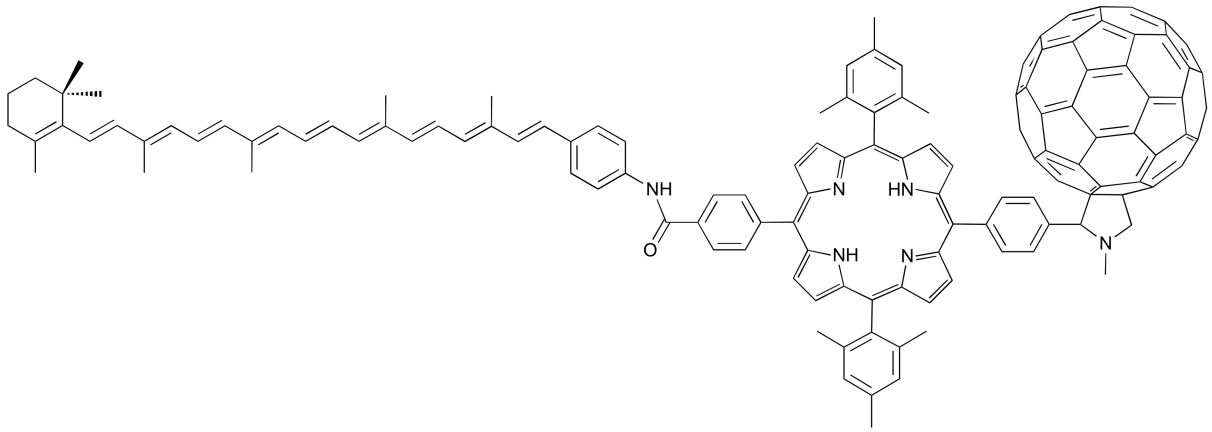

Figure 1.5 Structure of the CPF (carotenoid-porphyrin-fullerene) triad [37] molecule.

frequency electromagnetic field (EMF) recouples the transitions and thus alters the proportion of singlet and triplet yields. As the EMF frequency is scanned, resonances appear in the reaction yield corresponding to the energy separations of the RP. When the applied static field is relatively weak (milliTesla rather than Tesla) this technique is often referred to as MARY-ν. Even in the absence of a static magnetic field, oscillating magnetic fields alone can affect the outcome of RP reactions. These reactions are named **O**scillating **M**agnetic **F**ield **E**ffects – OMFE [40].

Magnetic isotope effects on reaction yield have also been observed [41, 42]. In this case changing the nature of the magnetic nuclei in the RP changes the hyperfine interactions and thus the rate of coherent evolution between states of different multiplicity [35]. This effect is often exploited by selective deuteration to alter natural MFEs in experimental model systems.

1.2.4 Biological Significance

The RPM provides a direct mechanism by which static and oscillating magnetic fields can affect chemical reactions, and by extension biochemical reactions. Several biological processes are known to proceed via radical intermediates, in fact this class of reaction encompasses most reactions with single electron transfers. However, relatively few biological reactions are known to exhibit long-lived spin-correlated RPs. To name just one well-studied example: modified pigment-protein reaction centres which mediate conversion of light to chemical energy in photosynthesis do so via spin-correlated radical pair intermediates and applied magnetic fields can affect the outcome of the RP reaction through the traditional RPM [43–45].

Many animals have been shown to use a magnetic sense for orientation [46–49]. Across the animal kingdom there is sensitivity to field polarity and inclination at Earth-strength fields (25 – 100 μT) and to small changes in field intensity within this range. The biophysical mecha-

nism of magnetoreception remains unclear but currently two suggested mechanisms are under investigation. Firstly, it has been suggested that small particles of biogenic magnetite may align in the Earth's field, akin to a normal human compass, which subsequently leads to a neural response [50]. Alternatively, the RPM has been proposed as a mediator for directional field information [51]. This is possible only when the RP has an intrinsically anisotropic interaction such that addition of a static field at different orientations relative to it leads to different rates of S-T interconversion [15]. Most organic radicals have anisotropic hyperfine interactions, though unfortunately these are often not very large, which could provide the required directionality. Investigation of the RPM as the putative biological magnetocompass is the subject of the latter part of this thesis and animal magnetoreception will be introduced more fully in Chapter 4.

There is some epidemiological evidence to suggest that weak EMFs might have an influence on human health. Thus far the most probable mechanism by which EMFs can have an effect on biological processes, and hence a macroscopic effect on development, is through the RPM. For example, magnetic fields have been shown to affect the singlet oxygen production by bacterial photosynthetic centres [52] and magnetic field effects on the hypocotyl growth of *Arabidopsis thaliana* have been reported [53] – though replication studies failed [54]. As yet no direct evidence for weak field (such as those in the vicinity of overhead power lines) effects on macroscopic animal biology, apart from orientation, has been reported.

Magnetic isotope effects on the yields from ATP (adenosine triphosphate) synthase have recently been reported *in vitro* [55, 56]. The suggested explanation is a radical reaction pathway, via a $\left[\mathrm{Mg}^{\bullet+} - \mathrm{PO}_3^{\bullet-}\right]$ pair, which has also been reported to exhibit MFEs [57, 58]. This suggestion has attracted some controversy as the radical pathway proposed is contrary to the concerted electron - nucleophilic substitution mechanism that has long been accepted and which is analogous to non-biological organic chemistry mechanisms for the same functional groups.

1.3 Theoretical Description

In order to understand the effect of magnetic fields on chemical reactions through the RPM it is necessary to understand the underlying spin dynamics. This theoretical framework may then be used to simulate the outcome, in terms of singlet and triplet yields, of RP reactions under a variety of conditions. Such simulations are vital to discern the processes which affect experimentally observed MFEs, to understanding the requirements of the animal magnetocompass and to direct further experimental studies. The important details of the quantum mechanical

description of spin chemistry are outlined in this section. A familiarity with the density matrix formalism is assumed.

1.3.1 Equation of Motion

The density matrix ρ evolves over time according to the Liouville-von Neumann equation [59, 60]:

$$\frac{\mathrm{d}\rho(t)}{\mathrm{d}t} = -\mathrm{i}\left[\hat{H}(t), \rho(t)\right] \tag{1.18}$$

where $\hat{H}(t)$ is the time-dependent spin Hamiltonian. Formal integration of Equation (1.18) gives:

$$\rho(t) = \hat{U}(t)\rho(0)\hat{U}(t)^{\dagger} \tag{1.19}$$

where

$$\hat{U}(t) = \hat{T}\exp\left\{-\mathrm{i}\int_0^t \hat{H}(t')\mathrm{d}t'\right\} \tag{1.20}$$

is the unitary propagator for some time interval $0 \rightarrow t$, $\hat{T}$ is the Dyson time ordering operator and $\rho(0)$ is the density operator of the system at time $t = 0$. The definition of $\hat{U}(t)$ as written in Equation (1.20) is a convenient short hand but the integral cannot actually be evaluated directly as written. It is often most efficient to approximate Equation (1.20) by discretising over time such that in any interval $\Delta t = \frac{t}{n}$ the Hamiltonian is essentially constant. The propagator is then given by:

$$\hat{U}(t) = \prod_{k=0}^{n-1} \exp\left\{-\mathrm{i}\hat{H}(k\Delta t)\Delta t\right\} \tag{1.21}$$

In the case of an entirely time-independent Hamiltonian the above result simplifies to:

$$\hat{U}(t) = \exp\left\{-\mathrm{i}\hat{H}t\right\} \tag{1.22}$$

which when substituted into Equation (1.19) gives the familiar solution to the Liouville-von Neumann equation for a system evolving under only time-independent interactions:

$$\rho(t) = \exp\left\{-\mathrm{i}\hat{H}t\right\}\rho(0)\exp\left\{\mathrm{i}\hat{H}t\right\} \tag{1.23}$$

We are predominantly interested in following a chosen observable rather than the whole system, to which end it is necessary to project out the relevant component of the density matrix. The projection of $\rho(t)$ onto the state i is given by the trace of the product of the projection operator, $\hat{Q}_i$, for that state with the density matrix:

$$P_i(t) = \left\langle \hat{Q}_i \right\rangle (t) = \mathrm{Tr}\left\{ \rho(t)\hat{Q}_i \right\} \tag{1.24}$$

where the projection operator is defined as:

$$\hat{Q}_i = |Q_i\rangle \langle Q_i| \tag{1.25}$$

Modelling time-resolved MFEs, for example the quantum beat experiments of Molin and co-workers (for examples see Ref [61]), requires the direct solution of Equation (1.24), achieved by substitution of Equation (1.23) into Equation (1.24) followed by direct propagation of the initial density matrix over suitably discretised time-steps approximating the form of the Hamiltonian at each.

1.3.2 Calculating the Singlet Yield

Many experimental observations of MFEs measure the total yield from a given reaction channel, commonly the yield from the singlet channel which goes to a diamagnetic product. To calculate this quantity it is necessary to integrate Equation (1.24), multiplied by an appropriate reaction decay function, over all time. It is convenient to assume that both channels, triplet and singlet, react by a first order process with equal rate constants. The kinetics of the reactions may then be accounted for using a simple exponential decay term, $k\mathrm{e}^{-kt}$, such that all populations and coherences decay with the same rate constant, k. The overall singlet yield is then given by [62]:

$$\Phi_S = k \int_0^\infty \mathrm{Tr}\left\{ \hat{Q}_S \rho(t) \right\} \exp\{-kt\}\, \mathrm{d}t \tag{1.26}$$

where k is the rate constant for reaction and $\hat{Q}_S$ is the singlet projection operator. This can be defined in several useful forms such that:

$$\begin{aligned}\hat{Q}_S &= |S\rangle\langle S| \\ &= \frac{1}{2}(|\alpha\beta\rangle - |\beta\alpha\rangle)(\langle\alpha\beta| - \langle\beta\alpha|) \\ &= \frac{1}{4}\hat{\mathbb{1}} - \hat{S}_{Ax}\hat{S}_{Bx} - \hat{S}_{Ay}\hat{S}_{By} - \hat{S}_{Az}\hat{S}_{Bz} \\ &= \frac{1}{4}\hat{\mathbb{1}} - \hat{S}_{Az}\hat{S}_{Bz} - \frac{1}{2}(\hat{S}_{A+}\hat{S}_{B-} + \hat{S}_{A-}\hat{S}_{B+}) \\ &= \frac{1}{4}\hat{\mathbb{1}} - \hat{S}^A \cdot \hat{S}^B \end{aligned} \tag{1.27}$$

and $\hat{S}_{Xi}$ is the i-operator for the electron on radical X ($X = A, B$) formed, according to Equation (1.14) with $\hat{\mathbb{1}}$ on all other spins (matrix sizes of two for the other electron and M for the nuclear configurations) as:

$$\hat{S}_{Ai} = \hat{S}_i \otimes \hat{\mathbb{1}}_2 \otimes \hat{\mathbb{1}}_M$$
$$\hat{S}_{Bi} = \hat{\mathbb{1}}_2 \otimes \hat{S}_i \otimes \hat{\mathbb{1}}_M$$

In order to evaluate the singlet yield, Equation (1.23) is substituted into Equation (1.26) [19]:

$$\Phi_S = \frac{k}{M}\int_0^\infty \mathrm{Tr}\left\{\hat{Q}_S \exp\left\{-\mathrm{i}\hat{H}t\right\}\hat{Q}_S \exp\left\{\mathrm{i}\hat{H}t\right\}\right\}\exp\{-kt\}\,\mathrm{d}t \tag{1.28}$$

where $\frac{1}{M}$ accounts for normalisation over the nuclear configurations of the initial singlet state.

It is possible to diagonalise the Hamiltonian such that $A^{-1}\hat{H}A = \hat{h}$ where $\hat{h}$ is a diagonal matrix of the eigenvalues of $\hat{H}$. The Hamiltonian is Hermitian and therefore A must be unitary and we can use the property $A^{-1} = A^T$ to avoid performing an unnecessary matrix inversion. If A diagonalises the Hamiltonian it will also diagonalise the matrix exponential:

$$A^T \exp\{\pm\mathrm{i}\hat{H}t\}A = \exp\left\{\pm\mathrm{i}\hat{h}t\right\} \tag{1.29}$$
$$\Rightarrow \exp\{\pm\mathrm{i}\hat{H}t\} = A\exp\left\{\pm\mathrm{i}\hat{h}t\right\}A^T \tag{1.30}$$

Substituting this into Equation (1.28) gives:

$$\Phi_S = \frac{k}{M}\int_0^\infty \mathrm{Tr}\left\{\hat{Q}_S A\exp\left\{-\mathrm{i}\hat{h}t\right\}A^T\hat{Q}_S A\exp\left\{\mathrm{i}\hat{h}t\right\}A^T\right\}\exp\{-kt\}\,\mathrm{d}t \tag{1.31}$$

Within a trace it is possible to perform a cyclic permutation to give:

$$\Phi_S = \frac{k}{M}\int_0^\infty \mathrm{Tr}\left\{\tilde{\hat{Q}}_S \exp\left\{-\mathrm{i}\hat{h}t\right\}\tilde{\hat{Q}}_S \exp\left\{\mathrm{i}\hat{h}t\right\}\right\}\exp\{-kt\}\,\mathrm{d}t \tag{1.32}$$

where $\tilde{\hat{Q}}_S = A^T\hat{Q}_S A$, *i.e.* the projection operators have been transformed into the eigenbasis of the Hamiltonian. We then expand the trace such that:

$$\Phi_S = \frac{k}{M}\int_0^\infty \sum_{m,n}(\exp\left\{-\mathrm{i}\hat{h}t\right\})_{mm}(\tilde{\hat{Q}}_S)_{mn}(\exp\left\{\mathrm{i}\hat{h}t\right\})_{nn}(\tilde{\hat{Q}}_S)_{nm}\exp\{-kt\}\,\mathrm{d}t \tag{1.33}$$

$$= \frac{k}{M}\int_0^\infty \sum_{m,n}\exp\{\mathrm{i}\omega_{nm}t\}\,(\tilde{\hat{Q}}_S)_{mn}(\tilde{\hat{Q}}_S)_{nm}\exp\{-kt\}\,\mathrm{d}t \tag{1.34}$$

where $\omega_{nm} = h_{nn} - h_{mm}$. As $\tilde{\hat{Q}}_S$ is Hermitian we can simplify further to give:

$$\Phi_S = \frac{k}{M}\int_0^\infty \sum_{m,n}\exp\{\mathrm{i}\omega_{nm}t\}\left|(\tilde{\hat{Q}}_S)_{mn}\right|^2\exp\{-kt\}\,\mathrm{d}t \tag{1.35}$$

The singlet yield is necessarily real, and so is $\left|(\tilde{\hat{Q}}_S)_{mn}\right|^2$ therefore we retain only the real part of the exponential:

$$\Phi_S = \frac{k}{M}\int_0^\infty \sum_{m,n}\cos\omega_{nm}t\left|(\tilde{\hat{Q}}_S)_{mn}\right|^2\exp\{-kt\}\,\mathrm{d}t \tag{1.36}$$

which is evaluated as:

$$\Phi_S = \frac{k}{M}\sum_{m,n}\left|(\tilde{\hat{Q}}_S)_{mn}\right|^2 f(\omega_{nm}) \tag{1.37}$$

$$f(\omega_{nm}) = \frac{k^2}{k^2+\omega_{nm}^2} \tag{1.38}$$

For simulations of MARY spectra Equation (1.37) is evaluated as a function of applied field strength. To calculate anisotropic reaction yields evaluation of Equation (1.37) is repeated over a range of field directions, usually defined by the polar coordinates θ and ϕ. As the absolute variation in yield with θ and ϕ is often very small it is helpful to display only the anisotropic part of the singlet yield which is defined as:

$$\Phi_S^{\mathrm{Aniso}}(\theta,\phi) = \Phi_S(\theta,\phi) - \overline{\Phi_S} \tag{1.39}$$

where $\overline{\Phi_S}$ is the spherical average of the singlet yield.

Although we are often interested in the singlet yield from singlet born RPs this is not always the case and it is equally possible to use any other projection operator or initial density matrix, the simplification step of Equation (1.35) is skipped.

1.3.3 The Hamiltonian

The total Hamiltonian for a spin system is the sum of all interactions and, as aforementioned, can be formed as a linear combination over the complete set of 2^N multi-spin operators with real coefficients. The values of the coefficients are determined by the interactions in effect for a particular system. In practice there are only a few interactions which need to be included in the Hamiltonian and so most coefficients in the expansion are simply zero.

Types of Interaction

Of those interactions the most practically significant can be categorised into one of three types: interactions linear, bilinear and quadratic in spin [63]. Linear interactions are those in which the spin, S, couples to an external vector, $\vec{V}$, with some interaction tensor A describing the system-dependent factors affecting the magnitude of interaction. These interactions can be described by the general Hamiltonian:

$$\hat{H}_{\text{Lin}} = \hat{S} \cdot A \cdot \vec{V} = \begin{pmatrix} \hat{S}_x & \hat{S}_y & \hat{S}_z \end{pmatrix} \begin{pmatrix} A_{xx}(t) & A_{xy}(t) & A_{xz}(t) \\ A_{yx}(t) & A_{yy}(t) & A_{yz}(t) \\ A_{zx}(t) & A_{zy}(t) & A_{zz}(t) \end{pmatrix} \begin{pmatrix} V_x \\ V_y \\ V_z \end{pmatrix} \tag{1.40}$$

The most common example is the Zeeman interaction, where the vector $\vec{V}$ is the applied field and the interaction tensor is, for example, chemical shielding (NMR) or the g-tensor (EPR).

Bilinear interactions describe the coupling between spins S and L.

$$\hat{H}_{\text{Bilin}} = \hat{S} \cdot A \cdot \vec{L} = \begin{pmatrix} \hat{S}_x & \hat{S}_y & \hat{S}_z \end{pmatrix} \begin{pmatrix} A_{xx}(t) & A_{xy}(t) & A_{xz}(t) \\ A_{yx}(t) & A_{yy}(t) & A_{yz}(t) \\ A_{zx}(t) & A_{zy}(t) & A_{zz}(t) \end{pmatrix} \begin{pmatrix} \hat{L}_x \\ \hat{L}_y \\ \hat{L}_z \end{pmatrix} \tag{1.41}$$

If S and L are both electron spins, A could describe the dipolar or exchange coupling, if they are both nuclei A is either the dipolar (through-space) or the scalar (through-bond) coupling tensor. If one spin is an electron and one a nucleus A is the hyperfine interaction tensor. Any

interaction between two distinct spins may be written in this form with its exact nature manifest only in the tensor A.

An alternative form for a bilinear interaction in its eigenframe can be derived in terms of the ISTs as defined in Equation (1.17) as:

$$\begin{aligned} &A_{xx}\hat{S}_x\hat{I}_x + A_{yy}\hat{S}_y\hat{I}_y + A_{zz}\hat{S}_z\hat{I}_z = \\ &\frac{2A_{zz} - (A_{xx} + A_{yy})}{\sqrt{6}}\hat{T}_{2,0} + \frac{A_{xx} - A_{yy}}{2}\left(\hat{T}_{2,2} + \hat{T}_{2,-2}\right) \end{aligned} \tag{1.42}$$

where A_{ii} can be identified with the principal components of a bilinear interaction tensor, Equation (1.41). Two further properties of the interaction can be defined, namely the axiality Ax and rhombicity Rh such that:

$$Ax = \frac{1}{6}\left(A_{xx} + A_{yy} - 2A_{zz}\right) \tag{1.43}$$

$$Rh = \frac{1}{2}\left(A_{xx} - A_{yy}\right) \tag{1.44}$$

If S and L are the same spin, for example when describing a quadrupolar interaction, the interaction is quadratic. This class of interaction is rarely encountered in spin chemical calculation, though it has been suggested that quadrupolar interactions may act as a source of anisotropy in RP reactions [64]. In the following those interactions which are commonly active in spin chemistry calculations are described.

Zeeman Interaction

An effect of magnetic fields on atomic emission spectra was first observed by Zeeman [65] and it is for him that the interaction of spin with magnetic fields is named, though of course the physics underlying the phenomenon he observed was not explained fully until much later. Moving charges possess a magnetic moment and for electrons and nuclei the motion is associated with their angular momenta [10]. Electrons have two main sources of angular momentum; from their motion within an orbital and from their intrinsic spin. Coupling with molecular rotations can also occur but is usually only significant in the gas-phase, for example this can be an important source of relaxation in gas-phase NMR [66]. First-order spin-orbit coupling between orbital and spin angular momenta occurs only when the electron is found in a degenerate electronic ground state. In most organic molecules the environment is sufficiently asymmetric to remove the degeneracy and hence quench the orbital angular momentum. We may thus consider the

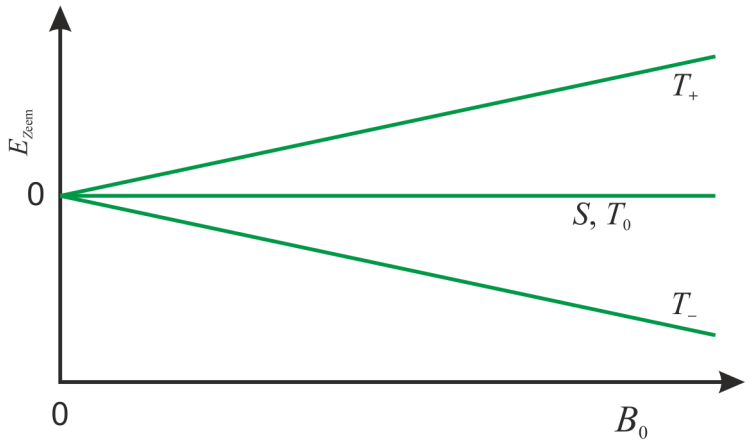

Figure 1.6. Energy levels of singlet, S, and triplets, $T_{0,\pm}$ in an applied magnetic field, B_0, in the absence of other interactions.

electron magnetic moment, like the nuclear one, as arising solely from the inherent spin. Of course higher order contributions to the spin-orbit coupling also occur in most radical species and are manifest in g-values which deviate from that of a bare electron.

The magnetic moment, μ, associated with a spin, I is given by $\mu = g\mu_{\mathrm{B}}I$ where g and μ_{B} are the g-value and Bohr magneton respectively. In EPR the g-value of an electron is akin to chemical shielding in NMR and contains information about the local magnetic environment. The energy operator, in angular frequency units, of the isotropic interaction of a spin with an applied magnetic field, $\vec{B}$, is given by:

$$\hat{H}_{\mathrm{Zeem}} = -\gamma_i \hat{S} \cdot \vec{B_0} \tag{1.45}$$

where the gyromagnetic ratio of a spin i is given by $\gamma_i = \frac{g_i \mu_{\mathrm{B}}}{\hbar}$. If the direction of $\vec{B}_0$ is used to define the laboratory z-axis then the Hamiltonian reduces to:

$$\hat{H}_{\mathrm{Zeem}} = -\gamma_i \hat{S}_z B_0 \tag{1.46}$$

for which a single electron has eigenvalues $E_{\mathrm{Zeem}} = -\gamma_e M_S B_0$, the Zeeman energies of the states. Fig 1.6 shows the energy levels of the RP singlet and triplet states as a function of field strength. The two triplet states with $M_S = \pm 1$ diverge in energy as B_0 increases, whereas the singlet and $M_S = 0$ triplet remain unaffected.

In cases where the Zeeman interaction is dominant, for example in high field spectroscopy, the field direction defines the eigenaxis of the system. However, at low field, which is the limit of interest in most of this thesis, the situation is distinctly more complicated.

Hyperfine Interaction

The hyperfine interaction couples the spin of an electron and a magnetic nucleus [25]. There are two contributions to the interaction, the first is a dipole-dipole interaction between the two magnetic moments. Like a simple point-dipole interaction this component of the hyperfine interaction is anisotropic, however the electron is not localised in space and to calculate the full contribution it is necessary to integrate over the electronic distribution. For a radical rapidly tumbling in solution this interaction is averaged to zero. The second component of the HFI is purely isotropic, named the Fermi contact interaction, and arises from the interaction of electronic and nuclear magnetic moments within the nucleus itself. Thus some electron density at the position of the nucleus is required which only occurs when the electron orbital has some *s*-orbital character.

The combination of the two contributions returns a 3-by-3 HFI tensor which may be used with Equation (1.41) to form the HFI part of the Hamiltonian [67]:

$$\hat{H}_{\mathrm{HFI}} = \sum_i \hat{S} \cdot A_i \cdot \hat{I}_i \tag{1.47}$$

where $\sum_i$ indicates a sum over all electron-nucleus pairs in the system.

Exchange Interaction

The exchange interaction describes the interaction between two electrons deriving from their spin states and arises from the Pauli exclusion principle. It results in a splitting between the triplet and singlet states under the Hamiltonian [68]:

$$\hat{H}_{\mathrm{Ex}} = -J\hat{S}_A \cdot \hat{S}_B \tag{1.48}$$

For electrons in distinct orbitals that are nevertheless close in space it is normally argued that the Pauli exclusion principle forbids two electrons of the same spin, or more precisely described as a pair by a symmetric spin wavefunction, to exist at the same point in space. This creates a fermi-hole in the probability distribution for both electrons coinciding and thus on average electrons in the triplet state spend more time further apart, experience less repulsion and are lower in energy than the corresponding singlet state. It is thus somewhat counterintuitive that in the RP case the singlet state is normally the lower in energy, Fig 1.7.

For a RP it is necessary to remember that the electrons do not necessarily occupy distinct

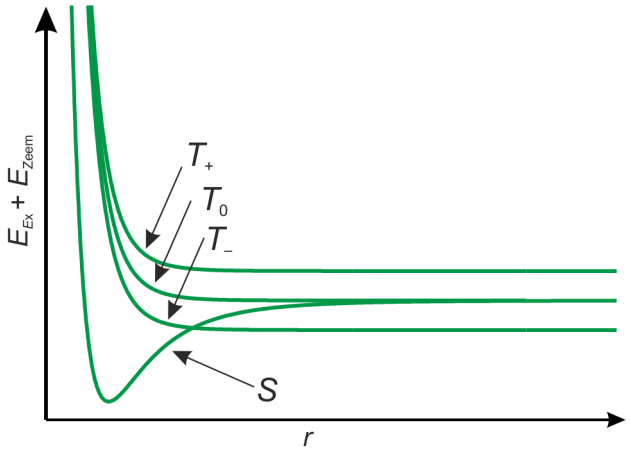

Figure 1.7. Energies of the singlet and triplet states as a function of inter-electron separation due to exchange and Zeeman interactions

orbitals, unlike for example when justifying Hund's rule of maximum multiplicity. Consider instead bringing together two hydrogen atoms, each has a single electron in a $1s$ orbital [68]. At a great separation there is no significant overlap of wavefunctions and the exchange interaction is negligible; however, as they get the closer the orbitals overlap. Two molecular orbitals (MOs) begin to form [69]: one bonding and one antibonding. The lower energy state will have both electrons in the bonding orbital – to exist in the same MO the electrons must have antiparallel spins. Thus the singlet electron configuration is lower in energy than the triplet which must exist with one bonding and one antibonding electron.[4]

Although the bonding picture in larger molecules is more complex the same principles apply – only the singlet state can form a bonding interaction when the inter-electron distance is reduced. The hydrogen atom model was used to derive the distance-dependence of $J(r)$ and this model is usually applied to all RPs in solution [14, 70]. The function is assumed to be independent of radical orientation and to decrease exponentially with distance:

$$J(r) \approx J_0 \mathrm{e}^{-\frac{r}{r_J}} \tag{1.49}$$

where r is the inter-radical separation, $J_0 \approx 2\times10^{17}$ rads^{-1} and $r_J \approx 50$ pm is a range parameter.

The singlet and triplet states are eigenstates of the exchange coupling and hence a large exchange interaction causes the RP system to collapse into this basis. This has the dual effect of removing the coherences between the singlet and triplet states and suppressing further evolution

[4]Of course within the electronic configuration $1\sigma^1 2\sigma*^1$ the triplet spin state is lower in energy than the corresponding singlet for the normal reasons – this second excited singlet does not appear in normal RP reactions as vibrational relaxation following photoexcition is assumed to be rapid.

between the states of different spin multiplicities. There can be no MFEs if the electrons are not sufficiently far apart, for radicals in solution it is usually an acceptable approximation to ignore exchange coupling, assuming it only comes into play when the radicals approach close enough to react anyway.

Dipolar Interaction

Each electron feels a magnetic field from its partner [71], at sufficient separation this may be approximated as the interaction between two point-dipoles [60]:

$$\hat{H}_{\mathrm{D}} = \frac{\mu_0 \gamma_e^2}{4\pi\hbar^2 r^3}\left[\hat{S}_A \cdot \hat{S}_B - \frac{3}{r^2}(\hat{S}_A \cdot \vec{r})(\hat{S}_B \cdot \vec{r})\right] \tag{1.50}$$

where μ_0 is the permeability of free space, r is the inter-electron separation and $\vec{r}$ is a unit vector along the spin-spin direction. When treating the electrons as point-dipoles the inter-radical separation is estimated from the centre of the electron distribution, though strictly this should be integrated over. Like the exchange coupling a strong dipolar interaction suppresses singlet-triplet interconversion and will prohibit the observation of a MFE, it too is considered negligible in most calculations. It has also been suggested that at certain separations the dipolar and exchange interactions effectively cancel out and have no overall effect on RP spin dynamics [21].

1.3.4 Liouville Space Simulations

Thus far all the influences on the radical pair have affected only the coherent evolution. When incoherent processes are considered, for example non-exponential reaction kinetics, relaxation and spatial diffusion, the Liouville-von Neumann equation, Equation (1.18), is no longer linear and the approach to its solution outlined above is no longer possible. In order to solve the equation in Hilbert space a numerical integration procedure over a time-propagated singlet probability is required [72]. Hence, under these conditions it is more convenient to move the simulation into Liouville space in which the spin dynamics can again be described by a linear equation but now incoherent as well as coherent terms appear in the equation of motion. The stochastic Liouville-von Neumann equation is defined as:

$$\frac{\mathrm{d}\hat{\rho}}{\mathrm{d}t} = -\mathrm{i}\hat{\hat{L}}(t)\hat{\rho}(t) \tag{1.51}$$

in which $\hat{\hat{L}}(t)$, the Liouvillian, is given by:

$$\hat{\hat{L}}(t) = \hat{\hat{H}}(t) + \mathrm{i}\hat{\hat{K}} + \mathrm{i}\hat{\hat{R}} + \mathrm{i}\hat{\hat{\Gamma}} \tag{1.52}$$

where $\hat{\hat{H}} = \hat{H} \otimes \hat{\mathbb{1}} - \hat{\mathbb{1}} \otimes \hat{H}^T$ is the commutator superoperator of the coherent Hamiltonian, $\hat{\hat{K}}$ is the kinetic superoperator, $\hat{\hat{R}}$ is the relaxation superoperator and $\hat{\hat{\Gamma}}$ describes radical pair motion [73]. $\hat{\rho}$ is the state vector and is the Liouville space equivalent of the density matrix in Hilbert space; it is formed from the density matrix by row-wise flattening. That is:

$$|\hat{\rho}\rangle = \begin{Bmatrix} \rho_{11} \\ \rho_{12} \\ \vdots \\ \rho_{21} \\ \rho_{22} \\ \vdots \\ \rho_{nn} \end{Bmatrix} \tag{1.53}$$

where ρ_{ij} is the element in the i^{th} row and j^{th} column of the density matrix, $\langle i|\,\rho\,|j\rangle$ and $|i\rangle$ are the basis states in Hilbert space.

The general solution of the Liouville-von Neumann equation is of the form:

$$\hat{\rho}(t) = \hat{T}\exp\left\{-\mathrm{i}\int_0^t \hat{\hat{L}}(t')\mathrm{d}t'\right\}\hat{\rho}(0) \tag{1.54}$$

and the expectation value of an observable is given by:

$$P_i(t) = \left\langle \hat{Q}_i^{\dagger} | \hat{\rho}(t) \right\rangle \tag{1.55}$$

where $\hat{Q}_i$ is the projection operator for the observable.

There are several possible ways of computing the time-dependence of the density operator numerically. Equation (1.54) could be treated using any ordinary differential equation (ODE) solving algorithm such as Runge Kutta. More commonly, a method of direct propagation is adopted. In this case the Liouvillian, Equation (1.51), is discretised in time, as in Equation (1.21), such that over a given period, $\Delta t = \frac{t}{n}$, it is independent of time. The density operator

is then given by:

$$\hat{\rho}(t) = \exp\left\{-\mathrm{i}\hat{\hat{L}}((n-1)\Delta t)\Delta t\right\}\exp\left\{-\mathrm{i}\hat{\hat{L}}((n-2)\Delta t)\Delta t\right\}\cdots\exp\left\{-\mathrm{i}\hat{\hat{L}}(0)\Delta t\right\}\hat{\rho}(0) \quad (1.56)$$

It is not necessary to step evenly in time, for example in cases of different pulsed NMR and EPR experiments the Hamiltonian is piece-wise constant over blocks of time that are rarely equal in duration. To evaluate Equation (1.56) the starting vector is multiplied sequentially by the exponentials of the Liouvillians, known as propagators, until $\sum_n \Delta t_n = t$. A time-independent Liouvillian, whose evolution is described by $\hat{\rho}(t) = \exp\left\{-\mathrm{i}\hat{\hat{L}}t\right\}\hat{\rho}(0)$, may be solved by any of the techniques outlined, though of course the application of the propagator occurs only once.

The integral over all time, required to calculate the total yield of a chosen observable, usually singlet product, is best solved by taking a Laplace transform, with $s \to 0$, such that:

$$\Phi_S = k\left\langle \hat{Q}_S \left| (s\hat{\hat{\mathbb{1}}} + \mathrm{i}\hat{\hat{L}})^{-1} \right| \hat{\rho}(0) \right\rangle \quad (1.57)$$

which can be efficiently computed using a left product function, for example the MATLAB 'backslash' function [74].

1.3.5 Reaction Kinetics

Traditionally, reaction kinetics with non-equal rate constants for the singlet and triplet channels have been accounted for using the Haberkorn kinetic superoperator [75]:

$$\hat{K}\rho = -\frac{k_S}{2}\left(\hat{Q}_S\rho + \rho\hat{Q}_S\right) - \frac{k_T}{2}\left(\hat{Q}_T\rho + \rho\hat{Q}_T\right) \quad (1.58)$$

where k_S and k_T are the singlet and triplet rate constants respectively. This can be more conveniently used in terms of anti-commutation superoperators ($\hat{\hat{Q}}_i = \hat{Q}_i \otimes \hat{\mathbb{1}} + \hat{\mathbb{1}} \otimes \hat{Q}_i$) in Liouville space where:

$$\hat{\hat{K}}\hat{\rho} = \left(-\frac{k_S}{2}\hat{\hat{Q}}_S - \frac{k_T}{2}\hat{\hat{Q}}_T\right)\hat{\rho} \quad (1.59)$$

This form of equation reduces to exponential decay in the limit that $k_S = k_T$.

This method of simulating reaction processes, via projection operators, has recently been called into question. It is claimed that the Haberkorn equation does not account for quantum measurement effects to which end an alternative definition was proposed by Kominis [76–78],

which has incited much discussion but attracted little support in itself. A second master equation was proposed by Jones and Hore following from quantum measurement arguments. For the full derivation see Ref [79] from which only the final result is reproduced here:

$$\hat{K}\rho = -(k_S + k_T)\rho + k_S\hat{Q}_T\rho\hat{Q}_T + k_T\hat{Q}_S\rho\hat{Q}_S \tag{1.60}$$

which in Liouville space is written as:

$$\hat{\hat{K}}\hat{\rho} = -(k_S + k_T)\hat{\rho} + k_S\left(\hat{Q}_T \otimes \hat{Q}_T^T\right)\hat{\rho} + k_T\left(\hat{Q}_S \otimes \hat{Q}_S^T\right)\hat{\rho} \tag{1.61}$$

where the subscript denotes the spin-state and the superscript T indicates a transpose.

Several independent researchers have rederived the Haberkorn master equation by considering the RP as coupled to vibrationally excited states of the ground state [80, 81]. It has also been suggested that different reaction mechanisms may require different master equations, see Refs [82–84] an idea also supported by the derivation of $\hat{\hat{K}}$ from a quantum optical approach by Tiersch [85] which arrives at the Haberkorn and Jones-Hore equations as two limiting cases.

In practice the only difference between the Haberkorn and Jones-Hore equations is a factor of two in the decay of S-T coherences. These coherences are also eroded by any relaxation processes at work in the system and so an experimental scheme by which the two may be distinguished is hard to envisage. Given the very small differences between the two master equations the simulations in this thesis use the traditional Haberkorn master equation.

1.3.6 Relaxation

Although we would often like to think that spin systems are isolated from the rest of the universe this is never the case in reality. Most spin systems are constantly interacting with their surroundings incurring time-dependent fluctuating interactions that bring about relaxation. It should be noted that we use the term relaxation to mean all dissipation processes, rather than decoherence induced by chemical reaction, by which we mean any incoherent processes which alter the populations of states or coherences between them.

Relaxation Mechanisms

In most cases the time-dependence of an interaction is generated by random thermal motion of the system or surroundings (or both), through translational and rotational diffusion in liquids or

lattice vibrations in the solid state. Translational motion and vibrations bring about fluctuation in the orientation and separation of two magnetic species which will lead to modulation of the distance-dependent interactions, such as dipolar and exchange couplings. Modulation of these interactions can also be achieved through electron transfer processes (Chapter 5). Anisotropic interactions are modulated by rotational diffusion, *i.e.* molecular tumbling. Such interactions include the Zeeman interaction when the g-tensor is anisotropic though the size of this contribution is strongly dependent on field strength. As organic radicals tend to have small anisotropies in their g-values this mechanism is usually insignificant for radicals at low field. Considerable anisotropic nuclear Zeeman interactions are rare and the effective nuclear equivalent of the electron g-tensor is the chemical shielding anisotropy. Again this is also only really important at high field where it is often the major contributor, along with rotational modulation of the direction-dependent dipole-dipole interaction, to relaxation in NMR experiments [86]. Modulation of the field-independent HFI is usually considered the dominant relaxation mechanism for radical pairs in solution.

There are some other more exotic relaxation mechanisms which are effective under specific conditions. For example, spin-rotation interaction, whereby molecular rotation causes the motion of the electrons and nuclei which, being charged, can induce small local magnetic fields which fluctuate in time and hence can cause spin-relaxation [66]. Degenerate electron exchange between radicals and their closed shell counterpart removes all coherence between the electron and its nuclei on the occurrence of every electron 'hop' – the effect of which is also relaxation [72].

Relaxation at High Field

Relaxation at high field is well understood and has been dealt with extensively [26, 60, 66, 86]. It is often described in terms of two distinct processes. The first is longitudinal or spin-lattice relaxation which is the return of a system to its equilibrium magnetisation, *i.e.* returning the populations of the α and β states to their Boltzmann equilibrium. For example in NMR, this is manifest as the build up or loss of magnetisation when the field is turned on or off respectively. This process requires an exchange of energy with the environment/lattice and is described by a characteristic time, T_1.

The second process is transverse or spin-spin relaxation which is the removal of coherences between spins. At high field this can be visualised using the vector model by considering the

precession of the magnetisation around the applied field direction at a rate dependent on the field strength. The magnetisations of all spins are produced in phase with one another, but fluctuations in the local field strength of each spin will cause them to experience varying Larmor frequencies, that is, precession at slightly different rates. As time goes on this will result in the randomisation of all phases, the coherences between spins are lost. This does not require energy transfer and is characterised by a time, T_2.

As T_1 and T_2 processes have very different energy dependencies, the two relaxation time scales can be several orders of magnitude apart, resulting in some experiments where only one form of relaxation is observed.

Relaxation at Low Field

At low field, when the applied field is less than or at most equal to the HFI strength, the picture is no longer so clear. To consider T_1 and T_2 processes in the same terms is unhelpful as the laboratory z-axis is no longer the eigenaxis of the system. The two radicals of a solution phase RP, with different nuclei and negligible exchange/dipolar interaction, will have different eigenaxes, hence the axis along which the spin angular momenta are quantised will be unique to each radical. There is no sense in describing the spin-lattice relaxation as a decay of magnetisation in such a system. However, a parallel may be drawn between the high and low field situations by generalising the T_1 process to the equilibration of populations in the eigenbasis of the system. At high field this coincides with the laboratory axis and at low fields is a composite of all interactions. The physical interpretation of the eigenstates of a low field system is rarely obvious. The T_2 process at low field is more readily extrapolated; we must now consider the coherences to be between the eigenstates of the system, not between the magnetisation of each spin.

In the density matrix formalism T_1 type processes evolve the diagonal elements, in the eigenbasis of the Hamiltonian, and T_2 processes erode the off-diagonal elements.

Lindblad Operators

In order to describe any system and its surroundings (environment) quantum mechanically it is necessary to make some approximations. In quantum optics a premium is placed on maintaining complete positivity (CP) throughout the course of system evolution. *A density matrix that is completely positive for all time will always have real positive eigenvalues.* The Lindblad master

equation was proposed as a form of dynamical map to propagate the system in time. For a very readable derivation see [87] Chapter 3, the most general result of which (Equation 3.66, p117) is reproduced here:

$$\mathcal{L}\rho_S = -\mathrm{i}\,[H, \rho_S] + \sum_{k=1}^{N^2-1} \Gamma_k \left(A_k \rho_S A_k^\dagger - \frac{1}{2} A_k^\dagger A_k \rho_S - \frac{1}{2} \rho_S A_k^\dagger A_k \right) \tag{1.62}$$

where A_k are the Lindblad operators, formed from linear combinations of the spin operators, and Γ_k are often considered in terms of correlation functions and may be seen as effective relaxation rates. The second term of Equation (1.62) when describing relaxation processes only (and not reaction) is often called the dissipator term. It is often convenient to use Equation (1.62) with artificial operators, i.e. not derived from a true description of the system, to describe relaxation phenomenologically, or to observe the effect of a particular form of dephasing [88].

One difficulty of using quantum dynamical semi-groups to derive a master equation for a particular system is in deriving the relevant Lindblad operators [89]. A microscopic derivation (Ref [87] p125) attempts to derive a master equation with a clear physical interpretation. In the process a series of approximations is applied and in so doing the guarantee of complete positivity is lost and the Redfield master equation is rederived.

Redfield Theory

There have been many treatments of relaxation in a spin dynamics context but the most prevalent description follows the work of Bloch, Redfield and Wangsness, often called BRW theory or simply Redfield theory [90, 91]. This accounts for relaxation through coupling of the system to an external classical bath or lattice and treats the latter perturbatively. For a system undergoing time-dependent fluctuations the Hamiltonian is written as the sum of time-independent $\hat{H}_0$ and time-dependent $\hat{H}_1$ terms. An excellent review of the theory of spin-lattice relaxation is provided by Goldman in Ref [92]. The assumptions made in the course deriving Redfield theory are summarised:

1. The Hamiltonians are in the perturbative limit *i.e.* $\|\hat{H}_1\| \ll \|\hat{H}_0\|$.

2. The perturbing Hamiltonian has a zero ensemble average.

3. There are only weak correlations between the spin system and the bath, *i.e.* the system is in the weak coupling limit.

4. Noise functions are stationary.

5. Correlation functions decay much faster than the system evolution due to relaxation.

(2-5 together are also known as the Born-Markov approximation). The regions of applicability of these assumptions for low field simulations have recently been investigated [93] with the conclusion that Redfield theory is usually accurate well beyond the normally expected range. At high magnetic field several further approximations are possible which allow for ready evaluation of the relaxation effects, most commonly the secular approximation. However at low field no terms may be discounted. Redfield theory of relaxation will be presented in more detail in Chapter 2.

1.4 Summary

This chapter has aimed to briefly introduce spin chemistry both as an experimentally observed phenomenon and as a well-developed area of quantum mechanical study. Despite being a thesis concerned exclusively with the theoretical description of spin dynamical processes all calculations are carried out with a view to better understanding the physical processes occurring in both laboratory experiments and in biological processes.

Chapter 2 describes the use of state-space restriction techniques to improve the efficiency of spin dynamics calculations, with particular application to radical pair reactions. A method to produce superoperators directly into an analytically derived reduced state-space is presented which greatly improves the efficiency of Liouville space spin chemical calculations [94]. A brief overview of the spin dynamics software library *Spinach* (http://spindynamics.org/Spinach.php) [95], in which this work is implemented, is given.

Chapter 3 introduces the concepts of coherence and entanglement and seeks to understand their role in the magnetic field sensitivity of the radical pair mechanism. The inherent anisotropy of the triplet states is explored as a source of directional information in RP reactions.

In Chapter 4 the avian magnetocompass is introduced along with an overview of the behavioural data collected to date. The main work of this chapter is concerned with understanding the influence of oscillating fields on RP reactions, particularly with a view to explaining the remarkable apparent sensitivity of birds to weak radio-frequency fields at the Zeeman resonance. The suggestion of oxygen or superoxide as a potential partner in the putative RPM is investigated [96]. Furthermore we explore whether it is possible to expect orientation from birds under

radio-frequency fields alone.

Chapter 5 reports the attempts to model MFE data recorded by co-workers in the Timmel group for *Escherichia coli* photolyase and *Arabidopsis thaliana* cryptochrome 1. Several relaxation models were trialled with only one particular form of dephasing fitting the data to a satisfactory degree.

In Chapter 6 the amplification of anisotropic MFEs for RPs with strong isotropic magnetic field-strength dependence using the direction dependent field-strength from nearby magnetic nanoparticles is considered. We investigate both one and two nanoparticle systems.

Chapter 7 takes a step away from radical pairs and weak magnetic fields. In this chapter we make use of the spin dynamics software *Spinach* to investigate the symmetry requirements of long-lived nuclear spins states in NMR systems [97].

Chapter 2

State Space Restriction

2.1 Introduction

The field of spin dynamics was developed to describe the interaction of electron and nuclear spins with their magnetic environment and with each other. This physical formalism, which was introduced in Chapter 1, has been used, for example, to simulate magnetic resonance experiments and the outcome of radical pair reactions. Ideally, we would like to be able to exactly simulate the spectra of any realistic molecule and to calculate the magnetic field effect on any chemically feasible radical pair. In reality this is rarely possible.

Every spin has an associated angular momentum, I, and correspondingly $2I+1$ projections onto the laboratory frame. To describe one spin of spin I we require a $2I+1$ by $2I+1$ matrix, for example a lone spin-$\frac{1}{2}$ is described by the 2×2 Pauli matrices. To describe the dynamics of two spins with spin angular momentum quantum numbers I and J, we must take direct products of the individual matrix representations and reach a representation of size $(2I+1)(2J+1)$. The state-space associated with a particular problem scales exponentially with the number of spins involved. The blue line of Fig 2.1 shows the Hilbert state-space size for a calculation of a system of spins-$\frac{1}{2}$. For calculations carried out in Liouville space, as is necessary if incoherent processes need to be included, the situation is even worse. The matrix dimensions in Liouville space are the square of those in Hilbert space, thus for the previous IJ system the Liouville space representation is now $(2I+1)^2(2J+1)^2$, *i.e.* the state-space size now scales with the square of the spin multiplicities. The green line in Fig 2.1 shows the Liouville space matrix size as a function of the number of spin-$\frac{1}{2}$.

Naturally, computers cannot manipulate enormous matrices. While very large ($\approx 100,000\times$

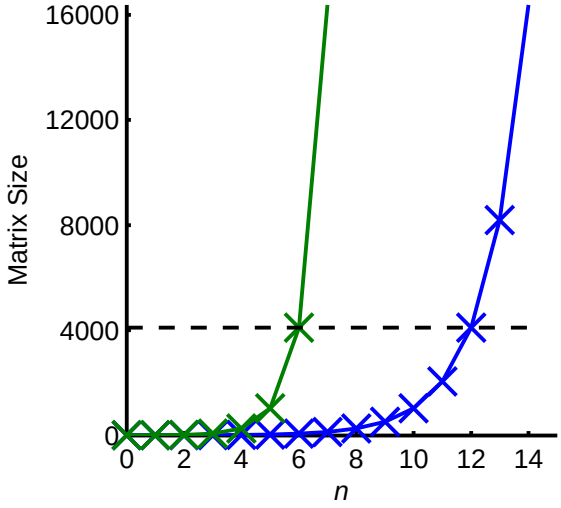

Figure 2.1. Matrix size for n spin-$\frac{1}{2}$ in Hilbert space blue, 2^n and Liouville space green, 4^n. The black dotted line indicates the approximate limiting size for normal workstation matrix manipulation in MATLAB.

$100,000$) sparse matrices can often be stored, carrying out operations on them increases the memory requirements and processing power needed. Matrix diagonalisation and multiplication, which are required for radical pair simulations in Hilbert space, scales as $\mathcal{O}(N^3)$, thus swiftly becomes prohibitively large. In addition diagonalisation even of sparse matrices produces dense eigenvectors which are much more memory-expensive to store.

The exponential scaling problem of spin dynamics calculations is well-known and there have been many 'tricks' suggested for reducing the size of the matrix representation describing the problem. In this chapter we have sought to investigate several state-space restriction (SSR) techniques, that had previously been applied with some success to Liouville-space NMR simulations [98, 99] to spin chemical problems. In the light of these results new techniques were developed for SSR in spin chemistry which could be extended to reduce matrix dimensions in other spin dynamics simulations. A procedure has been developed to analytically reduce the state-list of a simulation and subsequently to form the requisite operators directly into the reduced state-space and this was reported in Ref [94]. These techniques have been extended to include relaxation and chemical kinetics in the Liouvillian superoperator describing system evolution. Many of the procedures outlined in this chapter have been implemented in the *Spinach* library of codes, a spin dynamics software package which can be downloaded from http://spindynamics.org/Spinach.php and which was described in Ref [95].

2.1.1 Basis States

Many different sets of basis states can be used to carry out spin dynamics simulations. The most natural is perhaps the M_S basis (αs and βs for spin-$\frac{1}{2}$) in which the Pauli operators are defined but this is by no means the only possibility.

Hilbert Space Transformation

In order to transform between bases it is necessary to write a transformation matrix, $\hat{\Omega}$, in which the columns give the linear combination coefficients of the new basis state expanded in terms of the original basis states. For example, it is often deemed convenient to carry out Hilbert space calculations in the ST (singlet-triplet) basis instead. The singlet and triplet states of a two-spin system in terms of αs and βs were defined in Equations (1.3) and (1.4). For the transformation of basis $\{|\alpha\alpha\rangle, |\alpha\beta\rangle, |\beta\alpha\rangle, |\beta\beta\rangle\} \rightarrow \{|S\rangle, |T_+\rangle, |T_0\rangle, |T_-\rangle\}$, this leads to the transformation matrix:

$$\hat{\Omega}_{\alpha\beta\rightarrow ST} = \begin{pmatrix} 0 & 1 & 0 & 0 \\ \frac{1}{\sqrt{2}} & 0 & \frac{1}{\sqrt{2}} & 0 \\ -\frac{1}{\sqrt{2}} & 0 & \frac{1}{\sqrt{2}} & 0 \\ 0 & 0 & 0 & 1 \end{pmatrix} \tag{2.1}$$

such that, $\hat{A}_{ST} = \hat{\Omega}^\dagger \hat{A}_{\alpha\beta} \hat{\Omega}$, where $\hat{A}$ is an arbitrary operator.

Liouville Space Transformation

A basis transformation superoperator, $\hat{\hat{\Omega}}$, in Liouville space can be formed in one of two ways. The first makes use of the Hilbert space transformation operator which is simply is scaled up, $\hat{\hat{\Omega}} = \hat{\Omega} \otimes \hat{\Omega}$. Alternatively $\hat{\hat{\Omega}}$ can be formed following the same procedure as was used for Equation (2.1), *i.e.* the new basis vectors are written in terms of linear combinations of the original Liouville space basis vectors (which will often be the products of Hilbert space basis vectors, $|ijk\cdots\rangle\langle i'j'k'\cdots|$). The transformation is then carried out according to:

$$\hat{\hat{A}}_{\text{new}} = \hat{\hat{\Omega}}^\dagger \hat{\hat{A}}_{\text{old}} \hat{\hat{\Omega}} \tag{2.2}$$

Irreducible Spherical Tensors

For our purposes, the normalised irreducible spherical tensors (nISTs), Equation (1.11), have proven particularly convenient as a basis set.[1] They are directly proportional to the spin operators, are normalised and have well defined properties under 3D rotations [12]. The transformation matrix from the $\alpha\beta$ product basis to nIST basis is formed by row-wise stretching the nIST operators defined in the $\alpha\beta$ basis and then concatenating the resulting vectors into a matrix. For a spin system comprising one spin the Liouville space transformation superoperator for $\{|\alpha\rangle\langle\alpha|, |\alpha\rangle\langle\beta|, |\beta\rangle\langle\alpha|, |\beta\rangle\langle\beta|\} \rightarrow \left\{\hat{T}_{0,0}, \hat{T}_{1,1}, \hat{T}_{1,0}, \hat{T}_{1,-1}\right\}$ is:

$$\hat{\hat{\Omega}}_{\alpha\beta\rightarrow\mathrm{IST}} = \begin{pmatrix} \frac{1}{\sqrt{2}} & 0 & \frac{1}{\sqrt{2}} & 0 \\ 0 & -1 & 0 & 0 \\ \frac{1}{\sqrt{2}} & 0 & -\frac{1}{\sqrt{2}} & 0 \\ 0 & 0 & 0 & 1 \end{pmatrix} \tag{2.3}$$

For multi-spin systems the full basis set is made from the series of direct products of all 4^N combinations of the nISTs. These can be made by taking direct products of the constituent nISTs in Hilbert space and then stretching and concatenating the resulting matrices. The transformation matrix will be analogous to that of Equation (2.3) but larger.

Basis Indexing of nISTs

Each nIST can be uniquely identified by its rank, l, and order, m, thus it is possible to describe the basis vectors in terms of an indexing system rather than saving the matrices themselves, reducing the memory requirement. For example, a three spin-$\frac{1}{2}$ system has 64 basis states, formed from all combinations of the four possible nISTs associated with each spin:

$$\begin{Bmatrix} \hat{T}_{0,0} \\ \hat{T}_{1,1} \\ \hat{T}_{1,0} \\ \hat{T}_{1,-1} \end{Bmatrix} \otimes \begin{Bmatrix} \hat{T}_{0,0} \\ \hat{T}_{1,1} \\ \hat{T}_{1,0} \\ \hat{T}_{1,-1} \end{Bmatrix} \otimes \begin{Bmatrix} \hat{T}_{0,0} \\ \hat{T}_{1,1} \\ \hat{T}_{1,0} \\ \hat{T}_{1,-1} \end{Bmatrix} \tag{2.4}$$

where the first index represents the rank, l and the second index the order, m.

The 64 states may be indexed either via (l, m) or to further simplify the matter the indexing is linearised such that the nISTs are ordered in terms of increasing rank, and within rank in

[1] The ISTs must be normalised or the transformation matrix will not be unitary.

terms of descending order, and then consecutively numbered from 0 upwards. For example, the first four nISTs are given by $\hat{T}_{0,0} \Rightarrow 0, \hat{T}_{1,1} \Rightarrow 1, \hat{T}_{1,0} \Rightarrow 2, \hat{T}_{1,-1} \Rightarrow 3$ in the linear indexing form. Examples of basis indexing are shown for a three spin-$\frac{1}{2}$ system in Table 2.1. The order of labelling in the state description defines the order of tensors to be included when they are put together by direct product, for example (123) defines the basis state which is given in Hilbert space as the tensor product operator:

$$\hat{O} = \hat{T}_{1,1} \otimes \hat{T}_{1,0} \otimes \hat{T}_{1,-1} \tag{2.5}$$

Another useful property is that the nISTs are eigenstates of $\hat{\hat{L}}_z$:

$$\hat{\hat{L}}_z \hat{T}_{l,m} = m\hat{T}_{l,m} \tag{2.6}$$

and by extension a state formed from the direct product of n nISTs (one for each spin) has the eigenvalue $\sum_{i=1}^{n} m_i$ where m_i is the order of each nIST.

Before embarking on the SSR techniques applied in this chapter we briefly outline two other techniques already in use for radical pair reaction simulations within the Hore group, and elsewhere.

2.1.2 Separating the Radicals

In systems where the two electrons are non-interacting it is possible to reduce the matrix size of the problem by treating the two electrons (each with their coupled nuclei) separately [62]. Assuming that exchange and dipolar interactions are negligible it is possible to write the Hamiltonian as:

$$\hat{H} = \hat{H}^A + \hat{H}^B \tag{2.7}$$

$\hat{H}^i$ is the Hamiltonian for the i^{th} electron and in general comprises a sum over the hyperfine interactions (HFI) and a Zeeman interaction. The probability of finding the radical pair born as a pure singlet in the singlet state at time t is given by (from Equations (1.24) and (1.23)):

$$P_S(t) = \left\langle \hat{Q}_S \right\rangle (t) = \mathrm{Tr}\left\{ \rho(t) \hat{Q}_S \right\} \tag{2.8}$$

$$= \frac{1}{M} \mathrm{Tr}\left\{ \mathrm{e}^{-\mathrm{i}\hat{H}t} \hat{Q}_S \, \mathrm{e}^{\mathrm{i}\hat{H}t} \hat{Q}_S \right\} \tag{2.9}$$

Table 2.1. Basis indexing of the full 64 state state-space of a three spin-$\frac{1}{2}$ system. $T_{l,m}$ is an nIST of rank l and order m.

State	$\binom{l}{m}$ Indexing	Linear Indexing	State	$\binom{l}{m}$ Indexing	Linear Indexing
$\hat{T}_{0,0}\hat{T}_{0,0}\hat{T}_{0,0}$	$\begin{pmatrix}0&0&0\\0&0&0\end{pmatrix}$	000	$\hat{T}_{1,0}\hat{T}_{0,0}\hat{T}_{0,0}$	$\begin{pmatrix}1&0&0\\0&0&0\end{pmatrix}$	200
$\hat{T}_{0,0}\hat{T}_{0,0}\hat{T}_{1,1}$	$\begin{pmatrix}0&0&1\\0&0&1\end{pmatrix}$	001	$\hat{T}_{1,0}\hat{T}_{0,0}\hat{T}_{1,1}$	$\begin{pmatrix}1&0&1\\0&0&1\end{pmatrix}$	201
$\hat{T}_{0,0}\hat{T}_{0,0}\hat{T}_{1,0}$	$\begin{pmatrix}0&0&1\\0&0&0\end{pmatrix}$	002	$\hat{T}_{1,0}\hat{T}_{0,0}\hat{T}_{1,0}$	$\begin{pmatrix}1&0&1\\0&0&0\end{pmatrix}$	202
$\hat{T}_{0,0}\hat{T}_{0,0}\hat{T}_{1,-1}$	$\begin{pmatrix}0&0&1\\0&0&-1\end{pmatrix}$	003	$\hat{T}_{1,0}\hat{T}_{0,0}\hat{T}_{1,-1}$	$\begin{pmatrix}1&0&1\\0&0&-1\end{pmatrix}$	203
$\hat{T}_{0,0}\hat{T}_{1,1}\hat{T}_{0,0}$	$\begin{pmatrix}0&1&0\\0&1&0\end{pmatrix}$	010	$\hat{T}_{1,0}\hat{T}_{1,1}\hat{T}_{0,0}$	$\begin{pmatrix}1&1&0\\0&1&0\end{pmatrix}$	210
$\hat{T}_{0,0}\hat{T}_{1,1}\hat{T}_{1,1}$	$\begin{pmatrix}0&1&1\\0&1&1\end{pmatrix}$	011	$\hat{T}_{1,0}\hat{T}_{1,1}\hat{T}_{1,1}$	$\begin{pmatrix}1&1&1\\0&1&1\end{pmatrix}$	211
$\hat{T}_{0,0}\hat{T}_{1,1}\hat{T}_{1,0}$	$\begin{pmatrix}0&1&1\\0&1&0\end{pmatrix}$	012	$\hat{T}_{1,0}\hat{T}_{1,1}\hat{T}_{1,0}$	$\begin{pmatrix}1&1&1\\0&1&0\end{pmatrix}$	212
$\hat{T}_{0,0}\hat{T}_{1,1}\hat{T}_{1,-1}$	$\begin{pmatrix}0&1&1\\0&1&-1\end{pmatrix}$	013	$\hat{T}_{1,0}\hat{T}_{1,1}\hat{T}_{1,-1}$	$\begin{pmatrix}1&1&1\\0&1&-1\end{pmatrix}$	213
$\hat{T}_{0,0}\hat{T}_{1,0}\hat{T}_{0,0}$	$\begin{pmatrix}0&1&0\\0&0&0\end{pmatrix}$	020	$\hat{T}_{1,0}\hat{T}_{1,0}\hat{T}_{0,0}$	$\begin{pmatrix}1&1&0\\0&0&0\end{pmatrix}$	220
$\hat{T}_{0,0}\hat{T}_{1,0}\hat{T}_{1,1}$	$\begin{pmatrix}0&1&1\\0&0&1\end{pmatrix}$	021	$\hat{T}_{1,0}\hat{T}_{1,0}\hat{T}_{1,1}$	$\begin{pmatrix}1&1&1\\0&0&1\end{pmatrix}$	221
$\hat{T}_{0,0}\hat{T}_{1,0}\hat{T}_{1,0}$	$\begin{pmatrix}0&1&1\\0&0&0\end{pmatrix}$	022	$\hat{T}_{1,0}\hat{T}_{1,0}\hat{T}_{1,0}$	$\begin{pmatrix}1&1&1\\0&0&0\end{pmatrix}$	222
$\hat{T}_{0,0}\hat{T}_{1,0}\hat{T}_{1,-1}$	$\begin{pmatrix}0&1&1\\0&0&-1\end{pmatrix}$	023	$\hat{T}_{1,0}\hat{T}_{1,0}\hat{T}_{1,-1}$	$\begin{pmatrix}1&1&1\\0&0&-1\end{pmatrix}$	223
$\hat{T}_{0,0}\hat{T}_{1,-1}\hat{T}_{0,0}$	$\begin{pmatrix}0&1&0\\0&-1&0\end{pmatrix}$	030	$\hat{T}_{1,0}\hat{T}_{1,-1}\hat{T}_{0,0}$	$\begin{pmatrix}1&1&0\\0&-1&0\end{pmatrix}$	230
$\hat{T}_{0,0}\hat{T}_{1,-1}\hat{T}_{1,1}$	$\begin{pmatrix}0&1&1\\0&-1&1\end{pmatrix}$	031	$\hat{T}_{1,0}\hat{T}_{1,-1}\hat{T}_{1,1}$	$\begin{pmatrix}1&1&1\\0&-1&1\end{pmatrix}$	231
$\hat{T}_{0,0}\hat{T}_{1,-1}\hat{T}_{1,0}$	$\begin{pmatrix}0&1&1\\0&-1&0\end{pmatrix}$	032	$\hat{T}_{1,0}\hat{T}_{1,-1}\hat{T}_{1,0}$	$\begin{pmatrix}1&1&1\\0&-1&0\end{pmatrix}$	232
$\hat{T}_{0,0}\hat{T}_{1,-1}\hat{T}_{1,-1}$	$\begin{pmatrix}0&1&1\\0&-1&-1\end{pmatrix}$	033	$\hat{T}_{1,0}\hat{T}_{1,-1}\hat{T}_{1,-1}$	$\begin{pmatrix}1&1&1\\0&-1&-1\end{pmatrix}$	233
$\hat{T}_{1,1}\hat{T}_{0,0}\hat{T}_{0,0}$	$\begin{pmatrix}1&0&0\\1&0&0\end{pmatrix}$	100	$\hat{T}_{1,-1}\hat{T}_{0,0}\hat{T}_{0,0}$	$\begin{pmatrix}1&0&0\\-1&0&0\end{pmatrix}$	300
$\hat{T}_{1,1}\hat{T}_{0,0}\hat{T}_{1,1}$	$\begin{pmatrix}1&0&1\\1&0&1\end{pmatrix}$	101	$\hat{T}_{1,-1}\hat{T}_{0,0}\hat{T}_{1,1}$	$\begin{pmatrix}1&0&1\\-1&0&1\end{pmatrix}$	301
$\hat{T}_{1,1}\hat{T}_{0,0}\hat{T}_{1,0}$	$\begin{pmatrix}1&0&1\\1&0&0\end{pmatrix}$	102	$\hat{T}_{1,-1}\hat{T}_{0,0}\hat{T}_{1,0}$	$\begin{pmatrix}1&0&1\\-1&0&0\end{pmatrix}$	302
$\hat{T}_{1,1}\hat{T}_{0,0}\hat{T}_{1,-1}$	$\begin{pmatrix}1&0&1\\1&0&-1\end{pmatrix}$	103	$\hat{T}_{1,-1}\hat{T}_{0,0}\hat{T}_{1,-1}$	$\begin{pmatrix}1&0&1\\-1&0&-1\end{pmatrix}$	303
$\hat{T}_{1,1}\hat{T}_{1,1}\hat{T}_{0,0}$	$\begin{pmatrix}1&1&0\\1&1&0\end{pmatrix}$	110	$\hat{T}_{1,-1}\hat{T}_{1,1}\hat{T}_{0,0}$	$\begin{pmatrix}1&1&0\\-1&1&0\end{pmatrix}$	310
$\hat{T}_{1,1}\hat{T}_{1,1}\hat{T}_{1,1}$	$\begin{pmatrix}1&1&1\\1&1&1\end{pmatrix}$	111	$\hat{T}_{1,-1}\hat{T}_{1,1}\hat{T}_{1,1}$	$\begin{pmatrix}1&1&1\\-1&1&1\end{pmatrix}$	311
$\hat{T}_{1,1}\hat{T}_{1,1}\hat{T}_{1,0}$	$\begin{pmatrix}1&1&1\\1&1&0\end{pmatrix}$	112	$\hat{T}_{1,-1}\hat{T}_{1,1}\hat{T}_{1,0}$	$\begin{pmatrix}1&1&1\\-1&1&0\end{pmatrix}$	312
$\hat{T}_{1,1}\hat{T}_{1,1}\hat{T}_{1,-1}$	$\begin{pmatrix}1&1&1\\1&1&-1\end{pmatrix}$	113	$\hat{T}_{1,-1}\hat{T}_{1,1}\hat{T}_{1,-1}$	$\begin{pmatrix}1&1&1\\-1&1&-1\end{pmatrix}$	313
$\hat{T}_{1,1}\hat{T}_{1,0}\hat{T}_{0,0}$	$\begin{pmatrix}1&1&0\\1&0&0\end{pmatrix}$	120	$\hat{T}_{1,-1}\hat{T}_{1,0}\hat{T}_{0,0}$	$\begin{pmatrix}1&1&0\\-1&0&0\end{pmatrix}$	320
$\hat{T}_{1,1}\hat{T}_{1,0}\hat{T}_{1,1}$	$\begin{pmatrix}1&1&1\\1&0&1\end{pmatrix}$	121	$\hat{T}_{1,-1}\hat{T}_{1,0}\hat{T}_{1,1}$	$\begin{pmatrix}1&1&1\\-1&0&1\end{pmatrix}$	321
$\hat{T}_{1,1}\hat{T}_{1,0}\hat{T}_{1,0}$	$\begin{pmatrix}1&1&1\\1&0&0\end{pmatrix}$	122	$\hat{T}_{1,-1}\hat{T}_{1,0}\hat{T}_{1,0}$	$\begin{pmatrix}1&1&1\\-1&0&0\end{pmatrix}$	322
$\hat{T}_{1,1}\hat{T}_{1,0}\hat{T}_{1,-1}$	$\begin{pmatrix}1&1&1\\1&0&-1\end{pmatrix}$	123	$\hat{T}_{1,-1}\hat{T}_{1,0}\hat{T}_{1,-1}$	$\begin{pmatrix}1&1&1\\-1&0&-1\end{pmatrix}$	323
$\hat{T}_{1,1}\hat{T}_{1,-1}\hat{T}_{0,0}$	$\begin{pmatrix}1&1&0\\1&-1&0\end{pmatrix}$	130	$\hat{T}_{1,-1}\hat{T}_{1,-1}\hat{T}_{0,0}$	$\begin{pmatrix}1&1&0\\-1&-1&0\end{pmatrix}$	330
$\hat{T}_{1,1}\hat{T}_{1,-1}\hat{T}_{1,1}$	$\begin{pmatrix}1&1&1\\1&-1&1\end{pmatrix}$	131	$\hat{T}_{1,-1}\hat{T}_{1,-1}\hat{T}_{1,1}$	$\begin{pmatrix}1&1&1\\-1&-1&1\end{pmatrix}$	331
$\hat{T}_{1,1}\hat{T}_{1,-1}\hat{T}_{1,0}$	$\begin{pmatrix}1&1&1\\1&-1&0\end{pmatrix}$	132	$\hat{T}_{1,-1}\hat{T}_{1,-1}\hat{T}_{1,0}$	$\begin{pmatrix}1&1&1\\-1&-1&0\end{pmatrix}$	332
$\hat{T}_{1,1}\hat{T}_{1,-1}\hat{T}_{1,-1}$	$\begin{pmatrix}1&1&1\\1&-1&-1\end{pmatrix}$	133	$\hat{T}_{1,-1}\hat{T}_{1,-1}\hat{T}_{1,-1}$	$\begin{pmatrix}1&1&1\\-1&-1&-1\end{pmatrix}$	333

where M is the number of nuclear states over which the initial singlet must be normalised and $\hat{Q}_S$ is the singlet projection operator. Writing out the singlet projection operator in full gives:

$$P_S(t) = \frac{1}{M}\mathrm{Tr}\left\{\mathrm{e}^{-\mathrm{i}\hat{H}t}\left(\frac{1}{4}\hat{\mathbb{1}} - \hat{S}^A\cdot\hat{S}^B\right)\mathrm{e}^{\mathrm{i}\hat{H}t}\left(\frac{1}{4}\hat{\mathbb{1}} - \hat{S}^A\cdot\hat{S}^B\right)\right\} \tag{2.10}$$

$$= \frac{1}{M}\left\{\frac{1}{16}\mathrm{Tr}\left\{\hat{\mathbb{1}}\right\} - \frac{1}{2}\mathrm{Tr}\left\{\hat{S}^A\cdot\hat{S}^B\right\} + \mathrm{Tr}\left\{\mathrm{e}^{-\mathrm{i}\hat{H}t}\hat{S}^A\cdot\hat{S}^B\mathrm{e}^{\mathrm{i}\hat{H}t}\hat{S}^A\cdot\hat{S}^B\right\}\right\} \tag{2.11}$$

The trace of the unit operator is simply equal to the size of the matrix which is $4M$ for electrons and nuclei. The spin operators are traceless and it follows that any direct product of them must be likewise – removing the second term of Equation (2.11). Given Equation (2.7) the propagator is readily rewritten in terms of the two electrons separately, and as operators acting on different objects must commute it is possible to rewrite the third term of Equation (2.11) as:

$$\sum_{p,q=x,y,z}\mathrm{Tr}\left\{\hat{S}_p^A\mathrm{e}^{-\mathrm{i}\hat{H}^At}\hat{S}_q^A\mathrm{e}^{\mathrm{i}\hat{H}^At}\right\}\mathrm{Tr}\left\{\hat{S}_p^B\mathrm{e}^{-\mathrm{i}\hat{H}^Bt}\hat{S}_q^B\mathrm{e}^{\mathrm{i}\hat{H}^Bt}\right\} \tag{2.12}$$

Substituting in for each of the three terms gives:

$$P_S(t) = \frac{1}{4} + \frac{1}{M}\sum_{p,q=x,y,z}\mathrm{Tr}\left\{\hat{S}_p^A\mathrm{e}^{-\mathrm{i}\hat{H}^At}\hat{S}_q^A\mathrm{e}^{\mathrm{i}\hat{H}^At}\right\}\mathrm{Tr}\left\{\hat{S}_p^B\mathrm{e}^{-\mathrm{i}\hat{H}^Bt}\hat{S}_q^B\mathrm{e}^{\mathrm{i}\hat{H}^Bt}\right\} \tag{2.13}$$

Thus the size of the matrices to be used has been reduced to just the size of the spin system of each individual radical. Of course, the work required to recouple the two electrons to find the overall singlet yield is not inconsiderable, and much effort has gone into improving the efficiency of that procedure [100].

The same procedure can be followed for calculations in Liouville space, see Ref [93], to give:

$$\sigma_S(t) = \frac{1}{4} + \frac{1}{M}\sum_{p,q=x,y,z}\left\langle\hat{S}_p^{A\dagger}\right|\mathrm{e}^{-\mathrm{i}\left(\hat{\hat{H}}^A+\hat{\hat{R}}^A\right)t}\left|\hat{S}_q^{A\dagger}\right\rangle\left\langle\hat{S}_p^B\right|\mathrm{e}^{-\mathrm{i}\left(\hat{\hat{H}}^B+\hat{\hat{R}}^B\right)t}\left|\hat{S}_q^B\right\rangle \tag{2.14}$$

where $\hat{\hat{R}}^i$ is the relaxation superoperator for the i^{th} radical assuming it results from modulation of the interactions within that radical only, *e.g.* rotational modulation of anisotropic HFIs, hence $\hat{\hat{R}} = \hat{\hat{R}}^A + \hat{\hat{R}}^B$. In Ref [93] this expression is used for the derivation of a simple formula for the total singlet yield which makes use of the block diagonal nature of the operators. The resultant expression gives significant reduction in the matrix size of the problem, to which we shall return later.

2.1.3 M_S Block Diagonalisation

The $\alpha\beta$ basis is useful as the basis vectors are eigenstates of the individual spin projection operators, $\hat{S}_z^i$ and the total spin projection operator, $\hat{S}_z^{\text{Total}} = \sum_i \hat{S}_z^i$. It is obvious, therefore, that any operators built from $\hat{S}_z$ operators cannot change the spin state, *i.e.* are always diagonal in this basis. It is the raising and lowering operators which cause spin flips $\alpha \leftrightarrow \beta$, the representations of these operators in this basis are not diagonal. For the case of solely isotropic HFIs the Hamiltonian is given by:

$$\hat{H}_{\text{HFI}} = \sum_{X=A,B} \sum_i a_i^X \left(\hat{S}_z^X \hat{I}_z^{Xi} + \frac{1}{2} \left(\hat{S}_+^X \hat{I}_-^{Xi} + \hat{S}_-^X \hat{I}_+^{Xi} \right) \right) \tag{2.15}$$

where a_i^X is the isotropic coupling constant of the i^{th} nucleus on radical X and $\hat{I}_{+,-,z}^{Xi}$ the corresponding nuclear operators. Inspection of Equation (2.15) shows that the raising and lowering operators always work in concert, that is the hyperfine interaction brings about complimentary spin flips in a coupled electron-nucleus pair. Thus the total projection of spin angular momentum on the laboratory frame z-axis is unchanged by the HFI. The isotropic HFI Hamiltonian therefore commutes with the total spin projection operator:

$$\left[\hat{S}_z^{\text{Total}}, \hat{H}_{\text{HFI}} \right] = 0 \tag{2.16}$$

and it is correspondingly clear that the total Hamiltonian in this case is block diagonal with respect to M_S^{Total} [58, 101]. For example a three-spin system has a full Hilbert state-space size of eight, but block diagonalisation reduces the system to a direct sum of four blocks $\{1, 3, 3, 1\}$. If the calculation is scaled up into Liouville space the individual blocks are $\{1, 9, 9, 1\}$ as opposed to 64 for the full state-space.

This block diagonalisation is not possible in the case of anisotropic HFIs as these no longer have perfectly countered raising and lowering operators, and by extension relaxation superoperators arising from random modulation of anisotropic HFIs are also not block diagonal with respect to M_S^{Total}. However, the singlet and triplet projection anti-commutator superoperators required to account for non-exponential reaction kinetics are block diagonal with respect to the total spin angular momentum projection.

Formation of the reduced operators in Liouville space is achieved most readily by simple scaling up of the individual blocks directly from Hilbert space. In Hilbert space it is possible to form the reduced operators directly into the smaller blocks. Though having a smaller memory

footprint, this has proved slower than normal operator generation followed by transformation into the block diagonal form.

2.2 Initial Aims

Two procedures for SSR of NMR simulations were proposed in Refs [98] and [99]. These methods had been implemented in MATLAB in the first incarnations of the spin dynamics software *Spinach*. NMR systems tend to be sparsely coupled with each spin linked to only a small number of others. Spin chemical systems are somewhat different with each electron connected, to varying extents, to every nucleus in the radical and it was not clear whether the same techniques could be successfully applied to speed up spin chemical calculations. It was the initial aim of the work of this chapter to investigate the application of clusterisation and zero-track elimination to spin chemistry simulations and in doing so to contribute to the development of the spin chemistry section of the *Spinach* library.

The SSR techniques are briefly outlined in the following subsections along with their application to magnetic field effect (MFE) calculations of radical pair reactions.

2.2.1 Clusterisation

In the simulation of NMR spectra it is quite normal to calculate the spectra for small parts of the molecule individually, decided upon by chemical intuition, and simply add the results. This idea was extended in Ref [98] to provide an alternative means of dividing up the system of interest. If the spin system is considered as an interaction graph where nodes show spin position and connectors indicate a direct interaction, two criteria can be used to eliminate states from the basis (defined in terms of the nIST operators):

- Coherences between spins that are far apart on the interaction graph are unlikely to build up on the normal timescale of an NMR experiment.
- High-order coherences, that is across many spins, accumulate slowly but are relaxed rapidly.

Both statements are reasonably intuitive: to build up a coherence between far separated spins each individual pair-wise interaction along the connecting chain must have time to act. Similarly for high-order coherences several pair-wise interactions must have time to act but will concurrently be being relaxed by modulation of each individual interaction and thus undergo

rapid decoherence. A more formal mathematical justification was very recently reported and can be found in Ref [102].

The above criteria were implemented in *Spinach* by considering the spin coupling graph limited to clusters of n spins, where n could be defined by the user. Alternatively it was possible to input manually defined clusters. The full basis was then generated for each cluster and subsequently the clusters were recoupled to form the complete reduced state-space, and similarly the operators were recoupled.[2]

Application to Spin Chemistry

This procedure was shown to work well for NMR simulations [98], however it was unclear if the same approximations could be satisfactorily applied to spin chemical calculations. Initial consideration might suggest that in a densely coupled system, where every spin within a radical is only two interactions from any other spin, neither of the criteria listed above is likely to be satisfied.

Initially only coherent processes and equal rate constants from both spin states were considered for simplicity. State-space restricted Liouville space calculations could then be compared to the exact simulation carried out in Hilbert space, which is always much quicker. Many different systems were tested; the number and distribution (across the two radicals) of HFIs were varied as were the strengths of the couplings and magnitude of the rate constants. In addition the cut-off size of the clusters was also changed. An example is shown in Fig 2.2. As a general rule, the faster the rate constant the better the fit when using clusterisation SSR, and in such cases it was often just the fine structure of the simulation, which might not be resolved in experimental data, that was not reproduced.

In recent months, the clusterisation comparisons have been revisited by Edwards and Kuprov [103]. They have found that if relaxation is included in the simulations and rate constants are reasonably rapid ($> 10^7$ s^{-1}) it is possible to achieve reliable convergence of MFE calculations when the cluster size reaches eight. These calculations were carried out on the Cloud computing system (Amazon EC2). Given that in general a single system (one cluster) of eight spins would exceed the memory of a normal workstation this conclusion is not at present of practical use.

Overall it appeared that clusterisation would not produce significant reduction in the state-

[2]The original method of recoupling the operators was far from optimum and now makes use of the procedure derived later in this chapter for the formation of operators directly into a reduced basis when the state-list for that basis is defined.

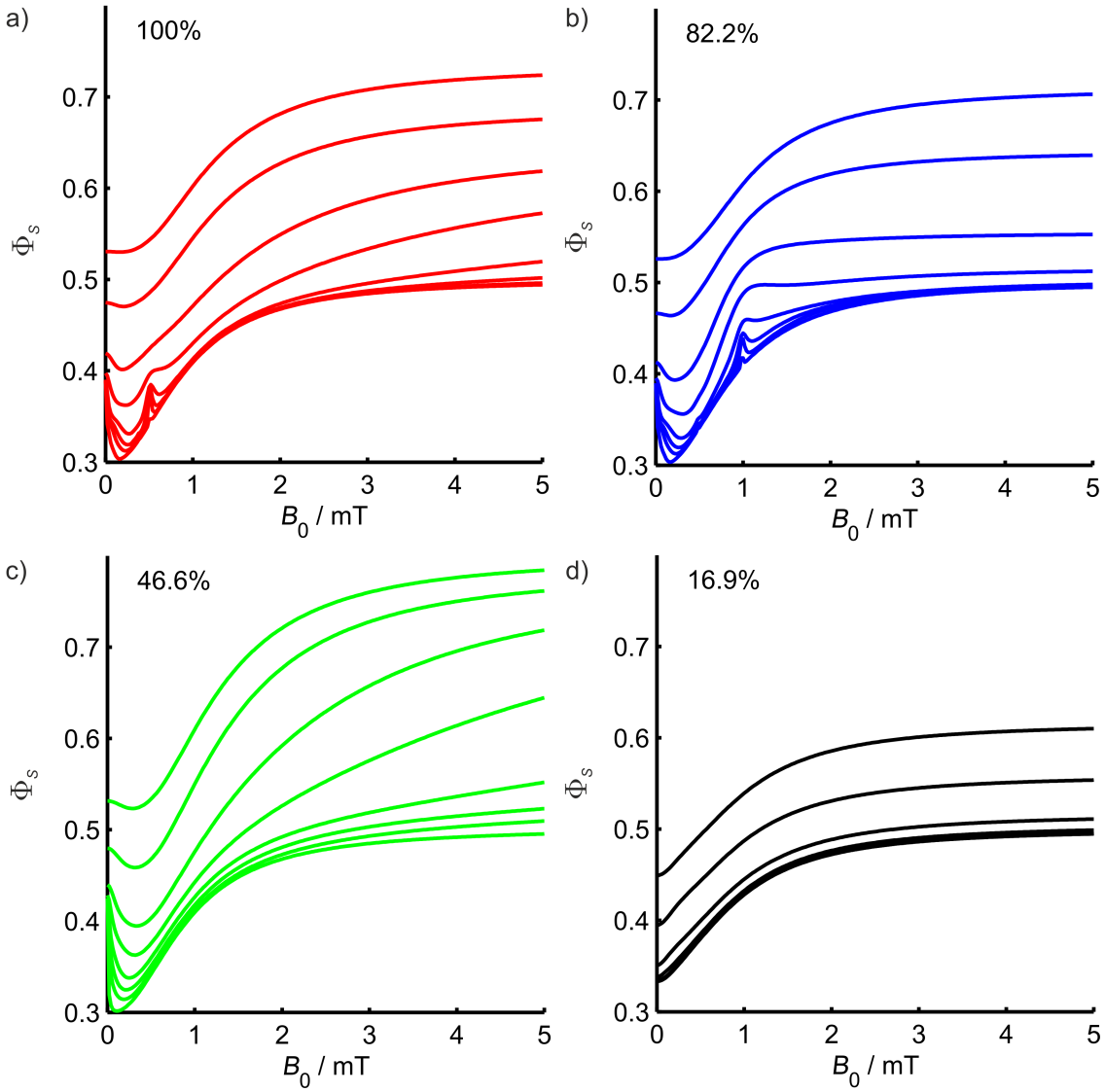

Figure 2.2. Isotropic MFE simulations for a four-nucleus system. Two nuclei on radical A both have $a = 0.295$ mT and the two nuclei on radical B have $a_1 = -0.714$ mT and $a_2 = 0.714$ mT. A range of rate constants were used, $\frac{k}{10^6} = [0.176\ 0.88\ 1.76\ 3.52\ 8.80\ 17.6\ 35.2\ 52.8]$ s^{-1}, these are assigned to the curves ascending up the graph, *i.e.* the faster k the greater the singlet yield, Φ_S. The simulations were run for clusters of size n, *i.e.* including n spins. a) Exact simulation, $n = 6$ ($\Rightarrow$ 100% of the 4096 states), b) $n = 5$ ($\Rightarrow$ 82.2%), c) $n = 4$ ($\Rightarrow$ 46.6%) and d) $n = 3$ ($\Rightarrow$ 16.9%). The clusters themselves were generated automatically by the *Spinach* codes according to the procedure in Ref [98].

space and does not reliably reproduce the exact simulation results. This avenue of state-space restriction was not considered further.

2.2.2 Zero-Track Elimination

Having observed that the operators resulting from the clusterisation SSR on NMR systems were still sparse Kuprov proposed (in Ref [99]) a second procedure to further prune the state-space. Clusterisation prunes the state-space based upon an analysis of the spin system. Zero-track elimination (ZTE) trims the state-space at the trajectory level. During this procedure the states

that are not populated during the simulation, and thus cannot contribute to any observable, are removed.

There exist efficient methods for the evaluation of the outcome of a matrix exponential on a vector which avoids actually calculating the matrix exponential itself (a process that, like matrix diagonalisation, scales as $\mathcal{O}(N^3)$) [104]. These were implemented by Kuprov in the *Spinach* ZTE module to allow efficient calculation of the Krylov subspace of the trajectory. For a time-discretised simulation the full system trajectory can be defined as [99]:

$$\left\{\hat{\rho}_0, \mathrm{e}^{-\mathrm{i}\hat{\hat{L}}\Delta t}\hat{\rho}_0, \mathrm{e}^{-2\mathrm{i}\hat{\hat{L}}\Delta t}\hat{\rho}_0, \cdots, \mathrm{e}^{-n\mathrm{i}\hat{\hat{L}}\Delta t}\hat{\rho}_0\right\} \tag{2.17}$$

where $\hat{\hat{L}}$ is the system Liouvillian, $\hat{\rho}_0$ is the starting vector, Δt is the time-step and $t = n\Delta t$ is the end point of the calculation. Each of the states in the series above can be inspected for basis vectors which are consistently zero and these can be projected out, reducing the size of the system. Of course in practice, if one has already propagated the full system through its full time span there is little left to calculate so reducing the system size at that point gives little advantage. However, a compromise is available; propagating the full system through m time-steps (where $m \ll n$) and inspecting the $m+1$ resulting state vectors for basis states which are never populated. This will give the Krylov subspace which spans:

$$\left\{\hat{\rho}_0, \mathrm{e}^{-\mathrm{i}\hat{\hat{L}}\Delta t}\hat{\rho}_0, \cdots\cdots, \mathrm{e}^{-m\mathrm{i}\hat{\hat{L}}\Delta t}\hat{\rho}_0\right\} \tag{2.18}$$

Strictly speaking, for zero-track elimination one propagation, assuming a time-independent superoperator, should be sufficient. If a state is not populated initially and is not populated at all by the action of the superoperator then it can never be populated unless the system interactions change. In practice for NMR simulations there were few basis states which were identically zero but it was also possible to eliminate those states which are populated to a very small degree [99]. This latter case is of course an approximation, the accuracy of which is defined by changing the degree of population required for a state to be kept and by altering the number of steps, m over which the initial screening propagations are run.

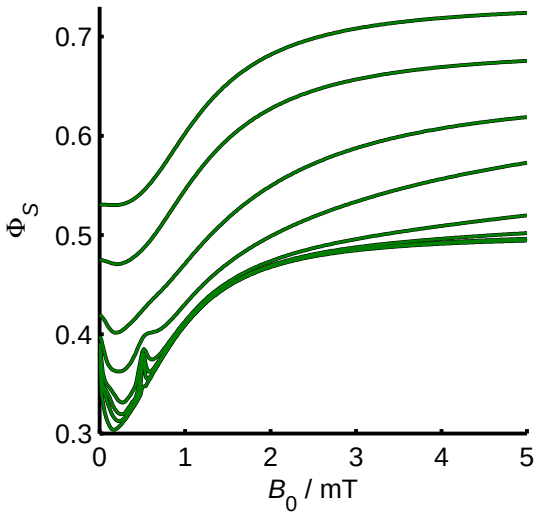

Figure 2.3. Isotropic MFE simulation for a four-nucleus system. Two nuclei on radical A both have $a = 0.295$ mT and the two nuclei on radical B have $a_1 = -0.714$ mT and $a_2 = 0.714$ mT. A range of rate constants were used, $\frac{k}{10^6} = [0.176\ 0.880\ 1.76\ 3.52\ 8.8\ 17.6\ 35.2\ 52.8]$ s^{-1}, these are assigned to the curves ascending up the graph, *i.e.* the faster k the greater the singlet yield, Φ_S. The solid black line indicates the exact simulation (state-space 4096) and the green indicates the zero-track eliminated state-space (757 states $\Rightarrow$ 18.5%) which runs identically over it.

Application to Spin Chemistry

Initially the ZTE procedure was applied to a conventional isotropic MFE (also known as MARY) simulation with zero ZTE tolerance, that is looking for the exactly zero basis states only.[3] The result of simulating the same system as in Fig 2.2 with ZTE is shown in Fig 2.3. Clearly there is a significant reduction in the state-space of the calculation with no loss of accuracy in the simulation whatsoever. Relaxing the tolerance of the ZTE analysis so as to remove additionally any low populated states made no difference to the state-space for a tolerance smaller than 10^{-4}. A tolerance of 10^{-4} removed only an extra 60 states at the expense of the simulation accuracy at low field. This SSR technique is clearly much more promising for isotropic spin chemistry calculations than the clusterisation.

2.2.3 Anisotropic Calculations

As a brief aside we note that clusterisation did not work any better for calculations of MFEs as a function of field direction with respect to anisotropic HFIs than for the MARY calculations above which had isotropic HFIs but changed the field strength. Furthermore, ZTE returned much less significant reductions for anisotropic MFE calculations than for the isotropic case. We therefore concern ourselves in the main with purely isotropic calculations hereafter.

[3] ZTE tolerance was set to machine precision in the calculation.

2.3 Summary One

Having at this point completed the initial aims of this project it is useful to summarise the key findings before continuing. Firstly the two SSR techniques that had been successfully applied to NMR simulations by Kuprov, [98, 99] were applied to MARY simulations in spin chemistry. Clusterisation proved ineffective at reducing the state-space of the simulation without affecting the accuracy. However, ZTE significantly compressed the state-space of the calculation with no cost to the accuracy at all. In fact, it was possibly to achieve an $\approx 80\%$ SSR by removing only states which are precisely zero throughout the course of the simulation, *i.e.* that are literally never populated. Thus, the ZTE elimination as used here is an exact SSR technique with no approximations at all. The natural question arising from this observation relates to the nature of the states that are never populated. Analytical criteria for removing redundant states would be more efficient than carrying out the Krylov propagations required for numerical determination of the minimal basis set. Therefore, the next section is concerned with the identification of the non-populated states and investigating the underlying cause of their isolation.

2.4 Unpopulated States

We begin with the simplest possible system; two electrons, one coupled to a single isotropic spin-$\frac{1}{2}$ nucleus and the other bare. The full state-space has 64 states, Table 2.1, which is reduced to 13 following ZTE. The retained and lost states are summarised in Table 2.2.

The most obvious common feature of the retained states is that they all have zero coherence order, that is, $M = \sum m = 0$. Dozens of other systems were investigated, varying all parameters and the numbers of nuclei included, and it was seen that this selection criteria always held true.[4] This can be justified in much the same way as the M_S block diagonalisation. For isotropic MFE calculations all raising and lowering operators act together in pairs as in Equation (2.15). Such operators bring about pair-wise spin flips, the electron may change $\alpha \rightarrow \beta$ but the coupled nucleus simultaneously undergoes a change $\beta \rightarrow \alpha$, thus overall there is no change in the total Ms or M by the action of these operators. Anisotropic systems however, do have unpaired

[4]The state-lists for these simulations are not included because they are simply too long.

raising and lowering operators. Even for one simple HFI tensor:

$$A = \begin{pmatrix} A_{xx} & 0 & 0 \\ 0 & A_{yy} & 0 \\ 0 & 0 & A_{zz} \end{pmatrix} \tag{2.19}$$

the HFI Hamiltonian is given by:

$$\begin{aligned} \hat{H}_{\text{HFI}} = \frac{1}{4} \Big((A_{xx} - A_{yy}) \left(\hat{S}_+ \hat{I}_+ + \hat{S}_- \hat{I}_- \right) + (A_{xx} + A_{yy}) \left(\hat{S}_+ \hat{I}_- + \hat{S}_- \hat{I}_+ \right) \Big) \\ + A_{zz} \hat{S}_z \hat{I}_z \end{aligned} \tag{2.20}$$

which clearly does not have all raising and lowering operators partnered, and hence the total M of the system is not conserved. This explains why the ZTE procedure brings about a smaller reduction for anisotropic spin systems.

Table 2.2. Fate of states after ZTE for a three spin-$\frac{1}{2}$ system. Spins are listed electron 1, electron 2, nucleus 1 (coupled to electron 1).

Retained States	$\sum m$	**Lost States**	$\sum m$
000	0	001	1
013	0	002	0
022	0	003	-1
031	0	010	1
123	0	011	2
130	0	012	1
132	0	020	0
213	0	021	1
220	0	023	-1
231	0	030	-1
310	0	032	-1
312	0	033	-2
321	0	100	1
		101	2
		102	1
		103	0
		110	2
		111	3
		112	2
		113	1
		120	1
		121	2
		122	1
		131	1
		133	-1
		200	0
		201	1
		202	0
		203	-1
		210	1
		211	2
		212	1
		221	1
		222	0
		223	-1
		230	-1
		232	-1
		233	-2
		300	-1
		301	0
		302	-1
		303	-2
		311	1
		313	-1
		320	-1
		322	-1
		323	-2
		330	-2
		331	-1
		332	-2
		333	-3

Having deduced that only the zero coherence order states are retained we might expect that all such states would be required for the calculation. However, it is clear from inspection of the second column in Table 2.2 that this is not the case. Seven states with $M = 0$ are discarded. Six of them have all zeros on one of the two radicals, *i.e.* have $\hat{T}_{0,0} \propto \hat{\mathbb{1}}$ on all the spins coupled to one of the electrons. In seeking to justify this observation there are three facts to remember:

- There are no operators acting to connect the two radicals, no exchange or dipolar coupling for example.
- The unit operator cannot evolve under any operation.
- The only initially populated state with unit operators on all spins of a radical is the unit state which has $\hat{\mathbb{1}}$s on every spin of the entire system.

Hence, we may consider the operators as acting distinctly on the two radicals. No operator can evolve a radical into its fully mixed state ($\hat{\mathbb{1}}$ on each spin) unless it begins as such, and the initial singlet state has only one state with a fully mixed radical – the state which is fully mixed on both radicals (000) and does not evolve at all. Thus any state which has all zeros on one radical, but not on both, can be eliminated, and indeed this was seen to be true in all simulations of this kind. By similar arguments we can see that no state with all 'Z's ($\hat{S}_z = \frac{1}{\sqrt{2}}\hat{T}_{1,0}$) on the spins of one radical can be populated, with the exception of a bare radical which starts with a 'Z' state in the initial singlet and does not evolve because it experiences no interactions. As the 'all-Z' case is not true in general for all RPs this was not used as a criterion for analytical basis set construction. These arguments will be revisited using path tracing procedures, section 2.5.1.

2.4.1 Conservation Laws

The loss of all $M \neq 0$ states (Table 2.2) through ZTE can be justified by consideration of conservation laws. All states that violate a conservation law can be eliminated from the state-space. An observable corresponding to operator $\hat{A}$ is conserved if $\hat{A}$ commutes with the system Hamiltonian:

$$\left[\hat{H}, \hat{A}\right] = 0 \tag{2.21}$$

which can be alternatively formulated in Liouville space as:

$$\hat{\hat{L}}\hat{A} = 0 \tag{2.22}$$

where we are now interested in operators which commute with the full system Liouvillian. States which do not have the same expectation value as the initial state of the system do not conserve that property, violate the conservation law and can be eliminated. The active, populated, subspace is then the intersection of states with expectation values arising from all operators that commute with the Hamiltonian matching those of the initial starting state. All other states can be discarded.

In the special case that the initial density matrix, $\hat{\rho}(0)$ is an eigenstate of the commutation superoperator defined by $\hat{\hat{A}}$ then the expectation value of $\hat{A}$ is the eigenvalue:

$$\hat{\hat{A}}\hat{\rho}(0) = \left[\hat{A}, \hat{\rho}(0)\right] = a\hat{\rho}(0) \tag{2.23}$$

and we may now consider the conservation of the eigenvalue of the chosen operator:

$$\begin{aligned}
\hat{\hat{A}}\hat{\rho}(t) &= \left[\hat{A}, \mathrm{e}^{-\mathrm{i}\hat{H}t}\hat{\rho}(0)\mathrm{e}^{\mathrm{i}\hat{H}t}\right] \\
&= \mathrm{e}^{-\mathrm{i}\hat{H}t}\left[\hat{A}, \hat{\rho}(0)\right]\mathrm{e}^{\mathrm{i}\hat{H}t} \\
&= \mathrm{e}^{-\mathrm{i}\hat{H}t}a\hat{\rho}(0)\mathrm{e}^{\mathrm{i}\hat{H}t} \\
&= a\hat{\rho}(t)
\end{aligned} \tag{2.24}$$

In this case subspaces of states may be defined according to common eigenvalues under the operator $\hat{A}$ (or under a common combination of eigenvalues arising from a set of operators commuting with the system Hamiltonian), and the simulation is confined to those subspaces which coincide with the eigenvalues of the initial density matrix. These subspaces, defined by the different values of a, do not interconvert.

Finding the conserved observables can be challenging, but we have already observed one in action. $\hat{S}_z^{\mathrm{Total}} = \sum_i \hat{S}_z^i$, the total projection of spin angular momentum along the z axis commutes with the system Hamiltonian, and thus M is a conserved eigenvalue as we observed in Table 2.2.

Hence, the use of the nISTs as basis vectors is particularly useful as they are eigenstates of $\hat{\hat{S}}_z$. The $\begin{pmatrix} l \\ m \end{pmatrix}$ state labelling shown in Table 2.1 provides an especially convenient means of inspecting the basis states for inclusion. The second row of the matrix, which lists the rank, m, of every state, can be summed over. If the result is not zero the state is excluded from the reduced basis.

2.5 Separating the Singlet State

The initial singlet state is formed from four constituents:

$$\hat{P}_S = \frac{\hat{\mathbb{1}}}{4} - \hat{S}_z^A\hat{S}_z^B - \frac{1}{2}\hat{S}_+^A\hat{S}_-^B - \frac{1}{2}\hat{S}_-^A\hat{S}_+^B \tag{2.25}$$

$$= \frac{1}{2}\hat{T}_{0,0}\hat{T}_{0,0}\hat{T}_{0,0} - \frac{1}{2}\hat{T}_{1,0}\hat{T}_{1,0}\hat{T}_{0,0} + \frac{1}{2}\hat{T}_{1,1}\hat{T}_{1,-1}\hat{T}_{0,0} + \frac{1}{2}\hat{T}_{1,-1}\hat{T}_{1,1}\hat{T}_{0,0} \tag{2.26}$$

$$= \frac{1}{2}\left((000) - (220) + (130) + (310)\right) \tag{2.27}$$

where the final line of Equation (2.27) gives the short hand notation of the basis vectors for a three-spin system (Table 2.1). As the singlet yield, Φ_S, is linear with respect to the starting vector it is possible to separate the calculation into four parts:

$$\Phi_S\left((000) - (220) + (130) + (310)\right) = \Phi_S\left(000\right) - \Phi_S\left(220\right) + \Phi_S\left(130\right) + \Phi_S\left(310\right) \tag{2.28}$$

We performed ZTE on the four calculations of singlet yield arising from splitting up the initial singlet vector and inspected the states retained from each starting vector, Table 2.3. There are no states which appear in more than one of the lists, that is, four independent, non-overlapping, subspaces are populated. This is shown schematically in Fig 2.4, which traces the connectivity of the states for a three-spin-$\frac{1}{2}$ system Liouvillian through the reduced basis remaining after ZTE. Only the HFI part of the Liouvillian is shown as the Zeeman operator is diagonal and therefore only connects a state with itself. There are clearly four distinct subspaces even within this already reduced state-list. Larger spin systems return the same subspaces. Finding the non-interacting subspaces in this way is entirely equivalent to block diagonalisation, but provides an easier method for establishing what the blocks should be.

The singlet yields resulting from a system beginning in states (130) and (310) are equal. The

Table 2.3. States retained from different parts of an initial singlet for a three spin-$\frac{1}{2}$ system. Spins are listed electron 1, electron 2, nucleus 1 (coupled to electron 1). The states found in the singlet itself are shown in bold.

000	**220**
	022
	123
	321
130	**310**
031	013
132	213
231	312

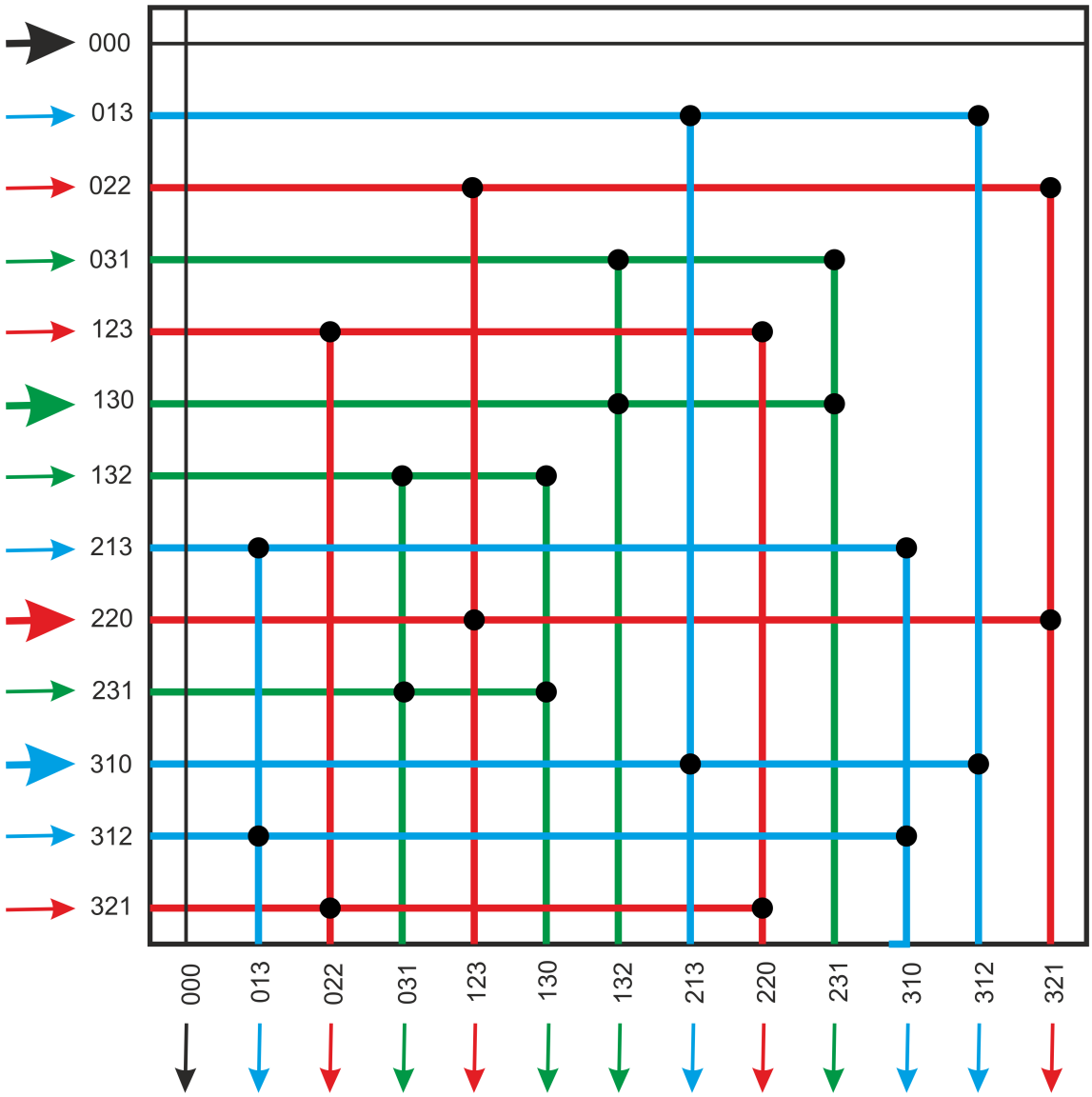

Figure 2.4. Connectivity of the HFI Liouvillian through the 13 states retained after ZTE was applied to a three spin-$\frac{1}{2}$ system. Different colours indicate the different non-interacting subspaces, the thin black line shows that the unit state converts with nothing else. The arrows indicate the flow of basis state populations through the matrix with the large arrows indicating the initially populated states.

non-evolving unit state always contributes $\frac{1}{4}$ to the total, thus the MFE calculation which in the full space uses 64×64 operators can be calculated exactly using:

$$\Phi_S = \frac{1}{4} - \Phi_S(220) + 2 \times \Phi_S(130) \tag{2.29}$$

where $\Phi_S(220)$ and $\Phi_S(130)$ both use only 4×4 matrices.[5] This is a massive reduction in the state-space, a factor 16 in terms of operator size which would result in a speed-up of ≈ 4000

[5]For implementation purposes the $\Phi_S(220)$ sub-space includes the state 222. The criterion which would remove states which have all 'Z's on either radical is not generally applicable to all types of RP (a radical carrying no magnetic nuclei is the exception to the rule) and so is best avoided. Application of a subsequent ZTE procedure will remove the few states that remain unpopulated for this reason.

in matrix-matrix multiplications, matrix diagonalisations and inversions. It should be noted at this point that this reduction equals that achieved by separating the radicals and exploiting matrix block diagonality, as described at the end of Section 2.1.2.

Conservation Laws and Non-Interacting Subspaces

It is fruitful, having discovered that there are non-interacting subspaces to try and understand the physical justification for them. In order to do this we consider again conservation of eigenvalues of the spin angular momentum projection operators. Not only does $\hat{S}_z^{\text{Total}}$ commute with the system Hamiltonian, but so too do $\hat{S}_z^A = \sum m_i^A$ and $\hat{S}_z^B = \sum m_i^B$:

$$\left[\hat{H}, \hat{S}_z^A\right] = \left[\hat{H}, \hat{S}_z^B\right] = 0 \tag{2.30}$$

Inspecting the subspaces of Table 2.3 for their quantum coherence (M_A and M_B) on each radical reveals that indeed these quantities are conserved within the subspaces:

$$\begin{gathered}
\left(000\right) \Rightarrow M_A = 0, M_B = 0, \quad \begin{pmatrix} 220 \\ 020 \\ 123 \\ 321 \end{pmatrix} \Rightarrow M_A = 0, M_B = 0, \\
\begin{pmatrix} 130 \\ 031 \\ 132 \\ 231 \end{pmatrix} \Rightarrow M_A = +1, M_B = -1, \quad \begin{pmatrix} 013 \\ 213 \\ 310 \\ 312 \end{pmatrix} \Rightarrow M_A = -1, M_B = +1
\end{gathered} \tag{2.31}$$

Thus we may more formally rewrite Equation (2.29) as:

$$\Phi_S(\hat{P}_S) = \frac{1}{4} + \Phi_S(M_A = 0, M_B = 0) + 2\Phi_S(M_A = +1, M_B = -1) \tag{2.32}$$

where $\Phi_S(M_A, M_B)$ indicates the subspace into which the operators and vectors have been projected.[6] Once again the $\begin{pmatrix} l \\ m \end{pmatrix}$ style state-list provides an efficient way of screening states for which subspace they belong in, the orders m on each radical are simply summed over individually

[6]Note this definition is essentially the same as Equation (2.29) but here we define the subspaces analytically by value of M on each radical. This has the advantage that the signs of the contributions in Equation (2.29) fall out naturally when the singlet state is projected into each subspace.

and unless the combination of (M_A, M_B) is $(0, 0)$ or $(+1, -1)$ the state is discarded. Such an analysis can then be used to form a reduction projection matrix, and to form the reduced state-list directly.

2.5.1 Path Tracing

Looking at the connectivity of even the reduced Liouvillian shows that the operator is still sparse and each state connects only with a few others, Fig 2.4. It was noted by Kuprov that the 'connect-the-dots' approach to connectivity analysis used in Fig 2.4 is equivalent to performing a graph-theoretical path tracing procedure through the matrix [105]. The basis states are treated as the nodes of a graph and off-diagonal elements in the Liouvillian as edges which connect the nodes. The Liouvillian can then be treated as the adjacency matrix describing the flow of magnetisation through the system as a result of a propagation step which drives it through the connections of the graph.

This procedure for SSR was implemented by Kuprov in the *Spinach* library and has been successfully used for the SSR of many spin dynamics calculations [94], not at all limited to spin chemistry. In fact, for spin chemistry the path tracing above which separates the subspaces according to the radical coherence orders is the best that can be achieved in the nIST basis for MFE calculations. It is perhaps worthwhile noting at this point that the path tracing protocol applied to isotropic MFE calculations in the $\alpha\beta$ basis not only returns the M_S block diagonalisation of section 2.1.3, but goes further and finds even more independent subspaces, see also Fig 3.2 in Chapter 3.

2.6 Summary Two

In the second part of this chapter we have identified the redundant states that are removed by ZTE analysis of the system Liouvillian from a singlet starting vector. Two types of states are never populated in this regime:

- States with non-zero coherence order, $(M \neq 0)$.
- States which do not have combinations of individual radical quantum coherences of (0,0), (+1,−1) or (−1,+1).

Both criteria can be analysed directly from the list of basis vectors in the state-space written in the $\begin{pmatrix} l \\ m \end{pmatrix}$ form, by summing over the relevant m's. This provides an easy means to find the indices of the retained states so that a reduction projection operator can be constructed, and hence the full matrix size can be reduced before the main work of the simulation is done.

However, given the exponential scaling of the problem it is often the case that the initial full matrix cannot be stored by the computer in the first place, or that, even if it is stored the matrix multiplications required to reduce its size are prohibitively slow or memory consuming. It would be far better to produce the vectors and matrices directly into the reduced state-space. The next section of this chapter is concerned with deriving a method for making operators directly into a reduced basis, without the need to make the full operators first.

2.7 Formation of Operators Directly into the Reduced Basis

It is clearly advantageous to produce the Liouvillian directly in the reduced state-space. We are working in the normalised IST basis, where every state is the direct product combination of the nISTs as written in the state definition. Similarly, any operator, or density matrix, can be written as a linear combination over the direct product combinations of nISTs on each spin, the tensor product operators (TPOs), $\hat{O}_k$.

$$\hat{O}_k = \bigotimes_{i=1}^{N} \hat{B}_i \tag{2.33}$$

where $\hat{B}_i$ are the generating operators *i.e.* the nISTs.

To begin, the density matrix, $\hat{\rho}(t)$ is expanded as a time-dependent linear combination of the normalised TPOs:

$$\hat{\rho}(t) = \sum_k b_k(t)\hat{O}_k \tag{2.34}$$

where $b_k(t)$ are the time-dependent expansion coefficients, most of which will be zero. The above may be substituted into the Hilbert space Liouville-von Neumann equation:

$$\frac{\mathrm{d}\hat{\rho}(t)}{\mathrm{d}t} = -\mathrm{i}\left[\hat{H}, \hat{\rho}(t)\right] \tag{2.35}$$

such that:

$$\sum_k \frac{\mathrm{d}b_k(t)}{\mathrm{d}t}\hat{O}_k = -\mathrm{i}\sum_n b_n(t)\left[\hat{H},\hat{O}_n\right] \tag{2.36}$$

Pre-multiplication by $\hat{O}_m^T$, and taking a trace on both sides gives:

$$\sum_k \frac{\mathrm{d}b_k(t)}{\mathrm{d}t}\mathrm{Tr}\left\{\hat{O}_m^T\hat{O}_k\right\} = -\mathrm{i}\sum_n b_n(t)\mathrm{Tr}\left\{\hat{O}_m^T\left[\hat{H},\hat{O}_n\right]\right\} \tag{2.37}$$

which, on noting the orthonormality of the normalised ISTs, can be simplified to:

$$\frac{\mathrm{d}b_m(t)}{\mathrm{d}t} = -\mathrm{i}\sum_n b_n(t)\mathrm{Tr}\left\{\hat{O}_m^T\left[\hat{H},\hat{O}_n\right]\right\} \tag{2.38}$$

Comparison of this expression with that for the Liouville-von Neumann in the $\alpha\beta$ product basis in Liouville space:

$$\frac{\mathrm{d}\left|\hat{\rho}(t)\right\rangle}{\mathrm{d}t} = -\mathrm{i}\hat{\hat{L}}\left|\hat{\rho}(t)\right\rangle \tag{2.39}$$

gives, in the nIST basis:

$$\hat{\hat{L}}_{mn} = \mathrm{Tr}\left\{\hat{O}_m^T\left[\hat{H},\hat{O}_n\right]\right\} \tag{2.40}$$

The Hamiltonian may also be written as a linear combination of TPOs:

$$\hat{H} = \sum_h a_h\hat{O}_h \tag{2.41}$$

and substitution of this into Equation (2.40) allows the calculation of the Liouvillian, element by element according to the following:

$$\hat{\hat{L}}_{mn} = \sum_h a_h\mathrm{Tr}\left\{\hat{O}_m^T\left[\hat{O}_h,\hat{O}_n\right]\right\} \tag{2.42}$$

Expanding the commutators, cyclically permuting the operators (allowed under a trace) and reforming a commutator gives:

$$\hat{\hat{L}}_{mn} = -\sum_h a_h\mathrm{Tr}\left\{\left[\hat{O}_m^T,\hat{O}_n\right]\hat{O}_h\right\} \tag{2.43}$$

An element is only non-zero if the commutator of its basis operators contains the transpose of an operator in the Hamiltonian.

If the commutator in Equation (2.43) is split into its two parts it is possible to calculate the left and right acting parts of the Liouvillian separately, which is particularly useful when dealing with anti-commutator superoperators as is required by the kinetics superoperator. The left and right acting Liouvillians are defined as:

$$\hat{L}\rho \Rightarrow \hat{\hat{L}}^L\hat{\rho} \tag{2.44}$$

$$\rho\hat{L} \Rightarrow \hat{\hat{L}}^R\hat{\rho} \tag{2.45}$$

respectively. Then the commutation superoperator is simply $\hat{\hat{L}}^L - \hat{\hat{L}}^R$. The elements of each of these operators can be extracted from Equation (2.43) to be:

$$\hat{\hat{L}}^L_{mn} = -\sum_h a_h \mathrm{Tr}\left\{\hat{O}_m^T\hat{O}_n\hat{O}_h\right\} \tag{2.46}$$

$$\hat{\hat{L}}^R_{mn} = -\sum_h a_h \mathrm{Tr}\left\{\hat{O}_n\hat{O}_m^T\hat{O}_h\right\} \tag{2.47}$$

The mixed product property of direct products allows the separation of the multiplication of two TPOs into normal matrix multiplications of the pairs of basis generators on each spin, numbered 1,2,3$\cdots$:

$$\hat{O}_m^T\hat{O}_n = \left(\hat{B}^T_{m1}\otimes\hat{B}^T_{m2}\otimes\hat{B}^T_{m3}\cdots\right)\left(\hat{B}^{\mathrm{gen}}_{n1}\otimes\hat{B}_{n2}\otimes\hat{B}_{n3}\cdots\right) \tag{2.48}$$

$$= \left(\hat{B}^T_{m1}\hat{B}_{n1}\right)\otimes\left(\hat{B}^T_{m2}\hat{B}_{n2}\right)\otimes\left(\hat{B}^T_{m3}\hat{B}_{n3}\right)\cdots \tag{2.49}$$

Additionally, the product of any pair of basis generators is a linear combination of the other operators in the set:

$$\hat{B}_i^T\hat{B}_j = \sum_k c_k^{i^T,j}\hat{B}_k^T \tag{2.50}$$

where

$$c_k^{i^T,j} = \mathrm{Tr}\left\{\hat{B}_i^T\hat{B}_j\hat{B}_k\right\} \tag{2.51}$$

These are known as the structure coefficients of the nISTs and are independent of multiplicity,

i.e. the structure coefficients of $\hat{T}_{m,l}\hat{T}_{m',l'}$ are functions of m, m', l, l' with no dependence on the actual size of the matrices. We remember that the operators of the Hilbert space Hamiltonians are direct products of relevant combinations of the Pauli spin operators, which are directly proportional to the normalised ISTs, and hence that Equation (2.41) can also be expanded according to Equation (2.33). Thus the elements of the left acting Liouvillian can be defined as:

$$\begin{aligned}
\hat{\hat{L}}^L_{mn} &= -\sum_h a_h \mathrm{Tr}\left\{\left(\sum_{k1} c_{k1}^{m1^T,n1}\hat{B}^T_{k1}\hat{B}_{h1}\right)\otimes\left(\sum_{k2} c_{k2}^{m2^T,n2}\hat{B}^T_{k2}\hat{B}_{h2}\right)\otimes\cdots\right\} \\
&= -\sum_h a_h \mathrm{Tr}\left\{\sum_{k1} c_{k1}^{m1^T,n1}\hat{B}^T_{k1}\hat{B}_{h1}\right\}\cdot\mathrm{Tr}\left\{\sum_{k2} c_{k2}^{m2^T,n2}\hat{B}^T_{k2}\hat{B}_{h2}\right\}\cdots \\
&= -\sum_h a_h \left(\sum_{k1} c_{k1}^{m1^T,n1}\mathrm{Tr}\left\{\hat{B}^T_{k1}\hat{B}_{h1}\right\}\right)\cdot\left(\sum_{k2} c_{k2}^{m2^T,n2}\mathrm{Tr}\left\{\hat{B}^T_{k2}\hat{B}_{h2}\right\}\right)\cdots \\
&= -\sum_h a_h c_{h1}^{m1^T,n1} c_{h2}^{m2^T,n2}\cdots
\end{aligned} \tag{2.52}$$

and similarly the right acting superoperator is:

$$\hat{\hat{L}}^R_{mn} = -\sum_h a_h c_{h1}^{n1,m1^T} c_{h2}^{n2,m2^T}\cdots \tag{2.53}$$

Putting these together to form the Hamiltonian commutator superoperator gives:

$$\hat{\hat{L}}_{mn} = -\sum_h a_h \prod_{i=1}^{n_{\mathrm{spins}}} c_{hi}^{mi^T,ni} + \sum_h a_h \prod_{i=1}^{n_{\mathrm{spins}}} c_{hi}^{ni,mi^T} \tag{2.54}$$

where n_{spins} is the number of spins in the system.

The left and right acting superoperators can be formed for any operator built from a linear combination of the direct products of spin operators. Such operators are necessary, for example, for the construction of kinetic superoperators in the Jones-Hore master equation [79, 82, 84] and for Lindblad type relaxation [87].

In this section we have outlined a method for the production of superoperators directly into state-space-reduced basis, which is applicable to any number of any kind of spin. This method may be applied to any reduced basis sets, not limited to the subspaces required for spin chemical calculations.

2.7.1 Implementation

Tables of the structure coefficients $c_h^{i^T,j}$ can be compiled for all the nISTs, *i.e* for each combination of generators, i, j, h, which can then be used with Equation (2.54) to form the Liouvillian

by walking through the reduced state-list element by element accounting, in the constant a_h, both for the proportionality constant between the normalised ISTs and the spin operators and for the system-dependent variables (Larmor frequency and HFIs *etc.*). As the operators are at most bilinear, Liouvillian generation may be accelerated by screening any pairs of states with more than two positions different. In addition the structure coefficients are saved and reloaded as necessary to make the required product. However, even with these accelerations the process of Liouvillian generation is fairly slow because it is necessary to loop over the state-list twice to fill in every element, *i.e.* to get every combination of states m, n one must loop over the state-list within a loop of the state-list.

An alternative, more efficient implementation of the theory outlined in this section for the construction of superoperators in the reduced basis was proposed by Kuprov and is currently used in the kernel of the *Spinach* library, in the code p_superop.m.

2.8 Symmetrisation

Many molecules possess some intrinsic symmetry, and if this property extends to the magnetic equivalence of different spins the symmetry may be harnessed to bring about further reductions in the size of the problem to be solved [106]. Two distinct methods for symmetry-derived SSR are discussed in this section.

2.8.1 Symmetry Adapted Linear Combinations

It is possible to make use of the magnetic equivalence of spins to form symmetry-adapted basis sets. That is, symmetry adapted linear combinations (SALCs) of states which differ only be a permutation of nISTs on the equivalent nuclei are formed according to the normal group theoretical procedure [10]. Naturally the resulting SALCs belong to different irreps, *i.e.* have different behaviour under different symmetry operations, cannot interconvert and thus form non-interacting subspaces. This procedure is not limited to Liouville space and was implemented for both Hilbert and Liouville spaces in the *Spinach* libraries by Kuprov; who went on to observe that only the A_{1g} irrep is populated in spin dynamical simulations performed in Liouville space. A full derivation of the procedure can be found in Ref [94], and is not reproduced here. It is sufficient for the purposes of this thesis to note two things:

- Retaining only the totally symmetric irrep, A_{1g} is equivalent to symmetrisation of the basis.

- All characters pertaining to the A_{1g} irrep are equal to 1.

Given that only one state from all symmetry adapted linear combinations is retained on symmetrisation of the basis the resulting reduction was extremely large. It seemed sensible therefore to investigate whether symmetrisation could be performed analytically on the state-list in such a way that the superoperators could be formed directly into the symmetry reduced state-space. It was found to be possible to do this, and an overview of the successfully implemented procedure is given in the remainder of this section for completeness, however, both formation of the state-list and of the superoperators becomes extremely slow for the large systems where it would be useful and it has proved more efficient to content ourselves with forming the operators in the $\{M_A, M_B\}$ blocks and subsequently performing the symmetry reduction on those operators before embarking on the main part of the simulation.

Analytical Symmetrisation of Basis States

Magnetically equivalent spins can be permuted without affecting the system. Hence, to symmetrise the basis, all states which are equivalent but for a permutation of the nISTs describing the magnetically equivalent spins in the state are added together with equal coefficients (only the A_{1g} irrep is populated and so the coefficients for forming the SALCs are +1 for every symmetry operation) to form the symmetric linear combination. For example, within the $\{M_A = 0, M_B = 0\}$ subspace for a RP with two equivalent nuclei on radical A the states:

$$\begin{pmatrix} 0202 \\ 0220 \end{pmatrix} \tag{2.55}$$

where the spins are ordered: $e_A e_B n_{A1} n_{A2}$, are reduced simply to $\frac{1}{\sqrt{2}}(0202 + 0220)$ following symmetrisation (the factor of $\frac{1}{\sqrt{2}}$ ensures the state is normalised). Saving a linear combination of states in one reduced state list is difficult (the indexing is likely to become extremely complex). Instead the symmetrised state may be represented in the new state list by just one of the basis states from the linear combination. We know that all the other states in that linear combinations are related to the stored one by a permutation of nIST-operators on the equivalent spins. That is, in the symmetry-reduced state-list only 0202 is actually retained in the list, but it is known to now represent the symmetric sum over both permutations of nISTs on the equivalent spins (02 and 20). In order to account for the normalisation of the symmetric linear combination it is necessary to have a coefficient associated with each state retained in the basis, equal to the

number of permutation-related states it represents. For systems with many sets of symmetric spins the coefficient on each state is simply the product of the coefficients with respect to each symmetry group.

To form the reduced state-list the states are added to the list one at a time. If a new state is only a permutation of equivalent spins away from a state already in the list the new state is not added itself, but +1 is added to the coefficient of the pre-listed state. For large spin systems this procedure turns out to be extremely slow in practice. Though in terms of the spin system memory this procedure is very efficient this is at the expense of a slow calculation time the first time a particular spin topology is simulated.

Forming Operators Directly in the Symmetry Reduced State-Space

Unfortunately, although it is sufficient for the purposes of state indexing to include just one state from the symmetric linear combination, this is not true when forming the operators.

In order to calculate the matrix element $\hat{\hat{L}}_{mn}$ it is necessary to expand the m-state into all the states it represents, calculate the coefficient of each 'hidden state' with each state represented by the n-state add them together and normalise with respect to the number of states hidden by each. Thus one element of the matrix is formed. Although this method has been successfully implemented, and gives a significant advantage to the memory footprint of a simulation this gain is at the expense of an extremely slow procedure for forming both the basis state-list and the operators. Saving the operators for each spin system topology brings some advantage but really, given the rapidity of symmetrisation codes and the sparsity of the matrices this pre-symmetrisation routine is somewhat redundant.[7]

2.8.2 Clebsch-Gordon Symmetrisation

An alternative method for symmetry reducing the basis is to combine the spin angular momenta of the equivalent spins by Clebsch-Gordon addition [11], the resulting angular momentum can be assigned to a single 'effective' spin. For example, two equivalent spin-$\frac{1}{2}$:

$$\frac{1}{2} + \frac{1}{2} \rightarrow (1, 0) \tag{2.56}$$

can be described by a spin 1 and spin 0. For a RP reaction which has two equivalent nuclei on one radical the yield calculated for those spins explicitly included, $\Phi_S\left(\frac{1}{2}, \frac{1}{2}\right)$ is equal to

[7] It was satisfying to prove it could be done however.

$\frac{3}{4}\Phi_S(1) + \frac{1}{4}\Phi_S(0)$ where the coefficients account for 'un-normalising' the initial singlet with respect to the effective system nuclei and re-normalising with respect to the true full system, *i.e.* the spin multiplicity of a spin-1 and spin-0 space is 3 and 1 respectively, but the spin multiplicity of two spin-$\frac{1}{2}$ is 4, and this must be accounted for when the sum over the simulations is taken. In terms of SSR the reduction in Hilbert space is matrix size of $16 \rightarrow 12 + 4$ which when scaled into Liouville space is $256 \rightarrow 144{+}16$. Obviously, the larger the number of magnetically equivalent nuclei the bigger the reduction. Furthermore, in systems where Clebsch-Gordon addition gives multiple equal effective spins only one instance need be calculated and the contribution to the total is then scaled by the number of times that effective spin recurs. For example, for a three spin-$\frac{1}{2}$ system:

$$\frac{1}{2} + \frac{1}{2} + \frac{1}{2} \rightarrow (1, 0) + \frac{1}{2} \rightarrow \left(\frac{3}{2}, \frac{1}{2}, \frac{1}{2}\right) \tag{2.57}$$

$$\Phi_S\left(\frac{1}{2}, \frac{1}{2}, \frac{1}{2}\right) = \frac{1}{8}\left(4 \times \Phi_S\left(\frac{3}{2}\right) + 2 \times 2 \times \Phi_S\left(\frac{1}{2}\right)\right) \tag{2.58}$$

In addition it is perfectly simple to apply this procedure to a series of symmetry groups, but all combinations of the resulting effective spins must be calculated over.

This procedure is well-known and has been often used for spin chemical calculations. Our contribution to the method has been to implement it in a manner compatible with the *Spinach* library and thus in combination with the analytical pre-reduction methods outlined above. Together it is possible to bring about massive reductions in the matrix size of spin chemical calculations with the relevant operators and vectors formed directly into the reduced basis.

2.9 Relaxation

Many theoretical treatments have been proposed for the description of relaxation, dephasing and decoherence processes a selection of which were used in the simulations of Chapter 5. For the moment however we concern ourselves solely with formulations built upon the perturbative treatment of a fluctuating magnetic interaction. The most general treatment of a perturbative time-dependent interaction fluctuation is via general cumulant expansion theory [107]. However, for most purposes Redfield theory is deemed sufficient [90], and is equivalent to truncating the cumulant expansion at second order, with some additional approximations. It is to Redfield theory that we restrict ourselves in the work that follows.

2.9.1 Redfield Theory

There are many excellent discussions of the derivation of Redfield theory in the literature and text books. However, for clarity we include here an outline of the derivation following, for the most part, the introduction of a very readable review by Goldman in Ref [92]. Although this derivation is given in Hilbert space the Liouville space analogue is readily extrapolated.

The Hamiltonian is divided into two terms, a static part (for RPs this includes the electronic Zeeman interactions and isotropic parts of the hyperfine interaction) and a time-dependent spin-lattice coupling term (usually for RPs arising from modulation of the anisotropic HFIs, in NMR systems this term will include rotational modulation of chemical shift anisotropies and dipole-dipole interactions):

$$\hat{H} = \hat{H}_0 + \hat{H}_1 \tag{2.59}$$

We then move into the interaction representation to remove the effects of the static Hamiltonian. All operators, $\hat{Q}$ in the laboratory frame are replaced with:

$$\tilde{\hat{Q}}(t) = \mathrm{e}^{\mathrm{i}\hat{H}_0 t}\hat{Q}\mathrm{e}^{-\mathrm{i}\hat{H}_0 t} \tag{2.60}$$

We can now rewrite the Liouville-von Neumann equation for the evolution of the density matrix in this representation as:

$$\frac{\mathrm{d}\tilde{\rho}(t)}{\mathrm{d}t} = \frac{\mathrm{d}}{\mathrm{d}t}\left\{\mathrm{e}^{\mathrm{i}\hat{H}_0 t}\rho(t)\mathrm{e}^{-\mathrm{i}\hat{H}_0 t}\right\} \tag{2.61}$$

$$= \mathrm{i}\hat{H}_0\tilde{\rho}(t) + \mathrm{e}^{\mathrm{i}\hat{H}_0 t}\frac{\mathrm{d}\rho(t)}{\mathrm{d}t}\mathrm{e}^{-\mathrm{i}\hat{H}_0 t} - \mathrm{i}\tilde{\rho}(t)\hat{H}_0 \tag{2.62}$$

$$= \mathrm{i}\left[\hat{H}_0, \tilde{\rho}(t)\right] - \mathrm{i}\mathrm{e}^{\mathrm{i}\hat{H}_0 t}\left[\hat{H}_0 + \hat{H}_1, \rho(t)\right]\mathrm{e}^{-\mathrm{i}\hat{H}_0 t} \tag{2.63}$$

and given that $\mathrm{e}^{-\mathrm{i}\hat{H}_0 t}\mathrm{e}^{\mathrm{i}\hat{H}_0 t} = \hat{\mathbb{1}}$ we can rewrite the final term of Equation (2.63):

$$\mathrm{e}^{\mathrm{i}\hat{H}_0 t}\left[\hat{H}_0 + \hat{H}_1, \rho(t)\right]\mathrm{e}^{-\mathrm{i}\hat{H}_0 t} = \left[\hat{H}_0 + \tilde{\hat{H}}_1(t), \tilde{\rho}(t)\right] \tag{2.64}$$

so that overall Equation (2.63) becomes:

$$\frac{\mathrm{d}\tilde{\rho}(t)}{\mathrm{d}t} = -\mathrm{i}\left[\tilde{\hat{H}}_1(t), \tilde{\rho}(t)\right] \tag{2.65}$$

The perturbation part of the Hamiltonian, $\tilde{\hat{H}}_1(t)$ now has two sources of time dependence, both

from its own random fluctuations and from moving to the interaction representation. Formally integrating Equation (2.65) and substituting the result back into the right side of (2.65) gives:

$$\frac{\mathrm{d}\tilde{\rho}(t)}{\mathrm{d}t} = -\mathrm{i}\left[\tilde{\hat{H}}_1(t), \tilde{\rho}(0)\right] - \int_0^t \left[\tilde{\hat{H}}_1(t), \left[\tilde{\hat{H}}_1(t'), \tilde{\rho}(t')\right]\right] \mathrm{d}t' \tag{2.66}$$

Up to this point we have made no approximations and the above expression is exact, within the assumptions of perturbation theory, *i.e.* that $||\hat{H}_0|| \gg ||\hat{H}_1||$. We now make a modification. Firstly an ensemble average is taken to account for the random processes being, by the very nature of randomness, different across the ensemble, symbolised by an overbar. As all parts begin in the same state, $\tilde{\rho}(0)$ and as $\tilde{\hat{H}}_1$ is assumed to a stationary Markov process it has a vanishing average and the first term of Equation (2.66) goes to zero. Thus we obtain:

$$\frac{\mathrm{d}\overline{\tilde{\rho}}(t)}{\mathrm{d}t} = -\int_0^t \overline{\left[\tilde{\hat{H}}_1(t), \left[\tilde{\hat{H}}_1(t'), \tilde{\rho}(t')\right]\right]} \mathrm{d}t' \tag{2.67}$$

Next, we expand $\hat{H}_1(t)$ as a sum over the spin operators, $\hat{V}_\alpha$, with time-dependent coefficients, $F_\alpha(t)$:

$$\hat{H}_1(t) = \sum_\alpha \hat{V}_\alpha F_\alpha(t) \tag{2.68}$$

At this point in the Goldman review [92] the operators $\hat{V}_\alpha$ are defined in the eigenbasis of $\hat{H}_0$. This proves very convenient for simplification later in the derivation, but at the expense of diagonalising $\hat{H}_0$ which is straightforward when a high-field Zeeman interaction dominates, but is non-trivial at low field when the isotropic HFIs are comparable in strength. Instead here we follow Refs [93, 108, 109] and use, as in Equation (2.41), the tensor product operators:

$$\hat{H}_1(t) = \sum_\alpha \hat{O}_\alpha F_\alpha(t) \tag{2.69}$$

With that in place we continue with the standard derivation. Substitution of Equation (2.69) into Equation (2.67) gives:

$$\frac{\mathrm{d}\overline{\tilde{\rho}}(t)}{\mathrm{d}t} = -\sum_{\alpha,\beta}\int_0^t \overline{\left[\tilde{\hat{O}}_\alpha(t), \left[\tilde{\hat{O}}^\dagger_\beta(t'), \tilde{\rho}(t'))\right]\right] F_\alpha(t) F^*_\beta(t')\mathrm{d}t'} \tag{2.70}$$

If the time-dependent interaction is just a scalar quantity then the $\hat{H}_1(t)$ at different times commute with each other and Equation (2.70) is readily solved. However, modulation of aniso-

tropic interactions is more frequently encountered, and unfortunately the time-dependent fluctuations at different times then do not commute. Exact solution of Equation (2.70) is no longer possible and instead certain approximations must be applied. Firstly, that the fluctuation of the interaction is rapid compared to the evolution of the system. During the correlation time, τ_c, of a fluctuation, the product $\hat{F}_\alpha(t)\hat{F}^*_\beta(t')$ has decayed significantly. We assume that τ_c is short compared to the timescale of evolution of the system, and choose $t \gg \tau_c$. As $\tilde{\rho}(t)$ is assumed to evolve slowly compared to τ_c, it is reasonable to assume that $\tilde{\rho}(t') = \tilde{\rho}(t)$ and this substitution is made. Secondly, as $t \gg \tau_c$ any density matrix $\tilde{\rho}(t)$ has experienced many τ_c's worth of relaxation and over such a long time the effect of random evolutions will cancel out. Thus $\overline{\tilde{\rho}(t)}$ can be replaced by $\tilde{\rho}(t)$. This acts to decouple the system (spin part) and lattice so that Equation (2.70) can be rewritten:

$$\frac{\mathrm{d}\tilde{\rho}(t)}{\mathrm{d}t} = -\sum_{\alpha,\beta}\int_0^t \left[\tilde{\hat{O}}_\alpha(t), \left[\tilde{\hat{O}}^\dagger_\beta(t'), \tilde{\rho}(t)\right]\right] \overline{F_\alpha(t)F^*_\beta(t')}\mathrm{d}t' \tag{2.71}$$

We make the substitution $\tau = t - t'$ and note that as $t \gg \tau_c$ we can extend the integral from t to ∞, removing the dependence on t within the integral. In addition we remember that the random fluctuations are assumed to be stationary and memory-less, hence $\overline{F_\alpha(t)F^*_\beta(t')} = \overline{F_\alpha(t')F^*_\beta(t)} = G_{\alpha\beta}(\tau)$. This is called the correlation function. Converting back into the laboratory frame gives us finally:

$$\frac{\mathrm{d}\rho(t)}{\mathrm{d}t} = -\mathrm{i}\left[\hat{H}_0, \rho(t)\right] - \sum_{\alpha,\beta}\int_0^\infty \left[\hat{O}_\alpha, \left[\mathrm{e}^{-\mathrm{i}\hat{H}_0\tau}\hat{O}^\dagger_\beta\mathrm{e}^{\mathrm{i}\hat{H}_0\tau}, \rho(t)\right]\right] G_{\alpha\beta}(\tau)\mathrm{d}\tau \tag{2.72}$$

the Redfield master equation. In Liouville space the first term above leads to the Hamiltonian superoperator and the second term is $\hat{\hat{R}}$ the relaxation superoperator:

$$\hat{\hat{R}} = -\sum_{\alpha,\beta}\int_0^\infty \hat{\hat{O}}_\alpha\mathrm{e}^{-\mathrm{i}\hat{\hat{H}}_0\tau}\hat{\hat{O}}^\dagger_\beta\mathrm{e}^{\mathrm{i}\hat{\hat{H}}_0\tau}G_{\alpha\beta}(\tau)\mathrm{d}\tau \tag{2.73}$$

2.9.2 Generating the Full Relaxation Superoperators

As aforementioned, the spin operators in Equation (2.73) are not written in the eigenbasis of $\hat{\hat{H}}_0$ and so there is no easy way to remove the time dependence from the integral. A numerical integration procedure was reported in Ref [109] which avoids numerical diagonalisation. This is currently implemented in the *Spinach* library's relaxation module and was used for the investigation of long-lived states in NMR systems presented in Chapter 7 of this thesis.

Extreme Narrowing Limit

In this section we make use of a result derived in the thesis of Wagner-Rundell, [93], specifically for low-field RP relaxation, and the following is reproduced from that work. At low field it is often true that the energy-level differences between eigenstates is very small, of the order of a few MHz. Thus for reasonably small molecules tumbling in solution the frequency of fluctuations is much larger than the coherent dynamics frequency of the system, and the system is in the extreme narrowing limit [110]:

$$\tau_c^2 \omega_{\alpha\beta}^2 \ll 1 \tag{2.74}$$

where $\omega_{\alpha\beta}$ is the largest eigenvalue difference in the system. If the static Hamiltonian is diagonalised by the unitary matrix $\hat{X}$ such that $\hat{X}^T \hat{H}_0 \hat{X} = \hat{\Lambda}$ where $\hat{\Lambda}$ is the diagonal matrix of eigenvalues, it is possible to rewrite the relaxation part of Equation (2.72) as:

$$\begin{aligned}
\hat{\hat{R}}\rho(t) &= -\hat{X}\hat{X}^T \sum_{\alpha,\beta} \int_0^t \left[\hat{O}_\alpha, \left[\mathrm{e}^{-\mathrm{i}\hat{H}_0\tau}\hat{O}_\beta^\dagger \mathrm{e}^{\mathrm{i}\hat{H}_0\tau}, \rho(t)\right]\right] G_{\alpha\beta}(\tau)\mathrm{d}\tau \hat{X}\hat{X}^T \\
&= \hat{X} \sum_{\alpha,\beta} \left(\int_0^\infty \hat{X}^T\hat{O}_\alpha\hat{X}\hat{X}^T\mathrm{e}^{-\mathrm{i}\hat{H}_0\tau}\hat{X}\hat{X}^T\hat{O}_\beta^\dagger\hat{X}\hat{X}^T\mathrm{e}^{\mathrm{i}\hat{H}_0\tau}\hat{X}G_{\alpha\beta}(\tau)\mathrm{d}\tau\hat{X}^T\rho(t)\hat{X} \right. \\
&\left. + \cdots \right) \hat{X}^T
\end{aligned} \tag{2.75}$$

where in the second line we have expanded the commutator and removed $\rho(t)$ from the integral as it has no dependence on τ. Letting $\mathbf{K}^{\alpha\beta}$ be the integral over each term of the commutation expansion, and writing $\hat{X}^T\hat{O}_i\hat{X} = \hat{O}_i^{(0)}$ then the first term is written as:

$$\mathbf{K}^{\alpha\beta} = \int_0^\infty \hat{O}_\alpha^{(0)}\mathrm{e}^{-\mathrm{i}\hat{\Lambda}\tau}\hat{O}_\beta^{\dagger(0)}\mathrm{e}^{\mathrm{i}\hat{\Lambda}\tau}G_{\alpha\beta}(\tau)\mathrm{d}\tau \tag{2.76}$$

An element of $\mathbf{K}^{\alpha\beta}$ is then given by:

$$\begin{aligned}
\mathbf{K}_{nm}^{\alpha\beta} &= \int_0^\infty \sum_j \left[\hat{O}_\alpha^{(0)}\right]_{nj} \mathrm{e}^{-\mathrm{i}\omega_j\tau} \left[\hat{O}_\beta^{\dagger(0)}\right]_{jm} \mathrm{e}^{\mathrm{i}\omega_m\tau} G_{\alpha\beta}(\tau)\mathrm{d}\tau \\
&= \int_0^\infty \sum_j \left[\hat{O}_\alpha^{(0)}\right]_{nj} \left[\hat{O}_\beta^{\dagger(0)}\right]_{jm} \mathrm{e}^{-\mathrm{i}\omega_{jm}\tau} G_{\alpha\beta}(\tau)\mathrm{d}\tau
\end{aligned} \tag{2.77}$$

where ω_i are the eigenvalues of the static Hamiltonian and $\omega_{jm} = \omega_j - \omega_m$. Finally, we assume an exponentially decaying correlation time, such that:

$$G(\tau) \propto \mathrm{e}^{-\frac{\tau}{\tau_c}} \tag{2.78}$$

Substitution of this into Equation (2.77) and evaluation of the integral, ignoring the imaginary parts which describe only small dynamic frequency shifts, gives:

$$\mathbf{K}^{\alpha\beta}_{mn} = \tau_c \sum_j \left[\hat{O}^{(0)}_\alpha\right]_{nj} \left[\hat{O}^{\dagger(0)}_\beta\right]_{jm} G'_{\alpha\beta} \frac{1}{\tau_c^2 \omega_{nj}^2 + 1} \tag{2.79}$$

where $G'_{\alpha\beta}$ accounts for the other, time independent, parts of the correlation function. Finally we note that in the extreme narrowing limit $\frac{1}{\tau_c^2\omega_{nj}^2+1} \approx 1$ so that:

$$\mathbf{K}^{\alpha\beta}_{mn} = \tau_c \sum_j \left[\hat{O}^{(0)}_\alpha\right]_{nj} \left[\hat{O}^{\dagger(0)}_\beta\right]_{jm} G'_{\alpha\beta} \tag{2.80}$$

The same can be done to each term of the commutation superoperator, and we can then transform it back out of the eigenbasis of $\hat{H}_0$ to give us finally, in the extreme narrowing limit:

$$\frac{\mathrm{d}\rho(t)}{\mathrm{d}t} = -\mathrm{i}\left[\hat{H}_0, \rho(t)\right] - \tau_c \sum_{\alpha,\beta} \left[\hat{O}_\alpha, \left[\hat{O}^\dagger_\beta, \rho(t)\right]\right] G'_{\alpha\beta} \tag{2.81}$$

from which it is possible to write the relaxation superoperator in terms of the perturbation Hamiltonian as [93]:

$$\hat{\hat{R}} = \overline{\hat{\hat{H}}_1 \hat{\hat{H}}_1} \tag{2.82}$$

Wigner Rotations and Correlation Functions

At low-field, the main source of relaxation for RPs is through the modulation of the anisotropic components of the HFIs.[8] As was noted in Chapter 1 any bilinear interaction can be expanded as a sum over the rank-2 spherical tensors, Equation (1.42), and these are therefore the natural operators to use in Equation (2.68) with time-dependent Wigner coefficients arising from the rotational motion. Of course, Equation (1.42) is true only in an interaction's own principal axis frame (PAF), and in cases where there is more than one interaction it is highly unlikely that the PAF's are aligned. For such systems it is much more convenient to work with each interaction

[8] It should be noted that rotational modulation of any other bilinear interaction can also be modelled thus.

in the same molecular frame (MF) where they are non-diagonal. Equation (1.42) then needed to be generalised to give:

$$\begin{aligned}\hat{H}_{\text{Bilin}} = &\frac{1}{2}\left(A_{1,1} - A_{2,2} - 2\mathrm{i}A_{1,2}\right)\hat{T}'_{2,2} \\ &- \left(A_{1,3} - \mathrm{i}A_{2,3}\right)\hat{T}'_{2,1} \\ &+ \sqrt{\frac{3}{2}}A_{3,3}\hat{T}'_{2,0} \\ &+ \left(A_{1,3} + \mathrm{i}A_{2,3}\right)\hat{T}'_{2,-1} \\ &+ \frac{1}{2}\left(A_{1,1} - A_{2,2} + 2\mathrm{i}A_{1,2}\right)\hat{T}'_{2,-2}\end{aligned} \tag{2.83}$$

where the ISTs are as defined in Equation (1.17) and are directly proportional to the normalised ISTs which define the basis. A rotationally random perturbation Hamiltonian $\hat{H}_1$ is then the sum over all anisotropic interactions in the molecular frame rotated into a random orientation with respect to the laboratory frame:

$$\hat{H}_1 = \hat{R}_{zyz}\left(\alpha(t), \beta(t), \gamma(t)\right)\hat{H}_{\text{Bilin}} \tag{2.84}$$

It is then necessary to make use of the rotation properties of the spherical tensors. Under a rotation, $\hat{R}_{zyz}$, $\hat{T}_{l,m}$ is transformed into a linear combination over all the ISTs of that rank [11]:

$$\hat{R}_{zyz}\left(\alpha(t), \beta(t), \gamma(t)\right)\hat{T}'_{l,m} = \sum_{m'=-l}^{l} \mathcal{D}^{(l)}_{m',m}\left(\alpha(t), \beta(t), \gamma(t)\right)\hat{T}'_{l,m'} \tag{2.85}$$

where $\mathcal{D}^{(l)}_{m',m}\left(\alpha(t), \beta(t), \gamma(t)\right)$ are the time-dependent Wigner coefficients of the Euler angles, $(\alpha(t), \beta(t), \gamma(t)) = \Omega(t)$ which are randomly changing over time due to the rotational motion. The correlation functions to be evaluated in forming the Redfield theory relaxation matrix are simply correlation functions of the time-dependent Wigner coefficients and conveniently analytical expressions for these are already known. We assume here isotropic rotational diffusion, which gives [11, 93]:

$$G_{m',m,k',k} = \overline{\mathcal{D}_{m',m}\left(\Omega(0)\right)\mathcal{D}^{*}_{k',k}\left(\Omega(\tau)\right)} \tag{2.86}$$

$$= \frac{1}{5}\delta_{m',k'}\delta_{m,k}\mathrm{e}^{-\frac{\tau}{\tau_c}} \tag{2.87}$$

Using this result with Equations (2.83) and (2.81) it is possible to calculate the relaxation superoperator. This was implemented efficiently by Wagner-Rundell and Kuprov using a symbolic

processing procedure [93, 108] which recognised the correlation function relationship of Equation (2.86) and instead of evaluating it explicitly merely made a replacement with Equation (2.87).

It is possible to separate out the contributions to the correlation function from the Wigner correlation functions and from the system-dependent coefficients. Rewriting Equation (2.83), with $c_m^{(j)}$ representing the coefficient of the m-order tensor on the j^{th} nucleus, gives:

$$\hat{H}_1 = \sum_{j}^{\text{nspins}} \sum_{m=-2}^{2} c_m^{(j)} \hat{T}'^{(j)}_{2,m} \tag{2.88}$$

which when applying a time-dependent rotation gives:

$$\hat{H}_1(t) = \sum_{j}^{\text{nspins}} \sum_{m'=-2}^{2} \sum_{m=-2}^{2} c_m^{(j)} \mathcal{D}_{m',m} \hat{T}'^{(j)}_{2,m'} \tag{2.89}$$

Then Equation (2.82) becomes:

$$\sum_{j}^{\text{nspins}} \sum_{j'}^{\text{nspins}} \sum_{m'=-2}^{2} \frac{1}{5} \hat{T}'^{(j)}_{2,m'} \hat{T}'^{(j')}_{2,-m'} (-1)^{-m'} \chi_{j,j'} \tag{2.90}$$

$$\chi_{j,j'} = \sum_{m=-2}^{2} (-1)^m c_m^j c_{-m}^{j'} \tau_c \tag{2.91}$$

making use of the property:

$$\mathcal{D}_{k',k} = (-1)^{k'-k} \mathcal{D}^*_{-k',-k}, \tag{2.92}$$

Equation (2.87) and noting that the system is in the extreme narrowing limit. The quantity $\chi_{j,j'}$ now contains all the system-dependent information.

2.9.3 Relaxation Superoperators Directly in the Reduced State-Space

When the relaxation superoperator was made using the procedure of Refs [93, 108] and included in the MFE calculations the ZTE procedure and path tracing returned the same SSR as in the absence of $\hat{\hat{R}}$. The relaxation superoperator does not change the overall coherence order of the states and nor does it change the overall coherence order of each radical. This is in agreement with the observation of Wagner-Rundell that when the radicals were treated separately, as was described in Subsection 2.1.2, the matrices were block diagonal. In addition it was observed that symmetrisation of the basis with respect to equivalent spins, that is retaining only the states belonging to the A_{1g} irrep, is still sufficient for an exact calculation. That is, the relaxation

superoperator does not introduce coherences between states of different symmetry [94].

We, in this instance, however are not satisfied with forming large matrices and shrinking them to the minimal possible basis. It is the aim here to form the matrices directly into that minimal state-space. In the extreme narrowing region the relaxation superoperator is essentially the time-dependent Hamiltonian squared, Equation (2.82) and we are interested in at most bilinear interactions, thus there cannot be more than four spins involved in any one correlation in the relaxation matrix. In addition the two radicals are assumed to be non-interacting and the interactions between the nuclei are negligible therefore each correlation must include one (and only one) of the electrons and at most two nuclei. We are limited to three-spin correlations.

In addition, there are just two kinds of three-spin combinations. Either electron-nucleus 1 electron-nucleus-1 (*i.e.* a self-correlation) or electron-nucleus 1 electron-nucleus 2 (*i.e.* a cross-correlation), with relaxation rates $\chi_{j,j'} = \chi_{1,1}$ and $\chi_{1,2}$ respectively, Equation (2.91). It is possible to divide the full relaxation matrix into a sum over self- and cross-correlation terms on different combinations of spin. A and B are the two electrons with nuclei $A1, A2\cdots$ and $B1, B2\cdots$ respectively:

$$\hat{\hat{R}} = \chi_{A1,A1}\hat{\hat{R}}_{A1,A1} + \chi_{A1,A2}\hat{\hat{R}}_{A1,A2} + \chi_{A2,A2}\hat{\hat{R}}_{A2,A2} + \cdots \tag{2.93}$$

With this in mind it is convenient to generate the sub-relaxation matrices for each part of the above equation separately for a given spin topology and simply reload them and multiply by the spin-dependent variables in the different χ's to give the appropriate total relaxation superoperator.

In the relaxation superoperator any element which connects two states with the nIST on more than three spins different must be zero. Furthermore, any element can be filled in by reference to either a two or three spin system reference for self- and cross-correlations respectively. That is, just like the structure coefficients were used as templates for the non-zero elements of coherent evolution superoperators so a small relaxation matrix calculated for two or three spins (for the RP one electron and two nuclei at a time) is the template for larger relaxation superoperators. Naturally, the multiplicity of the spins must be reflected in the multiplicity of the spin used to calculate the template but fortunately the Wigner correlation functions are dependent only on the rank and order of the two Wigner coefficients and are independent of the matrix multiplicity.

In order to form the templates, the relaxation matrices are generated according to the symbolic processing procedure in Mathematica [111] for a single radical at a time, transformed into

the nIST basis and then 'copied and pasted' into MATLAB for subsequent referencing.

Initially this was implemented by walking through the state-list element by element, expanding out any symmetry-hidden states, and cross-referencing between the nISTs of the active spins in the states defining a particular element and the corresponding entry in the template. Thus the relaxation sub-matrices were built up, (and stored) and then multiplied by the relevant value of χ derived for a particular system.

If pre-symmetrisation was excluded a more rapid method for forming the relaxation sub-matrices can be implemented by direct analogy with Kuprov's implementation of formation of the left and right superoperators which proved to be much more efficient. This method is the fastest implementation of forming Redfield relaxation superoperators in the extreme narrowing limit at low field, however it should be noted that Kuprov's numerical implementation of Redfield theory is applicable beyond the extreme narrowing limit and is only marginally slower. The recent implementation of that in *Spinach* really renders the above somewhat redundant, but it was useful before it became out-dated.

2.10 Reaction Kinetics

As was discussed in Chapter 1, a major reason for moving to Liouville space is to be able to model reaction kinetics that are not mono-exponential decays with the same rate constant from both singlet and triplet species while maintaining a linear equation of motion. Equations (1.58), (1.59), (1.60) and (1.61) give the two currently favoured expressions for the kinetic superoperator [75, 79, 82, 84].

2.10.1 State-Space Restriction of Kinetic Superoperators

Both the Haberkorn and Jones-Hore descriptions require a commutator superoperator form of the singlet and triplet projection operators. These operators are built from products of operators across the pair of electrons, the radicals can no longer be considered independently and as expected the path-tracing approach to SSR does not return the four independent subspaces typical of the normal exponential model. Despite the fact the the singlet and triplet projection operators do not commute with the individual radical angular momentum projection operators, they do commute with $\hat{L}_z^{\mathrm{Total}}$ and so the zero coherence order screening is still viable. Reaction kinetics of course cannot affect the symmetry of the system as it reacts as a whole, and the symmetry derived SSR is still significant in systems with equivalent spins.

The anti-commutator superoperators are readily built into the reduced state-space simply by adding the left and right acting operators rather than taking the difference. The Jones-Hore master equation may be rewritten from Equation (1.61) in terms of left and right acting superoperators:

$$\hat{\hat{K}}\hat{\rho}(t) = -(k_S + k_T)\hat{\rho}(t) + k_S\hat{\hat{Q}}_T^{\text{Left}}\hat{\hat{Q}}_T^{\text{Right}}\hat{\rho}(t) + k_T\hat{\hat{Q}}_S^{\text{Left}}\hat{\hat{Q}}_S^{\text{Right}}\hat{\rho}(t) \tag{2.94}$$

which are formed according to Equations (2.52) and (2.53)

2.11 Summary Three

In the previous few sections we have investigated which states were eliminated by ZTE and determined that only the states with zero coherence order are necessary for an exact simulation of an isotropic MFE. This brings about a reduction of approximately a factor of four in the matrix size. In addition we have noted that the separate terms of the singlet starting vector may be simulated separately resulting in a further quartering of the state-space, though two simulations of this size must be run. As advantageous as it is to reduce the matrix size at all, it is even better to form the matrices directly into the reduced state-space and a means of doing so has been derived and implemented. This procedure is entirely general for any number of any type of spin. Two methods for symmetry factorisation have been presented both of which can be carried out before forming the full operator matrices. The reductions brought about by these reduction methods, considering the A_{1g} style symmetrisation, for some example RP simulations are given in Table 2.4.

In addition to simple coherent evolution we have also investigated the possibility of SSR on

Table 2.4. Examples of the reductions in the Liouville state-space for RPs containing different numbers of equivalent spin-$\frac{1}{2}$ nuclei. The final two columns show the size of the retained state-list, the number in brackets is the percentage of the full state-space retained.

Radical A	**Radical B**	**Full state-space**	$M_A = M_B = 0$	$M_A = +1, M_B = -1$
C_2	-	256	11(4.3%)	9 (3.5%)
C_3	-	1024	19(1.9%)	16(1.6%)
C_3	C_2	16,384	209(1.3%)	144(0.88%)
C_3C_3	-	65,536	291(0.44%)	262(0.40%)
C_4	C_3	262,144	551(0.21%)	400(0.17%)
$C_2C_2C_2C_2$	-	1,048,576	6843(0.65%)	6254(0.60%)
C_6	C_2	1,048,576	605(0.058%)	441(0.042%)
C_8	-	1,048,576	89(0.0085%)	81(0.0077%)

relaxation and kinetic superoperators. The same reductions are possible for relaxation superoperators as for the Hamiltonian commutator superoperators, and a procedure has been presented to form the relaxation matrix, again for any number of any type of spin, directly into the reduced state-space. The kinetic superoperators gain only from the zero coherence order filter and symmetry factorisations, but both of these can be exploited by forming the anti-commutator and left/right acting superoperators directly into the reduced basis set.

At this point it seems fruitful to compare the SSR techniques arising in this chapter, and Table 2.5 presents a summary of the techniques and when they are most beneficial for RP reaction yield calculation. Anisotropic RP reactions gain somewhat from ZTE, like the isotropic case any states with all $\hat{\mathbb{1}}$s on either radical, except for the all $\hat{\mathbb{1}}$ state itself are cut as are all states with $\hat{S}_z$'s on each spin of the radical (except when one radical bears no nuclei), but the zero coherence order filter and path-tracing do not help. Symmetry factorisation is possible for anisotropic systems, though exact magnetic equivalency is less likely to be found when full interaction tensors are considered.

It is clear from Table 2.5 that the optimum basis set for one problem is not necessarily the same for all problems. It is also possible that an alternative basis set, that has not been considered thus far, might bring about improved reductions in some cases.

Table 2.5 Summary of state-space restriction techniques and which procedure is most efficient.

	Isotropic Only	**Relaxation**	**Reaction Kinetics**	**Anisotropic**
Zero-Track Elimination	✓	✓	✓	✓
Zero-Quantum Coherence Filter	✓	✓	✓	×
Path-Tracing	✓	✓	×	×
Symmetrisation	✓	✓	✓	✓
Ms Block Diagonalisation	✓	×	✓	×
Most Efficient Method	Hilbert space	Liouville Space nIST basis	Liouville Space $\alpha\beta$ basis	Hilbert space

2.12 *Spinach*

The overall aim of this chapter was to investigate SSR techniques for spin chemical simulations with a view to developing the spin chemistry part of the *Spinach* library. *Spinach* has been mentioned at several points through the chapter and it is pertinent at this point to briefly introduce this piece of software.

Due to the wide-ranging applications of magnetic resonance techniques many different simulation packages have been published (in addition to which it is likely that most groups have their own internal code libraries). SIMPSON provides a versatile environment for the accurate numerical simulation of solid state NMR spectra. This software can in principle deal with any spin type and number of spins, limited only by the exponentially scaling state-space [112]. Another numerical package focusing on, but not limited to, solid state NMR is SpinEvolution [113] which makes use of matrix sparsity in order to accelerate the simulations. An example of a symbolic software is MathNMR [114], implemented in Mathematica, which deals with operator formation and manipulation for spin-$\frac{1}{2}$ and spin-1. In a slightly different area EASYSPIN allows numerical simulation of liquid and solid state EPR and electron-nucleus double resonance (ENDOR) spectra, as well as providing data analysis tools and usefully is available as a toolkit for MATLAB. This software is general for any number of nuclear and electron spins, limited only by the computing power. The examples mentioned in this paragraph are just the tip of the iceberg of spin dynamics simulation functionalities available. However, a comprehensive review is beyond the scope of this thesis.

Spinach is yet another library of codes for the numerical spin dynamical simulations. Written in MATLAB, *Spinach* aims to improve the efficiency of such calculations by performing all calculations using the smallest possible matrices with maximum sparsity. The spin system of a particular problem, be it NMR, EPR or spin chemistry, is entered and the function create.m writes the parameters into the *Spinach* 'spin_system' structure. Various options exist for the description of the basis set, from which the reduced state-list is formed. Using this, and the procedures presented in Section 2.7, the superoperators are formed directly into the reduced state-space. Additional ZTE and path-tracing can then be performed to weed out any other unpopulated states. Symmetrisation of the basis and projection of the operators into the subspace belonging to the A_{1g} irrep brings about the final reduction. Having formed the minimal operators any calculation can be carried out with them, and many possible experiments are already implemented in the *Spinach* 'exp' folder. Alternatively, the operators may be exported

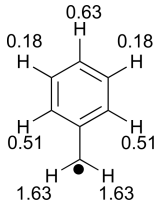

Figure 2.5 Benzyl radical. The HFI, in mT, of each nucleus is shown [115].

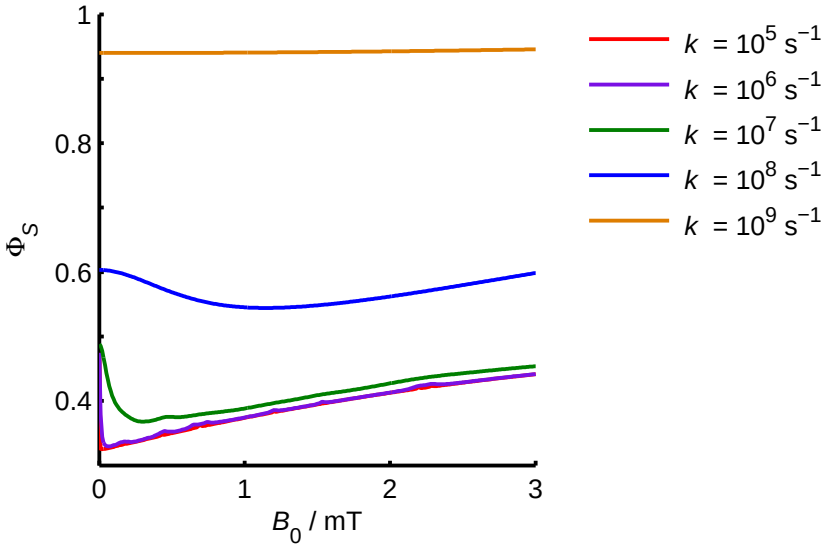

Figure 2.6. MFE on the recombination of a benzyl radical (HFI shown in Fig 2.5) with a radical bearing no signficant magnetic nuclei. The RP is born in a singlet starting state, and the singlet yield Φ_S calculated. The exact Hilbert space calculation is exactly reproduced despite the SSR applied.

from *Spinach* and used in any other simulation environment.

A full introduction can be found in Ref [95] and the codes themselves can be downloaded from http://spindynamics.org/Spinach.php. Of course development of *Spinach* is an enormous collaboration orchestrated by Kuprov with contributions from Hogben, Krzystyniak, Charnock, Hore and more recently Edwards and Karabanov. Work is ongoing to extend the scope of *Spinach* and to improve the efficiency of each stage of the calculation.

2.13 Some Examples

In order to demonstrate the scope of the techniques developed above we include here a few example simulations of radical pair reaction yields [94].[9]

The yield of singlet product formed from the recombination of a benzyl radical with a radical carrying only negligible HFIs is shown in Fig 2.6. Isotropic hyperfine couplings, Fig 2.5, were

[9]Dozens of examples of different types of spin dynamics simulations can be found in the *Spinach* examples folder.

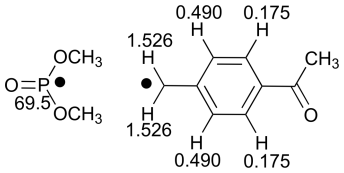

Figure 2.7. Dimethoxyphosphonyl and p-acetylbenzyl RP, HFIs that are greater than 0.1 mT are shown for each nucleus (in mT) [115, 116].

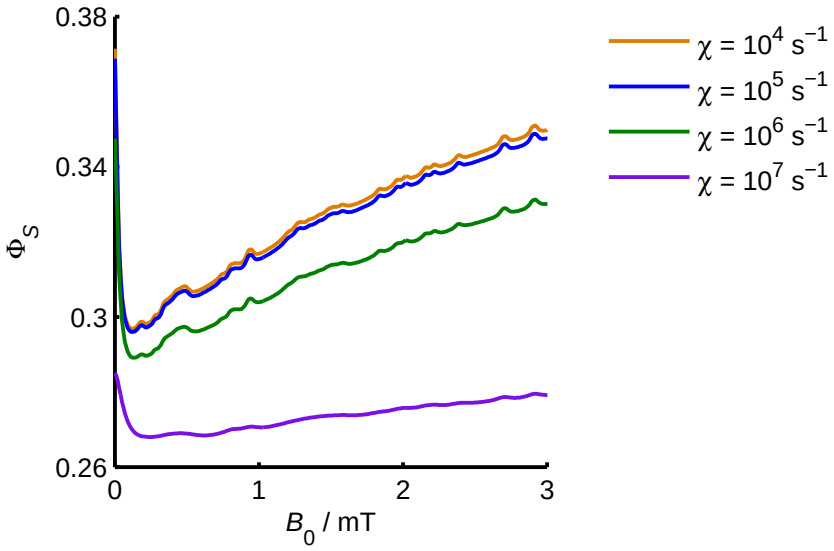

Figure 2.8. Simulated MFE on the singlet yield of a dimethoxyphosphonyl - p-acetylbenzyl RP. The relaxation rate, χ was varied as shown. $k = 10^6$ s^{-1} and HFIs are as shown in Fig 2.7.

taken from the work of Dust and Arnold [115] and for these simulations relaxation was assumed to be negligible and exponential kinetics were used. The reduced state-spaces have dimensions of 2933 and 2646, about 90 times smaller than the full Liouville space of $4^9 = 262{,}144$. The dependence on the magnetic field strength and the recombination rate constant is completely identical to the results of Hilbert space calculations.

One of the main motivations for performing simulations in Liouville space, rather than the much smaller Hilbert space, is to include incoherent processes such as spin relaxation. Fig 2.8 shows the MFE on singlet yield for a radical pair comprising dimethoxyphosphonyl and p-acetylbenzyl, Fig 2.7, the simulation of which requires reduced lists of just 3875 and 2764 states (the full state-space is again 262,144). Isotropic hyperfine coupling data were taken from Refs [115] and [116], and nuclei with couplings less than 0.1 mT were neglected. The phosphorus in dimethoxyphosphonyl has a much larger anisotropic hyperfine interaction than any other nuclear spin and is thus expected to dominate the spin relaxation arising from rotational modulation of HFIs and therefore all other hyperfine anisotropies were neglected. The parameters, correlation time, $\tau_c = 2.4$ ps and $[A : A] = 186$ mT$^2 = 1.46 \times 10^{16}$ Hz [116] were used to ensure we are in the

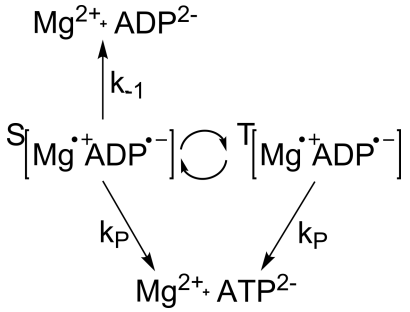

Figure 2.9. Simplified reaction scheme proposed to explain the magnetic isotope effect observed in the phosphorylation of ADP. k_{-1} is the recombination reaction rate constant and k_{P} the rate constant for formation of product.

extreme narrowing limit. In addition using $\chi = \frac{1}{6}\left(Ax^2 + 3Rh^2\right)\tau_c$ $(= [A:A]\,\tau_c = 3.5 \times 10^5\ \mathrm{s}^{-1})$ we estimated the relaxation rate, χ, and then varied it in this region. The very steep low-field effect probably arises because the phosphorus isotropic HFI is so much larger than the other HFIs and thus the system is somewhat similar to the one-nucleus RP case which often exhibits a strong magnetic field dependence at very low field. As expected, an increase in the relaxation rate causes the singlet product yield to approach the statistical value of 0.25 and faster relaxation also attenuates the low field effect and smooths out the fine structure.

A third example seeks to exhibit some more complicated reaction kinetics and the involvement of nuclei with $I > \frac{1}{2}$. To this end we consider a slightly controversial example. The magnetic isotope effect, and MFE, observed for the kinetics of enzymatic synthesis of adenosine triphosphate (ATP) from adenosine diphosphate (ADP) proposed to arise from the RP intermediate $\left[\mathrm{Mg}^{\bullet+}\mathrm{ADP}^{\bullet-}\right]$. The magnetic isotope effect arises because ^{25}Mg has spin-$\frac{5}{2}$ and ^{24}Mg and ^{26}Mg are non-magnetic [58, 117]. The proposed reaction scheme is shown in Fig 2.9. This leads to the kinetic superoperator, using the traditional Haberkorn method:

$$\hat{\hat{K}} = -k_{\mathrm{P}}\,\hat{\mathbb{1}} - \frac{k_{-1}}{2}\left(\hat{Q}_S \otimes \hat{\mathbb{1}} + \hat{\mathbb{1}}\hat{Q}_S^T\right) \tag{2.95}$$

where k_{-1} is the reverse reaction rate constant and k_{P} the rate constant for formation of product.

The isotope effect (IE) on the steady state rate of product formation was calculated, as a function of the applied field B, as [57]:

$$IE(B) = \frac{\mathrm{Tr}\left(^{25}\hat{\hat{L}}(B)^{-1}\hat{Q}_S\right)}{\mathrm{Tr}\left(^{24,26}\hat{\hat{L}}(B)^{-1}\hat{Q}_S\right)} \tag{2.96}$$

where the superscript identifies the magnetic isotope.

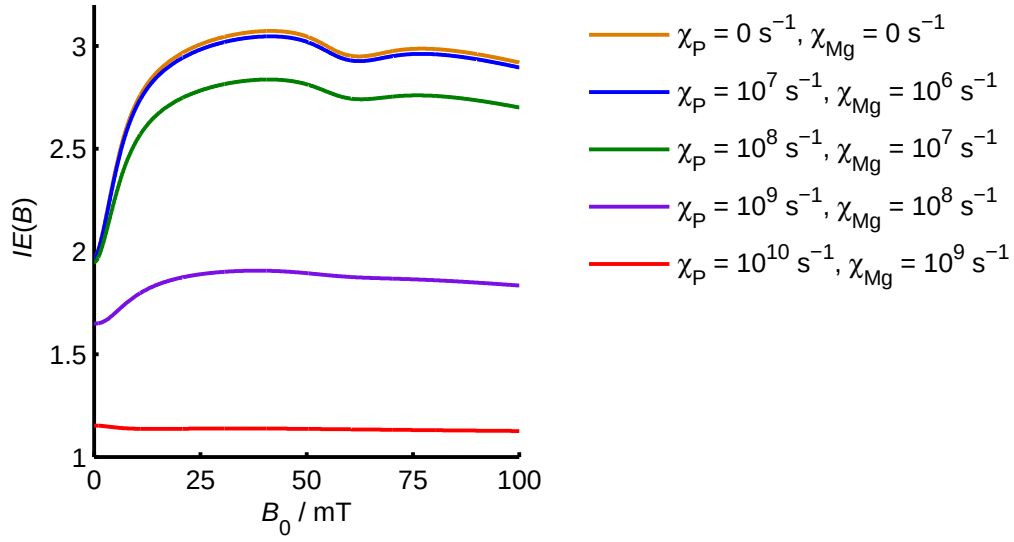

Figure 2.10. MFE on the Mg IE of the reaction in Fig 2.9. A range of relaxation rate values, χ were used for P and Mg. $k_{-1} = 10^{10}$ s^{-1} and $k_{\mathrm{P}} = 10^{8}$ s^{-1}, $a_{\mathrm{P}} = 3$ mT, $a_{\mathrm{Mg}} = 21$ mT. The isotope effect is defined in Equation (2.96). The extreme narrowing limit is not strictly valid for all parameters, so that the simulations are likely to overestimate relaxation effects, particularly at high field.

The rotational correlation time of the enzyme-ATP complex was estimated at ≈ 30 ns [118]. As the anisotropy of the magnesium HFI is expected to be approximately ten times smaller than that of the phosphorus this ratio was reflected in the choice of relaxation rates chosen for the two nuclei. The isotropic hyperfine couplings and rate constants were taken from Ref [57]: $k_{-1} = 10^{10}$ s^{-1}, $k_{\mathrm{P}} = 10^{8}$ s^{-1} and isotropic hyperfine interactions $a_{\mathrm{P}} = 3$ mT, $a_{^{25}\mathrm{Mg}} = 21$ mT. As the isotropic coupling of Mg is very large, as are some of the static fields, it is unlikely that we are truly in the extreme narrowing limit and hence the relaxation in these simulations is likely to be an overestimate.

These calculations have full state-spaces of 64 and 2304 for ^{24,26}Mg and ^{25}Mg respectively which can be reduced to 20 and 324 by the SSR techniques presented in this chapter. The results are shown in Fig 2.10. As expected, when the relaxation rate becomes faster than the smaller of the two rate constants, k_{P}, the effect is to attenuate the calculated magnetic isotope effect.

Further examples of the application of SSR techniques and use of the *Spinach* library can also be found in the rest of this thesis. Chapter 7 is concerned with finding long-lived states in NMR systems which resist relaxation arising from the modulation of dipole-dipole interactions. Chapter 3 uses the path tracing procedure to analyse state connectivities with a view to understanding the role of entanglement. In Chapter 5 we attempt to model some experimental data which has complicated reaction kinetics and required the inclusion of relaxation processes.

2.14 Conclusion

In conclusion we have shown that drastic speed-ups are possible for RP reaction simulations using a variety of state-space restriction techniques, and that it is possible to optimise the reduction through a judicious choice of basis. We have derived a series of criteria for reducing state-lists without performing any operator manipulation, and have proceeded to work out a method for forming operators directly into the reduced state-space. We have also made use of symmetrisation and path tracing techniques to carry out large scale spin chemical calculations. A procedure to form Redfield relaxation superoperators, in the extreme narrowing limit, into a reduced basis has been described and can be implemented for any number of any kind of spin.

The spin dynamics software *Spinach* includes many aspects of the spin chemical calculations included in this chapter and the method for forming reduced state-space operators is in use for all operator formation in *Spinach* as it requires only a state-list and is otherwise general for any spin superoperator, commutator, anti-commutator, left or right acting for any kind of nucleus and any number of spins. There continues to be much development of the *Spinach* library and its functionality continues to grow.

In terms of spin chemistry, it would be wonderful to find a better method of restricting the state-space of anisotropic interactions. In neither the $\alpha\beta$ product nor the nIST bases is there much scope for simulation acceleration, but that does not mean that there is no basis which would allow for significant ZTE or path tracing reduction. This would certainly be a very useful area for further work.

Chapter 3

Entanglement, Triplet States and the Radical Pair Mechanism

3.1 Introduction

Spin-correlation between the electrons of the radical pair (RP) is vitally important for magnetic interactions to affect chemical reactions through the radical pair mechanism (RPM). In the most general terms any pair of electrons described by a density matrix for which $\rho \neq \frac{1}{4}\hat{\mathbb{1}}$ may be described as correlated.[1] A perhaps more useful definition of correlation restricts the term to only those electrons described by a density matrix which in the eigenbasis of the system Hamiltonian has off-diagonal elements. Correlation can arise either through spin-selective formation of the pair of radicals or through differential rates of reaction down spin-selective reaction channels. By requiring correlation it is necessary that the spins of the two electrons be related, even if they are not necessarily interacting directly, and that their overall spin-state has some bearing on their reaction. It has recently been suggested that not only is correlation necessary between the two electrons but that the electron spin-states must also be entangled [88, 119]. The original proponents of this suggestion approached the issue from the field of quantum information processing (QIP) and this chapter seeks to understand the argument in a form more familiar from a spin chemistry perspective and subsequently to investigate, through simulation, what role, if any, entanglement plays in isotropic and anisotropic magnetic field effects (MFEs). Furthermore, in the course of these calculations it was observed that the triplet state itself has

[1] This means that the first electron, aware of its own spin state, 'knows' the spin state of its another with a greater than 50% certainty. In this way even the small Boltzmann population difference across states in an equilibrium leads to some degree of correlation by this definition.

an inherent directionality complicating the discussion of the function of entanglement. Perhaps more interestingly, this provides an alternative source of directionality that might be harnessed in a chemical compass system.

3.2 Some Definitions

There are many definitions associated with the concept of entanglement and for clarity we begin with some basic quantum mechanics and work through the definitions of interest for vector states and density matrices [120, 121]. It should be noted that in quantum information theory, and correspondingly many of the sources referenced in this chapter, it is conventional to refer to the $|\alpha\rangle$ and $|\beta\rangle$ spin-states as $|0\rangle$ and $|1\rangle$ but this formalism will not be used here. We are only interested in the possible entanglement relationship between the two electrons, not between the electrons and any coupled nuclei. This is mostly due to the fact that methods for the quantification of entanglement have only been developed thus far for two-state two-spin systems. To date most studies have focused on applications pertaining to two-spin systems and so examples of such are likely to be more useful at present.

A wavefunction, $|\Phi\rangle$, is a solution to the Schrödinger equation [69]. This serves well as a descriptor of a single system but often we are more interested in an ensemble of systems to which end the density matrix, $\rho = \overline{|\Phi\rangle\langle\Phi|}$, is used to account for the statistical variation across the ensemble [59]. A wavefunction, depending on the basis, may comprise a single state or a sum over several. In the latter case the wavefunction is said to be in a superposition of two or more states, in general defined as:

$$|\Phi\rangle = \sum_i c_i |\phi_i\rangle \tag{3.1}$$

where ϕ_i are the basis vector states and c_i are the expansion coefficients. Considering a two-state basis ($|a\rangle$ and $|b\rangle$) example the coherent superposition of Equation (3.1) becomes:

$$|\Phi\rangle = c_a |a\rangle + c_b |b\rangle \tag{3.2}$$

There is a phase between the states, determined by the coefficients c_i and this determined phase relationship between two (or more) states is the defining characteristic of their coherence. Hence states which are added with fixed phase are said to be in coherent superposition. In the density

matrix formalism (3.2) becomes:

$$\rho = \overline{|\Phi\rangle \langle\Phi|} \tag{3.3a}$$

$$= (c_a |a\rangle + c_b |b\rangle)(c_a^* \langle a| + c_b^* \langle b|) \tag{3.3b}$$

$$= |c_a|^2 |a\rangle \langle a| + |c_b|^2 |b\rangle \langle b| + c_a c_b^* |a\rangle \langle b| + c_b c_a^* |b\rangle \langle a| \tag{3.3c}$$

$$\equiv \begin{pmatrix} |c_a|^2 & c_a c_b^* \\ c_b c_a^* & |c_b|^2 \end{pmatrix} \tag{3.3d}$$

where Equation (3.3d) is the matrix representation of the the operator ρ and the overbars are omitted from b)-d) for clarity.

The off-diagonal elements in Equation (3.3d) indicate the coherences between the basis states and the diagonal elements represent the populations of $|\alpha\rangle$ and $|\beta\rangle$ states, or more precisely the probability of finding a particular system of the ensemble in such a state. It is always possible to diagonalise a density matrix, in which case there are no longer any coherences between the basis states. The basis states following diagonalisation are the eigenstates but these may not always be identified with a useful physical interpretation. Also, if the eigenstates of the density matrix are not eigenstates of the Hamiltonian describing its evolution then they are not stationary states and coherences are likely to develop as the system evolves. Only if the eigenstates of the density matrix and the Hamiltonian coincide will there be no coherence and no potential for developing it in that basis. The unit operator, $\hat{\mathbb{1}}$, which commutes with all Hamiltonians, is often referred to as the *incoherent state* – transformation of $\hat{\mathbb{1}}$ into any imaginable basis can never result in a coherence.

Equation (3.1) is, despite being a coherent superposition, also an example of a pure state. A *pure state* is any state which can be written in the form of a wavefunction, perhaps as a combination of other wavefunctions. Conversely, a *mixed state* is a density matrix which cannot be written in the form of Equation (3.1) and can only arise from a combination of ensembles. The most general mixed state is defined as:

$$\rho = \sum_i p_i \overline{|\Phi_i\rangle \langle\Phi_i|} \tag{3.4}$$

where $\sum_i p_i = 1$ is the sum over the probabilities of each state i of the system and must sum to one (*i.e.* trace$\{\rho\} = 1$). In comparison with the pure state of Equations (3.3c) and (3.3d) an

example of a mixed state of similar form is:

$$\rho = |c_a|^2 |a\rangle \langle a| + |c_b|^2 |b\rangle \langle b| \tag{3.5a}$$

$$= \begin{pmatrix} |c_a|^2 & 0 \\ 0 & |c_b|^2 \end{pmatrix} \tag{3.5b}$$

$$\neq |\Psi\rangle \langle \Psi| \tag{3.5c}$$

where Ψ is any wavefunction.

A *product state*, also known as a separable state, is a two-particle (or more) state which can be described, either in wavefunction or density matrix form, as the direct product of descriptions of the two particles separately. In wavefunction form this is defined as:

$$|\Phi\rangle = |\phi_1\rangle \otimes |\phi_2\rangle \tag{3.6}$$

where $|\phi_1\rangle$ and $|\phi_2\rangle$ describe particles 1 and 2 exclusively. In the density matrix form this state is written as:

$$\rho = |\phi_1\rangle \langle \phi_1| \otimes |\phi_2\rangle \langle \phi_2| \tag{3.7}$$

A state which cannot be written as a product state in any basis is *entangled*. Entanglement is a property arising from quantum mechanics, and with no classical analogue, which can cause, by the outcome of a measurement on one particle, a direct effect on the outcome of a measurement on its partner which may be physically remote from it. The states of the two particles are somehow related to each other despite the fact that they need not be interacting, and in fact non-interacting entangled particles are usually considered more interesting, for example for quantum teleportation [122]. Both pure and mixed states are capable of being entangled, though entangled pure states are usually considered to be more useful. There are several ways to determine if a state is entangled and to what extent, and these are outlined in the next section. First we briefly summarise the definitions arising in this section.

- **Coherence**: The existence of a determined phase between basis states, described either by the expansion coefficients in a superposition or the off-diagonal elements in a density operator. Basis dependent.

- **Pure state**: A density operator which is entirely described by a single wavefunction, defined as: $\rho = |\Phi\rangle \langle\Phi|$. Basis independent.

- **Mixed state**: A density operator which cannot be written as the product of two (or more) wavefunctions, defined as: $\rho \neq |\Phi\rangle \langle\Phi|$. Basis independent; a mixed state is mixed in all bases.

- **Product/Separable state**: Either a wavefunction (pure state) or a density operator (mixed state) which may be written as the direct product of two separate systems, defined as: $|\Phi\rangle = |\phi_1\rangle \otimes |\phi_2\rangle$ and $\rho = |\phi_1\rangle \langle\phi_1| \otimes |\phi_2\rangle \langle\phi_2|$ respectively. Basis independent.

- **Entangled state**: Either a wavefunction (pure state) or a density operator (mixed state) which cannot, in any basis, be written as the direct product of two (or more) separate systems. Defined as $|\Phi\rangle \neq |\phi_1\rangle \otimes |\phi_2\rangle$ and $\rho \neq |\phi_1\rangle \langle\phi_1| \otimes |\phi_2\rangle \langle\phi_2|$.

3.2.1 Quantifying Entanglement

It is often hard to tell at a first glance whether a particular state is entangled or not. To avoid trying every possible basis set, several more convenient procedures have been proposed to determine if a system is entangled [120, 121]. These will be outlined in the sections below.

Partial Trace

For a pure state the partial trace can be used to indicate if the state is entangled or not. For any density matrix it is possible to trace out one component of a bipartite system to leave a description of just the remaining component. The partial trace of density matrix ρ with respect to particle B is defined as:

$$\rho_A = \sum_j {}_B\langle j| \rho |j\rangle_B \tag{3.8}$$

where $|j\rangle_B$ are the basis states of just particle B. A density matrix is defined such that:

$$\rho = \begin{array}{c} \\ \langle\alpha\alpha| \\ \langle\alpha\beta| \\ \langle\beta\alpha| \\ \langle\beta\beta| \end{array} \begin{array}{c} \begin{array}{cccc} |\alpha\alpha\rangle & |\alpha\beta\rangle & |\beta\alpha\rangle & |\beta\beta\rangle \end{array} \\ \begin{pmatrix} a & b & c & d \\ e & f & g & h \\ i & j & k & l \\ m & n & o & p \end{pmatrix} \end{array} \tag{3.9}$$

The 2-spin α,β basis is shown in Equation (3.9) for clarity. Tracing out B leaves:

$$\rho_A = \begin{pmatrix} a+f & c+h \\ i+n & k+p \end{pmatrix} \tag{3.10}$$

and similarly tracing out A gives:

$$\rho_B = \begin{pmatrix} a+k & b+l \\ e+o & f+p \end{pmatrix} \tag{3.11}$$

If the initial state was pure the matrices resulting from taking the partial trace can then be inspected for their pure/mixed character. As has already been established, a pure density matrix can be defined by a single wavefunction, which itself may be a linear combination over the basis states, in addition it has the property that $\text{trace}\{\rho^2\} = 1$. A pure matrix indicates that the initial pure state was separable and a mixed matrix is indicative of entanglement.

Partial Transpose

If the matrix resulting from taking the partial transpose of a density matrix has negative eigenvalues it can no longer be considered a density matrix. The diagonal elements of a density matrix represent populations and hence negative values are unphysical. The formation of such a matrix on partially transposing a density matrix is thus indicative that the original state was entangled.

The procedure to carry out a partial transpose with respect to the second particle requires that the states are exchanged according to $\alpha_B \leftrightarrow \beta_B$. For the density matrix defined in Equation

(3.9) this procedure results in:

$$\rho^{T_B} = \begin{pmatrix} a & e & c & g \\ b & f & d & h \\ i & m & k & o \\ j & n & l & p \end{pmatrix} \tag{3.12}$$

Similarly a partial transpose with respect to particle A, $\alpha_A \leftrightarrow \beta_A$, returns:

$$\rho^{T_A} = \begin{pmatrix} a & b & i & j \\ e & f & m & n \\ c & d & k & l \\ g & h & o & p \end{pmatrix} \tag{3.13}$$

Diagonalisation of a partially transposed density matrix allows for inspection of its eigenvalues; if any are negative the state is definitely entangled. The degree of entanglement can be further quantified by defining the negativity, $\mathcal{N}(\rho)$, as:

$$\mathcal{N}(\rho) = \frac{1}{2}\left(||\rho^{T_A}|| - 1\right) = \left|\sum_i \lambda_i\right| \tag{3.14}$$

where λ_i are the negative eigenvalues of ρ^{T_A}, and $||\cdots||$ denotes the trace norm. The larger $\mathcal{N}(\rho)$ the more entangled ρ is.

Concurrence

Concurrence provides a measure of entanglement which may be applied to pure or mixed states, *i.e.* may be calculated for a wavefunction directly as well as the associated density matrix. For a mixed state an analytical solution for the calculation of concurrence, C, has been derived for a system with two particles each with two-levels [123, 124]:

$$C = \max\left\{0, \sqrt{\lambda_1} - \sqrt{\lambda_2} - \sqrt{\lambda_3} - \sqrt{\lambda_4}\right\} \tag{3.15}$$

where λ_i are the eigenvalues, in decreasing order of magnitude, of the matrix:

$$\rho \cdot (\sigma_y \otimes \sigma_y) \cdot \rho^* \cdot (\sigma_y \otimes \sigma_y) \tag{3.16}$$

and σ_y is the y Pauli operator. Analogously, for a pure state the concurrence is defined as:

$$C(\Phi) = |\langle\Phi|\,\sigma_y \otimes \sigma_y\,|\Phi\rangle| \tag{3.17}$$

The entanglement $\mathcal{E}$ is then defined, on a monotonic scale from 0 (separable) to 1 (maximally entangled), as [124]:

$$\mathcal{E} = h\left(\frac{1+\sqrt{1-C^2}}{2}\right) \tag{3.18}$$

$$h(x) = -x\log_2 x - (1-x)\log_2(1-x) \tag{3.19}$$

3.2.2 Singlet State

Now that the required definitions and mathematical tests have been introduced it will be useful to apply them to the singlet state, S, ubiquitous in RP reactions and as shall be proven below, an example of a maximally entangled state. The singlet is clearly a pure state as it can be defined in wavefunction form, $|S\rangle\langle S|$. With the product expanded – and written in the $\alpha\beta$ basis: $|S\rangle\langle S| = \frac{1}{2}(|\beta\alpha\rangle\langle\beta\alpha| + |\alpha\beta\rangle\langle\alpha\beta| - |\alpha\beta\rangle\langle\beta\alpha| - |\beta\alpha\rangle\langle\alpha\beta|)$ – the singlet is equally clearly a coherent superposition which in matrix form, in this basis, is:

$$\rho = \begin{pmatrix} 0 & 0 & 0 & 0 \\ 0 & \frac{1}{2} & -\frac{1}{2} & 0 \\ 0 & -\frac{1}{2} & \frac{1}{2} & 0 \\ 0 & 0 & 0 & 0 \end{pmatrix} \tag{3.20}$$

As the singlet is a pure state, in order to establish whether it is entangled we can take the partial trace over Matrix (3.20) for either the first or second spin. Each of which gives:

$$\rho_1 = \begin{pmatrix} \frac{1}{2} & 0 \\ 0 & \frac{1}{2} \end{pmatrix} = \rho_2 \tag{3.21}$$

which is obviously a mixed state, $\frac{1}{2}(|\alpha\rangle\langle\alpha| + |\beta\rangle\langle\beta|)$. More specifically it is directly proportional to $\hat{\mathbb{1}}$, the completely mixed state indicating that the singlet is maximally entangled. A similar conclusion is reached by taking the partial transpose over either spin, for example the partial

transpose of Matrix (3.20) with respect to spin 2 is:

$$\rho^{T_2} = \begin{pmatrix} 0 & 0 & 0 & -\frac{1}{2} \\ 0 & \frac{1}{2} & 0 & 0 \\ 0 & 0 & \frac{1}{2} & 0 \\ -\frac{1}{2} & 0 & 0 & 0 \end{pmatrix} \tag{3.22}$$

with eigenvalues $\{-0.5, 0.5, 0.5, 0.5\}$. At least one is negative hence S is entangled, and has $\mathcal{N} = 0.5$. Finally calculating the concurrence and entanglement using Equations (3.15) and (3.16) gives:

$$\mathcal{C} = 1 \tag{3.23}$$

$$\mathcal{E} = 1 \tag{3.24}$$

This result agrees with the result from taking the the matrix partial transpose and partial trace – the singlet state is maximally entangled. The same procedures were applied to two further states which will be of interest in this chapter. Firstly the $M_S = 0$ triplet state, T_0 (which is equivalent to T_z if the triplets are defined in the Cartesian basis instead). This state has the same components as the singlet but with opposite phase, $|T_0\rangle\langle T_0| = \frac{1}{2}(|\alpha\beta\rangle + |\beta\alpha\rangle)(\langle\alpha\beta| + \langle\beta\alpha|)$, and like the singlet has $\mathcal{E} = 1$ and is fully entangled. Secondly the combination in equal measure of S and T_0 ensembles $\frac{1}{2}(|S\rangle\langle S| + |T_0\rangle\langle T_0|) = \frac{1}{2}(|\alpha\beta\rangle\langle\alpha\beta| + |\beta\alpha\rangle\langle\beta\alpha|)$ is a classically mixed state. This state has, $\mathcal{E} = 0$ and is thus completely separable *i.e.* not entangled.

3.3 Entanglement and the RPM

In Refs [88] and [119] it has been suggested that the entanglement between electrons in a singlet state is required for sensitivity to magnetic fields. Calculations in Ref [119] compare the magnitude of the LFEs for a system starting in a pure S state with that of a system born in a classically mixed (separable) state defined above. The anisotropic response of a RP reaction to changing field direction was also inspected.[2] It was concluded that entanglement is inherently necessary for RPs to show the field-strength-dependent MFEs under the influence of isotropic HFIs, but not for an anisotropic response. In fact they saw that the yields from some mixed

[2]The authors went on to investigate the effect of 'quantum control' (the application of well defined RF pulses designed to protect electron coherence) on MFEs and yield anisotropy but these results, while interesting, are not relevant to the studies outlined in this chapter.

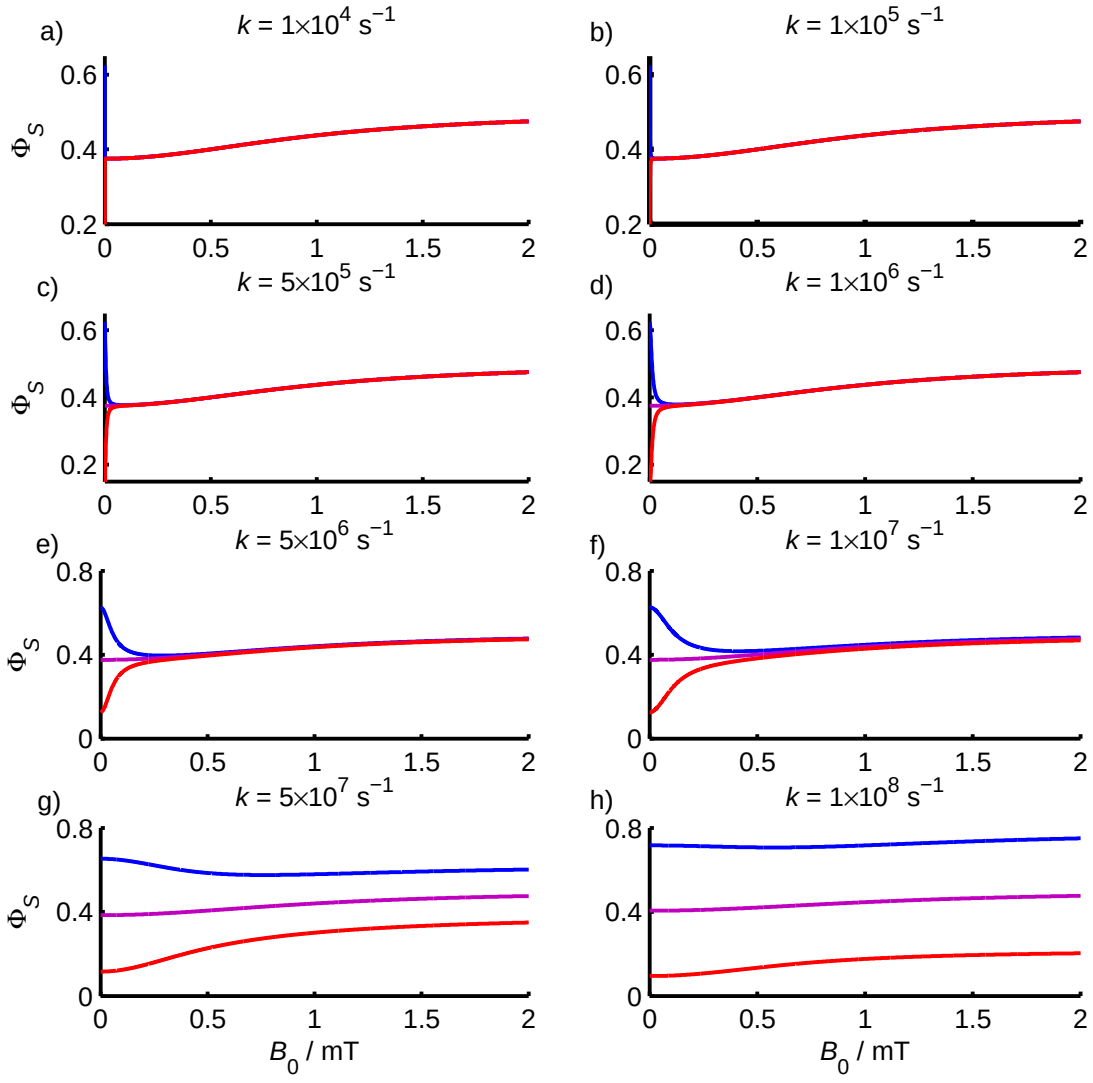

Figure 3.1. Singlet yield from S, blue, T_0, red, and the separable mixed state $\frac{1}{2}(S+T_0)$, purple. k is varied as shown, $a = 1$ mT, B_0 applied along the z-axis (the reason for specifying the axis will be made clear later in the chapter).

states demonstrate larger angle-dependence than from the pure singlet. These studies prompted several questions. How does the sensitivity to entanglement arise in the case of isotropic HFI couplings? Are there any exceptions? Why should the role of entanglement be so different between the isotropic and anisotropic cases?

3.3.1 Isotropic Low-Field Effect

It is always sensible to begin an analysis with the simplest possible system. Thus the following calculations are concerned with a RP with identical g-values for both radicals and no dipolar or exchange coupling between them. Radical A carries a single nucleus with isotropic HFI

$a = 1$ mT and the field is applied along the z-axis. A comparison is made between the S, T_0 and $\frac{1}{2}(S + T_0)$ starting state vectors. S and T_0 are maximally entangled but have opposite phase and the mixture of the two is not entangled. The singlet yield, Φ_S, in the latter case is just the average of the yields from the S and T_0 starting vectors:

$$\Phi_S\left(\rho_0 = \frac{1}{2}(S + T_0)\right) = \frac{1}{2}\Phi_S\left(\rho_0 = S\right) + \frac{1}{2}\Phi_S\left(\rho_0 = T_0\right) \tag{3.25}$$

The simulated MARY (magnetically altered reaction yield) curves for these starting vectors are given in Fig 3.1. There are clearly two different parts to the overall magnetic field effect; a steep curve in the low field region (a LFE) and a shallower curve tending to $\Phi_S = 0.5$ at higher field. The latter is present for all three starting states but the LFE is absent for the mixed state.

Understanding the Role of Coherence

To understand the roots of the two different aspects of the MFEs it was expedient to consider the calculation in Liouville space as then each element of the density matrix may be considered a state on which the superoperator acts; the full state-list is given in Table 3.1. Following the procedure outlined in Chapter 2 the connectivity of the Liouvillian was analysed to identify the nature of any independent subspaces, a scheme of this procedure is shown in Fig 3.2. As an example we consider the path followed by the 'population' of population state 28, following the yellow track of Figure 3.2. We walk horizontally through the Liouvillian matrix until we reach

Table 3.1. State-list for the three-spin system in the order electron A, electron B, nucleus on A. Numbers highlighted ^{*p} are populations, and ^{*c} coherences, in the initial S or T_0 state. The notation is such that the state represented by $\alpha\beta\alpha\beta\alpha\alpha$ denotes $|\alpha\beta\alpha\rangle\langle\beta\alpha\alpha|$.

1	$\alpha\alpha\alpha\alpha\alpha\alpha$	17	$\alpha\beta\alpha\alpha\alpha\alpha$	33	$\beta\alpha\alpha\alpha\alpha\alpha$	49	$\beta\beta\alpha\alpha\alpha\alpha$
2	$\alpha\alpha\alpha\alpha\alpha\beta$	18	$\alpha\beta\alpha\alpha\alpha\beta$	34	$\beta\alpha\alpha\alpha\alpha\beta$	50	$\beta\beta\alpha\alpha\alpha\beta$
3	$\alpha\alpha\alpha\alpha\beta\alpha$	19^{*p}	$\alpha\beta\alpha\alpha\beta\alpha$	35^{*c}	$\beta\alpha\alpha\alpha\beta\alpha$	51	$\beta\beta\alpha\alpha\beta\alpha$
4	$\alpha\alpha\alpha\alpha\beta\beta$	20	$\alpha\beta\alpha\alpha\beta\beta$	36	$\beta\alpha\alpha\alpha\beta\beta$	52	$\beta\beta\alpha\alpha\beta\beta$
5	$\alpha\alpha\alpha\beta\alpha\alpha$	21^{*c}	$\alpha\beta\alpha\beta\alpha\alpha$	37^{*p}	$\beta\alpha\alpha\beta\alpha\alpha$	53	$\beta\beta\alpha\beta\alpha\alpha$
6	$\alpha\alpha\alpha\beta\alpha\beta$	22	$\alpha\beta\alpha\beta\alpha\beta$	38	$\beta\alpha\alpha\beta\alpha\beta$	54	$\beta\beta\alpha\beta\alpha\beta$
7	$\alpha\alpha\alpha\beta\beta\alpha$	23	$\alpha\beta\alpha\beta\beta\alpha$	39	$\beta\alpha\alpha\beta\beta\alpha$	55	$\beta\beta\alpha\beta\beta\alpha$
8	$\alpha\alpha\alpha\beta\beta\beta$	24	$\alpha\beta\alpha\beta\beta\beta$	40	$\beta\alpha\alpha\beta\beta\beta$	56	$\beta\beta\alpha\beta\beta\beta$
9	$\alpha\alpha\beta\alpha\alpha\alpha$	25	$\alpha\beta\beta\alpha\alpha\alpha$	41	$\beta\alpha\beta\alpha\alpha\alpha$	57	$\beta\beta\beta\alpha\alpha\alpha$
10	$\alpha\alpha\beta\alpha\alpha\beta$	26	$\alpha\beta\beta\alpha\alpha\beta$	42	$\beta\alpha\beta\alpha\alpha\beta$	58	$\beta\beta\beta\alpha\alpha\beta$
11	$\alpha\alpha\beta\alpha\beta\alpha$	27	$\alpha\beta\beta\alpha\beta\alpha$	43	$\beta\alpha\beta\alpha\beta\alpha$	59	$\beta\beta\beta\alpha\beta\alpha$
12	$\alpha\alpha\beta\alpha\beta\beta$	28^{*p}	$\alpha\beta\beta\alpha\beta\beta$	44^{*c}	$\beta\alpha\beta\alpha\beta\beta$	60	$\beta\beta\beta\alpha\beta\beta$
13	$\alpha\alpha\beta\beta\alpha\alpha$	29	$\alpha\beta\beta\beta\alpha\alpha$	45	$\beta\alpha\beta\beta\alpha\alpha$	61	$\beta\beta\beta\beta\alpha\alpha$
14	$\alpha\alpha\beta\beta\alpha\beta$	30^{*c}	$\alpha\beta\beta\beta\alpha\beta$	46^{*p}	$\beta\alpha\beta\beta\alpha\beta$	62	$\beta\beta\beta\beta\alpha\beta$
15	$\alpha\alpha\beta\beta\beta\alpha$	31	$\alpha\beta\beta\beta\beta\alpha$	47	$\beta\alpha\beta\beta\beta\alpha$	63	$\beta\beta\beta\beta\beta\alpha$
16	$\alpha\alpha\beta\beta\beta\beta$	32	$\alpha\beta\beta\beta\beta\beta$	48	$\beta\alpha\beta\beta\beta\beta$	64	$\beta\beta\beta\beta\beta\beta$

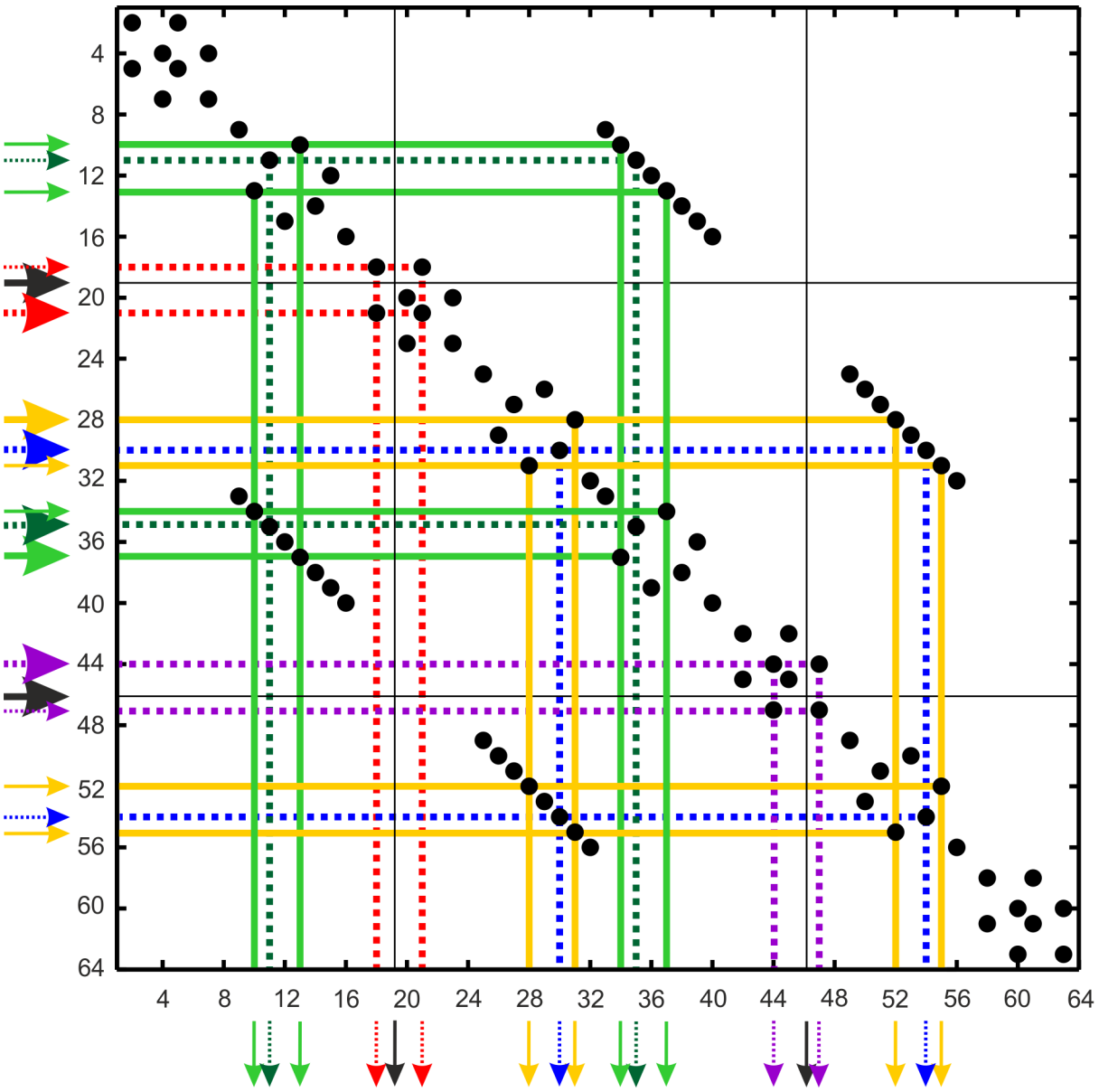

Figure 3.2. Path tracing, Section 2.5.1, through the isotropic Liouvillian from each of the basis states comprising an initial S or T_0 state. The black dots indicate the positions of non-zero elements in the Liouvillian-matrix. The numbering corresponds to the state-list in Table 3.1. The large arrows indicate the basis states that are non-zero in the starting vector. We enter our population in along a horizontal line corresponding to a state found in the starting vector. When the horizontal track meets a node the population is deflected and we follow the vertical line out of the matrix, this may or may not be the same state as we began in. This represents the non-zero elements of the Liouvillian causing evolution between states. If the exit state and entry state are not the same we repeat the process starting in the exit state in order to observe which states that may evolve into. The small arrows represent the states which are populated only after one (or more) trips through the Liouvillian, *i.e.* which would only be populated after one or more applications of the matrix propagator. In practice it is clear that there are several distinct subspaces with no evolution between them, none of the black dots connect states between these subspaces. The non-interacting subspaces are shown in different colours, dashed lines are subspaces begun as coherences (21, 30, 35, 44) in ρ_0 and solid lines subspaces from populations (19, 28, 37, 46). The thin solid lines which run through no non-zero matrix elements are the non-evolving population states (19 and 46).

a non-zero element (a black node on the graph), at this point we are deflected at right angles and walk along a vertical line to the edge of the matrix, or continue until we reach another node and then are deflected. The states at the exit points in this example are 31 and 52. The process is then repeated beginning in these states, from state 31 we reach states 28 and 55 and from state 52 we reach states 28 and 55. We have already begun a path at state 28, so finally we trace through the path from state 55, this leads to states 31 and 52 which we have already encountered. In short we have traced a path between four states (28, 31, 52 and 55) which connect only between themselves, this is one independent subspace.

The same procedure may be begun in any state and thus the full state space is divided into smaller subspaces, though of course we are interested mainly in those states which are initially populated. There are in total 36 non-interacting subspaces, of which only at most eight are populated – these are shown in Fig 3.2. Each populated subspace begins in one of the states appearing in the starting vectors; S and T_0 are linear combinations over the eight states (19, 21, 28, 30, 35, 37, 44, 46) highlighted in Table 3.1 and the mixed state is a sum over just the four population states (19, 28, 37, 46).

To discover how each subspace contributes to the total, the singlet yield from each subspace was calculated individually and the results are shown in Fig 3.3. There are three types of contributions to the singlet yield and thus the subspaces may be grouped into three types:

1. Evolving populations (green-solid and yellow-solid lines in Fig 3.2). These begin from the initial population states that have different spin-states on the paired electron and nucleus and hence can evolve via a HFI driven spin flip: $|\alpha\ldots\beta\rangle \leftrightarrow |\beta\ldots\alpha\rangle$. These states (Fig 3.3a-c) are responsible for the smooth MFE.

2. Non-evolving populations (thin black lines in Fig 3.2). These begin from the initial population states that have the same spin-state on the paired electron and nucleus and therefore cannot be spin-flipped by the HFI. These states exist in a single-state subspace and contribute $\frac{1}{8}$ to the singlet yield at all field strengths.

3. Coherences (dotted-lines in Fig 3.2). These states have opposite phase (sign) for S and T_0 and cancel out in the mixture. They contribute (Fig 3.3d,e) the steep MFE observable at low field. If these states are not populated initially (Fig 3.3f) there is no LFE.

It would be interesting to understand how the contribution from the coherence depends on the system parameters, a, k and B_0 of a one-nucleus RP spin-system. Therefore one of the coherence

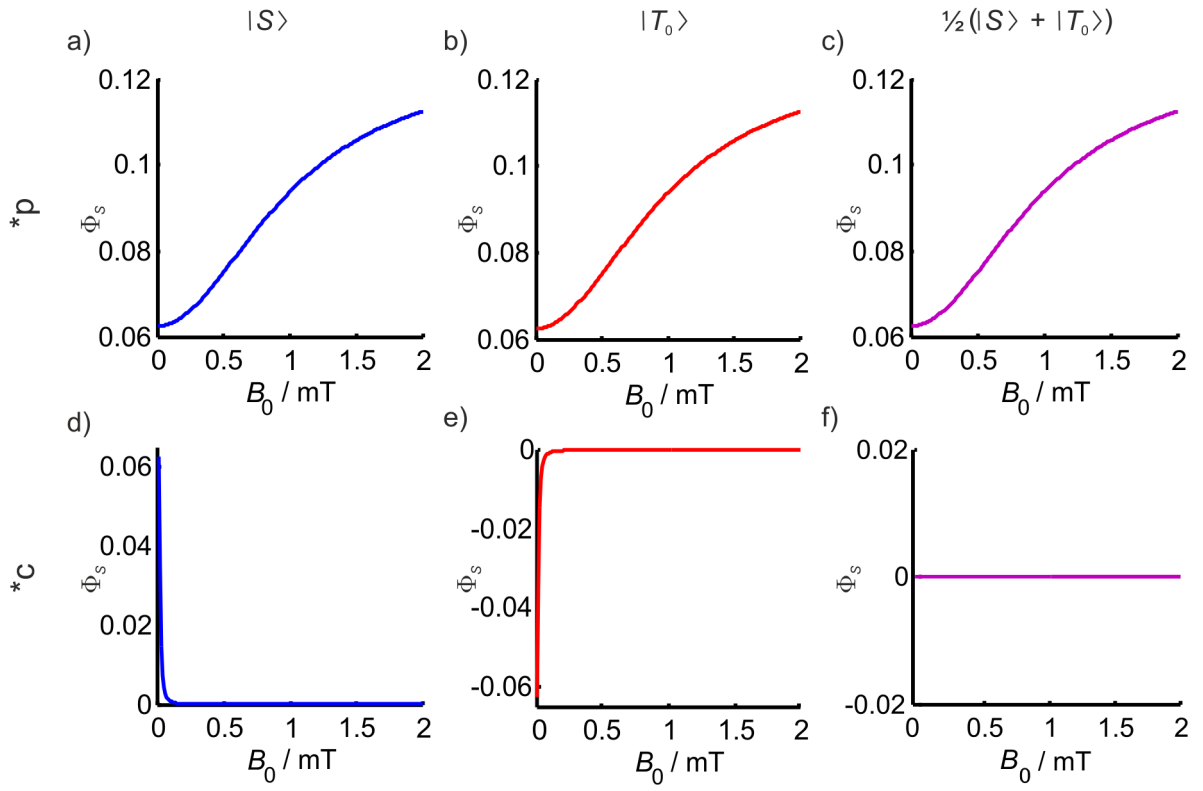

Figure 3.3. Singlet yield contribution from each type of subspace for a one-nucleus RP, $a = 1$ mT, $k = 1 \times 10^6$ s^{-1}. a)-c) S, T_0 and mixed starting vector respectively – population subspaces (solid-green and solid-yellow subspaces in Fig 3.2). d)-f) S, T_0 and Mixed starting vector respectively – coherence subspaces (all dashed subspaces in Fig 3.2). The solid black line one-state population subspaces of Fig 3.2 do not evolve and contribute $\frac{1}{8}$ to the singlet yield at all fields for each starting vector.

subspaces, each of which spans only two states, is examined more closely. The reduced Liouvillian spans the basis states, $\{|1) = |\alpha\alpha\beta\alpha\beta\alpha) = |\alpha\alpha\beta\rangle\langle\alpha\beta\alpha|, |2) = |\beta\alpha\alpha\alpha\beta\alpha) = |\beta\alpha\alpha\rangle\langle\alpha\beta\alpha|\}$. These states are 11 and 35 in the state-list of Table 3.1 with 35 the initially 'populated' coherence and 11 the coherence into which it evolves. In the reduced basis the Hamiltonian superoperator is:

$$\hat{\hat{H}} = \begin{pmatrix} \omega - \frac{a}{2} & \frac{a}{2} \\ \frac{a}{2} & -\frac{a}{2} \end{pmatrix} \tag{3.26}$$

which, including kinetics, gives a reduced Liouvillian, $\hat{\hat{L}} = \hat{\hat{H}} + \mathrm{i}\hat{\hat{K}}$:

$$\hat{\hat{L}} = \begin{pmatrix} \omega - \frac{a}{2} - \mathrm{i}k & \frac{a}{2} \\ \frac{a}{2} & -\frac{a}{2} - \mathrm{i}k \end{pmatrix} \tag{3.27}$$

The starting states of interest in this basis are:

$$\rho_0^S = -\frac{1}{4}\,|2) \tag{3.28a}$$

$$\rho_0^{T_0} = \frac{1}{4}\,|2) \tag{3.28b}$$

$$\rho_0^{S+T_0} = 0\,|2) \tag{3.28c}$$

and $\hat{Q}_S$ is the singlet projection operator in the reduced basis:

$$\hat{Q}_S = -\frac{1}{2}\,|2) \tag{3.29}$$

The starting vector can be generalised so that x is the coefficient of $|2)$ in the starting vector. When $x = 0$ the state is fully mixed and when $x = \pm\frac{1}{4}$ it is maximally entangled. Using the above and Equations (1.52) and (1.57), the singlet yield is:

$$\Phi_S^{\text{coh}} = -\frac{kx}{2}\left(\frac{-\mathrm{i}\frac{a}{2} + k + \mathrm{i}\omega}{k\,(k - \mathrm{i}a) + \omega\left(\frac{a}{2} + \mathrm{i}k\right)}\right) \tag{3.30}$$

This is clearly a complex number but the imaginary parts cancel across the different coherent contributions so we need only retain the real part:

$$\Phi_S^{\text{coh}} = -\frac{kx}{2}\left(\frac{k\left(k^2 + \omega^2 + \frac{a^2}{2} - \omega a\right)}{\left(k^2 + \frac{a\omega}{2}\right)^2 + k^2\,(\omega - a)^2}\right) \tag{3.31}$$

The linear dependence on x clearly explains why opposite yields are observed from the T_0 and S starting vectors, however the expression remains complicated in terms of the other coefficients. Table 3.2 summarises Equation (3.31) in a number of limiting cases. These values explain the results of the simulations shown in Fig 3.3d)-f). Under the modest rate constant of that example

Table 3.2. Real part of the contributions of the coherence sub-spaces to the total singlet yield, *i.e.* the coherence singlet yield Φ_S^{coh}, for some limiting cases.

$\omega = 0$	$k \ll a$	$\Phi_S^{\text{coh}} \approx -\frac{x}{4}$
	$k = a$	$\Phi_S^{\text{coh}} = -\frac{3x}{8}$
	$k \gg a$	$\Phi_S^{\text{coh}} \approx -\frac{x}{2}$
$\omega = a$	$k \ll a$	$\Phi_S^{\text{coh}} \approx 0$
	$k = a$	$\Phi_S^{\text{coh}} \approx -\frac{x}{3}$
	$k \gg a$	$\Phi_S^{\text{coh}} \approx -\frac{x}{2}$
$\omega \gg a$	$k \ll a$	$\Phi_S^{\text{coh}} \approx 0$
	$k = a$	$\Phi_S^{\text{coh}} \approx 0$
	$k \gg a$	$\Phi_S^{\text{coh}} \approx -\frac{x}{2}$

the zero-field limit is $\pm\frac{1}{4} \times \frac{1}{4} = \pm\frac{1}{16}$ for the singlet and triplet respectively. There is a rapid decrease in the coherence contribution as the field increases, tending to 0 when $\omega \gg a$. Thus the singlet yield MARY curves from the three different starting states converge at high field. This explains why only the LFE is lost when coherence (and entanglement) are removed.

It is clear that in these simulations the initial coherences are responsible for the LFE. Having non-zero coherences is a natural result of entanglement (or perhaps entanglement is a necessary by-product of these coherences) and hence in this situation, isotropic HFI and field applied along the z axis, it may be concluded, in agreement with Ref [119], that entanglement is necessary for the LFE.

3.3.2 Isotropic Low-Field Effect – The Directional Triplet

The simulation frame (SF) is defined here as the frame in which the calculation is carried out – that is the axis along which the αs and βs (or irreducible spherical tensors, or product operators etc.) of the basis are defined. This is introduced to account for the quantisation axis of the initial state. For convenience this may be assumed to be coincident with either the molecular frame (MF) of the HFI tensors or the laboratory frame (LF) defined by an external applied field, but it does not have to be and hence it will prove useful to define a more general reference frame.

Defined in the initial SF $\alpha\beta$ basis neither an initial S nor T_z state has a magnetic moment along the SF z axis. As in this frame $m_S = 0$, the T_z state may be termed a T_0^z state – the equivalent of T_0 defined along the SF z-axis rather than along the applied field. However T_0^z does have a magnetic moment in the plane perpendicular to z. Importantly, by possessing a net spin angular momentum ($\boldsymbol{S} = 1$) the T_0^z state has an inherent directionality and would be expected to show an anisotropic response to an applied field even if the HFI remains isotropic. The calculation for Fig 3.1d) was repeated with B_0 applied along the SF x-axis, (in spherical polar coordinates $\theta = \frac{\pi}{2}$ and $\phi = 0$). The resulting MARY curves are shown in Fig 3.4a).

There is now no LFE from the T_0^z state despite its entanglement. The yield from this starting state tends smoothly to zero as the field strength is increased. This is readily justified in the high field limit where the eigenaxis of the system lies along the applied field direction (SF x-axis), perpendicular to the SF z-axis. Transforming a T_0^z state into the system eigenbasis is equivalent to defining the x-axis as the quantisation axis and thus the original T_0^z is equivalent to the linear

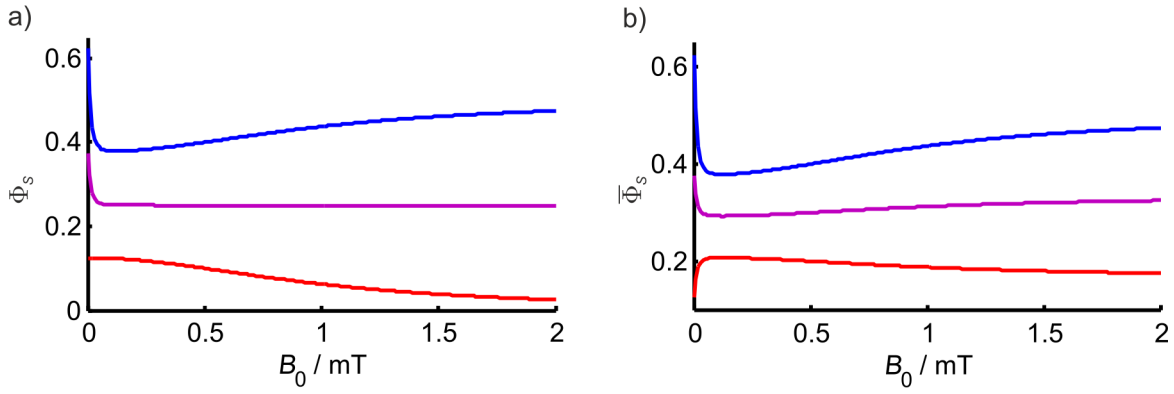

Figure 3.4. Angular dependence of the singlet yield from S, blue, T_0^z, red and the separable state $\frac{1}{2}(S + T_0^z)$, purple, starting states. $k = 1 \times 10^6$ s^{-1}, $a = 1$ mT, $Ax = 0$ mT. a) B_0 is applied along the x-axis b) Spherical average over B_0 orientations.

combination:

$$|T_0^z\rangle\langle T_0^z| = \frac{1}{2}\left(|T_+^x\rangle\langle T_+^x| + |T_-^x\rangle\langle T_-^x| - |T_+^x\rangle\langle T_-^x| - |T_-^x\rangle\langle T_+^x|\right) \tag{3.32}$$

where the superscript denotes the principal axis of the frame. At high field the T_+ and T_- states are energetically isolated from T_0 and S and thus interconversion is blocked. Hence at high field a triplet state with its angular momentum in the same plane as the applied field (that is a T_0^i state where the axis, i, along which the angular momentum projection is zero is perpendicular to the field) cannot interconvert with the S and the singlet yield goes to zero. Of course a triplet born by coherent interconversion from an initial S state is produced in the eigenaxis system of the spin-system and not necessarily along the SF. In Fig 3.4a) the mixed state does show a distinct change in gradient between low and high fields, *i.e.* a LFE despite its lack of entanglement.

In order to remove the effect of triplet directionality from the MARY simulation an average was taken over yields calculated with B_0 directed across the full range of θ and ϕ relative to the SF. Sampling points were defined using the 642-icosahedral grid from the *Spinach* library and the spherical average yield, $\overline{\Phi_S}$, was then calculated as a simple average over these data points (with this grid no weighting factor is required). In the SF with an isotropic HFI the T_x, T_y and $T_z(= T_0^z)$ starting states return the same spherical average. The results are shown in Fig 3.4b). These curves show some LFE for all three starting states. The role of entanglement in the LFE is no longer clear, though it appears to be unnecessary in this instance.

3.3.3 Anisotropic Reaction Yields

The singlet yield from a system evolving under an axial HFI and an applied field is sensitive to the relative orientation of the HFI principal axis system (PAS) and the direction of the field. Using the HFI PAS as the SF, the angle-dependent MFE curves of Fig 3.5 were calculated. All three starting vectors display a directional response, and in some cases the mixed state shows a greater sensitivity to the field direction than the singlet. This result agrees with the system investigated in Ref [119] which goes on to conclude that entanglement is not necessary for an anisotropic MFE. The authors explain the different dependencies on entanglement for the isotropic and anisotropic systems they study on the different rate constants of reaction.

The only isotropic states are the singlet, S, the incoherent state, $\hat{\mathbb{1}}$, and any linear combinations of the two, of which probably the most significant is $\hat{\mathbb{1}} - S = (T_+ + T_- + T_0) = (T_x + T_y + T_z)$, the mixture of triplets. Any other state, that is, any state with non-equal population of the triplet sub-levels will have an inherent directionality arising from its angular momentum vector. With this in mind it is not surprising that Ref [119] found, contrary to their result for the isotropic case, that mixed states with no entanglement are as, if not more, effective at returning anisotropic yields than the pure maximally entangled singlet. However, there are potentially two different sources of anisotropy present. The first is due to the relative angle between the HFI principle axis and the applied field, which may or may not require entanglement to be effective, and the second arises from directionality of the starting state. As it is not possible to form a non-entangled mixed state which has equal triplet populations there is no way to form a non-entangled state without an inherent directionality of its own and thus separating the two sources of anisotropy is non-trivial. Unless a method can be identified to separate the two factors, that is, to remove the effects of state directionality it does not seem likely that the role of entanglement in anisotropic reaction yields can be properly isolated.

3.3.4 Entanglement Conclusion

It appears that in the absence of anisotropic HFIs and when the applied field is along the SF z-axis a state with either no net spin angular momentum or with angular momentum in the xy plane must be entangled in order to produce a low field effect. It is possible to identify precisely the part of the reaction yield arising from the coherent terms and thus explain the origin of the LFE in more detail than previously. However, the situation is more complicated than initially anticipated due to the directionality of the triplet sub-levels. When a field is

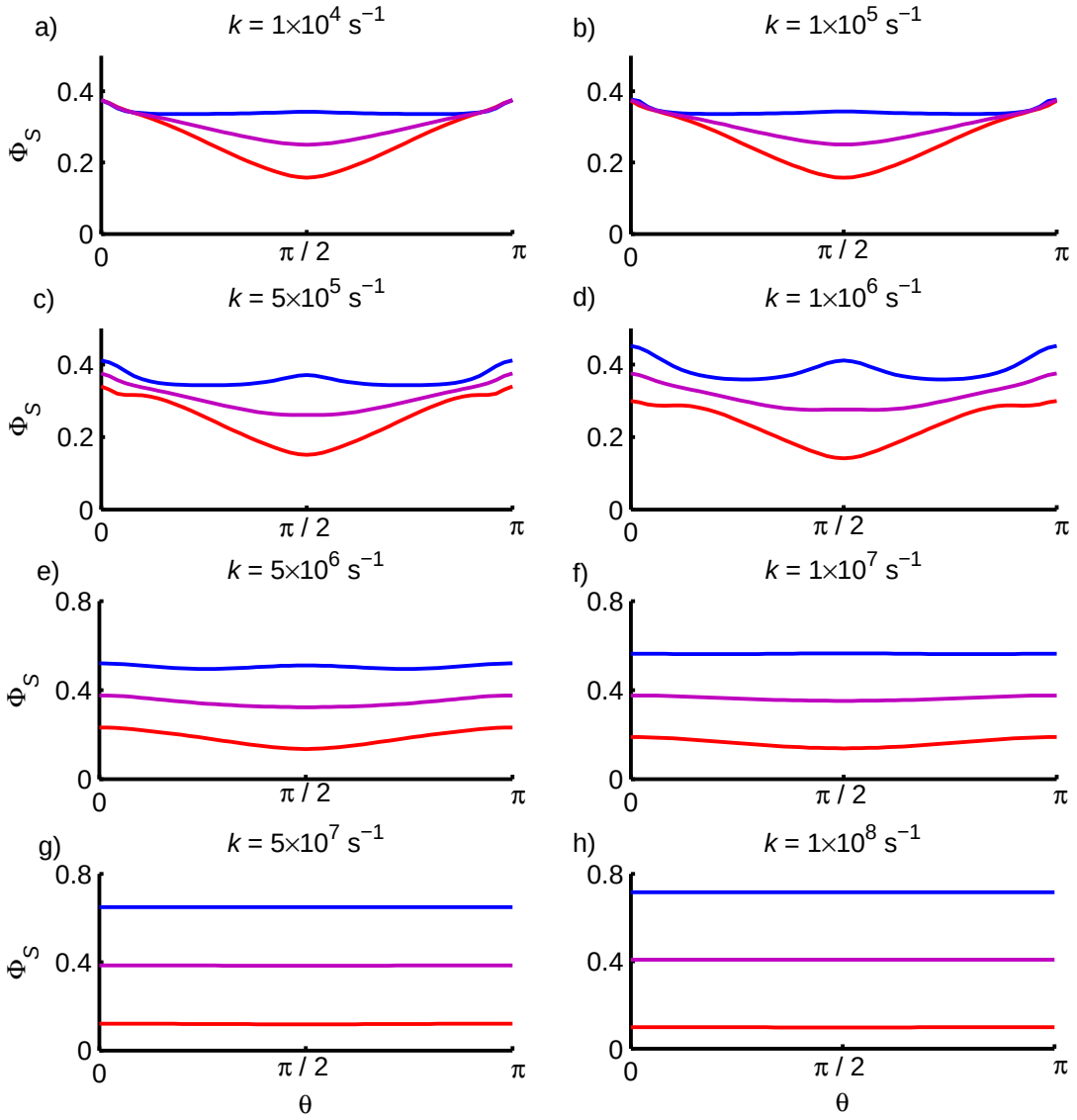

Figure 3.5. Singlet yield from S, blue, T_0^z, red and the separable state $\frac{1}{2}(S + T_0^z)$, purple, starting states. $a = 1$ mT, $Ax = -0.02$ mT and $Rh = 0$ mT. The SF is aligned with the HFI PAS and $B_0 = 50$ μT is rotated around y by an angle θ (in radians) from being parallel to the symmetry axis of the axial HFI when $\theta = 0$ to perpendicular to it at $\theta = \frac{\pi}{2}$.

applied perpendicular to the axis of the initial T_0 state, *i.e.* in the same plane as its angular momentum vector, the LFE is lost. As the singlet state is isotropic and the mixed state is just the average over S and T_0 the mixed state then picks up some degree of LFE despite its lack of entanglement. Entanglement is neither necessary nor sufficient for a LFE. While it is not clear how to separate the anisotropy arising from coherent evolution driven by an anisotropic HFI from that yielded by the directional starting vector, it is evident that there is no need whatsoever for entanglement between the electrons in order to see an anisotropic MFE.

3.4 The Directional Triplet

Although the exact role of entanglement remains elusive it certainly appears that it is not necessary for the directional response of a RP reaction yield and in the process of this study we have identified an alternative source of directional information which may be of use in producing large anisotropic reaction yields. Ref [125] also made use of initial non-equlibrium triplet states, though in this instance they were invoked to create a RP system that returns significantly different reaction yields when simulated using the Kominis and Haberkorn models of reaction kinetics. In the course of their study it was noted that an "exquisite angular sensitivity" is achievable from such states, but this was used more as an argument for the usefulness of the Kominis kinetic superoperator than as a point of interest in its own right. The next section of this chapter investigates further the yield anisotropies arising from polarised triplet states.

3.4.1 Intersystem Crossing

Intersystem crossing (ISC) is a non-radiative process which transfers a molecule between states of different multiplicity.[3] For most molecular excited states ISC is driven by spin-orbit coupling with a transition probability given by [126]:

$$\left\langle m^{\mu}\Gamma_0, \gamma_S | \hat{H}_{\mathrm{SO}} | n^{\nu}\Gamma_0', \gamma_S' \right\rangle \tag{3.33}$$

where m and n are the initial and final states, μ and ν are the initial and final spin multiplicities, Γ_0 and γ_S define the orbital and spin parts of the wavefunction respectively (the prime identifies the final state wavefunctions) and $\hat{H}_{\mathrm{SO}}$ is the spin-orbit coupling Hamiltonian [127]. It is possible to examine the symmetry of the initial state (normally the first excited singlet state S_1) and the sub-levels $\{\tau_x, \tau_y, \tau_z\}$ of the closest triplet state (often but not always T_1) to deduce rules for the probability of each transition, $S_1 \rightarrow \{\tau_x, \tau_y, \tau_z\}$ as was done in Ref [126]. For excited states with some local symmetry (*i.e.* some symmetry in the molecular orbitals of interest) the triplet sub-levels often transform as different irreps (irreducible representations) and hence the transition probabilities to $\{\tau_x, \tau_y, \tau_z\}$ are far from being equal [126]. By convention the frame of the triplet sub-levels is defined in the eigensystem of the zero-field splitting (ZFS), that is, the dipolar coupling interaction between the two electrons [128].

[3] The normal $S - T$ evolution encountered in the RP mechanism is in some instances referred to as ISC which is technically not incorrect, however herein we use the term ISC only to refer to conversion between states of different multiplicities in molecular excited states – i.e. before the radicals are formed.

Different transition probabilities will lead to different rates of population of the three triplet sub-levels, and thus it is often the case that a molecular triplet is born with unequal sub-level populations. However, a state with non-Boltzmann populations in the ZFS frame (ZFSF), does not show a net spin polarisation, *i.e. no net magnetisation*, which can be shown by considering the initial density matrix transformed from the ZFSF to the eigenbasis of the Zeeman interaction Hamiltonian ($+0-$) for a field applied along the ZFS z-axis:

$$\rho^{\mathrm{ZFS}}(0) = \begin{pmatrix} p_x & 0 & 0 \\ 0 & p_y & 0 \\ 0 & 0 & p_z \end{pmatrix} \Rightarrow \rho^{+0-}(0) = \frac{1}{2} \begin{pmatrix} (p_x + p_y) & 0 & -(p_x - p_y) \\ 0 & 2p_z & 0 \\ -(p_x - p_y) & 0 & (p_x + p_y) \end{pmatrix} \tag{3.34}$$

where p_i are the populations of the triplet sub-levels. Clearly the populations of $|T_{\pm}\rangle$ are equal and no net spin polarisation will be observed, and similarly it can be shown that $\left\langle \hat{S}_x \right\rangle = \frac{1}{2}\left\langle \hat{S}_+ + \hat{S}_- \right\rangle = 0$ [129]. If the system is allowed to evolve under, for example, unequal g-values or different HFIs, or is subject to differential relaxation, the populations alter and a spin polarisation can be observed [130, 131]. When this is followed by permanent separation of the electrons strong polarisation of the individual radical spins can be observed. This is the triplet mechanism (TM) responsible for some examples of chemically induced dynamic electron polarisation (CIDEP). It is entirely possible for the TM and the RPM (responsible for the other observations of CIDEP) to work together, *i.e.* an initially polarised triplet state is the starting state of a radical pair which subsequently undergoes coherent evolution and a spin-sorting reaction [129].

As the ZFSF is not the eigenbasis of the full Hamiltonian the triplet states populated through ISC are non-stationary, they are coherent superpositions over the full spin Hamiltonian eigen-states. Quantum oscillation of the electron magnetisation was predicted as a direct result of the coherent evolution of the non-stationary starting states [132], and such oscillations have been observed by EPR [133]. Furthermore in Ref [133] oscillations in nuclear spin polarisation were also observed, and could only be successfully modelled if second-order HFI were included in the original triplet basis set, *i.e.* if nuclear spin-states contribute to ISC. The frame of the initial triplet sub-level may thus need to be the eigenbasis of the extended ZFSF $\hat{H}_{\mathrm{ZFS}} + \hat{H}_{\mathrm{HFI}}$. For the purposes of the simulations in the rest of this chapter we will continue to use the SF which may be identified with either the eigenbasis of the ZFS or the extended ZFS, or if necessary something else.

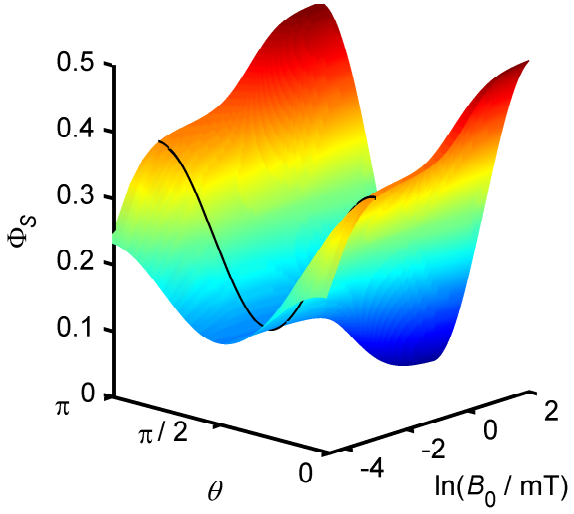

Figure 3.6. Singlet yield as a function of B_0 and θ, the angle between the SF z axis and $\vec{B}_0$. $k = 1 \times 10^6$ s^{-1}, $a = 1$ mT, $Ax = Rh = 0$ mT. The system starts in the T_z state defined in the SF. The black line shows the angular dependence at 50 μT.

3.4.2 Chemical Compass

Magnetic field effects have been observed in the reaction yield of radicals from a molecular triplet state with differential rates of ISC to the ground state [134], and a similar mechanism was once suggested as a possible mechanism of a chemical compass [135]. However, we are concerned predominantly with MFEs arising via the RPM which may be enhanced by a directional starting state.

As aforementioned, a system starting in a T_z state can return a directional yield in the absence of any anisotropic interactions. The variation of angular dependence over a range of fields is shown in Fig 3.6 for a system with a single isotropic HFI. There is a 100% change in the reaction yield at high field – when the field is along z, the T_z state is identical to T_0 in the eigenbasis of the interaction and there is complete mixing between T_z and S hence $\Phi_S = 0.5$. However when a strong field is applied perpendicular to T_z there is no T_0 character in the eigenbasis of the Hamiltonian and all evolution to S is prohibited, therefore $\Phi_S = 0$.

The three-dimensional angular dependence of the yield is often depicted as a polar plot, for a particular field. The surface position is dictated by the polar coordinates θ and ϕ and $|r| = \Phi_S^{\text{Aniso}} = \Phi_S(\theta, \phi) - \overline{\Phi_S}$. Φ_S^{Aniso} also defines the colour, ranging from bright red indicating the maximum yield to bright blue at the minimum. The anisotropic yields from T_x, T_y and T_z starting vectors are shown in Fig 3.7b)-d) to have the 3D shape directed along different axes. Obviously there is no anisotropy from the singlet state, Fig 3.7a). With such an enormous

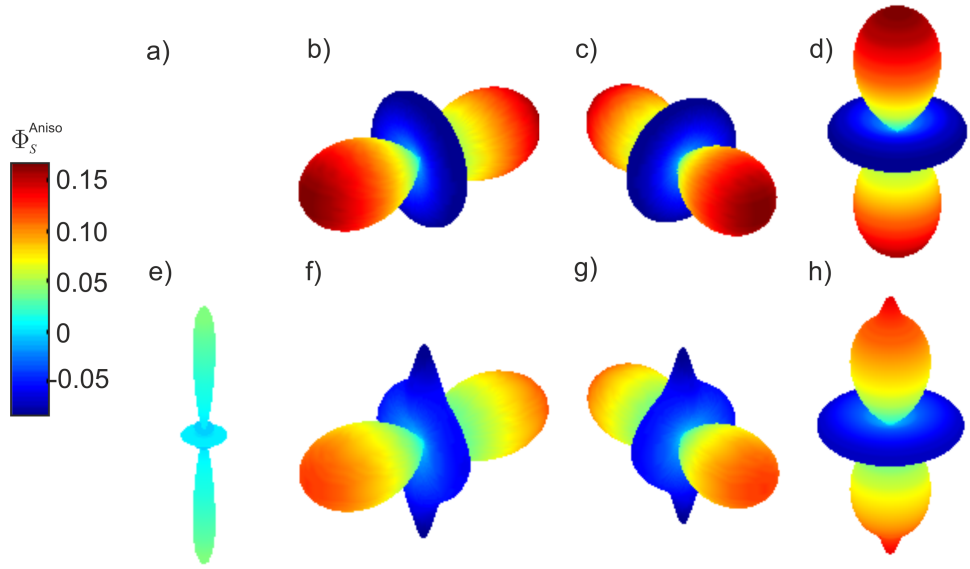

Figure 3.7. Polar plots for Φ_S^{Aniso} from (left to right) S, T_x, T_y, T_z pure starting vectors. The colour indicates the magnitude of Φ_S^{Aniso}, red regions and blue regions have greater than (max = +0.16) and less than (min = −0.08) the average singlet yield respectively – all polar plots are shown on the same colour scale. $k = 2 \times 10^5$ s^{-1}, $a = 1$ mT, $B_0 = 50$ μT. a)-d) $Ax = 0$ mT, e)-h) $Ax = -0.02$ mT.

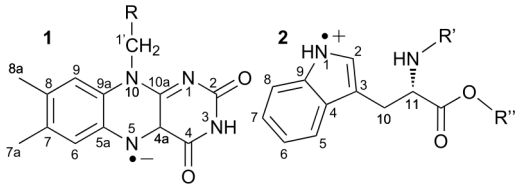

Figure 3.8. Chemical structures of **1** the flavin isoalloxazine radical anion and **2** a tryptophan radical cation.

variation in singlet yield from any of the initial triplet states, a system with unequal populations of the triplet states, if it could be physically realised, could make an excellent chemical compass.

In practice a spin-system is unlikely to have no anisotropic HFIs, thus Fig 3.7 e)-h) were calculated for the four pure starting vectors with an additional axiality to the HFI, $Ax = -0.02$ mT, and are shown on the same colour range as Fig 3.7 b)-d). Comparison of the anisotropic yield limits show that the triplet states give a much larger anisotropy than the singlet, but that all three triplets return a slightly weaker directional dependence than in the absence of the axiality, Fig 3.7b)-d). This result is in accord with the general observation that increasing the number of anisotropic HFI in a system, particularly if they do not align, reduces the overall directional response [15].

To establish if a directional triplet starting state can produce any gain in anisotropy over the pure singlet in systems with many HFIs a more complicated model system was simulated. The [FAD$^{\bullet-}$ $\cdots$ TrpH$^{\bullet+}$] RP provides a convenient example, Fig 3.8. This particular system

will be discussed in much more detail in later chapters. It is sufficient to note here that from the calculations of Ref [137] there is reason to expect some anisotropy in the ISC of excited molecular flavin S_1 states to the triplet manifold. Such anisotropy is not likely to be 100% and the competition between ISC and radical formation is likely to allow for a mixture of both singlet and triplet starting state RPs. A general starting vector may be defined as:

$$|\rho\rangle\langle\rho| = \lambda|S\rangle\langle S| + (1-\lambda)\left(P_x|T_x\rangle\langle T_x| + P_y|T_y\rangle\langle T_y| + P_z|T_z\rangle\langle T_z|\right) \tag{3.35}$$

where $0 \leq \lambda \leq 1$ and $P_x + P_y + P_z = 1$. As the singlet yield is linear with respect to the starting vector, the yield from any mixed state may be calculated by taking appropriate sums over the

Table 3.3. Hyperfine interactions included in the simulation of Fig 3.9 for the $FAD^{\bullet-}$ radical anion and $TrpH^{\bullet+}$ radical cation. HFI were calculated, by Kuprov, using density functional theory in Gaussian 03 and using the UB3LYP/EPR-III level of theory. Numbering is as shown in Fig 3.8 and in the calculations $R = R' = R'' = H$ [136].

Radical	**Spin**	**HFI / μT**	**HFI principal axes**
$FAD^{\bullet-}$	N5	$\begin{pmatrix} -100.1 & 0 & 0 \\ 0 & -86.8 & 0 \\ 0 & 0 & 1756.9 \end{pmatrix}$	$\begin{pmatrix} 0.9518 & -0.3068 & 0 \\ 0.3068 & 0.9518 & 0 \\ 0 & 0 & 1 \end{pmatrix}$
	N10	$\begin{pmatrix} -24.1 & 0 & 0 \\ 0 & -14.4 & 0 \\ 0 & 0 & 604.6 \end{pmatrix}$	$\begin{pmatrix} 0.6845 & 0.7291 & 0 \\ 0.7291 & -0.6845 & 0 \\ 0 & 0 & 1 \end{pmatrix}$
$TrpH^{\bullet+}$	N1	$\begin{pmatrix} -63.7 & 0 & 0 \\ 0 & -53.0 & 0 \\ 0 & 0 & 1081.2 \end{pmatrix}$	$\begin{pmatrix} 0.3223 & 0.9353 & -0.1463 \\ 0.9172 & -0.3468 & -0.1963 \\ 0.2343 & 0.0710 & 0.9696 \end{pmatrix}$
	H10	$\begin{pmatrix} 1498.1 & 0 & 0 \\ 0 & 1559.0 & 0 \\ 0 & 0 & 1756.7 \end{pmatrix}$	$\begin{pmatrix} 0.2968 & -0.3935 & 0.8701 \\ 0.8180 & 0.5749 & -0.0190 \\ -0.4928 & 0.7174 & 0.4925 \end{pmatrix}$
	H1	$\begin{pmatrix} -1082.6 & 0 & 0 \\ 0 & -705.4 & 0 \\ 0 & 0 & -6.9 \end{pmatrix}$	$\begin{pmatrix} 0.7540 & 0.6139 & -0.2336 \\ 0.2344 & 0.0808 & 0.9688 \\ -0.6136 & 0.7852 & 0.0830 \end{pmatrix}$
	H5	$\begin{pmatrix} -740 & 0 & 0 \\ 0 & -536.0 & 0 \\ 0 & 0 & -187.9 \end{pmatrix}$	$\begin{pmatrix} 0.5359 & 0.8279 & -0.1653 \\ 0.2657 & 0.0205 & 0.9638 \\ 0.8014 & -0.5604 & -0.2089 \end{pmatrix}$
	H8	$\begin{pmatrix} -558.2 & 0 & 0 \\ 0 & -423.1 & 0 \\ 0 & 0 & -109.7 \end{pmatrix}$	$\begin{pmatrix} 0.5779 & 0.7959 & -0.1803 \\ 0.2498 & 0.0378 & 0.9676 \\ 0.7769 & -0.6042 & -0.1769 \end{pmatrix}$

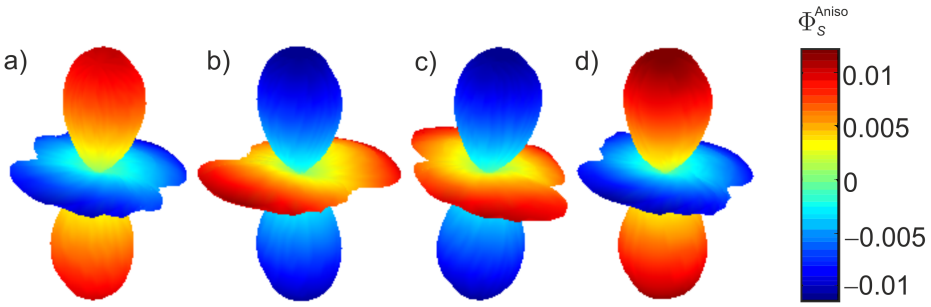

Figure 3.9. Polar plots for Φ_S^{Aniso} from (left to right) S, T_x, T_y, T_z pure starting vectors. The colour indicates the magnitude of Φ_S^{Aniso}, red regions and blue regions have greater than (max = +0.012) and less than (min =−0.011) the average singlet yield respectively. All polar plots in this figure are shown with the same colour scale. $k = 2 \times 10^5$ s^{-1}, $B_0 = 50$ μT. HFIs are detailed in Table 3.3.

yields from the pure states:

$$\Phi_S = \lambda \Phi_S^S + (1-\lambda)\left(P_x \Phi_S^{T_x} + P_y \Phi_S^{T_y} + P_z \Phi_S^{T_z}\right) \tag{3.36}$$

In the first place we assume the initial states are populated with complete selectivity and so calculate Φ_S^i. This will give an indication of the likely limiting behaviour and any mixed state chosen at this stage would be completely arbitrary. The HFI parameters included in the simulation are listed in Table 3.3, this is the largest number of nuclear spins that could be simulated in a sensible time-frame, and reaction kinetics were treated with the exponential model. The results of the singlet yield calculation from each of S, T_x, T_y and T_z pure starting states are given in Fig 3.9 and it is evident that the anisotropy of the system has generally decreased compared to the one nucleus example. The yields from a singlet-born RP, Fig 3.9a) and Fig 3.7e), show a decrease in anisotropy on adding more nuclei to the system. While there is still some gain in directional sensitivity when the reaction starts in any one of the pure triplet states, and most from T_z, this gain is extremely small (about 0.3%) in this instance. The maximum anisotropy in reaction yield occurs when $P_x = P_y = 0,\ P_z = 1$.

3.5 Conclusion

In this chapter we have investigated the implications of entanglement for the RPM. It is clear that many states commonly involved in RP reactions, of which the singlet state is the most common, do have strong entanglement between the two electrons, but it also appears that such entanglement is unnecessary for either field-strength or field-direction dependent MFEs. By studying the types of terms appearing in the initial density matrices we were able to fully

identify the origin of the LFE in the case of an isotropic HFI and an initial singlet state as arising from the coherences, between $|\alpha\beta\rangle$ and $|\beta\alpha\rangle$, and the dependence of this contribution on rate constants, field strength and HFI was investigated.

Further analysis of the role of entanglement leads to the observation that the initial triplet states have an inherent directionality which can lead to an anisotropic reaction yield even in the absence of anisotropic magnetic interactions. When this effect is accounted for it becomes difficult to isolate the role of entanglement in MFEs from the effects of relative orientation between field (or HFI PAS) and initial state. Only for the special case which has the magnetic field applied along the axis defining the basis states, *i.e.* coincident with the SF, and an isotropic HFI is entanglement necessary for a LFE, and even then the high-field effect is retained even for a mixed starting state. In most cases it is clear that entanglement is not required for MFEs of any kind. It would be interesting to attempt to remove the effects of the initial directionality from the outcome and thus probe the true role of entanglement but it is not obvious how to proceed with this.

Finally we have briefly investigated the significance of the triplet directionality for anisotropic RP reaction yields. Very large anisotropies are possible, but the addition of more anisotropic magnetic interactions, namely HFIs, reduces the contribution from the initial state so that for complex systems there is little gain in directionality from an initial triplet state compared to the singlet. Further work in this area should establish more precisely the relationship between state directionality and reaction yield in the presence of anisotropic HFIs with a view to identifying a potential candidate system for experiment. Such a system must be born in a polarised triplet state, will ideally have predominantly isotropic HFIs, and hence might then be expected to show large anisotropic reaction yields experimentally, *i.e.* the desirable chemical compass behaviour.

Further work investigating the effect on the LFE and of the anisotropy of a mixed starting state with different proportions of the triplet sub-levels and singlets might provide an interesting measure of the effect of state directionality on yield anisotropy. It would be interesting to investigate the effects of, for example, relaxation and radio-frequency fields on systems born in a polarised triplet state to understand to what extent, if any, they behave differently to the normal singlet.

Chapter 4

The Effects of Radio-Frequency Fields on the Avian Magnetocompass

4.1 Introduction to Animal Navigation

All sorts of animals across many phyla have been shown to possess the ability to respond to magnetic fields. To name but a few examples, birds [46, 138, 139], sea turtles [49], monarch butterflies [48], fruit flies [140], mice [141], newts [142] and bees [47, 143]. Even some strains of bacteria are affected by magnetic fields [144].

Despite the prevalence of magnetoreception in the animal kingdom the biophysical mechanism which underpins it is still a matter of much contention. A wide range of behavioural studies both in the wild and in the laboratory shed some light on the characteristics of the various animal compasses and magnetic maps but a consensus as to the underlying mechanism has not been reached for any animal. Magnetotactic bacteria, which strictly speaking do not 'sense' the field but simply align passively with it, do so due to long chains of biogenic magnetite particles but it is certainly not clear that any animal uses a similar physical response.

It is known that animals are capable of using many cues for orientation. The sky provides several possibilities; the sun, stars and polarised light [145, 146], and other more local visual cues are also important. Some animals use their olfactory sense in order to successfully orientate [147]. Many species have been shown to possess more than one of these mechanisms with the dominant source of information depending on the environmental conditions at the time of

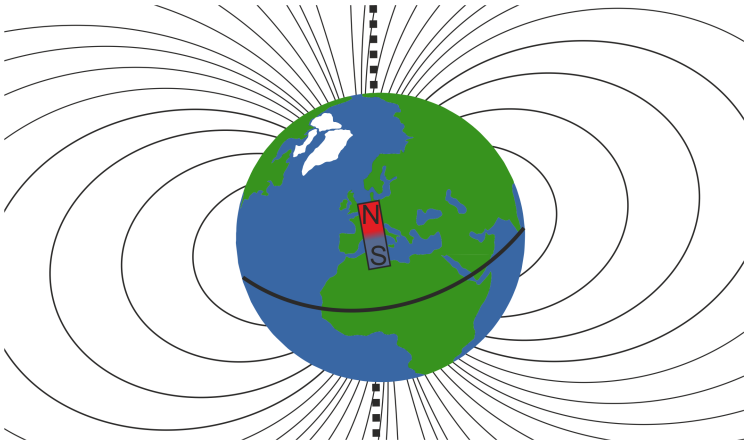

Figure 4.1. Schematic of the Earth's magnetic field. Solid lines represent magnetic flux lines and the dashed line indicates the rotation axis. The picture of the Earth was drawn by Jason Lau.

orientation. There is also likely to be calibration between the different compasses [148, 149]. This chapter, and those that follow, are concerned only with the animal magnetic sense.

Features of the Earth's Magnetic Field

Before moving on to discuss the biophysical mechanism of magnetoreception it is helpful to understand the nature of the magnetic field that is to be detected. The Earth can be imagined as a ball with a large bar magnet in the centre, from which field lines emanate, Fig 4.1. Clearly the magnetic field lines make an angle with the surface of the Earth and this is known as the inclination angle. Normal human compasses detect the horizontal component of the field, and thus can distinguish north and south. It is not necessary that animals use the field in the same way, and indeed as will be discussed subsequently, in many cases they do not.

4.1.1 Proposed Biophysical Mechanisms of Magnetoreception

Although several different mechanisms have been proposed to explain animal magnetoreception only three have gained a significant following, only two of which can begin to explain magnetoreception in land animals. For sharks, skates and other elasmobranch fish it was proposed that they can detect electromagnetic fields induced in the ampullae of Lorenzini as they swim through the geomagnetic field [150, 151]. As we are predominantly interested in avian navigation, and given that most birds do not swim significantly during migration, we focus on the two remaining main hypotheses for the mechanism of magnetoreception, magnetite versus the radical pair mechanism (RPM). Though there is still much debate surrounding the two proposals, it is becoming increasingly likely that both mechanisms are active in many species. It is thought

that a magnetite-based system allows for a magnetic map function and perhaps a fixed-direction response, while the RPM provides a compass heading [138, 152–154].

Magnetite

The magnetite mechanism is in essence the microscopic analogue of a man-made compass. The needle, a large metal pointer with a strong magnetic moment, is replaced with a single-domain nano-particle of magnetite, or alternatively with a chain of superparamagnetic magnetite particles that interact with each other to form one large magnetic moment [155]. Magnetite has been located in several species for example in salmon, *Oncorhynchus tshawytscha* [156] and in birds [157]. Several different transduction mechanisms have been proposed to account for experimental observations, though most centre around a magnetite particle being attached to a membrane so that a motion in response to the applied field pulls/releases a pull on the membrane thus changing the membrane permeability and initiating a nervous response [50]. Alternatively, it was proposed that the magnetite may sit in between nerve cells so that as it rotates in the Earth's field the conductance across the synapse is altered [47].

Radical Pair Mechanism

A popular alternative to the magnetite mechanism is built upon the RPM which has already been discussed in detail in earlier chapters. It was back in 1978 that Schulten first proposed the RPM as a potential mediator of directional magnetic field information for animal magnetoreception [51]. This was the first suggestion of a 'chemical compass', that is a chemical reaction whose outcome is dependent not only on the strength of the applied field, but also on its direction. The sensitivity to field direction arises from the inherently anisotropic interactions in the radicals themselves and hence the relative orientation of the field and internal interactions affects the coherent evolution of the RP between spin states and correspondingly the product yields. Despite being a fascinating suggestion, and the accumulation of a wealth of experimental and theoretical results pertaining to the RPM *in vitro* in intervening years [1], the chemical compass was mostly overlooked because there was no molecule or protein suitable for the task. However, in 2000, Ritz, Adem and Schulten proposed cryptochrome (CRY) as a candidate molecule [158]. A more detailed discussion of the suitability of CRY in this role can be found in Chapter 5. It is sufficient for the moment to note that it can be excited by blue light to form a radical pair [159].

For now we outline the Ritz *et al.* proposal in a little more detail [158]. It was proposed that

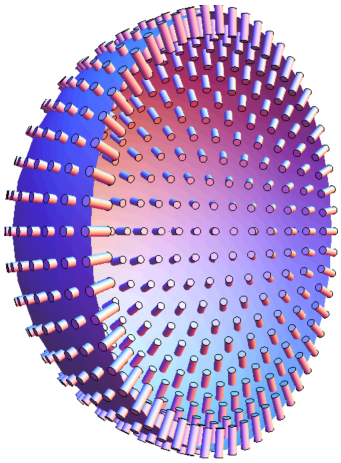

Figure 4.2. Representation of cryptochrome (CRY) ordering around the retina, cones represent the periodic arrangements of CRY proteins, ordered relative to the surface of the retina. Figure provided by P. J. Hore.

the RP reactions occur in CRY molecules that are regularly spaced, and orientationally ordered, around the retina of the eye, Fig 4.2. It has been speculated that the direction-dependent reaction yields somehow 'piggy-back' on the visual system. The reaction yield at each point on the retina will depend on the relative direction of the magnetic field compared to the CRY axis at that point. Therefore across the whole eye a visual modulation pattern could be envisaged which shows, perhaps, a brighter spot when the animal looks in a particular direction. It was thought initially that almost perfect ordering of the CRYs, as is shown in Fig 4.2 would be required to see a satisfactory response but recent work reported in Refs [160, 161] suggest that significant disorder is possible while retaining directional sensitivity. Alternatively, work is on-going to investigate whether it is possible that animals take advantage of the inherent polarisation of natural light to bring about selective excitation of only certain orientations of the CRY, thus achieving the effect of orientational ordering without actually having any order at all [162].

4.1.2 Avian Magnetoreception

Behavioural experiments to try and deduce the characteristics of the animal magnetic sense have been carried out with many different species. However, the largest set of experimental data has been collected from night migrant birds, in particular European robins (*Erithacus rubecula*), Fig 4.3. Henceforth we focus on the avian magnetocompass.

The development of new technologies has increased the number of ways to investigate bird navigation. For example GPS (global positioning system) has been used to track the entire routes of homing pigeons [163] and radar antennae are used to record the vanishing bearing of

Figure 4.3 Photograph of a European robin (*Erithacus rubecula*).

birds as they fly away in addition to simply watching the birds with binoculars [164]. These methods are used to study birds in the wild, however far more control over the environmental conditions can be achieved in a laboratory environment.

In the general procedure pioneered by the Wiltschkos (eg. [165]), birds are captured during autumn migration, undergo testing then and are held over the winter and tested again in the spring. The light conditions are artificially controlled to mimic those the birds would experience when it is time to begin the return leg of their migratory journey, thus inducing 'migratory restlessness' in the birds. At the time of the experiment the birds are removed to the experiment hut and placed in the bottom of an Emlen Funnel [166]. The walls of the funnel are covered in typewriter correction paper which leaves a mark when scratched at by the birds. At dusk, when night migratory birds such as the robins and garden warblers want to begin their flights the birds exhibit migratory restlessness and scratch at the paper to try and get out. They tend to scratch most frequently in the direction that they wish to migrate. Once the bird is removed from the funnel the typewriter paper is divided into sections and the number of scratches in each section is counted. The experiments are carried out in huts with a light source provided above the funnel so that there are no external cues, for example sun or star compasses, for orientation apart from the magnetic field. Once in this controlled environment other factors may be varied.

Characteristics of the Avian Magnetocompass

Unlike the familiar human compass it was shown in Ref [139] that robins derive directional information not from the absolute polarity of the field but instead from the inclination of the field lines relative to the ground, as shown in Fig 4.1. Presumably an internal gravitational sense is used as a reference axis when the birds are out of sight of the ground [139]. When the horizontal component of the field was reversed relative to the natural field (that is changing both

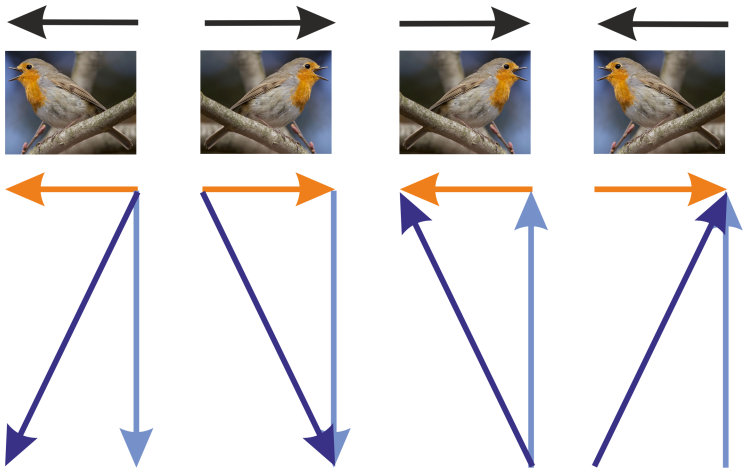

Figure 4.4. Scheme showing the preferred migratory direction (black arrow) of robins when the different components of the geomagnetic field (horizontal shown in orange, vertical shown in blue) are varied [139].

the inclination angle and the pole) the birds were orientated 180° from their natural heading, Fig 4.4. The same was true when only the vertical component was flipped. However, when both components of the field were reversed, that is, the field line was at the same inclination but the direction was inverted the birds were orientated as if under the natural field. As the Earth's field is approximately symmetric about the equator this means that birds can identify either a polewards or equator-wards direction but cannot distinguish the north from the south pole. It was suggested that this may provide an evolutionary advantage when considering that the Earth's magnetic field inverts every now and again [167]. This feature of the avian compass is consistent with the RPM as anisotropic HFIs have a centre of inversion and hence all reaction yields have inversion symmetry, consider for example the polar plots of earlier chapters. However, the RPM is not the only way to explain the inclination compass, although magnetite is capable of detecting field polarity, several mechanisms have been suggested that would give the observed inclination compass [168].

The Wiltschkos also showed that the avian compass is light-dependent [165, 169–171]. An overview of their results is shown in Fig 4.5. European robins are able to orientate under UV, blue, turquoise and green light but are disorientated under longer wavelength light (red and yellow). This is consistent with a light-activated RP reaction which has a chromophore absorbing light only in the shorter wavelength range. It has also been reported that birds left under red light can adapt and begin to orientate successfully [172]. This has lead to the suggestion that more than one RP based compass mechanism may be in action [169].

There is a body of work that has investigated the effects of strong magnetic field pulses on avian (and other animal's) orientation. An excellent discussion of these studies can be found

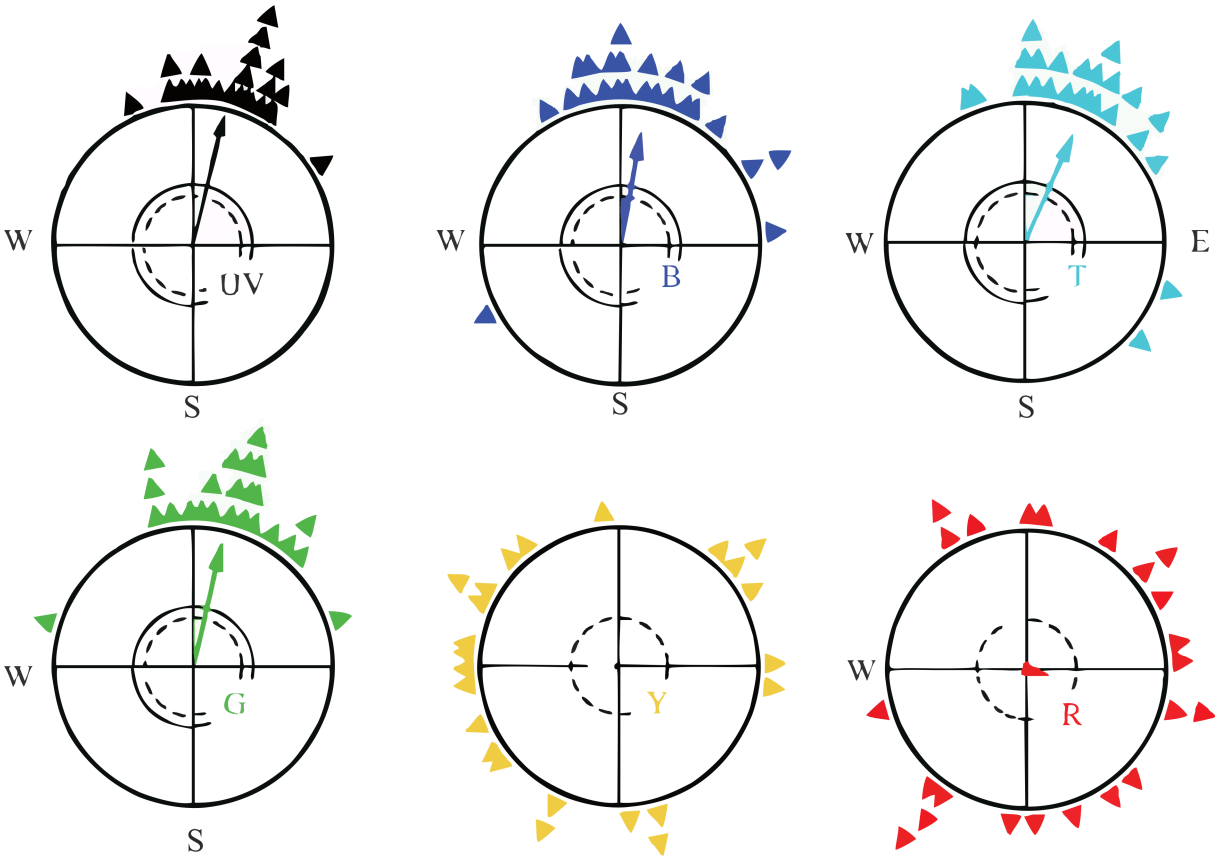

Figure 4.5. Orientation of European robins during their spring migration under monochromatic light of wavelength: 373 nm, 424 nm, 502 nm, 565 nm, 590 nm and 635 nm, at 0.8×10^{15} quanta $s^{-1}m^{-2}$ and $7-8 \times 10^{15}$ quanta $s^{-1}m^{-2}$ for UV and visible light respectively. The triangles indicate the main heading of individual birds over three recordings, the arrows represent the mean direction vector. The dotted and solid circles represent the 5% and 1% significance border (of the Rayleigh test). Arrows beyond these circles indicate significant orientation. Reproduced from Ref [169] with permission from the Royal Society and R. Wiltschko.

in Ref [173]. The responses are somewhat mixed. Robins and reed warblers (*Acrocephalus scirpaceus*) in the wild were shown to be disorientated by a pulse applied perpendicular to the natural field but not by a pulse parallel or anti-parallel to it [173] . However several species have failed to show any response at all. That under some conditions many species are affected by a strong magnetic pulse perpendicular to the natural field is considered to be evidence for a magnetite-involving mechanism of magnetoreception [156, 170, 173].

It has been suggested that a magnetite-derived magnetic sense in birds is conducted via the trigeminal nerve from the upper beak [174]. Complex magnetite based structures have been identified in the upper beak of several species [157], but these findings have not been replicated [175]. It has been shown that severing the trigeminal nerve does not prevent a bird from successful orientation, though lesion of the Cluster N region of the brain which is associated with night vision [176], does cause disorientation [177]. It has also been shown that the Cluster

N region shows high neuronal activity when night-migratory birds are carrying out magnetic orientation [178]. This region is evidently necessary for compass-like orientation.

Birds have been shown to become disorientated when exposed to field strengths outside of the normal functional region, that is fields varied significantly from the natural intensity. However it was also shown that they can adapt to a field twice the normal intensity of the local Earth field if exposed to the field for some time in advance of testing [179]. This result can perhaps be explained by considering that the birds are capable of adapting to changes in the visual modulation patterns proposed by Ritz *et al.* [158]. This was explored in Ref [15] in which the polar plots for a RP reaction under different static fields were compared and strong differences in the directional distribution of the product yields were predicted.

The evidence available to date is not sufficient to firmly prove or disprove either the chemical compass or magnetite model of compass-like magnetoreception, though many aspects could be consistent with either. The precise nature of the biophysical mechanism of magnetoreception may yet turn out to be an entirely different mechanism but for now it is worthwhile investigating the models we have.

Response to Radio-Frequency Fields

Perhaps the most remarkable evidence for the RPM is that birds have been shown to be disorientated by the application of an applied radio-frequency (RF) field. Zebra finches, *Taeniopygia guttata*, are unable to orientate using their magnetic sense when exposed to a 1.156 MHz oscillating magnetic field at 0.47 μT amplitude (about 1% of the local static field) [181]. In Ref [182] it was reported that robins are disorientated by an RF-magnetic field at 1.315 MHz with an amplitude of 0.48 μT, again about 1% of the static field. This frequency matches the energy splitting arising from an electron in the geomagnetic field at the site of the experiment ($\approx$ 46 μT). Further work by the Wiltschkos in this area, and reported in Ref [180], showed an even more remarkable response, Fig 4.6. European robins are disorientated by a 15 nT RF-field applied at the Zeeman resonance frequency (1.315 MHz) of a bare electron (in the local static field), but are well-orientated under a field of the same amplitude but at double or half the frequency. If, however, the static field is doubled, the resonance moves to twice the frequency. The observed 'resonance' in orientational capability alters with the applied field strength and remains coincident with the Zeeman resonance.[1]

[1] Although we focus here on the bird experiments, similar results have also been reported for American cockroaches [183] and work is in progress to determine if similar factors affect mouse orientation [184].

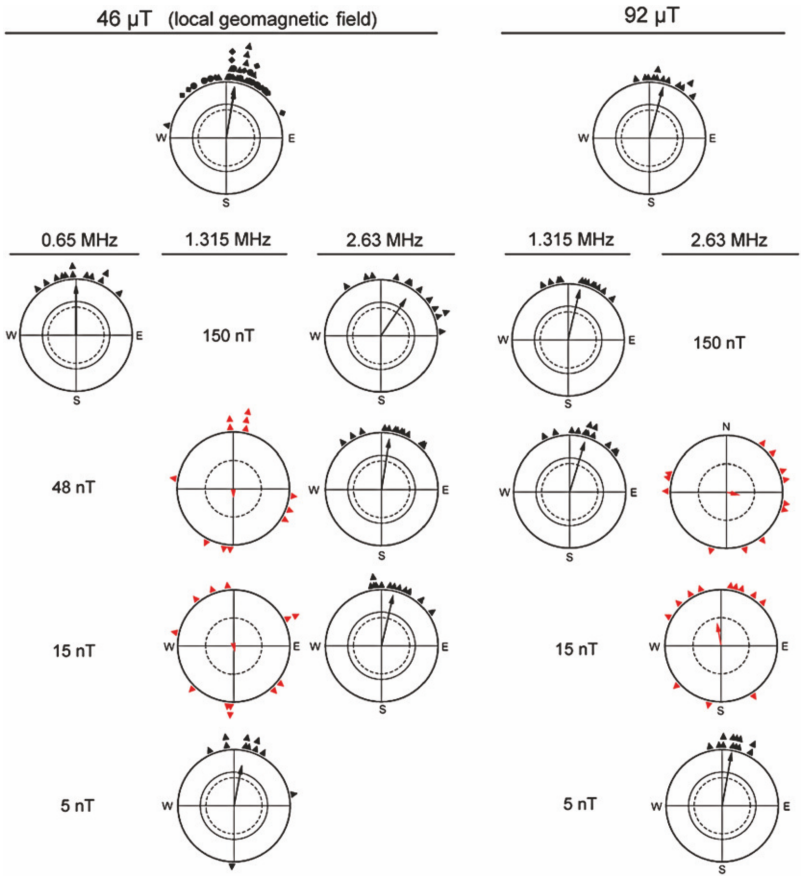

Figure 4.6. Orientation of European robins and the effects of adding oscillating fields over various intensities and frequencies. The three columns on the left indicate responses in the local geomagnetic field (46 μT) and the two columns on the right are the responses of the birds under a magnetic field of twice the natural intensity (92 μT) to which the birds had been pre-exposed for three hours. The uppermost diagrams show the orientation of the birds under static fields alone. The vector indicates the mean direction vector. The two inner circles are 5% (dotted) and 1% significance limits. The diagrams below show the responses when oscillating magnetic fields were added at the intensities and frequencies shown. Figure reproduced from Ref [180] with the permission of Elsevier.

4.2 Disruption of the RPM by RF-Fields

Effects of RF (or microwave) fields on spins is the basis for all magnetic resonance. However, the interactions are not limited to NMR and EPR spectroscopies but have been seen to affect RP reaction yields. Reaction yield detected magnetic resonance (RYDMR) [38, 39] exploits the effects of RF-fields on the coherent interconversion of singlet and triplet spin-states, usually at high field, which are manifest in the reaction yields. Such experiments are sometimes referred to as optically detected EPR [185] and at low fields (mT rather than T) these experiments are often called MARY-ν. Independent of the name, many experiments have shown that RF-fields can affect the outcome of RP reactions and there is no reason to believe this would not be true for RP reactions at very low fields, such as that of the Earth, even when the RF-field power is also weak. This was therefore proposed as a possible explanation for the disorientation of the

birds at certain RF-field frequencies, *i.e.* that the behavioural experiments [180] are in fact the first example of so-called animal-detected magnetic resonance (ADMR).

4.2.1 Calculation of Time-Dependent Field Effects Using γ-COMPUTE

The problem of efficiently simulating the yields of RP reactions under the influence of oscillating magnetic fields was addressed by Rodgers in his DPhil thesis and associated publications [136, 180, 186]. This section presents an overview of his methods. The Hamiltonian for a radical under the influence of an RF-field is time-dependent and may be defined as:

$$\begin{aligned}\hat{H} &= \gamma_e B_0 \left(\sin\theta\cos\phi\hat{S}_x + \sin\theta\sin\phi\hat{S}_y + \cos\theta\hat{S}_z\right) \\ &+ \gamma_e B_1 \left(\sin\left(\theta+\epsilon\right)\cos\phi\hat{S}_x + \sin\left(\theta+\epsilon\right)\sin\phi\hat{S}_y + \cos\left(\theta+\epsilon\right)\hat{S}_z\right)\sin\left(\omega_{\mathrm{RF}}t+\gamma\right) \\ &+ \hat{H}_{\mathrm{HFI}}\end{aligned} \tag{4.1}$$

where θ and ϕ are the spherical polar angles, ϵ is relative angle between the static and oscillating fields, ω_{RF} is the frequency of the RF-field (in angular frequency units) and γ is the initial phase of the RF-field. Strictly speaking, unless the two fields are parallel they form a 3D shape and in order to sample all relative orientations the third Euler angle (usually α) should be invoked. In the case of isotropic HFIs, rotating the field has no effect and the only angle of interest is the relative angle between the fields and thus α may be neglected, such systems are the focus of most of this chapter. The only anisotropic reaction yields under RF-fields of interest herein are those for which the static field is set to zero and so once again only the normal polar coordinates are required.

In addition to the difficulties associated with a time-dependent Hamiltonian such calculations are further complicated by the fact that RPs created by continuous illumination, under a continuous RF-field, are equally likely to be formed at any time during an RF-field cycle, that is, the singlet yield must be averaged over all possible initial phases, $\gamma = 0 \rightarrow 2\pi$.

This system is mathematically similar to problems in magic angle spinning (MAS) NMR of solid-state samples. There are random orientations of crystals in the sample which must be averaged over, γ-averaging, and modulation of anisotropic interactions by the MAS causes the Hamiltonian to be periodic, *i.e.* the spins evolve under a time-dependent Hamiltonian. The COMPUTE algorithm (Calculation over One Modulation Period Using Time Evolution) was proposed by Éden *et al.* [187] as an efficient procedure for simulating periodic NMR problems.

This was extended to include γ-averaging to give γ-COMPUTE [188]. Rodgers then employed the same methods for the problem of periodic time-dependent fields applied, without phase locking,[2] to reacting radical pairs.

It is not necessary to reproduce the derivation of the method here, Refs [136, 186–188] give excellent accounts. However, we do highlight the main aspects of the algorithm as implemented by Rodgers. The efficiency gains are made by exploiting the symmetry of the time-dependent part of the Hamiltonian due to its periodicity:

$$\hat{H}\left(t;\gamma\right) = \hat{H}\left(t + \frac{2m\pi}{\omega_{\mathrm{RF}}};\gamma\right) \tag{4.2}$$

where m is an integer and ω_{RF} is the frequency of the RF-field in angular frequency units. $\frac{2m\pi}{\omega_{\mathrm{RF}}}$ is equal to m time periods of the oscillating field. As phase and time are related the initial phase can also be treated as a time-shift:

$$\hat{H}\left(t,\gamma\right) = \hat{H}\left(t + \frac{\gamma}{\omega_{\mathrm{RF}}};0\right) \tag{4.3}$$

The propagators for system evolution are calculated for n, the discretisation parameter, steps within one time period. The product of these propagators can be used to generate the average Hamiltonian over one period. The singlet probability at any time t can then be calculated by applying the average Hamiltonian for every complete period and choosing the appropriate propagator to account for the 'left over' time in addition to an integer number of periods. Furthermore, as the initial phase can be treated as a time shift this can be incorporated by pre-multiplying the density matrix by an appropriate time propagator. The singlet probability is combined with an appropriate recombination function, usually a simple exponential decay, to allow the calculation of the total singlet yield.

A γ-COMPUTE 'toolbox' in MATLAB for RP reaction yield simulations was developed by Rodgers and remains in use in the Hore group. Simulations carried out in this chapter made use of these codes, incorporating some modifications to account for changes in the spin-system.

Criteria for a RF-Field Zeeman Resonance

A radical with no HFIs placed in a static field has very simple energy separations. The splitting that arises is due only to the interaction of the electron with the static field. In the limit that

[2] Phase-locked systems create the radical pairs via laser-flashes synchronised to a particular phase of the RF radiation.

the RF-field applied is much weaker than the static field, as is the case in the behavioural experiments, the RF-field can behave analogously to a micro-wave pulse (or continuous wave) applied to an EPR sample at high-field and drives population transfer between energy levels, *i.e.* there is an EPR-type resonance for the bare electron. This was expected to be made manifest in RP reaction yields by a change in the product yield at the resonant frequency, and indeed simulations by Rodgers showed this to be the case [136, 180].

For more complicated radicals, that is, those that experience one or more HFI the energy levels are far more complicated. This is particularly true of the low static fields of interest here, as the HFIs are often comparable, if not larger than, the static field. A radical with n spin-$\frac{1}{2}$ and m spin-1 nuclei will have $2^{n+1} \times 3^m$ energy levels and hence $2^n \times 3^m \times \left(2^{n+1} \times 3^m - 1\right)$ energy separations, not all of which will be associated with allowed transitions, some of which will be degenerate and none of which are expected to correspond exactly to the Larmor frequency. Such a radical was not expected to show a clear Zeeman resonance in the reaction yields, and again this proved to be the case in simulations [136, 180].

It was shown that in order for a radical pair to demonstrate a resonance at the frequency of the Zeeman splitting it is necessary for one radical to bear either no magnetic nuclei at all, or to have an even number of equivalent spin-$\frac{1}{2}$ [136, 180]. As was mentioned in Chapter 2, it is possible to combine the spin angular momenta of equivalent nuclei, using Clebsch-Gordon addition. An even number of spin-$\frac{1}{2}$ nuclei will always have an $S^{\text{Total}} = 0$ component which is equivalent to there being no nuclei at all. Of course the larger the group of equivalent nuclei the smaller the $S^{\text{Total}} = 0$ component becomes as a proportion of the whole and the smaller the RF-field Zeeman response.

In addition, the size of the RF-field response was shown to be proportional to $\sin^2\epsilon$ where ϵ is the angle between the static and oscillating field. Therefore, all simulations below were carried out with $\epsilon = \frac{\pi}{2}$ to maximise any possible response.

In order for the chemical compass mechanism of avian magnetoreception to explain the observed *in vivo* Zeeman resonance the RP must have certain characteristics. Specifically one of the two radicals must carry no magnetic nuclei, or $2n$ equivalent spin-$\frac{1}{2}$ nuclei. The original proposal for the magnetically-sensitive RP was based on a flavin-tryptophan RP in CRY (which will be discussed in much more detail in Chapter 5) but both radicals carry significant HFIs and so cannot explain the observed resonance.[3] As it is the flavin that undergoes photoexcitation

[3]Of course it is entirely possible that the RF-field is not affecting the actual chemical compass but rather the transduction mechanism, or the processing of the directional information, or the birds motivation to orientate

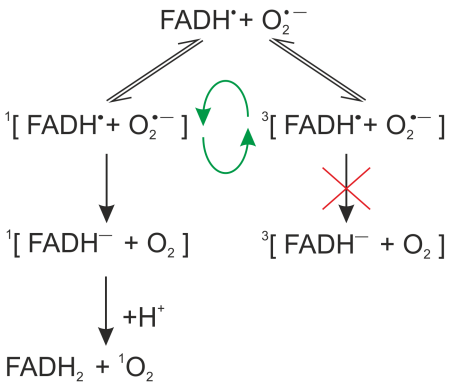

Figure 4.7 Reaction scheme as proposed in Ref [189] to incorporate a $\left[\mathrm{FADH}^{\bullet}\cdots\mathrm{O}_2^{\bullet-}\right]$ RP.

in the first place it seems unlikely that a flavin based radical is not involved in the RP. Thus the tryptophan was demoted from an active role in the RPM and an alternative paramagnetic species, that carries no hydrogen, nitrogen, phosphorus etc. atoms was envisaged.

4.2.2 Oxygen/Superoxide as Possible Counter Radicals

The role of oxygen or superoxide in the chemical compass was first questioned in the work by Maeda *et al.* in Ref [37]. This was further investigated by Ritz *et al.* in Ref [180], when reporting the remarkable observation of an *in vivo* Zeeman resonance.

Some of the theoretical aspects of the proposal were presented by Solov'yov and Schulten [189] which was published while the work of this chapter was being carried out. Ref [189] provides an assured argument detailing the maximisation of yield anisotropy when one radical carries no magnetic nuclei, discusses the possible approach of a superoxide molecule to the flavin in CRY and proposes a reaction scheme. We propose three further possible reaction schemes, as will be discussed in the next subsection. However, the main focus of our study has been to explain the Zeeman resonance observed in the Wiltschkos' experiments, and thus we turn our attention to the magnetic properties of oxygen and superoxide for the majority of what follows.

Chemistry

There is little purpose proposing a paramagnetic species to partner the flavin radical if there is no chance of these species reacting. The scheme shown in Fig 4.7 was proposed by Solov'yov and Schulten to show feasible chemistry involving a $\left[\mathrm{FADH}^{\bullet}\cdots\mathrm{O}_2^{\bullet-}\right]$ RP intermediate. The reduced flavin (FADH_2 or $\mathrm{FADH}^{\bullet}$) is formed by photoreduction of the fully oxidised FAD state

or indeed something else. However, it is difficult to see why any of these would show a response to a Larmor frequency and so we focus on the effect of RF-fields on the RPM.

of the protein. Inspection of this scheme raises a couple of questions:

1. Why can the triplet state of the RP not undergo electron transfer (ET) to form triplet oxygen, which is the ground state of molecular oxygen, and the fully reduced flavin?

2. What happens to the singlet oxygen following ET from the singlet state? Singlet oxygen is toxic.

3. Does $FADH^{\bullet}$ really oxidise oxygen?

The redox potentials of FAD in *Arabidopsis thaliana* cryptochrome 1 (AtCRY) were reported in Ref [190] (within an estimated error of $\pm 20\%$). We are interested in the excited state of the flavin following photo-excitation and the electrode potentials from this state may be somewhat different from the following, however to the best of our knowledge no excited state electrode potentials have been reported. The electrode potentials for the oxidation of oxygen and superoxide are also shown (at pH 7) [191]:

$$\begin{aligned}
FAD + e^- + H^+ &\rightleftharpoons FADH^{\bullet} \quad && E = -150 \text{ mV} \\
FADH^{\bullet} + e^- &\rightleftharpoons FADH^- && E = -160 \text{ mV} \\
{}^3O_2 + e^- &\rightleftharpoons O_2^{\bullet -} && E = -180 \text{ mV} \\
{}^1O_2 + e^- &\rightleftharpoons O_2^{\bullet -} && E = +810 \text{ mV} \\
O_2^{\bullet -} + e^- + 2H^+ &\rightleftharpoons H_2O_2 && E = +910 \text{ mV}
\end{aligned} \tag{4.4}$$

The first thing to note from these is that the reverse reaction of superoxide to singlet oxygen is rather disfavoured thermodynamically and for the reaction:

$$FADH^{\bullet} + O_2^{\bullet -} \rightleftharpoons FADH^- + {}^1O_2 \tag{4.5}$$

$E = -970$ mV. As $\Delta G = -nEF$ (where n is the number of electrons involved in the reaction and F is the Faraday constant) and reactions with positive free energy changes do not occur spontaneously, this reaction is not likely to proceed. The reaction to form triplet oxygen however has $E = 20$ mV and is thermodynamically feasible from the consideration of these electrode potentials. The major difference in free energy change could lead to significant differences in the reactivity of the two spin states and hence could allow for a MFE, if the reaction scheme in Fig 4.7 is modified very slightly . However, there is greater precedent for the oxidation of reduced

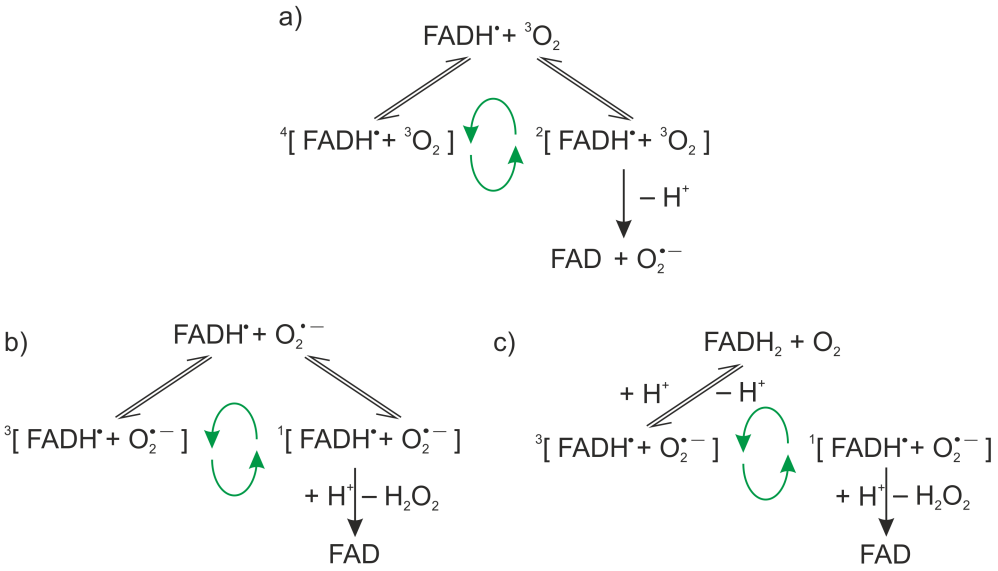

Figure 4.8. Three reaction schemes including a spin-correlated paramagnetic intermediate [96], either $\left[\mathrm{FADH}^{\bullet}\cdots{}^{3}\mathrm{O}_2\right]$ (a) or $\left[\mathrm{FADH}^{\bullet}\cdots\mathrm{O}_2^{\bullet-}\right]$ (b,c). The reduced flavins are formed on photoreduction of FAD.

flavins by molecular oxygen [192]. Although from the electrode potentials of Equation (4.4) the formation of the fully oxidised FAD coupled to $\mathrm{O}_2/\mathrm{O}_2^{\bullet-}$ is not favourable ($E = -30$ mV), the reduction potentials for the FAD/FADH$^{\bullet}$ couple in LOV domains, BLUF proteins and in the free flavin are significantly less than -180 mV [193], suggesting that a small change in the flavin environment can alter the balance of potentials significantly. In addition acidic conditions favour the reduction of oxygen to superoxide and would also shift the conditions in favour of flavin oxidation. Finally we note that the resting state of flavin in cryptochromes is known to be the fully oxidised form [194, 195]. The oxidation of FADH$^{\bullet}$ by molecular oxygen therefore seems rather likely. Even more favourable by thermodynamic arguments is the oxidation of FADH$^{\bullet}$ by superoxide, for which $E = 1060$ mV. Bearing these facts in mind we proposed in Ref [96] three possible reaction schemes which we consider more likely, Fig 4.8.

Ignoring the underlying chemistry and considering only the components in terms of the RPM, schemes b) and c) in Fig 4.8 are identical to the scheme in Fig 4.7. That is, they consider the $\left[\mathrm{FADH}^{\bullet}\cdots\mathrm{O}_2^{\bullet-}\right]$ RP with forward reaction only possible from the singlet state. In order to see a MFE, there must be spin correlation between the two radicals.[4] This can arise, as in Fig 4.8c) due to spin conservation in the step forming the RP intermediate. Alternatively, if the two radicals meet by diffusion as an F-pair we assume that the spin-allowed reaction occurs immediately so that only the unreactive spin-state remains after the initial encounter. The

[4]It should be noted that hereafter for convenience we use the word radical to describe both triplet oxygen and superoxide though strictly the former is a bi-radical triplet.

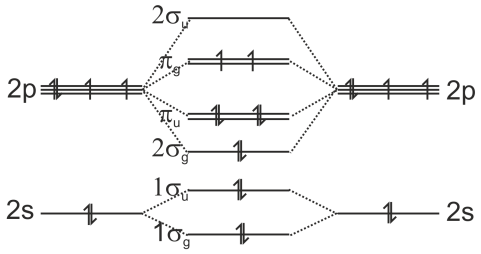

Figure 4.9 Molecular orbital diagram of molecular oxygen.

unreacted RPs have now gained spin-correlation and can evolve and react as normal.

An additional simplification must be made to the kinetics of the reaction schemes to allow the simulation to occur in Hilbert space (for which γ-COMPUTE was designed). It is necessary to assume that the rate constants of reaction from both spin states are identical and that each state can follow only one reaction path. To this end we assume that only the singlet (or doublet) state can progress to product while the triplet (or quartet) state alone undergoes a reverse reaction. We treat both reactions with the same rate constant and with the exponential model. As the RF field affects the coherent evolution, and should have no effect on kinetics, this approximation will not change the existence or position of a resonance, however it may well affect the magnitude. For now we are interested only if a Zeeman resonance of any kind can be predicted for superoxide/oxygen RPs rather than seeking an accurate estimation of its size.

Oxygen

Fig 4.9 shows the molecular orbital (MO) diagram for molecular oxygen from which it is clear that, as has already been mentioned, the ground state of molecular oxygen has two unpaired electrons and is a triplet state, $^3\Sigma_g$. Although we would like to be able to treat oxygen as a simple triplet (*i.e* $S = 1$) spin species subject only to external magnetic factors this unfortunately is not the case.

The two unpaired electrons of ground state $^3O_2$ experience a strong dipolar coupling, and some spin-orbit coupling, giving $D \approx 4.24$ T (= 119 GHz = 3.96 cm^{-1} = 0.019 k_BT at room temperature) [196], which is is massively larger than the applied field (Earth-strength ≈ 50 μT). The zero-field splitting (ZFS) in the oxygen causes a splitting between the $M_S = \pm 1$ and $M_S = 0$ sub-levels of the electronic triplet state, Fig 4.10, with the energy levels of the states given by:

$$E = D\left(M_S^2 - \frac{2}{3}\right) \tag{4.6}$$

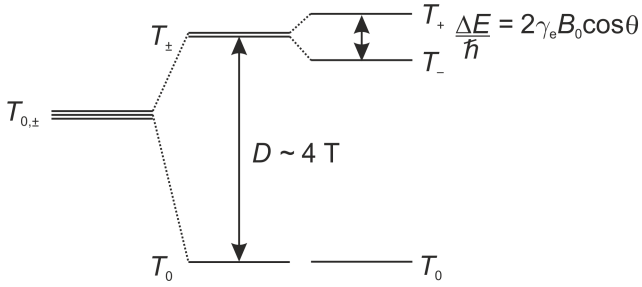

Figure 4.10. Energy level splittings of $^3O_2$ in zero-field and under a static magnetic field, B_0 applied at an angle θ to the molecular frame and assuming $g = 2.0$.

Due to the axial molecular symmetry, the dipolar interaction is directed along the internuclear axis, and thus the total spin is quantised in the molecular frame along this axis as well. Therefore, the angle, θ, that the static field, B_0, makes with the molecular axis affects the Zeeman splitting. In addition, of course, the T_0 state is far removed in energy from the $T_\pm$ states and there is no chance that the allowed $\Delta M_s = \pm 1$ transition that might be driven by an applied RF field will be at the Zeeman frequency. Even if a $\Delta M_s = \pm 2$ transition was not formally forbidden, the transition between the $T_\pm$ states would occur at the Zeeman resonance only when the field was directed at $\theta = \frac{\pi}{3}$ to the molecular axis. It seems unlikely that a triplet oxygen partner for the flavin radical could be responsible for the observed *in vivo* Zeeman resonance.

To confirm this the γ-COMPUTE toolbox of MATLAB codes was modified to calculate the yield of doublet product from a system undergoing coherent evolution between doublet and quartet spin states. In order to start with a spin-correlated state, pairs of radicals encountering as doublets were assumed to react immediately thus the initial vector was defined by the unreacted quartet states. In addition, in order to be able to use the normal exponential model, and hence perform the calculation in Hilbert space, the scheme of Fig 4.8a) was simplified such that the only reaction route available to intermediates in the doublet spin state was forward reaction to product. The projection operators for doublet and quartet states are as follows:

$$\hat{Q}_D = \frac{1}{3}\hat{\mathbb{1}} - \frac{2}{3}\hat{S}^A \cdot \hat{S}^B \tag{4.7}$$

$$\hat{Q}_Q = \hat{\mathbb{1}} - \hat{Q}_D = \frac{2}{3}\hat{\mathbb{1}} + \frac{2}{3}\hat{S}^A \cdot \hat{S}^B \tag{4.8}$$

where $\hat{S}^A \cdot \hat{S}^B = \hat{S}^A_x \hat{S}^B_x + \hat{S}^A_y \hat{S}^B_y + \hat{S}^A_z \hat{S}^B_z$. These projection operators were simply used in place of the singlet (and triplet) projection operators in the normal product yield calculations. Defining the system in the principal axis system (the molecular frame of oxygen) of the dipolar

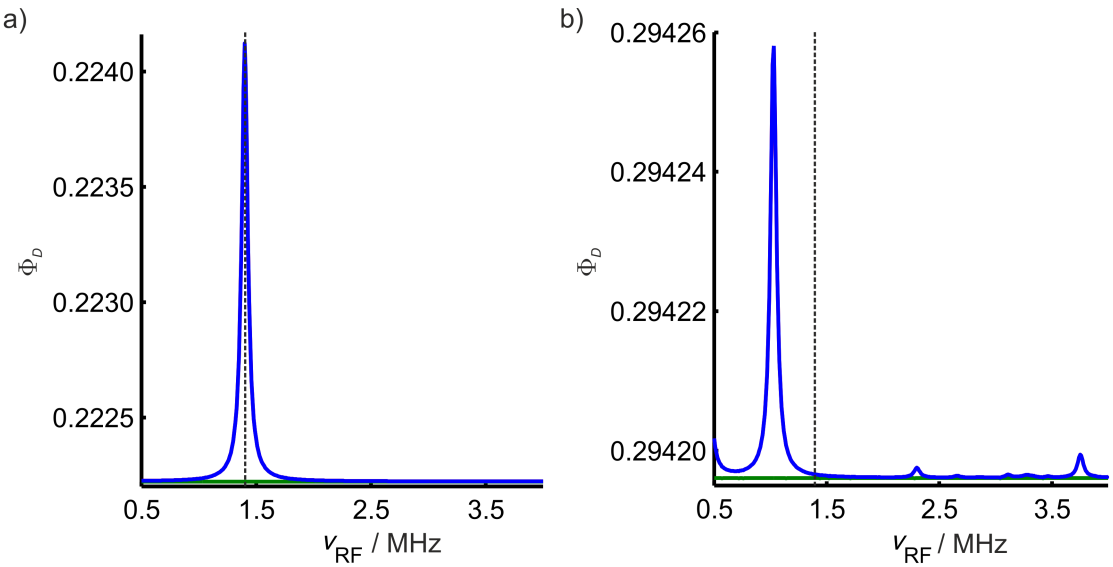

Figure 4.11. Doublet yield from a $\left[{}^3O_2 \cdots B^\bullet\right]$ RP reaction where a) radical B is a bare electron and b) radical B carries two nitrogen atoms (Table 4.1). Red is the RF turned on for both radicals, blue shows the yield when the RF field is turned on for the bare electron counter radical only (this runs directly over the red curve) and green is the doublet yield when the RF field is turned on for the ${}^3O_2$ only. The black dashed line is at $\nu_{\mathrm{RF}} = 1.4$ MHz. $k = 2 \times 10^5$ s^{-1}, $\epsilon = \frac{\pi}{2}, \theta = 0, B_0 = 50$ μT, $B_1 = 0.3$ μT, $D = 4$ T and $n = 4096$.

interactions, the Hamiltonians for the spin-1 oxygen moiety and counter radical are respectively:

$$\hat{H}^A = D\left(\left(\hat{S}_z^A\right)^2 - \frac{2}{3}\hat{\mathbb{1}}\right) + \omega_0\left(\hat{S}_x^A \sin\theta + \hat{S}_z^A \cos\theta\right) + \hat{H}_{\mathrm{RF}}^A \tag{4.9}$$

$$\hat{H}^B = \hat{H}_{\mathrm{HFI}} + \omega_0\left(\hat{S}_x^B \sin\theta + \hat{S}_z^B \cos\theta\right) + \hat{H}_{\mathrm{RF}}^B \tag{4.10}$$

where θ is the angle between the inter-oxygen axis and the applied field. Fig 4.11a) shows the results of calculating the doublet product yield, Φ_D, using the modified γ-COMPUTE for the simplest possible case, that in which there are no magnetic nuclei on the counter radical. In order to locate the source of the resonance we have repeated the calculation with the RF field turned on for both radicals, just the oxygen moiety (A) and just the electron (B). The latter two cases are achieved by manually zeroing $\hat{H}_{\mathrm{RF}}^B$ and $\hat{H}_{\mathrm{RF}}^A$ respectively within the simulation. From Fig 4.11a) it is clear that the Zeeman resonance (at 1.4 MHz for an Earth-strength field of 50 μT) arises solely from the bare electron, there is no resonance in this range of frequencies arising from interaction of the RF field with the triplet oxygen.

Repeating the calculation with a more realistic counter radical, one bearing some HFIs, should remove the Zeeman resonance from radical B. There is no longer a clear EPR transition at that frequency once the additional hyperfine splittings are considered, and there is no reason to expect any change in the response of the oxygen. In order to test this two reasonably

realistic nitrogen HFIs were added to the counter radical, listed in Table 4.1. For the purpose of this calculation the readily available theoretical HFIs were perfectly sufficient to demonstrate the expected behaviour, though experimentally determined $FAD^{\bullet-}$ nitrogen HFIs have been reported [197]. The results of this simulation are shown in Fig 4.11b). It is clear that there is indeed no longer a Zeeman resonance, though the counter radical displays a RF-field response corresponding to some of its many energy gaps.

The evidence thus far does not favour the proposal that oxygen is involved in a chemical compass sense which is sensitive to RF fields at the Zeeman resonance. In the next section we move on to access the role of superoxide in this response.

However, first we make a a brief aside to consider the possibility of using the orientational dependence of the Zeeman interaction of the $T_{\pm}$ levels as a source of directional information. Polar plots representing the singlet product yield were introduced in Chapter 3; here we are interested in the doublet yield but the anisotropy of a reaction yield is defined in the same way, as the difference between the reaction yield, $\Phi(\theta, \phi)$ and the spherically averaged reaction yield, $\overline{\Phi}$:

$$\Phi^{\text{Aniso}}(\theta, \phi) = \Phi(\theta, \phi) - \overline{\Phi} \tag{4.11}$$

where θ and ϕ are the spherical polar coordinates representing the orientation of the applied field with respect to the molecular frame. As before, Φ^{Aniso} gives the distance from the origin to the surface and its colour at that point, bright red indicating the maximum and bright blue the minimum yields. Fig 4.12 shows the anisotropic yields derived from oxygen with a bare electron co-radical and from a RP consisting of oxygen with the 2N-radical of Table 4.1. In the former case it is clear that there can be a large directional response arising from the axiality of the dipolar interaction, however, when additional anisotropic HFI are included, as in Fig 4.12b) the directional response is diminished to a range (the anisotropic yield now varies from -0.008 to

Table 4.1. Example theoretical nitrogen HFIs reported in Ref [15] as the two dominant anisotropic HFI of $FAD^{\bullet-}$, chosen as a reasonably realistic example of a slightly more complicated counter radical species.

Nucleus	**HFI tensor / mT**	a_{iso} **/ mT**
N1	$\begin{pmatrix} -0.098853 & 0.003884 & 0 \\ 0.003884 & -0.088056 & 0 \\ 0 & 0 & 1.7569 \end{pmatrix}$	0.5233
N2	$\begin{pmatrix} -0.018967 & -0.004841 & 0 \\ -0.004841 & -0.019578 & 0 \\ 0 & 0 & 0.60458 \end{pmatrix}$	0.1887

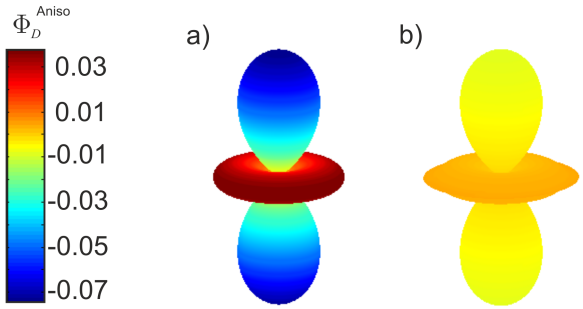

Figure 4.12. Polar plots showing the doublet yield relative to the spherical average, both plots are shown on the same colour scale for ready comparison from bright red (max = 0.037) to bright blue (min = −0.0740). a) O_2 and bare electron RP and b) O_2 and radical with the 2 N's of Table 4.1. $k = 2 \times 10^5$ s^{-1} and $B_0 = 50$ μT.

+ 0.0048) almost ten times smaller than the oxygen-bare electron pair.

Superoxide

Consultation of the MO diagram for superoxide, Fig 4.13, reveals that this species has an unpaired electron in one of a pair of degenerate π orbitals and therefore the ground state is $^2\Pi_g$. Thus, in contrast to most organic radicals, superoxide has a significant component of orbital angular momentum which is not quenched by a low symmetry environment that would remove the degeneracy of the π-orbitals. Hence, there is a spin-orbit coupling between the spin and orbital angular momenta which complicates the magnetochemistry. The spin-orbit coupling constant is $\lambda \approx -153$ cm^{-1} (=−164 T = − 0.74 $k_B T$ at room temperature) [20, 198].

In linear diatomic molecules there is axial symmetry and hence only the component of the orbital angular momentum, L, along the molecular axis is a constant of motion [199], that is, L precesses around the internuclear axis. The projection of the orbital angular momentum along the axis is $\Lambda = \pm 1$ and therefore there is a magnetic moment along the internuclear axis. As the spin-orbit coupling is strong, it causes a precession of the resultant spin angular momentum about the same axis and S becomes a poor quantum number. However, Σ (the projection of S onto the internuclear axis) remains a constant of motion. The total electronic angular momentum along the internuclear axis is $\Omega = |\Lambda \pm \Sigma|$ [199]. The ground state of superoxide is $^2\Pi_{\frac{3}{2}}$ and the excited state is $^2\Pi_{\frac{1}{2}}$, both are doubly degenerate.

When the axial symmetry of the radical is not removed, for example by asymmetric coordination of the radical, the spin angular momentum is quantised along the internuclear axis and hence the radical **g**-tensor is strongly anisotropic, a property we shall return to later. Rotational motion of the radical brings about modulation of the anisotropic Zeeman interaction

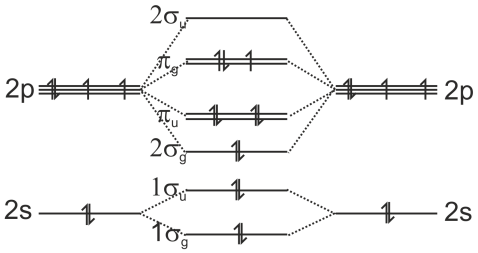

Figure 4.13 Molecular orbital diagram of superoxide.

which results in relaxation. Perhaps even more significantly, asymmetric hydrogen-bonding of the superoxide in aqueous solution (or to positively charged protein residues) temporarily reduces the cylindrical symmetry of the radical and hence quenches, to some extent, the spin-orbit coupling. The superoxide is therefore likely to experience strong fluctuation of its spin-orbit coupling strength which in turn brings about rapid electron spin relaxation, predicted to occur on the same timescale as molecular rotation (*i.e.* picoseconds) [200].

Karogodina *et al.* recently reported the observation of a high-field MFE for a reaction involving $NO^{\bullet}$ and $O_2^{\bullet -}$ as radical intermediates [200, 201]. The different g-values of the two radicals allow for fast coherent spin-state interconversion, comparable to the relaxation time, when the applied field is very large but this is not likely to be significant at weak field where relaxation times need to be closer to microseconds for MFEs to be seen [15]. Solov'yov and Schulten did not consider relaxation effects in their discussion of the role of superoxide in the magnetocompass though they were principally concerned with a superoxide reversibly docked in a protein binding pocket [189]. Binding a superoxide to a protein by means of asymmetric hydrogen-bonding for the duration of the RP reaction should reduce the modulation of the g-tensor and of the spin-orbit coupling strength, and will minimise fluctuation of the spin-orbit coupling constant, thus spin-relaxation may be considered slow compared to the timescale of the reaction. For simplicity we choose to investigate the magnetic properties of RPs involving superoxide in the limit of negligible spin relaxation however it is important to remember that relaxation effects are likely to be significant except in the conditions outlined above.

It is possible to quench the orbital angular momentum of the superoxide unpaired electron by removing the axial symmetry, that is, by forming asymmetric bonds. The crystal field splitting, Δ arising from asymmetric coordination of the superoxide leads to the mixing of ${}^2\Pi_{\frac{1}{2}}$ and ${}^2\Pi_{\frac{3}{2}}$. The new levels have energies [202]:

$$\frac{E_{\pm}}{\hbar} = \pm\frac{1}{2}\sqrt{\lambda^2 + \Delta^2} \tag{4.12}$$

Applying a magnetic field removes the degeneracies and allows the EPR spectrum of superoxide complexes to be measured [203]. The electron can be treated with an effective spin-$\frac{1}{2}$ which has g-values defined by the positive square root of [96]:

$$g_{\pm}^{2}\left(\theta,\alpha\right)=g_{\pm,zz}(\alpha)^{2}\cos^{2}\theta+g_{\pm,xx}(\alpha)^{2}\sin^{2}\theta \tag{4.13}$$

where θ is the angle between the field and the internuclear axis and [202]:

$$\tan 2\alpha=\frac{\lambda}{\Delta} \tag{4.14}$$

$$g_{\pm,zz}(\alpha)\approx 2\left(1\pm\sin 2\alpha\right)=2\mp 2\sqrt{\frac{\lambda^{2}}{\Delta^{2}+\lambda^{2}}}$$

$$g_{\pm,xx}(\alpha)\approx g_{\pm,yy}(\alpha)=2\cos 2\alpha=2\sqrt{\frac{\Delta^{2}}{\Delta^{2}+\lambda^{2}}} \tag{4.15}$$

Table 4.2 gives a summary of the g-value components and the energy levels in the three limiting cases, $\Delta\ll|\lambda|, \Delta=|\lambda|$ and $\Delta\gg|\lambda|$. When Δ is small the upper level is dominated by ${}^{2}\Pi_{\frac{1}{2}}$ character which has no magnetic moment, $g_{+,xx}=g_{+,zz}=0$, and so does not contribute to the MFE, despite being significantly populated. When Δ is very large ΔE will be much larger than $k_{\mathrm{B}}T$ and the higher energy level will be barely populated. For intermediate values of Δ the situation is a little less clear but for simplicity, in the simulations that follow only the lower energy level is considered as it gives a fair representation of the range of Zeeman splittings likely to be encountered and thus is sufficient to model the response of the MFE to a RF field.

The Hamiltonian for the interaction of the effective spin-$\frac{1}{2}$ of the lower level with a static applied field is now described by the Hamiltonian:

$$\hat{H}^{A}=\frac{\gamma_{e}}{2}g_{-,xx}B_{0}\sin\theta\cos\phi\hat{S}_{x}^{A}+\frac{\gamma_{e}}{2}g_{-,yy}B_{0}\sin\theta\sin\phi\hat{S}_{y}^{A}+\frac{\gamma_{e}}{2}g_{-,zz}B_{0}\cos\theta\hat{S}_{z}^{A} \tag{4.16}$$

Table 4.2. Summary of **g**-tensor components and energy levels (in units of $\hbar$) in the limiting cases of the magnitude of Δ the ligand field splitting.

	$\Delta\ll\lvert\lambda\rvert$	$\Delta=\lvert\lambda\rvert$	$\Delta\gg\lvert\lambda\rvert$
$g_{+,xx}$	0	$\frac{1}{\sqrt{2}}$	2
$g_{+,zz}$	0	$2-\sqrt{2}$	2
$g_{-,xx}$	0	$\frac{1}{\sqrt{2}}$	2
$g_{-,zz}$	4	$2+\sqrt{2}$	2
ΔE	λ ($\approx 0.74\ k_{\mathrm{B}}\mathrm{T}$)	$\sqrt{2}\lambda$ ($\approx k_{\mathrm{B}}\mathrm{T}$)	Δ ($\gg\ k_{\mathrm{B}}\mathrm{T}$)

where $g_{-,ii}$ are as defined in Equation (4.15). The time-dependent Hamiltonian describing the interaction of the RF-field also uses an effective spin-$\frac{1}{2}$ and the g-values defined above. Fig 4.14 shows the singlet yield (from a triplet born RP) as a function of the RF-frequency and the magnitude of the ligand field splitting for superoxide paired with a bare electron and with the 2-nitrogen radical of Table 4.1. When the radical B bears no nuclei, Figure 4.14a)-c), the Zeeman resonance can be observed from the counter radical, but this is lacking when nuclei are added Figure 4.14d)-f). In Figure 4.14 the static field is applied along the molecular axis of the superoxide ($\theta = 0$) and thus we are probing the Zeeman splitting dependent on g_{zz} and the RF-field is applied perpendicular to that ($\epsilon = \frac{\pi}{2}$). When there is no quenching $g_{zz} = 4$ and a Zeeman resonance would appear at 2.8 MHz. However, as the RF field is applied along the x-axis it cannot interact with the superoxide because $g_{xx} = g_{yy} = 0$ and this transition is therefore not observed Figure 4.14a) and d). As we would expect, increasing Δ causes g_{xx} and g_{yy} to increase from zero, facilitating the interaction of the RF field with the superoxide spin and hence leading to a Zeeman resonance. In Figure 4.14 b) and e) the resonance occurs at a frequency less than 2.8 MHz because increasing Δ also reduces g_{zz} from its limiting value of 4. As Δ is further increased all three g-values to tend towards the normal electron value ($g_e = 2$) and thus in both RPs there is a (relatively) strong resonance near the Zeeman resonance of a free electron in an Earth-strength magnetic field (50 μT $\rightarrow$ 1.4 MHz) in Figure 4.14c) and f).

Considering just the superoxide radical, diagonalising the Zeeman interaction Hamiltonian gives the energy levels as a function of the g-values and θ:

$$\frac{E_{\pm}}{\hbar} = \pm\sqrt{\frac{\omega_0^2\left(g_{xx}^2 + g_{zz}^2 + (g_{zz}^2 - g_{xx}^2)\cos 2\theta\right)}{32}} \tag{4.17}$$

$$\Rightarrow \omega_{\mathrm{RF}} = \frac{\Delta E}{\hbar} = \sqrt{\frac{\omega_0^2\left(g_{xx}^2 + g_{zz}^2 + (g_{zz}^2 - g_{xx}^2)\cos 2\theta\right)}{8}} \tag{4.18}$$

where $\omega_0 = \gamma_e B_0$. The Zeeman resonance occurs when the frequency of the RF-field matches the energy separation between the electron energy levels. In order to explain the *in vivo* resonance we require that $\omega_0 = \omega_{RF} = 2\pi\nu_{RF}$. Solving Equation (4.18) for the values of θ for which this

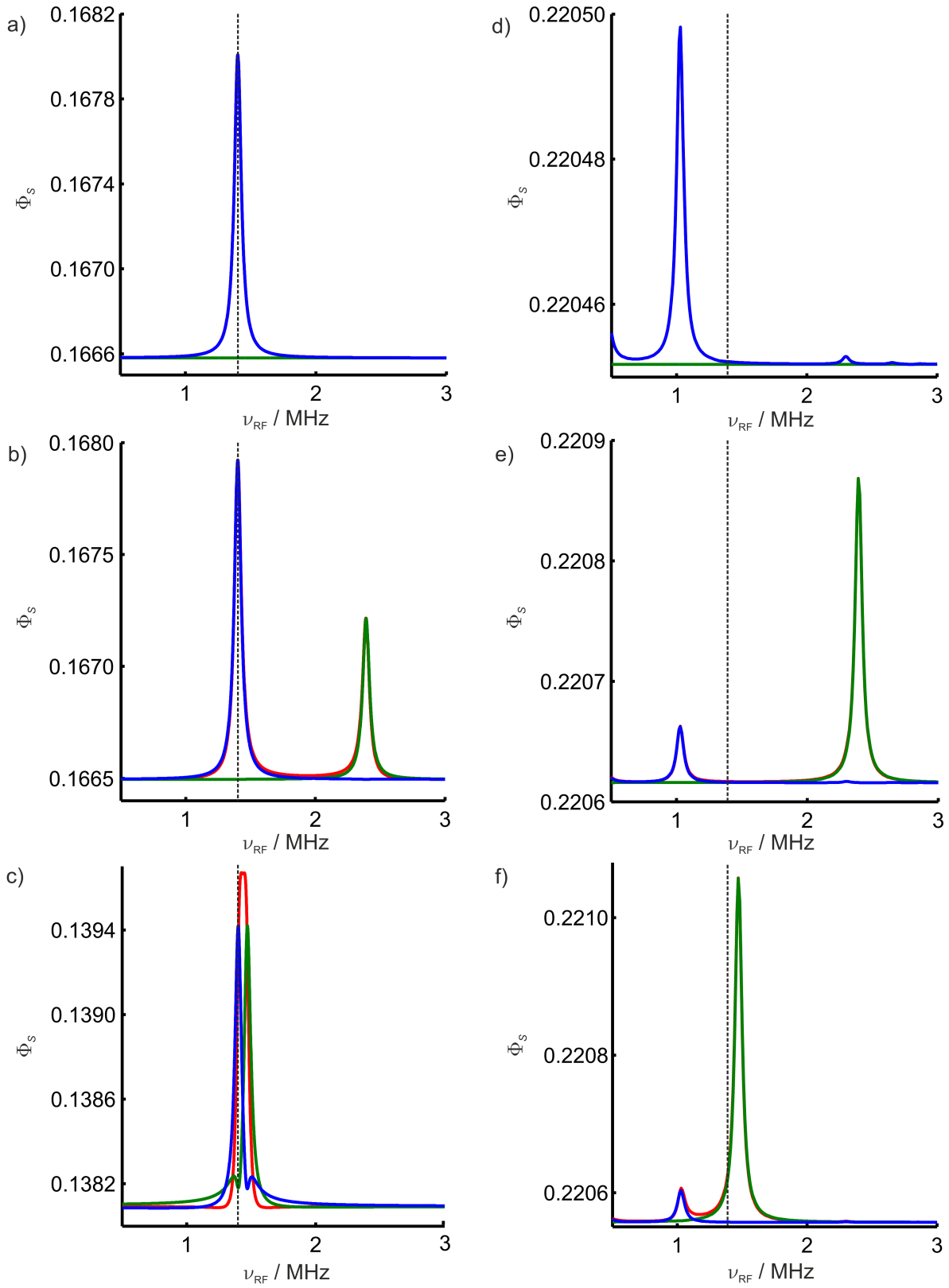

Figure 4.14. Singlet yield from a $\left[O_2^{\bullet -} \cdots B^{\bullet}\right]$ RP reaction, where red is the RF turned on for both radicals, blue shows the yield when the RF field is turned on for radical B only and green is the singlet yield when the RF field is turned on for the $O_2^{\bullet -}$ only. The black dotted line is at $\nu_{\mathrm{RF}} = 1.4$ MHz. B carries: a)-c) no nuclei, d)-f) Two nitrogens as in Table 4.1. a) and d) $\Delta = 0$, b) and e) $\Delta = -\lambda$, c) and f) $\Delta = -20\lambda$. $k = 2 \times 10^5$ s^{-1}, $\epsilon = \frac{\pi}{2}, \theta = 0, B_0 = 50$ μT, $B_1 = 0.3$ μT, $\lambda = -153$ cm^{-1} and a)-c) $n = 32$, d)-f) $n = 128$.

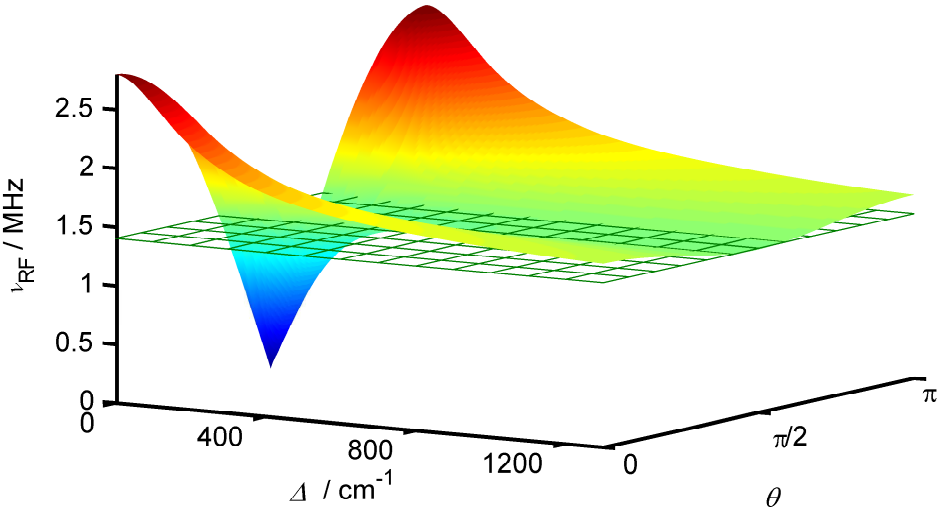

Figure 4.15. Expected RF-field resonance frequency (in linear Hz) arising from the $O_2^{\bullet -}$ as a function of θ and Δ according to Equation (4.18). The mesh shows the $\nu_{RF} = 1.4$ MHz plane. $B_0 = 50\ \mu$T.

is true gives:

$$\theta = \pm\frac{1}{2}\cos^{-1}\left(\frac{-8 + g_{xx}^2 + g_{zz}^2}{g_{xx}^2 - g_{zz}^2}\right) \tag{4.19}$$

$$= \pm\frac{1}{2}\cos^{-1}\left(\frac{-\Delta^2 - \lambda^2 + \Delta^2\sqrt{\frac{\lambda^2}{\Delta^2+\lambda^2}} + \lambda^2\sqrt{\frac{\lambda^2}{\Delta^2+\lambda^2}}}{\Delta^2}\right) \tag{4.20}$$

assuming $g_{xx} \neq g_{zz}$. There is a clear angle dependence for the resonance unless $g_{xx} = g_{zz} = 2$. Figure 4.15 shows the dependence of the resonance frequency ν_{RF} on θ and Δ. As would be expected, the angle-dependence of the resonance frequency decreases as the ligand-field splitting increases and correspondingly all three components of the **g**-tensor tend to the free-electron g-value. Thus, when Δ is large, and the orbital angular momentum is predominantly quenched, the superoxide radical gives rise to a change in the singlet yield when exposed to a RF-field at 1.4 MHz (in a 50 μT field). This would account for the observed *in vivo* Zeeman resonance.

In order to achieve a ligand-field splitting of 20λ or greater, as is required to see a strong resonance near the $g_e = 2$ Zeeman splitting, the superoxide must experience reasonably strong asymmetric coordination. It was shown in Ref [203] that strong hydrogen bonds, as are formed when superoxide is solvated in water, lift the degeneracy of the π orbitals and thus quench the orbital angular momentum – g-values observed in frozen protic solution are often not far from two. The protein binding pocket proposed for the approach of superoxide to the flavin [189] is very different from frozen aqueous solution. However, in order for the superoxide to

remain at a suitable distance from the flavin co-factor it may be fixed, at least temporarily, by hydrogen bonding to positively charged protein residues [189]. Hydrogen bonding would solve many difficulties associated with the superoxide model as the bonds are likely to be formed asymmetrically and so should lead to the required Zeeman resonance. Fortunately these conditions coincide with those expected to slow the electron spin relaxation of a superoxide radical, as the relatively long-lived hydrogen bonds both limit the rotational motion of the superoxide and minimise the fluctuations in spin-orbit coupling strength.

However, forming hydrogen bonds will necessarily spread some of the electron density onto the hydrogens, the radical is therefore likely to experience some hyperfine interactions. Kuprov performed a DFT calculation (B3LYP/EPR-II) for superoxide solvated by four water molecules, which predicted HFIs of up to 3.3 MHz (120 μT). Such large couplings would significantly split the Zeeman resonance of the superoxide and it would no longer be expected to occur sharply at 1.4 MHz. From the behavioural studies the maximum width of the Zeeman resonance can be estimated at less than 0.7 MHz (28 μT) [180]. HFIs smaller than this will tend to broaden the expected response to RF-fields but larger values will cause a significant splitting and the Zeeman resonance will no longer remain.

It is very difficult to envisage a biologically sensible situation whereby the superoxide is sufficiently strongly coordinated to achieve a g-value of approximately two without forming hydrogen bonds which incur HFIs that remove the resonance.

4.2.3 Other Possible Candidates

Having shown that molecular oxygen and superoxide are not terribly promising in the role of flavin counter-radical, though of course they should not be entirely dismissed, some other potential candidates were considered.

$OH^{\bullet}$

$OH^{\bullet}$ occurs biologically, via the Fenton reaction [204], and is known to damage the optic nerve as well as causing other site-dependent problems [204]. Reactive oxygen species (ROS) (such as $OH^{\bullet}$, $O_2^{\bullet -}$ *etc.*) can react with transport proteins altering Ca^{2+} homeostasis [205], can act as messengers for signal transduction [206], and in heart cells $OH^{\bullet}$ acts as a signal agent [207].

The first requirement, that $OH^{\bullet}$ is biologically occurring, has been met. However, like superoxide this species has a $^2\Pi$ ground state and is unlikely to have $g = 2$, added to which

there is a significant HFI and $OH^{\bullet}$ is known to experience very rapid relaxation [200]. However, it was shown by Rodgers [136] that a radical with two equivalent hydrogen nuclei is capable of showing a Zeeman resonance at the appropriate frequency. This arises from the $\frac{1}{2} - \frac{1}{2} = 0$ component of total spin angular momentum from the Clebsch-Gordon addition. Thus perhaps if $OH^{\bullet}$ were to form a strong hydrogen bond the two H atoms might become almost equivalent, and in addition the orbital angular momentum would be at least partially quenched. Of course the HFI tensors of the two H atoms would need to be identically orientated, which seems unlikely, for the two protons to be truly equivalent. Although the water radical is known to occur biologically this is almost exclusively following exposure to ionizing radiation.

$CO_2^{\bullet -}/CO_3^{\bullet -}$

Neither of these radical species carries any magnetic nuclei, ≈1% natural abundance ^{13}C is not very significant, however inspection of their biological roles is not very promising. $CO_2^{\bullet -}$ is a by-product of the reaction of peroxynitrases with pyruvate [208], and it reacts with carotenoid radicals [209]. The carbonate radical is formed by certain xanthine oxidase (which carries a flavin in each of two subunits) reactions predominantly, but not exclusively, in the liver and intestines [210]. The carbonate radical is strongly reducing and has a $^2\Pi$ ground state, unfortunately.

A Sulphur Based Radical

Sulphur has >99% I=0 nuclei, so perhaps a radical based on sulphur could be responsible for the observed resonance. Neither $SO_2^{\bullet}$ nor $CS_2^{\bullet}$ appears to occur biologically though alkyl sulphur radicals are common [211], for example glutathione (GSH) which is an anti-oxidant and also involved in cell signalling. However, in such radicals the unpaired electron is in an orbital with predominately p_z character, localised on sulphur, and hence spin-orbit coupling must be considered. Sulphur has greater effective nuclear charge than oxygen and so the spin-orbit coupling is expected to be larger. Additionally there may be some small spread of electron density onto the alkyl chain resulting in HFI with the hydrogens.

Solvated Electron

A hydrated electron normally exists in some sort of water cluster, occupying a cavity at the centre. This has been established for frozen alkali solution where it is possible to extract a hyperfine coupling interaction to both the first shell of hydrogens and ^{17}O which probably

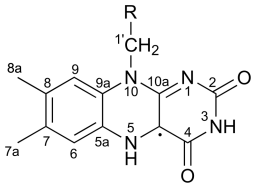

Figure 4.16 Chemical structure of the $FADH^{\bullet}$ radical.

relates to an approximately octahedral cavity with the 'lone pairs' of the oxygen pointing inwards [212, 213]. The isotropic HFI constants are estimated at ≈0.05 mT to the nearest hydrogens and much larger to ^{17}O. In solution EPR only a narrow peak has been recorded with $g \approx 2.0043$ [214], which is shown to decrease in intensity on addition of inorganic salts. However, no HFI splittings were resolved, which is promising for our purposes as this means that a Zeeman resonance might remain. Unfortunately, there is no evidence thus far of a biologically occurring free electron in the absence of UV (or high frequency) radiation. Tyrosine does photo-ionize to give a free electron but only when subjected to UV photolysis [215]. Tryptophan with oxygen can be ionized with UV irradiation to give various radical products and in the presence of chloroform there is electron exchange followed by recombination, hence the presence of chloroform accelerates tryptophan decay [216]. Neither of these reaction pathways is likely to occur in real biological conditions under normal light conditions.

4.2.4 Summary

While the hypothesis of a molecular oxygen or superoxide partner for flavin was initially very attractive in terms of maximising the anisotropy and explaining the *in vivo* Zeeman resonance it appears that neither species has the requisite magnetic properties. Triplet oxygen with its strong dipolar coupling does not have the correct energy separations and superoxide has a distinctly anisotropic **g**-tensor unless its is strongly coordinated. In a biological environment it is difficult to imagine how such a binding might occur without resorting to the formation of hydrogen-bonds which results in the radical no longer showing the same Zeeman splittings as a bare electron, and thus the Zeeman resonance is likely to be lost. Although there are other biologically occurring radical species that *might* be involved none of those considered thus far seem very promising.

It seems that superoxide is still the most likely candidate. Perhaps it docks in the CRY binding pocket in such a way as to form several weak hydrogen bonds which do not significantly spread the electron density on to the hydrogens but do quench the molecular symmetry. The conditions much also be such that relaxation is slow. It would be very interesting to carry

out docking studies on the $O_2^{\bullet -}$-protein complex to establish its most likely binding site. The resulting geometry could then be used in a DFT calculation to estimate the size of the HFIs.

4.3 Orientation Using RF-Fields Only

Just because we are not yet in a position to explain the *in vivo* resonance does not mean that it can be ignored and the remarkable resonance does suggest some further questions in addition to trying to explain it. If it is possible to disorientate birds by applying a RF-field at a suitable frequency perhaps it is possible to orientate them under RF-fields alone, that is, with the static field turned off. This section presents some preliminary work attempting to establish firstly whether it is possible to see an anisotropic reaction yield in the absence of a static field and secondly how this compares to a static field-only reference. In all the work that follows we assume that the second radical bears no magnetic nuclei, though as the former discussion highlights we do not know the identity of this species.

Table 4.3. Hyperfine interactions, included in the simulations of Figs 4.17 and 4.18, for the $FADH^{\bullet}$ radical analogue, numbering as in Fig 4.16. These data were summarised in Ref [136] from HFIs that were calculated for a vacuum optimised geometry using density functional theory in Gaussian 98 by Kay *et al.* [217, 218]. The geometry run used the PM3 semi-empirical method and the HFI calculation used UB3LYP/EPRII. Nuclei were included in the order shown starting with just the two, almost co-axial nitrogens.

Spin	**HFI / μT**	**HFI principal axes**
N5	$\begin{pmatrix} -104.9 & 0 & 0 \\ 0 & -99.6 & 0 \\ 0 & 0 & 1382.6 \end{pmatrix}$	$\begin{pmatrix} 0.4380 & 0.8655 & -0.2432 \\ 0.8981 & -0.4097 & 0.1595 \\ -0.0384 & 0.2883 & 0.9568 \end{pmatrix}$
N10	$\begin{pmatrix} -30.5 & 0 & 0 \\ 0 & -22.2 & 0 \\ 0 & 0 & 678.2 \end{pmatrix}$	$\begin{pmatrix} 0.9703 & -0.2207 & 0.0992 \\ 0.2383 & 0.9426 & -0.2340 \\ -0.0419 & 0.2506 & 0.9672 \end{pmatrix}$
H5	$\begin{pmatrix} -1385 & 0 & 0 \\ 0 & -937.2 & 0 \\ 0 & 0 & 14.3 \end{pmatrix}$	$\begin{pmatrix} 0.9819 & 0.1883 & -0.0203 \\ -0.0348 & 0.2850 & 0.9579 \\ -0.1861 & 0.9398 & -0.2864 \end{pmatrix}$
N1	$\begin{pmatrix} 33.2 & 0 & 0 \\ 0 & 37.8 & 0 \\ 0 & 0 & 300.4 \end{pmatrix}$	$\begin{pmatrix} 0.7387 & 0.6586 & -0.1437 \\ -0.6699 & 0.6937 & -0.2645 \\ -0.0745 & 0.2916 & 0.9536 \end{pmatrix}$
H6	$\begin{pmatrix} -218.0 & 0 & 0 \\ 0 & -201.6 & 0 \\ 0 & 0 & -54.4 \end{pmatrix}$	$\begin{pmatrix} -0.0362 & 0.2937 & 0.9552 \\ 0.7948 & 0.5879 & -0.1507 \\ -0.6059 & 0.7537 & -0.2546 \end{pmatrix}$

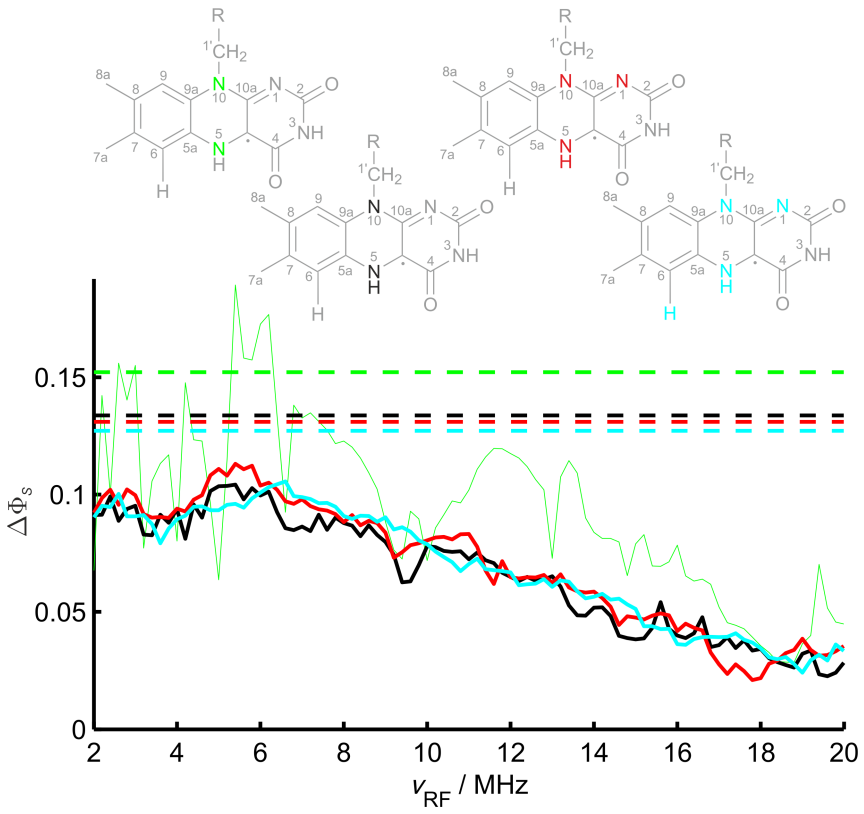

Figure 4.17. Maximum anisotropic response, $\Delta\Phi_S = \max\Phi_S(\theta,\phi) - \min\Phi_S(\theta,\phi)$, as a function of RF-field frequency, ν_{RF} for four systems based upon a $FADH^\bullet \cdots B^\bullet$ RP, where B is a radical carrying no magnetic nuclei. The RP begins in a pure singlet state. The nuclei included in each data set are shown on the $FADH^\bullet$ structures with HFI from Table 4.3. $B_1 = 500\ \mu T$, $k = 2 \times 10^5\ s^{-1}$ and $n = 32$. The dashed horizontal lines indicate the static field reference, $B_0 = 50\ \mu T$. Angles are sampled over the range $\theta = 0$ to π in steps of $\frac{\pi}{20}$ and $\phi = 0$ to 2π in steps of $\frac{\pi}{10}$.

As ever, the exponential scaling of spin chemical calculations with system size poses a problem, particularly when we consider that γ-COMPUTE carries out n (the discretisation parameter) matrix exponentiations as well as the normal diagonalisation. We are interested now in the anisotropic yield which requires recalculation of the singlet yield over a range of polar coordinates and additionally the optimum RF-field frequency is unclear and thus it was necessary to sample many frequencies. Put together these factors lead to very long simulation times. In an attempt to overcome these problems the calculation was initially carried out on the smallest sensible spin system, a $FADH^\bullet$ radical (Fig 4.16) bearing just the two nitrogens that have the largest axiality. The calculation was then repeated three further times on each occasion adding an extra nucleus to the simulation, shown in Table 4.3.

In Fig 4.17 the maximum difference in singlet yield, $\Delta\Phi_S = \max\Phi_S(\theta,\phi) - \min\Phi_S(\theta,\phi)$ is shown as a function of RF-field frequency for the different spin systems. There is clear convergence of the response on addition of the third, fourth and fifth nucleus. At frequencies of approximately 2−8 MHz the maximum difference in singlet yield is quite close to that of

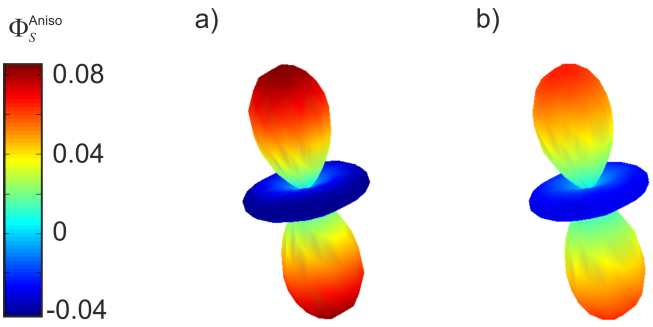

Figure 4.18. Polar plots, shown on the same colour scale (from $\max(\Phi_S^{\text{Aniso}}) = 0.0856$ to $\min(\Phi_S^{\text{Aniso}}) = -0.0416$) for the five nucleus spin system of Table 4.3. a) the reference static field system, $B_0 = 50$ μT $B_1 = 0$ μT and b) the same system exposed to a RF-field at ν_{RF}=5.4 MHz and $B_1 = 500$ μT, $n = 32$. For both, $k = 2 \times 10^5$ s^{-1}.

the static reference at $B_0 = 50$ μT. As it was shown in Ref [180] that birds can adapt to field intensities outside of their normal functional window, it seems plausible that birds could potentially adapt to a different distribution of singlet yields. For the five-nucleus system the polar plots for the static-only reference and the 5.4 MHz RF-field-only systems were compared, Fig 4.18. Inspection of these polar plots shows that only the absolute intensity changes, not the overall 3-dimensional pattern/shape of the yield and thus it seems plausible that the birds could learn to orientate using RF-fields only.

4.4 Conclusions

In this chapter we have attempted to explain the remarkable *in vivo* Zeeman resonance observed in the orientational ability of European robins, by considering paramagnetic species that may be involved in a reactive RP and which bear no magnetic nuclei. Oxygen and superoxide had previously been suggested as potential contenders for the role and their instrinsic magnetic properties were investigated. Oxygen, with its strong dipolar coupling seems extremely unlikely to be responsible for the observed Zeeman resonance, as the corresponding allowed transitions between triplet sub-levels are far from the simple Zeeman splitting. Superoxide provides a slightly more feasible explanation of the Zeeman resonance, if a chemically realistic system can be imagined in which the superoxide is asymmetrically coordinated, but not by hydrogen bonds which would introduce HFIs. As was mentioned earlier it would be very informative to model the binding of superoxide in the cryptochrome near the flavin co-factor in order to establish what type and strength of interactions exist. Although superoxide cannot be ruled out, it is sensible to continue searching for an alternative biologically occurring radical species that bears

no magnetic nuclei, is low spin, has a non-degenerate ground state and is slowly relaxing.

Having accepted that there is such a counter radical acting in the chemical compass, though it has not yet been firmly identified, it was possible to investigate the yield anisotropies arising under the influence of RF-fields but in the absence of a static field. For the $FADH^{\bullet}$ radical an RF-field of $\approx 500\ \mu$T is capable of producing a singlet yield anisotropy similar in magnitude to the static-field-only case at Earth-strength when the RF-field frequency is around 4-8 MHz. At higher frequency the yield anisotropy is considerably lower. In the optimum frequency range the singlet yield distribution is very similar to the static reference though with slightly smaller amplitude. It seems plausible that the birds could adapt to such a field and thus orientate under RF-field-only conditions. It would be extremely interesting to see if this is true of the behavioural experiments. If possible it would be helpful to consider the optimal RF-field frequency region at greater resolution and for RPs carrying more magnetic nuclei, the more realistic the system the better the guide for experimentation.

Chapter 5

Modelling Experimentally Observed Magnetic Field Effects in *Arabidopsis thaliana* Cryptochrome 1 and *Escherichia coli* Photolyase

5.1 Introduction

Schulten first proposed the radical pair mechanism as a potential chemical compass, that is, at the heart of a chemical reaction which is sensitive not only to the magnitude of the applied field but also its direction, in the 1970s [51]. However, this model of animal navigation only truly began to gain momentum after Ritz *et al.* Ref [158] proposed cryptochrome (CRY) as a candidate molecule. CRY has many of the properties required of the chemical compass [219]:

- It contains a blue-light absorbing chromophore - the isoalloxazine of a flavin-adenine-dinucleotide (FAD) co-factor.
- Upon excitation with blue light a spin correlated RP is formed [159].
- The lifetime of the radical pair (RP) is of the order of microseconds [220], theoretically long enough to show a MFE [15].

- The FAD radical state is thought to be involved in signalling [195].
- Several types of CRY have been found in birds' eyes [220–222].
- In nocturnal migrants at least one type of cryptochrome has been identified at relatively high levels in the ganglion cells co-localised with neuronal activity markers during periods of magnetic orientation (non-migrant species show decreased CRY expression during the night) [222].
- Genetic and behavioural studies performed on drosophila have shown that animal CRYs, specifically types 1 and 2 from monarch butterflies, can function in magnetosensitive responses. However the wavelengths of light required for successful magnetosensitivity is not consistent with the absorption spectrum of the fully oxidised FAD [140].
- Magnetic field effects have been observed in the growth of *Arabidopsis thaliana*. Inhibition of hypercotyl (stem) growth occurred in a 500 μT field (relative to the 40 μT natural field) under blue light but no effects were seen for plants grown in darkness or under red light only. No MFEs were observed in CRY 1 and 2 deficient *Arabidopsis* species [53]. These results could not be reproduced elsewhere [54].
- It has been found co-localised with Ultraviolet/violet cone cells [223], providing a means of some orientational ordering required to prevent the overall directional response averaging to zero [160, 161].

Until recently it was not known whether a CRY protein could be sensitive to magnetic field strengths as weak as that of the Earth's (≈ 50 μT), specifically to the direction of such a field. However, the effect of weak magnetic fields on the outcome of RP reactions in photolyases, specifically *Escherichia coli* photolyase (EcPL), has been observed by transient absorption spectroscopy [224]. Photolyases are structurally very similar to cryptochromes, sharing the photoactive flavin co-factor and the chain of three tryptophans (Trp) thought to be responsible, via sequential intramolecular electron transfer (ET) steps, for forming the spin correlated RP.

Optimising the measurements concerning EcPL magnetic field effects (MFEs) and investigating the effects of magnetic fields on *Arabidopsis thaliana* cryptochrome 1 (AtCRY) has been the subject of much experimentation by co-workers in the Timmel group over recent years. The data presented in this chapter were collected by **Alexander Robinson**, **Kiminori Maeda** and **Kevin Henbest** [225].

In order to better understand the origin of the MFE and to justify theoretically the presence of the observed, but strongly variable, low field effect (LFE) the data were modelled. The results of modelling these data are presented in this chapter.

5.2 The Photolyase/Cryptochrome Family

5.2.1 Biological Role

Photolyases are DNA repair proteins, specifically acting to undo damage to DNA through radical reactions, usually precipitated by exposure to ultra-violet light. The two major types of DNA damage incurred by irradiation with UV light are the formation of cyclobutane pyrimidine dimers (CPDs) and pyrimidine adducts called 6-4 photoproducts (6-4PPs) [226]. Correspondingly there are two main types of DNA PL, CPD-PL and 6-4PL, that bind selectively for their particular form of damaged DNA. In both sub-groups a reduced flavin is excited by blue light and subsequently donates an electron for transfer to the DNA to form a RP with one radical on the FAD and one on the DNA. This latter electron then causes fission of the unwanted bonds, resurrecting the DNA to a healthy state [227, 228].

Photolyases can also undergo photoactivation from the catalytically inactive $FADH^{\bullet}$. Photoexcitation of the flavin is followed by sequential intramolecular electron transfers along the chain of three Trp residues, known as the Trp-triad, which leads from the protein surface to the flavin binding pocket buried deep in the protein (Tryptophans W382, W359 and W306 in Fig 5.1b) [229]. This ET results in restoration of the fully reduced flavin required for DNA repair function and a $TrpH^{\bullet}$ radical which is eventually quenched. To date this process has only been observed *in vitro*. Given that the Trp-triad is highly conserved throughout the PL family it has been suggested that its role may be to act in photoactivation *in vivo* [230] but this is still a matter of debate.

If the flavin begins in its fully oxidised form, brought about by reaction with a chemical oxidizing agent, photoexcitation and sequential electron transfers from the Trps results in the formation of a spin correlated RP, $\left[FAD^{\bullet -} \cdots TrpH^{\bullet +}\right]$. This RP provides an interesting system to study as it is a close relative of the RP thought, in cryptochromes, to act as a chemical compass.

Unlike photolyases, most cryptochromes have shown no DNA repair activity. Instead they are known to play an important role in many different physiological processes, for example in

controlling circadian rhythms, *i.e.* the biological clock with an approximately daily cycle that can be reset by exposure to light or other external signals [231]. Cryptochromes are involved in the calibration of the clock with respect to light and it is for this purpose that cryptochromes are expressed in a wide range of different organisms [232].

Whether CRY proteins also have a role in magnetoreception has yet to be determined. In order to better establish if CRY provides a feasible chemical compass system work is ongoing to explore their properties with this functionality in mind.

5.2.2 Structures of Photolyases and Cryptochromes

Not only do members of the photolyase-cryptochrome family have a strong amino-acid sequence homology but also all structurally known members share the same overall fold, for example see Refs [233–236]. The FAD cofactor, in a u-shaped conformation which brings the adenine part adjacent to the isoalloxazine ring, is found in a binding pocket at the heart of the protein and the Trp-triad chain provides an efficient ET pathway from the protein surface to the FAD. These two components are vitally important for the formation of intramolecular RPs which have been observed in a number of members of this protein family. The crystal structures of EcPL and AtCRY are given in Fig 5.1 from which the similarity in structure, and in particular the conservation of the FAD and Trp-triad can be seen.

The most significant difference in structure between photolyases and most cryptochromes is a C-terminus extension that is only found in cryptochromes. This region seems to be intrinsically unstructured and correspondingly the solved AtCRY structure contains only the photolyase homology region (PHR) [233]. While it has been suggested that the C-terminal extension may be involved in signalling in plant cells [237] its influence on the photochemistry of AtCRY (which occurs in the PHR) is unknown. In contrast to the crystal structure, the AtCry proteins used for the experiments modelled herein are full-length proteins containing the C-terminal extension.

5.2.3 Observation of Radical Pairs in Photolyases and Cryptochromes

As has already been mentioned members of the photolyase-cryptochrome family form radical pairs after blue-light excitation of the the flavin co-factor and subsequent electron transfer. More specifically, and for the purposes of this thesis more interestingly, they can form spin-correlated radical pairs. The spin state interconversion of such RPs is susceptible to the influence of applied magnetic fields and modelling the impact of this on reaction yields is the subject of the majority

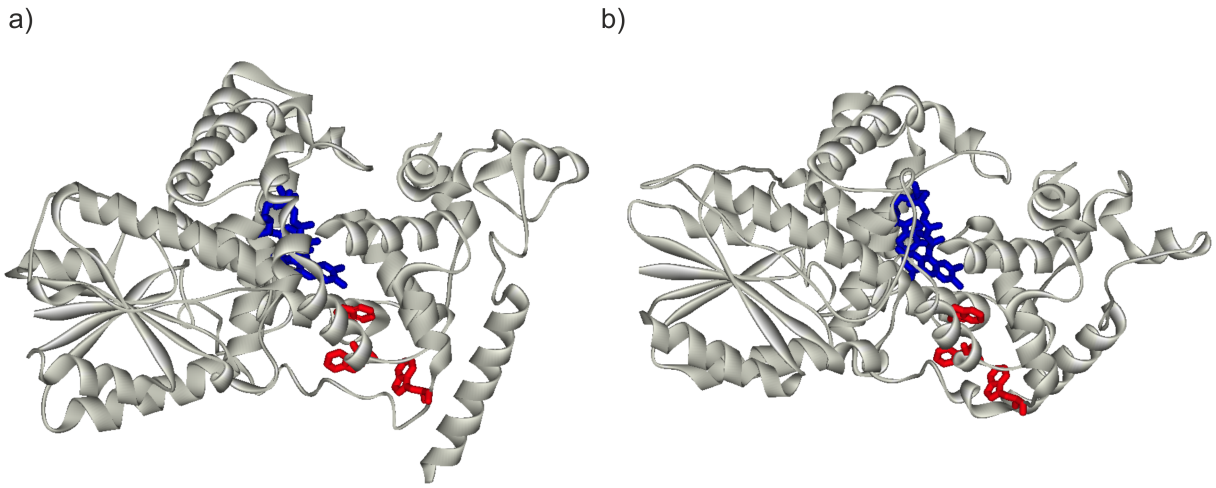

Figure 5.1. Crystal structures of a) AtCRY [233], (1U3D in PDB) and b) EcPL [234], (1DNP in PDB). FAD co-factors are highlighted in blue and the tryptophan triads in red. The tryptophans are residues 324, 377 and 400 in AtCRY and 306, 359 and 382 in EcPL.

of this chapter. However, before examining the effects of magnetic fields on EcPL/AtCRY RPs it is instructive to note briefly some of the evidence which shows that these RPs exist at all.

Transient absorption (TA) and time-resolved electron paramagnetic resonance (trEPR) spectroscopies have provided much of the experimental evidence for RP formation in PL and CRY. In the presence of damaged DNA an intermolecular spin-correlated RP associated with the FAD and CPD moieties was observed with trEPR in the protein-DNA complex of DNA PL from *E. coli* [228]. When the flavin is in its fully oxidised form, and in the absence of damaged DNA, an intramolecular ET occurs after photoexcitation of the flavin resulting in a spin-correlated biradical. In *Xenopus laevis* PL, trEPR showed the RP to be located on the FAD and a tyrosine (Tyr) residue [238], whereas in EcPL the RP sits on the FAD and a Trp residue (the terminal Trp of Fig 5.1) [239]. It is interesting to note that similar proteins do not display identical ET processes. The first direct evidence for a FAD-Trp (or possibly Tyr) RP in AtCRY came from TA spectroscopy in 2003 [240]. This technique has also been used to observe RPs in bird (garden warbler) CRY following excitation by blue-light flash photolysis [220]. Since then trEPR has further characterised the light-induced spin correlated RP in cryptochromes, (Cry-DASH from *Xenopus laevis* (XlCRY) [159, 241]) where the RP was shown to be singlet born. RP formation in CRYs is extremely robust, mutagenesis of the Trp triad does not necessarily prevent ET, though amino acid residues other than those in the conserved Trp-triad become involved [242].

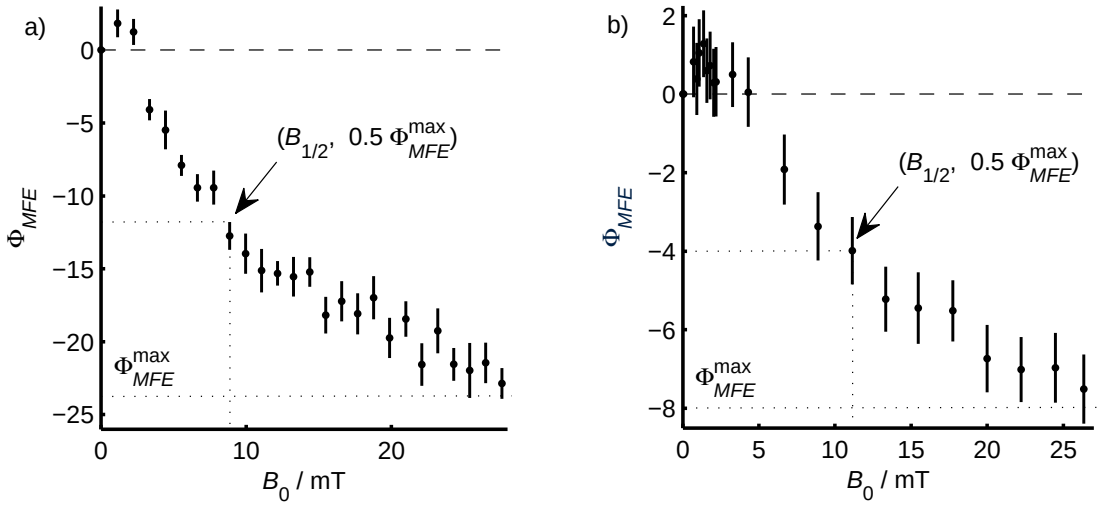

Figure 5.2. Experimental MFE data, Φ_{MFE}, as a function of field strength, B_0, for a) AtCRY and b) EcPL. The dashed line indicates 0% Φ_{MFE} values. Data falling below this indicate a traditional high field effect and the inverted region at low field is indicative of a low field effect. The dotted lines indicate the maximum, Φ^{max}_{MFE}, and estimate the field at which $\Phi_{MFE} = \frac{1}{2}\Phi^{\text{max}}_{MFE}$, this is the $B_{\frac{1}{2}}$.

5.3 Experimental Observation of Magnetic Field Effects in Photolyases and Cryptochromes

The first MFEs on this family of proteins were observed by Henbest *et al.* in EcPL using TA, the methods are reported in Ref [224]. Using similar experimental techniques, Robinson, Henbest and Maeda continued MFE studies of EcPL and began their studies of AtCRY. A detailed account of the experimental procedure can be found in Ref [243]. The results of these studies in EcPL and AtCRY are given in Fig 5.2. The error bars are estimated from noise levels in the time-resolved absorption spectra.

Summarised below are the important points about the experimental procedure used to collect the data modelled herein.

- There are several absorbing species observable in the TA spectrum.
- A secondary (non-magnetically sensitive) RP can be distinguished in the spectrum.
- Following the laser flash the absorbance of the secondary RP is recorded and time resolved spectrum integrated over time to give the total yield, Φ_{RP_2} from this non-spin-selective path.

- The magnetic field effect, Φ_{MFE}, is defined as the percentage:

$$\Phi_{MFE} = \frac{\Phi_{RP_2}(B_{\text{on}}) - \Phi_{RP_2}(B_{\text{off}})}{\Phi_{RP_2}(B_{\text{off}})} \times 100 \tag{5.1}$$

- B_{off} is not zero-field but the absence of any external static field applied in addition to that of the Earth. The local Earth-strength field is estimated to be ≈ 50 μT in Oxford. Partial shielding of the Earth's field is expected due to the large metal base of the experimental setup hence the basic field is likely to be something less than this and was estimated as ≈ 40 μT by Maeda [244] and this was used in our simulations.

- Experiments were carried out at 260 K and in approximately 60% glycerol solution.

There are three main features to the the data shown. Firstly there is a strong response to high field, secondly the maximum MFE is approached along a shallow gradient at intermediate fields and finally there is some indication of a small inverse MFE at very weak fields, a low field effect (LFE). For a RP to show chemical compass behaviour at the weak field of the Earth it should show some sensitivity to changing field strengths in this vicinity. However the error bars on the data are large in the low-field region, for most data points they extend below the zero-line, and the existence of a genuine LFE is perhaps somewhat questionable. To establish whether the LFE is likely to be real it was necessary to model the whole data set and ascertain whether a model which successfully fits the intermediate and high field regions also predicts the existence of a LFE.

The rest of this chapter is concerned with finding a model to fit the experimental data. This was less straightforward than expected and several models were tested.

5.4 Relaxation-Free Model

Following excitation of the flavin there are three sequential transfers along the Trp triad, Fig 5.3, resulting in a $\left[\text{FAD}^{\bullet-} \cdots \text{TrpH}^{\bullet+}\right]$ RP, Fig 5.4. In AtCRY and EcPL the ET is sufficiently fast to outstrip all intersystem crossing (ISC) in the flavin excited state and thus the RP is believed to be exclusively born in the singlet, S, state. At high field evolution $S \rightarrow T_+, T_-$ is energetically blocked and thus the yield of singlet product from a singlet starting state should increase. The yield from the non-singlet path is correspondingly decreased and a negative high-field effect is expected. The current data displays such a negative MFE, consistent with a singlet starting

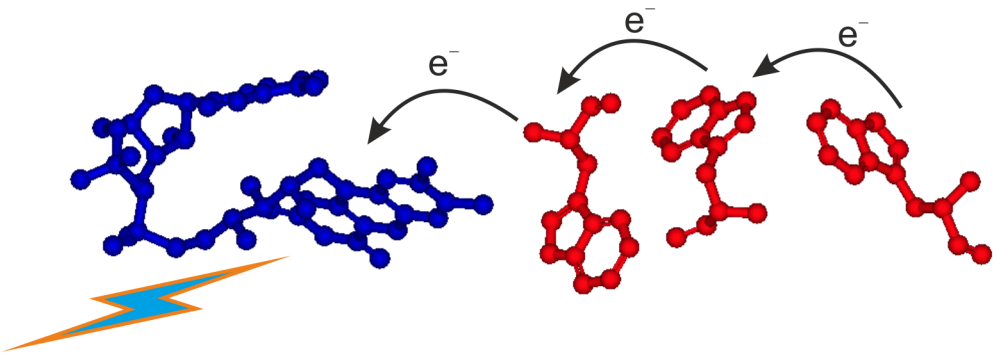

Figure 5.3. Step-wise electron transfer path to the FAD (blue) via three tryptophans (red) resulting in RP formation in EcPL and AtCRY.

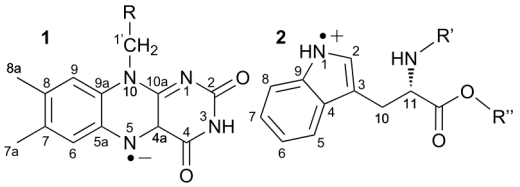

Figure 5.4. Chemical structures of **1** the flavin isoalloxazine radical anion and **2** a tryptophan radical cation.

state. In addition, in Ref [241] trEPR studies of the XlCRY could be successfully modelled only if the spin-correlated RP is born as a pure singlet state.

The exchange coupling between electrons for RPs on FAD and the first or second Trp is extremely strong [21], and hence coherent evolution can only begin once the second radical is located on the terminal Trp.

The singlet RP can undergo reverse ET along the chain or ET by some other path to return to the diamagnetic ground state. Irreversible proton transfer, protonation of $FAD^{\bullet -}$ or more likely the deprotonation of the $TrpH^{\bullet +}$, can occur from either spin state to form the non-magnetically sensitive secondary RP. This RP is not expected to show a MFE because it is too long lived and simply decays slowly to the ground state. The reaction mechanisms for AtCRY and EcPL are shown in Fig 5.5 along with the simplified scheme of reaction kinetics used in our model for both species.

Because of the need to include reaction kinetics more complicated than the usual exponential model, *i.e.* $k_S \neq k_{DP}$, it was necessary to carry out the simulations in Liouville space. To this end the theory developed in Chapter 2 and now found as part of the *Spinach* library was used. Theoretical Φ_{MFE} values were calculated using the theory outlined in Chapter 1 section 1.3 and Equation (1.37) was used to calculate the singlet yield. The yield of the secondary RP, RP_2, is

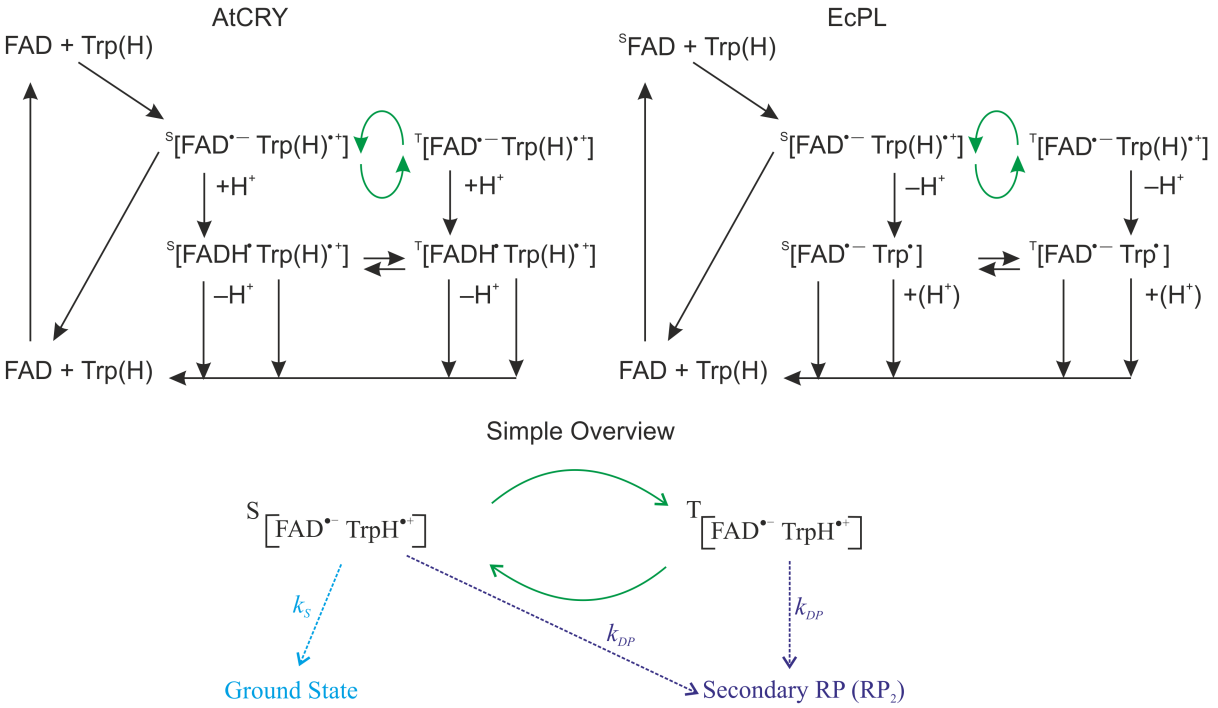

Figure 5.5. Reaction mechanism for AtCRY, EcPL and the simplified reaction kinetics sufficient for the simulation at hand. k_S and k_{DP} are the singlet recombination and (de)protonation rates respectively.

then given simply by:

$$\Phi_{RP_2} = 1 - \Phi_S \tag{5.2}$$

which is used in Equation (5.1) to calculate the Φ_{MFE}. Unless otherwise stated the reaction kinetics were treated with Haberkorn's master equation, Equation (1.59). Optimisation was carried out using a non-linear least squares fitting procedure.[1]

Kinetic Parameters

Spin-correlated RP lifetimes and maximum Φ_{MFE}, that is Φ_{MFE} at the high field asymptote, were measured for EcPL over a range of glycerol concentrations (which affects proton transfer rates [245] as well as viscosity) and an approximately linear trend can be seen between the two [225]. In order to see a substantial MFE it is necessary to have competitive rates of reaction along the different reaction paths. Slowing down the rate of formation of the secondary RP increases the MFE as the rate of return to the ground state from the singlet RP is generally predicted to be a rather slower process [229]. At $\Phi_{MFE} \approx 8\%$ (the high field Φ_{MFE} observed

[1]The routine 'lsqnonlin.m' from the 'Optimization Toolbox' for MATLAB 2010b, The Mathworks, Inc., Natick, MA, USA

under the conditions of the experiment modelled here) the lifetime, $\tau \approx 1/k \approx 4$ μs. This lifetime was extracted from Figure 4B of Ref [225] the current draft of which can be found in the appendix. Given the approximately equal solvent accessibilities of the terminal Trps in EcPL and AtCRY this provides a sensible estimate for the rate of non-spin-selective reaction and thus the value of k_{DP} was fixed at $k_{DP} = 2.5 \times 10^5$ s^{-1}. In the first case only the singlet reaction kinetic parameters, k_S was optimised, k_S was unbounded in the optimisation, though was expected to be similar to k_{DP} in order to provide suitable competition between the the two paths.

Hyperfine Interactions

Simulation of the full spin system of the $\left[\mathrm{FAD}^{\bullet-} \cdots \mathrm{TrpH}^{\bullet+}\right]$ RP is impossible on any current computer due to the enormous size of the full state-space. Even using the state-space restriction techniques of Chapter 2 (of which in this case only the zero-quantum coherence was applicable) it was only possible to include five nuclei in addition to the two electrons in the calculation.

The largest isotropic HFIs on each radical were included explicitly while the remaining HFIs were amalgamated into one effective isotropic HFI, $\tilde{a}$, per radical. An effective hyperfine interaction on a given radical is calculated according to:

$$\tilde{a} = \sqrt{\frac{4}{3}\sum_i a_i^2 I_i(I_i+1)} \tag{5.3}$$

As the radicals are most likely the same molecular species in both proteins the same HFIs are used in both simulations. The HFIs were taken from DFT calculations performed in Gaussian 03 (and listed in Ref [136]) which were in reasonably good agreement with experimentally determined values [197, 246]. The isotropic HFIs as used in the model simulations are listed in Table 5.1.

For preliminary fits fewer HFIs were included explicitly in order to accelerate the optimisation. If an initial fit was promising, the nuclei with the next largest HFI were added to the simulation. Including more HFIs individually improves the accuracy of the optimised parameters, and the fit at very low field, but does not change the overall quality of the model, *i.e.* if a model completely failed to reproduce the data including an additional HFI gave no discernible improvement. In simulations involving isotropic HFI, all HFI were accounted for in the simulation either via an effective HFI, $\tilde{a}$, or individually.

5.4.1 $B_{\frac{1}{2}}$

The empirical parameter $B_{\frac{1}{2}}$ is often used to relate HFI to the observed MFE. The $B_{\frac{1}{2}}$ value is equal to the magnetic field required to half-saturate the high field effect, that is, the field at which the MFE is half the difference between high field and zero field [247], as indicated on Fig 5.2. Defined in terms of effective HFI, Equation (5.3), $B_{\frac{1}{2}}$ is given by [247]:

$$B_{\frac{1}{2}} \approx \sqrt{3}\frac{\tilde{a}_A^2 + \tilde{a}_B^2}{\tilde{a}_A + \tilde{a}_B} \tag{5.4}$$

where A and B are the two radicals.

Calculations by Rodgers in Ref [136] sought to evaluate the accuracy of this expression for $B_{\frac{1}{2}}$. The results are summarised here for three limiting cases: When $k \ll \tilde{a}$, $B_{\frac{1}{2}}$ provides an upper bound to the true value, when $k \approx \tilde{a}$, $B_{\frac{1}{2}}$ shows good correlation with the true value and when $k \gg \tilde{a}$, $B_{\frac{1}{2}}$ is a dramatic underestimation.

From the estimation of k_{DP} for the two proteins it is clear they fall into the first category, we expect the calculated $B_{\frac{1}{2}}$ to provide an upper bound to the experimentally observed value (which can be estimated by extrapolation of the data to its limiting value). The calculated and experimental $B_{\frac{1}{2}}$ values are summarised in Table 5.2. Clearly the calculated $B_{\frac{1}{2}}$ values massively underestimate the actual value suggesting that some other process is occurring to broaden the MFE.

5.4.2 First Optimised Fit

Having examined the $B_{\frac{1}{2}}$ values it seems unlikely that the initial model proposed will successfully fit the data and indeed the 'optimised', fit, Fig 5.6, is extremely unsatisfactory. Clearly the gradient of the line of best fit is far too steep from HFI-driven coherent evolution processes only. Using this model it is possible to reproduce the absolute high field Φ_{MFE} but at the

Table 5.1. List of isotropic HFIs included in model simulations, numbering according to Fig 5.4. $\tilde{a}$ is the effective HFI calculated using Equation (5.3) from the remaining nuclei. (HFI were calculated, by Kuprov, using density functional theory in Gaussian 03 and using the UB3LYP/EPR-III level of theory and in the calculations R = R′ = R″ = H [136].)

Radical	**Spin**	**HFI / mT**
$FAD^{\bullet -}$	N5	0.5233
	$\tilde{a}$	1.1065
$TrpH^{\bullet +}$	H10	1.6046
	H1	−0.5983
	$\tilde{a}$	0.9157

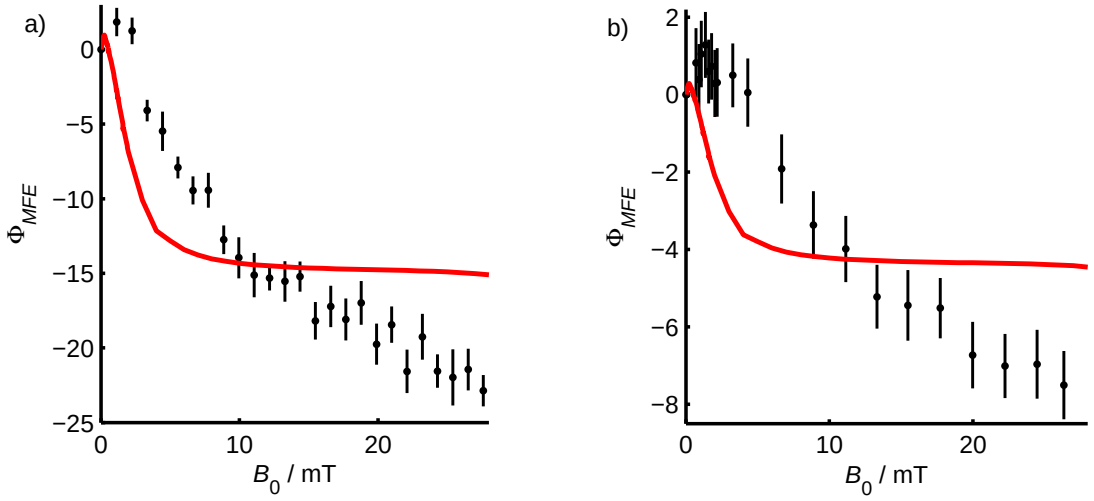

Figure 5.6. Optimised fit (red line) of the experimental Φ_{MFE} data using a relaxation-free model and with fixed $k_{DP} = 2.5 \times 10^5$ s^{-1} for a) AtCRY (optimised $k_S = 2.9 \times 10^5$ s^{-1}) and b) EcPL (optimised $k_S = 6.2 \times 10^4$ s^{-1}).

expense of all other data points. Some account must be taken of the broadening observed in the experimental data. The simplest possible cause is lifetime broadening due to rapid rates of reaction, inconsistent with the lifetimes derived from the optimisation, and which did not result in an improved fit anyway.

Investigations of MFEs in micellised RPs are usually described theoretically by the combination of HFI driven coherent evolution, reaction kinetics and relaxation processes. The lineshape of the MFE is determined by the interplay of these factors. Relaxation, from modulation of anisotropic HFI and singlet-triplet dephasing brought about by modulation of the exchange and dipolar coupling interactions, is always required for a successful fit [248, 249]. By analogy, relaxation processes are expected to bring about broadening of the MFE profile in the data of interest here though the bi-radical system under consideration is very different from the organic radicals of the micelle and it is questionable whether that the same type of relaxation process(es) will be dominant in both. The next section outlines the different models of relaxation tested for their fit against the AtCRY and EcPL MFE data.

Table 5.2 Calculated, using Equation (5.4), and experimentally determined, from Fig 5.2, $B_{\frac{1}{2}}$ values.

	AtCRY	**EcPL**
Calculated	3 mT	3 mT
Experimental	$\approx$ 9 mT	$\approx$ 11 mT

5.5 Models for Relaxation

To include relaxation in the model an extra relaxation superoperator, $\hat{\hat{R}}$ is added to Liouville-von Neumann equation so altogether we must solve:

$$\frac{\mathrm{d}\hat{\rho}}{\mathrm{d}t} = \left(-\mathrm{i}\hat{\hat{H}}(t) + \hat{\hat{R}} + \hat{\hat{K}}\right)\hat{\rho}(t) \tag{5.5}$$

as described in Chapters 1 and 2.

5.5.1 Failed Models

Considering the system at hand, proteins tumbling in solution, rotational modulation of anisotropic interactions seems most likely to be the dominant relaxation mechanism. At the low fields of interest here any anisotropy in the Zeeman interaction is unlikely to be significant. Similarly the separation between electrons on the FAD and terminal Trp renders the dipolar and exchange couplings extremely small [21] and rotational modulation thereof will probably bring about a negligible effect on the MFE. There remains only the anisotropic HFIs, comparable in size with the low fields of this investigation, which cannot be neglected. Redfield theory was used to account for rotational modulation of the anisotropic HFIs through isotropic rotational diffusion. The general theory for forming the Redfield theory relaxation superoperator was described in Chapter 2 and the numerical integration method, implemented in the *Spinach* library, was used for these simulations [109].

Table 5.3. Hyperfine interactions for the $FAD^{\bullet-}$ radical anion and $TrpH^{\bullet+}$ radical cation included in the optimisations requiring anisotropic interactions. HFI were calculated, by Kuprov, using density functional theory in Gaussian 03 and using the UB3LYP/EPR-III level of theory. Numbering is as shown in Fig 5.4 and in the calculations $R_1 = R_2 = R_3 = H$ [136].

Radical	**Spin**	**HFI / μT**	**HFI principal axes**
$FAD^{\bullet-}$	N5	$\begin{pmatrix} -100.1 & 0 & 0 \\ 0 & -86.8 & 0 \\ 0 & 0 & 1756.9 \end{pmatrix}$	$\begin{pmatrix} 0.9518 & -0.3068 & 0 \\ 0.3068 & 0.9518 & 0 \\ 0 & 0 & 1 \end{pmatrix}$
	H8a	$\begin{pmatrix} 610.6 & 0 & 0 \\ 0 & 612.5 & 0 \\ 0 & 0 & 724.8 \end{pmatrix}$	$\begin{pmatrix} 0.6882 & 0.05170 & 0.7237 \\ 0.6968 & -0.3254 & -0.6393 \\ 0.2024 & 0.9442 & -0.2600 \end{pmatrix}$
$TrpH^{\bullet+}$	H1	$\begin{pmatrix} -1082.6 & 0 & 0 \\ 0 & -705.4 & 0 \\ 0 & 0 & -6.9 \end{pmatrix}$	$\begin{pmatrix} 0.7540 & 0.6139 & -0.2336 \\ 0.2344 & 0.0808 & 0.9688 \\ -0.6136 & 0.7852 & 0.0830 \end{pmatrix}$

The preliminary optimisation was carried out with just the three anisotropic HFIs listed in Table 5.3, chosen to maximise both the anisotropy of the coupling tensors and their isotropic coupling strength. The second largest isotropic HFI was included on the $TrpH^{\bullet+}$ as nucleus H10, which has by far the largest isotropic HFI, has relatively little anisotropy to its tensor. The second HFI on the $FAD^{\bullet-}$ radical is a methyl proton and so might be expected to be averaged out through methyl rotations, however it has the second largest calculated isotropic HFI and was therefore included. As there are many significant HFI on both radicals selection of any three is always going to be an approximation, particularly as there is no anisotropic equivalent to the effective hyperfine interaction and correspondingly the $B_{\frac{1}{2}}$ for these simulations was even smaller than in the relaxation-free case. This might have been expected to result in a moderate over-estimation of the relaxation rate. However, the optimised fit using this model, allowing k_S and τ_c (the rotational correlation time) to vary, gave no improvement whatsoever compared to the relaxation-free model. Manual manipulation of the parameters could achieve a fit of the absolute high field Φ_{MFE} but at the expense of the intermediate field slope. Increasing the rate of relaxation broadens the Φ_{MFE} curve only by diminishing the absolute intensity, this is in agreement with Ref [250] which found that HFI-induced relaxation has little effect on MFE lineshape.

Although Redfield theory is expected to give a reasonable estimate of relaxation behaviour beyond its strictly defined regions of applicability [93], it is useful to estimate the rotational correlation time, τ_c, expected of the protein. This is done using the Stokes-Einstein equation [69]:

$$\tau_c = \frac{4\pi r_0^3 \eta}{3k_B T} \tag{5.6}$$

to estimate τ_c for the proteins. Using r_0, the protein radius, as approximately 2 nm and the viscosity, $\eta \approx 0.72$ Pa s (estimated as a weighted average of the viscosities over water and glycerol) gives $\tau_C \approx 7$ μs, certainly not within the traditional limit of Redfield applicability. However whether Redfield theory is strictly applicable or not does not seem important given the poor quality of the resulting fits – it is simply not the right model.

Many other methods for including relaxation have been used in the literature and were tested as models to fit these data. The failed relaxation models, that is, those that failed to offer any improvement compared to the relaxation-free model, are summarised in Table 5.4. In addition to relaxation, and considering the long rotational correlation time predicted, residual anisotropy

contributions were also considered as a possible cause of line broadening. The possibility of some RPs starting in a (non-polarised) triplet state was also looked at. These too failed to reproduce the shallow gradient at intermediate fields and the absolute value of the HFE.

Table 5.4. Overview of all the relaxation models that did not succeed in fitting the data acceptably. The description summarises the basic characteristics of the given model together with some details as to why it failed to reproduce the data.

Model	**Description**
Redfield [109]	Rotational modulation of anisotropic HFI through isotropic molecular tumbling.
Phenomenological exponential relaxation [61]	Traditional high, and zero, field approximations lead to exponential terms with time constants, T_0 at zero-field and T_1 and T_2 high-field. Constant and field dependent T_0, T_1 and T_2 values were trialled but failed to fit the slope at intermediate field strengths.
Lindblad master equation [87]	Simulates random field effects along the *x, y* and *z* axes. The axes can be defined in any arbitrary frame and both the laboratory frame and a highly artificial spin-system eigenframe were used. Both failed to fit the experimental data.
Anisotropic contributions	Arises from random orientation of RPs over the ensemble of proteins and slow tumbling which fails to average the anisotropic HFIs to leave purely isotropic contributions. Some, though insufficient, broadening of the Φ_{MFE} appeared in the predicted curve when a spherical average is taken over a range of RP orientations. Using weighted combinations of anisotropic and isotropic contributions also failed to fit the data.
Mixture of singlet and triplet starting states	No broadening at all, just changes in absolute Φ_{MFE}.
The Jones-Hore kinetic superoperator [79]	This operator is expected to show twice the dephasing of the Haberkorn model, but could not fit this data any better than the traditional kinetic model. It is perhaps interesting to note that if k_{DP} is not limited to 2.5×10^5 s^{-1} the Jones-Hore model can fit the data whereas Haberkorn cannot, but only when k_{DP} is very large.
Combinations of the above	Using various combinations of the above models did not fare any better.

5.5.2 Singlet-Triplet Dephasing

Having exhausted the usual, and less usual, relaxation mechanisms for intramolecular RPs without success it was necessary to consider alternative models. For small radicals in solution and in micelles singlet-triplet dephasing (ST-dephasing) is well known as an important contributor to relaxation [251].

The electronic eigenstates of a RP under the influence of a large exchange coupling are the singlet and triplets. If a RP remains in such an environment then no interconversion can occur. If, however, the radicals diffuse apart and J, the exchange coupling parameter, becomes smaller, population interconversion will occur and coherences (or phase) between the singlet and triplet states will develop. When the radicals diffuse close together again J increases and each RP must collapse into either the singlet or one of the triplet states. Across the whole ensemble the proportion in each will depend on the populations and coherences just prior to J being 'switched on'. Having diffused together the RP can either react, selectively down the singlet channel, or separate again. When the radicals separate again, and J has been effectively switched off, there will be no coherences remaining between the singlet and triplet states and so the RP begins its evolution again from either a pure singlet or pure triplet starting state. The re-encounter has acted as a strong dephasing event.

More generally any process which brings about strong modulation of the J coupling strength will cause dephasing. This is described by the phenomenological operator [251]:

$$\hat{\hat{R}} = -k_{ST}\Omega^{T}\left\{\sum_{i=+,0,-}\left(|ST_i\rangle\langle ST_i| + |T_iS\rangle\langle T_iS|\right)\right\}\Omega \tag{5.7}$$

where Ω transforms the operator from the ST basis into a convenient basis for calculation (in this case into the IST (irreducible spherical tensor) basis used in *Spinach*), and k_{ST} is the dephasing rate.

5.5.3 Optimised Fit

Despite the RP in AtCRY and EcPL being intramolecular, and at a separation such that exchange coupling is approximately negligible, and with no possibility, short of massive protein structural change, of the RPs diffusing relative to each other, the ST-dephasing model was evaluated. The dephasing rate constant, k_{ST}, was optimised without any bounds. The results of the optimisation, with data points weighted according to the standard deviation, are given in

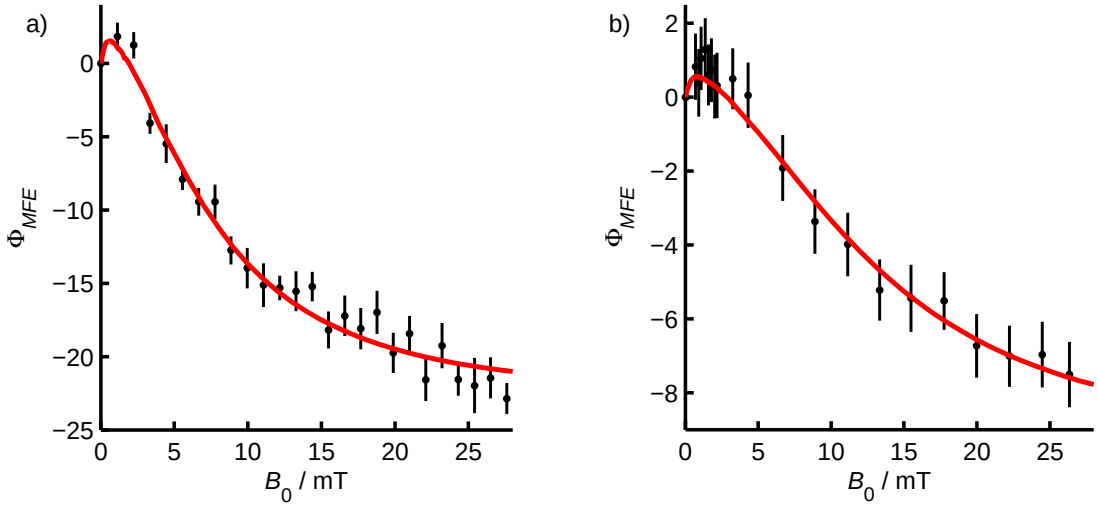

Figure 5.7. Optimised fit (red line) of the experimental Φ_{MFE} data using a ST-dephasing model, with $k_{DP} = 2.5 \times 10^5$ s^{-1} fixed, for a) AtCRY, ($k_S = 4.8 \times 10^5$ s^{-1}, $k_{ST} = 1.2 \times 10^7$ s^{-1}) and b) EcPL ($k_S = 1.3 \times 10^5$ s^{-1}, $k_{ST} = 3.1 \times 10^7$ s^{-1}).

Fig 5.7. Clearly the fit is much improved in comparison with previous models: The gradient of the intermediate fields is matched, the absolute HFE reproduced, and the LFE predicted. The optimised parameters from these fits are given in Table 5.5.

5.5.4 Speculation About Reverse Electron Transfers

Most physical models for the kind of ST-dephasing required to fit the experimental data are based on radical pairs which diffuse relative to each other, varying the distance between them and hence modulating the exchange coupling. A large enough displacement is not possible for the intramolecular RP of EcPL or AtCRY.

What may be possible, however, is reverse electron transfer along the Trp-triad such that occasionally the RP exists on the middle (Trp_2) rather than the terminal (Trp_3) tryptophan, Fig 5.8. This seems feasible as reverse electron transfer along the triad has been suggested as the mechanism by which singlet recombination occurs.

Calculations in Ref [21] estimate the exchange coupling to be negligible between electrons on FAD and Trp_3 but 100-1000 mT when the second radical is located on Trp_2. The latter

Table 5.5 Optimised parameters from ST-dephasing model. k_{DP} was fixed at $2.5{\times}10^5$ s^{-1}.

	AtCRY	**EcPL**
k_S	4.8×10^5 s^{-1}	1.3×10^5 s^{-1}
k_{DP}	2.5×10^5 s^{-1}	2.5×10^5 s^{-1}
k_{ST}	1.2×10^7 s^{-1}	3.1×10^7 s^{-1}

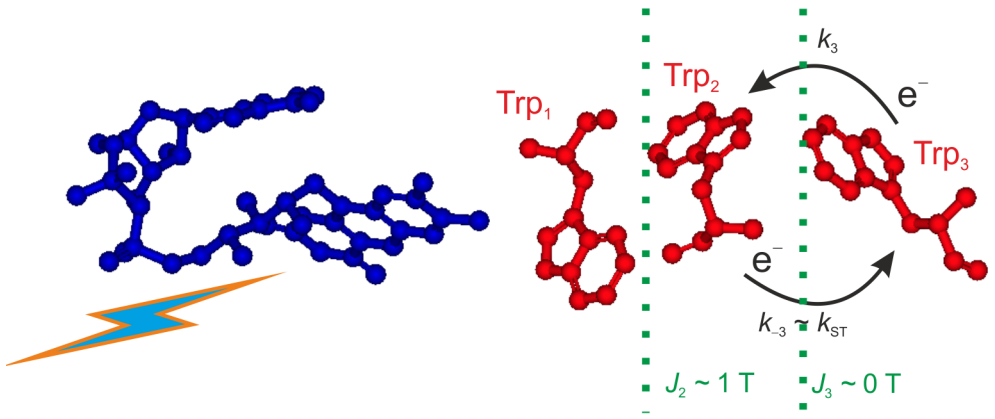

Figure 5.8. Proposed electron transfers, during RP evolution, to account for strong singlet-triplet dephasing, k_3 and k_{-3} are the rate constants for ET to and from Trp_2 respectively.

interaction is at least fifty times larger than the largest HFI and five times larger than the largest applied field. A FAD$\cdots$Trp$_2$ RP will be almost instantly collapsed into a singlet or triplet state and prevented from further evolution until a forward electron transfer takes it back to Trp$_3$. As the ET from Trp$_2$ to Trp$_3$, k_{-3}, is expected to be much slower than from Trp$_3$ to Trp$_2$, k_3 [252], and J when the second electron is located on Trp$_2$ is enormous, the rate of dephasing will be approximately equal to the rate of reverse ET, *i.e.* $k_{ST} \approx k_{-3}$. A calculation performed on EcPL in Ref [253] estimates $k_{-3} \approx 3 \times 10^7$ s^{-1} which is in excellent agreement with the optimised parameter, $k_{ST} = 3.1 \times 10^7$ s^{-1}, Table 5.5, derived from fitting the MFE data.

5.6 Anisotropic Contributions and S-T Dephasing

Although including anisotropic contributions alone could not fit the experimental MFE data, the rotational correlation time, τ_C, estimated from Equation (5.6), is of the same order of magnitude as the lifetime of the RP. It seems unlikely therefore that the anisotropic interactions are completely quenched by isotropic tumbling. Thus the fitting was repeated including a spherical average across the anisotropic yield as well as including ST-dephasing.

The optimisation used the average Φ_{MFE} over an ensemble of thirty molecular frame orientations. Only three HFI were included in this calculation due to time constraints – the inclusion of anisotropic terms invalidates the zero-quantum coherence screening so that almost the entire state-space must be used for such calculations. The anisotropic HFI tensors were taken from DFT calculations [136]. The same HFIs were included in this simulation as were used for the Redfield theory relaxation model and are given in Table 5.3. As aforementioned there is no

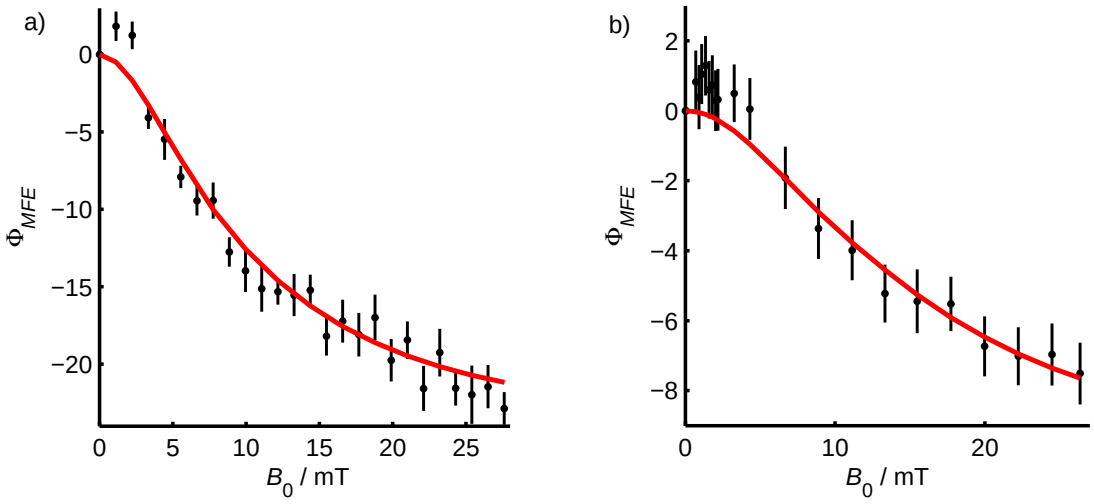

Figure 5.9. Including a spherical average over anisotropic contributions and ST-dephasing giving the optimised fit (red line) of the experimental Φ_{MFE} data. Spin-unselective rate constant fixed, $k_{DP} = 2.5\times10^5$ s^{-1}. a) AtCRY ($k_S = 4.6\times10^5$ s^{-1}, $k_{ST} = 4.4\times10^7$ s^{-1}) and b) EcPL ($k_S = 9.1\times10^4$ s^{-1}, $k_{ST} = 4.0\times10^7$ s^{-1}). The spherical average was taken for combinations of cosθ is 0 to 1 in steps of 0.1 and ϕ equal to 0 to $2\pi - \frac{2\pi}{5}$ in steps of $\frac{2\pi}{5}$.

equivalent to the effective isotropic HFI for anisotropic interactions and so the model used in this simulation does not have a $B_{\frac{1}{2}}$ consistent with the real RP. The optimised parameters, while likely to be in the right area, will not be precise.

The results of the optimisation with this model are given in Fig 5.9. The shallow slope at intermediate field strengths and the absolute value of the HFE are well reproduced. The LFE is not predicted by this model.

Given the similarity between $\tau_C \approx 7\mu s$ and $\tau_L = \frac{1}{k_{DP}} \approx 5\mu s$ it seems plausible that there are contributions from both isotropically averaged molecular interactions and from residual anisotropy. Slight variations to the composition or temperature of the sample will cause changes to the correlation time and hence might affect the interplay of isotropic and anisotropy contributions to the Φ_{MFE}. This might in some part explain the large variation in Φ_{MFE} particularly at low field. It may be possible to enhance the size of the LFE by decreasing τ_C, either by decreasing glycerol content or increasing temperature, but of course in complex systems changing the conditions rarely affects just a single factor.

5.7 Impact of S-T Dephasing on Anisotropic Yield

The AtCRY protein (*Arabidopsis thaliana* is a plant) is investigated as it is a close relative of the suggested chemical compass molecules of animal orientation, for example there is a strong

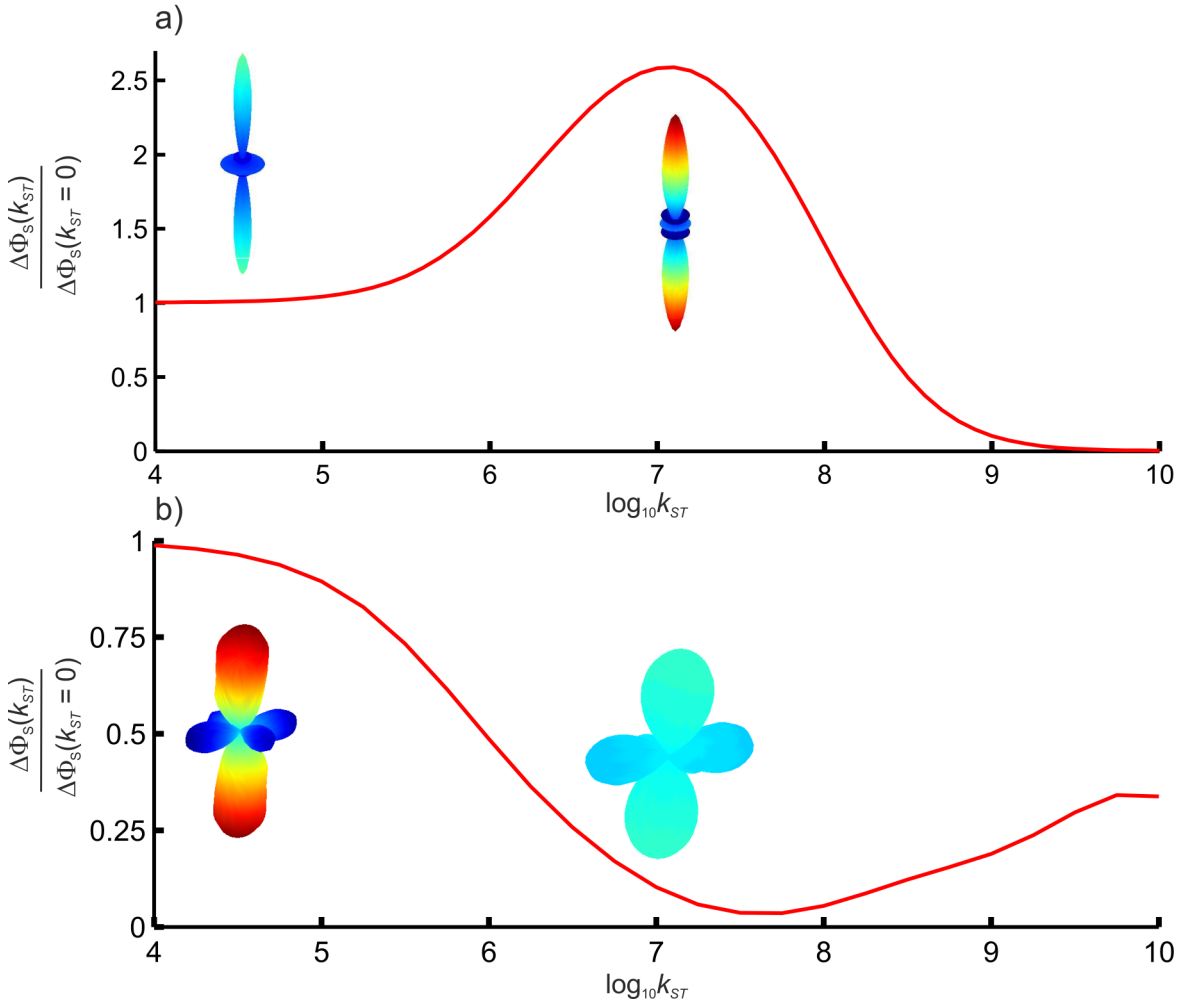

Figure 5.10. Ratio of maximum singlet yield difference, $\Delta\Phi_S$, as a function of ST-dephasing rate. The polar plots are coloured according to singlet yield relative to the spherical average, blue and red indicate $\Phi_S(\theta, \phi)$ less than and greater than the average respectively. Plots within a sub-figure are referenced to the same colour scale for easier comparison. a) A one nucleus RP, $Ax = -0.02$ mT, $k_S = k_{DP} = 2 \times 10^5$ s^{-1} and $B_0 = 50$ μT. Plots show the anisotropic yield at $k_{ST} = 0$ s^{-1} and at $k_{ST} \approx 10^7$ s^{-1} and b) The $FAD^{\bullet -} \cdots TrpH^{\bullet +}$ RP, $k_S = 4.8 \times 10^5$ s^{-1}, $k_{DP} = 2.5 \times 10^5$ s^{-1} and $B_0 = 50$ μT. Polar plots are for $k_{ST} = 0$ s^{-1} and at $k_{ST} = 1 \times 10^7$ s^{-1}

sequence homology between AtCRY and gwCRY (garden warbler – *Sylvia borin*) [232]. To be effective in the role of chemical compass the RP reaction must have a yield which varies with magnetic field direction. Having suggested a specific form of relaxation, which will occur even if the RP is at a fixed orientation, as necessary to explain the isotropic Φ_{MFE} data it seems sensible to examine briefly the effect this type of dephasing has on anisotropic reaction yields.

The singlet yield difference, $\Delta\Phi_S$ is defined as:

$$\Delta\Phi_S = \max\Phi_S(\theta, \phi) - \min\Phi_S(\theta, \phi) \tag{5.8}$$

where $\Phi_S(\theta, \phi)$ is the singlet yield calculated as a function of the spherical coordinates, θ and

ϕ defined by θ is zero to π in steps of $\frac{\pi}{40}$ and ϕ is zero to 2π in steps of $\frac{2\pi}{40}$. The effect of ST-dephasing on anisotropy is quantified by taking the ratio of $\Delta\Phi_S$ with and without ST-dephasing *i.e.* for systems with non-zero k_{ST} compared to the non-dephased reference.

In the simplest case we consider a one-nucleus radical pair with axial symmetry, Fig 5.10a. For this RP system ST-dephasing can increase the directionality of the yield. In general the yield anisotropy is due to the different extents of S-T mixing occurring at different orientations. It is likely that reaction yields from orientations for which spin state evolution is much more rapid than the dephasing rate will be only weakly affected by this form of relaxation. However, if S-T mixing occurs slower than the dephasing rate then the spin-state evolution will be effectively blocked by almost instantaneous dephasing of S-T coherences as soon as they appear. Thus some orientations may be much more strongly affected by the dephasing relaxation than others and this may possibly provide an explanation for the rather surprising enhancement in yield anisotropy observed in Fig 5.10. As the ST-dephasing rate constant is increased it will overtake the evolution rate at all angles, and thus anisotropy would be expected to decrease again. This indeed appears to be the case as increasing the dephasing rate beyond the optimum leads to an angle-independent singlet yield tending to 50%.

To see if there can be the same enhancement of directional response from larger spin systems, similar calculations were performed for a simplified AtCRY system using the HFIs of Table 5.6. In this case we are seeking to maximise the directional response and hence the two nitrogens from the $FAD^{\bullet-}$ that are coaxial and strongly anisotropic were chosen for this simulation, along

Table 5.6. Hyperfine interactions for the $FAD^{\bullet-}$ radical anion and $TrpH^{\bullet+}$ radical cation included in the investigation of the effect of ST-dephasing on singlet yield anisotropy. HFI were calculated, by Kuprov, using density functional theory in Gaussian 03 and using the UB3LYP/EPR-III level of theory. Numbering is as shown in Fig 5.4 and in the calculations $R_1 = R_2 = R_3 = H$ [136]. The nuclei were chosen to maximise axiality and thus the expected anisotropy of the yield.

Radical	**Spin**	**HFI / μT**	**HFI principal axes**
$FAD^{\bullet-}$	N5	$\begin{pmatrix} -100.1 & 0 & 0 \\ 0 & -86.8 & 0 \\ 0 & 0 & 1756.9 \end{pmatrix}$	$\begin{pmatrix} 0.9518 & -0.3068 & 0 \\ 0.3068 & 0.9518 & 0 \\ 0 & 0 & 1 \end{pmatrix}$
	N10	$\begin{pmatrix} -24.1 & 0 & 0 \\ 0 & -14.4 & 0 \\ 0 & 0 & 604.6 \end{pmatrix}$	$\begin{pmatrix} 0.6845 & 0.7291 & 0 \\ 0.7291 & -0.6845 & 0 \\ 0 & 0 & 1 \end{pmatrix}$
$TrpH^{\bullet+}$	H1	$\begin{pmatrix} -1082.6 & 0 & 0 \\ 0 & -705.4 & 0 \\ 0 & 0 & -6.9 \end{pmatrix}$	$\begin{pmatrix} 0.7540 & 0.6139 & -0.2336 \\ 0.2344 & 0.0808 & 0.9688 \\ -0.6136 & 0.7852 & 0.0830 \end{pmatrix}$

with H1 from $TrpH^{\bullet+}$. The optimised reaction parameters of Table 5.5 were used. Again k_{ST} was varied and the results are shown in Fig 5.10b). In this system it does not appear that k_{ST} can enhance the anisotropy of the yield and unfortunately, in the region of the optimised k_{ST} parameter the anisotropy of the yield is much lower than the maximum. However, this is true of a simplified system and it is not clear how including more nuclei would affect the interplay of k_{ST} and angle dependence. It is at least possible that this type of relaxation may allow for optimisation of the directional response from the RP reaction and there are certainly many reasons why k_{ST} in a magnetoreceptor *in vivo* might differ from that of a plant cryptochrome *in vitro*.

5.8 Conclusion

The effect of magnetic fields on the reaction yields of AtCRY and EcPL radical pair reactions has been successfully modelled. Initial analyses demonstrated that the shallow slope of the data was far too great to originate from coherent interactions alone and it was necessary to model the system relaxation. Several models were trialled for this purpose and failed to even remotely reproduce the data. The only relaxation model which could satisfactorily replicate the low field effect, shallow gradient at intermediate fields and absolute high field effect was singlet-triplet dephasing.

We sought, by modelling the data, to establish whether the observed LFE is truly predicted by a reasonable model. The ST-dephasing model of relaxation not only fits well with the intermediate and high-field data but also predicts a LFE. The existence of such a sensitivity to weak fields under isotropic conditions *in vitro* gives some support for the hypothesis that an optimised *in vivo* magnetoreceptor would be sensitive to fields of ≈ 50 μT.

ST-dephasing occurs when a strong exchange coupling is modulated, normally through radical diffusion. In the case of the fairly rigid bi-radicals of interest here such motion is not possible. Instead we propose a reverse electron transfer from the middle Trp of the triad to the terminal one such that for short periods of time (forward ET is expected to occur in < 30 ps [254]) the RP exists between the $FAD^{\bullet-}$ and second Trp with an exchange coupling of $\approx 100 - 1000$ mT. Such a large change in J on ET would account for the strong ST-dephasing required to fit the data, and the optimised rate constant for this process is in good agreement with literature values for the back ET.

The proposed mechanism is however still very speculative and should of course be tested

against new experimental results in the future. The nuclei with small HFI have greatest effect on the low field data and ideally to investigate this region better more nuclei should be included in the simulation this of course will require greater computer memory capability. Further simulations to investigate the effects of ST-dephasing on anisotropic yields to serve as predictors/fitting models for anisotropic experiments should consider the possible involvement of this particular type of relaxation.

It might be interesting to carry out simulations to study how ST-dephasing enhances or reduces the directionality of the singlet yield. We have suggested that this may be due to different effects of competition between spin-state evolution rate and dephasing rate across the different orientations but thus far only a RP with one axial HFI and the complicated three-spin $FAD^{\bullet -} \cdots TrpH^{\bullet +}$ RP have been studied. A more systematic study of different spin systems is necessary in order to identify the root of this effect and hence, perhaps, to establish whether ST-dephasing could be considered an additional optimisation mechanism within the biological chemical compass, *i.e.* whether reversible back ET at a optimised rate might hold an evolutionary advantage.

Note Following submission of this thesis Henbest and Maeda reanalysed the data fitted in this chapter which resulted in small changes to the absolute values of MFE and the error bars. New optimisations were carried out for publication in [225] which returned values very similar to those reported in this chapter. For this work the field off value was set to 0 mT for convenience. No significant changes to the interpretation of the data or fitting arose from this work. The current draft of this manuscript, prior to submission to *Proc. Natl. Acad. Sci. USA*, is included as an Appendix for completeness.

Chapter 6

Magnetite-Amplified Directional Response of Magnetically Sensitive Radical Pair Reactions

6.1 Introduction

One of the most enigmatic problems in sensory biology is understanding the biophysical mechanism by which animals sense the Earth's magnetic field. As was introduced in Chapter 4, behavioural evidence suggests that there are two distinct systems at work. One uses an intensity map for local navigation and the other is compass-like giving absolute directional information [138].

The mechanism underlying the magnetoreception systems remains unknown, though there are two prevailing proposals which have attracted much attention; a physical mechanism built upon biogenic magnetite particles [50, 155] and a light-dependent magnetically sensitive radical pair (RP) reaction, *e.g* [15, 37, 51, 158]. Within the former theory several subtly different mechanisms have been put forward (for a comprehensive review see Ref [168]) and the latter has been discussed in depth in previous chapters. In this chapter we consider the possibility of combining the two to allow for an amplified directional response from a RP reaction due to the magnetic field of a nearby magnetite particle.

6.1.1 Field-Gradient Enhanced Coherent Evolution

It is known that the field in the vicinity of a magnetite nanoparticle (MNP) can be much larger than the $\approx 50\ \mu$T of the Earth and that the field strength falls off rapidly with increasing distance ($B \propto \frac{1}{r^3}$). It was suggested in Ref [255] that the strong field gradients around the MNPs may affect RP spin-state dynamics. If two radicals of a pair are at different distances from the MNP surface they will experience very different magnetic fields bringing about evolution between the singlet and triplet states, called the ΔB-mechanism. It was proposed that from a RP in an initial singlet state the ΔB-mechanism would enhance the coherent singlet-triplet evolution, decreasing the singlet yield and hence increasing the yield of free radicals in the wrong spin-state for recombination. Radicals are known to cause damage to DNA and this was therefore suggested as a possible mechanism by which magnetic fields may be carcinogenic. Ref [255] also discussed the effects of oscillating magnetic fields on the dynamics of superparamagnetic (SPM) particles but this is not relevant to this chapter and is not considered further.

It was reported by Chalkias *et al.* that the presence of stable single domain (SSD) MNPs in a horseradish peroxidase (HRP) enzyme assay causes a 30-fold increase in the rate of reaction [256]. HRP is known to have paramagnetic intermediates and it was suggested that the fields arising from the MNPs affects singlet-triplet interconversion of the RPs and thus alters the overall enzyme kinetics. Larger magnetite particles showed a stronger effect and superparamagnetic particles, which have a fluctuating magnetic moment, resulted in no discernible change in reaction rate.

In Ref [257] it was predicted theoretically that solutions of MNPs will accelerate singlet-triplet interconversion in RPs randomly orientated on their surface due to the strong field gradients very close to the particle. The authors went on to deposit patterns of MNPs on a surface which was then submerged in a solution of pyrene/DMA. In the vicinity of the MNPs there is enhanced ISC and thus a different proportion of singlet and triplet spin states which is manifest as a change in the exciplex fluorescence intensity. The spatially resolved differences in fluorescence mark out the positions of the MNP pattern [258].

The aforementioned systems are promising for heterogeneous catalysis but will not show a directional response as the RPs are either attached to the MNP surface and hence move with the MNP when it rotates under the influence of the applied field or are randomly orientated around the MNP such that any anisotropic response will be averaged out across the ensemble. While the work of this chapter was underway Cai approached the possibility of using the field gradients

from MNPs to enhance an anisotropic RP reaction yield [259]. If the field from the MNP is large on radical A and negligible on radical B then there is enhanced spin-state evolution from the ΔB-mechanism. In addition, if radical A is at a fixed orientation relative to the MNP, *i.e.* there is not an ensemble of RPs across all relative orientations, then rotating the weak Earth-strength static field relative to the strong MNP field will bring about an anisotropic reaction yield, even in the absence of anisotropic hyperfine interactions (HFIs), due to the relative orientation of the resultant static fields on the two radicals.

Here we seek a similar outcome, the enhancement of the directional response of a RP reaction yield using the field from a MNP. However instead of assuming a fixed MNP moment we consider a MNP that itself responds to the applied field and rotates so that its magnetic moment and the field are aligned. We also consider RPs at some significant distance from the MNP, where the field gradient is rather small. As the MNP moment behaves like a point dipole the total field strength experienced by a RP will depend on the relative orientation between the RP and MNP. Directional information, as required by a chemical compass, can then be derived from the isotropic magnetic field effect (MFE). This is an attractive prospect as it avoids the requirement for a RP to be rotationally ordered, and may give larger yield anisotropies than can be derived from anisotropic HFIs.

6.2 Magnetite

Magnetite, Fe_3O_4, has an inverse spinel structure with overall cubic symmetry and antiferromagnetically coupled Fe^{3+} ions occupy octahedral and tetrahedral vacancies such that their moments cancel out. There remain Fe^{2+} ions in the rest of the octahedral sites with their moments parallel, resulting in a permanent magnetic moment [260]. This is ferrimagnetism. Magnetite has a saturation magnetisation of $M_S = 4.8 \times 10^5$ Am^{-1} [255], and the net magnetic moment, assuming uniform magnetisation, is given by [261]:

$$\mu_{sat} = M_S V \tag{6.1}$$

where V is the volume of the particle.

A region of uniform magnetisation, called a domain, instantaneously has net North and South poles. As the domain size increases so does the strength of the magnetic moment. The cost of a domain wall, that is a region in which the individual moments are antiparallel, is outweighed

by the favourable interaction of having the North and South poles of two domains adjacent. Thus, magnetite particles above a critical volume ($r \approx 100$ nm for a spherical particle) become multi-domain and have no net magnetic moment [261]. These are of no use for our purposes.

6.2.1 Single Domain Nanoparticles

Single domain particles are fully magnetised at any instant with the magnetisation along an 'easy-axis' of the particle. In an isotropic solution, *i.e.* with no external stresses, the direction of the easy-axis is determined by the crystal symmetry, particle shape and applied field anisotropies. All of these contributions depend linearly on particle volume. In most cases there is more than one easy axis, in which case the magnetisation flips between axes at a rate determined, in an Arrhenius-style, by the energy barrier, E_A. The timescale of this process, the Néel time, τ_N, is given by [262]:

$$\tau_N = \tau_0 \exp\left\{\frac{E_A}{\zeta k_{\mathrm{B}} T}\right\} \tag{6.2}$$

Where ζ is a statistical factor arising from the number of equivalent paths on the energy surface to different easy-axes and $\tau_0 \approx 10^{-9}$ s, is the attempt time of magnetite [262]. Particles for which τ_N is less than the timescale of observation (≈ 1 μs for magnetically sensitive RPs) have a magnetisation which appears to average to zero over time and are called superparamagnetic. The name arises because an ensemble of such particles will respond strongly to an applied field. The average magnetic moment, μ, across an ensemble of superparamagnetic particles, for example characterising a ferrofluid, or for a single superparamagnetic particle over time, is described by the Langevin equation [255]:

$$\mu = \mu_{sat}\left(\coth\left(\frac{\mu_{sat} B_0}{k_{\mathrm{B}} T}\right) - \frac{k_{\mathrm{B}} T}{\mu_{sat} B_0}\right) \tag{6.3}$$

B_0 is the applied field and μ_{sat} is the magnetic moment for a particle of volume V, Equation (6.1). However, the system of interest here does not involve RPs associated with an ensemble of MNPs. We are interested instead in the net field of individual MNPs responding to an applied field, so this treatment is of no further use and we must turn our attention to individual particle dynamics.

Both SPM (superparamagnetic) and SSD (stable single domain) particles might be expected to respond to an applied field in such a way that their magnetisation becomes aligned with B_0.

That is, the applied field forces a transition SPM → SSD by removing the degeneracy of the easy-axes in the first instance and causes a physical rotation of the particle in the second. The magnitude of the interaction of a magnetic moment with an applied field at an angle θ is given by [26]:

$$E = -\mu B_0 \cos\theta = -M_S V B_0 \cos\theta \tag{6.4}$$

Hence both of the effects depend not only on the magnitude of the applied field but also on the total volume of the particle which is crucial in defining SPM/SSD behaviour. It is important to understand the nature of a suitable MNP and we therefore consider the factors which determine the size of the energy barrier between easy axes and hence the SPM *vs.* SSD character.

Crystal Anisotropy

The crystal anisotropy affects the easy axes due to the intrinsic symmetry of the crystal structure. For a cubic system such as magnetite the energy as a function of polar angles, θ and ϕ, is given by [261]:

$$E = K_1 V \left(\frac{1}{4}\sin^2\theta \sin^2 2\phi + \cos^2\theta\right) \sin^2\theta + \frac{K_2 V}{16}\left(\sin^2 2\phi \sin^2 2\theta \sin^2\theta\right) \tag{6.5}$$

where K_1 and K_2 are constants and for magnetite have the values -1.3×10^4 Jm^{-3} and -4×10^3 Jm^{-3} respectively [262]. This gives eight equivalent easy-axes, with each one linked via a low energy barrier to three others, Fig 6.1a) [155].

Shape Anisotropy

A single-domain particle has a North and a South pole which have a magnetic field between them opposite in direction to the underlying magnetisation which brings about their existence. Shape anisotropy arises because the extent of 'demagnetisation' depends on the separation of the North and South poles in the particle. Therefore, if a MNP is non-spherical the magnitude of demagnetisation depends on orientation, *i.e.* the relative orientation of the magnetic moment and the particle long-axis. This effect is well documented in the literature for ellipsoid particles [263], in which the energy is given by [261]:

$$E = \frac{1}{2}\left(D_X - D_Z\right) M_S^2 V \mu_0 \sin^2\theta \tag{6.6}$$

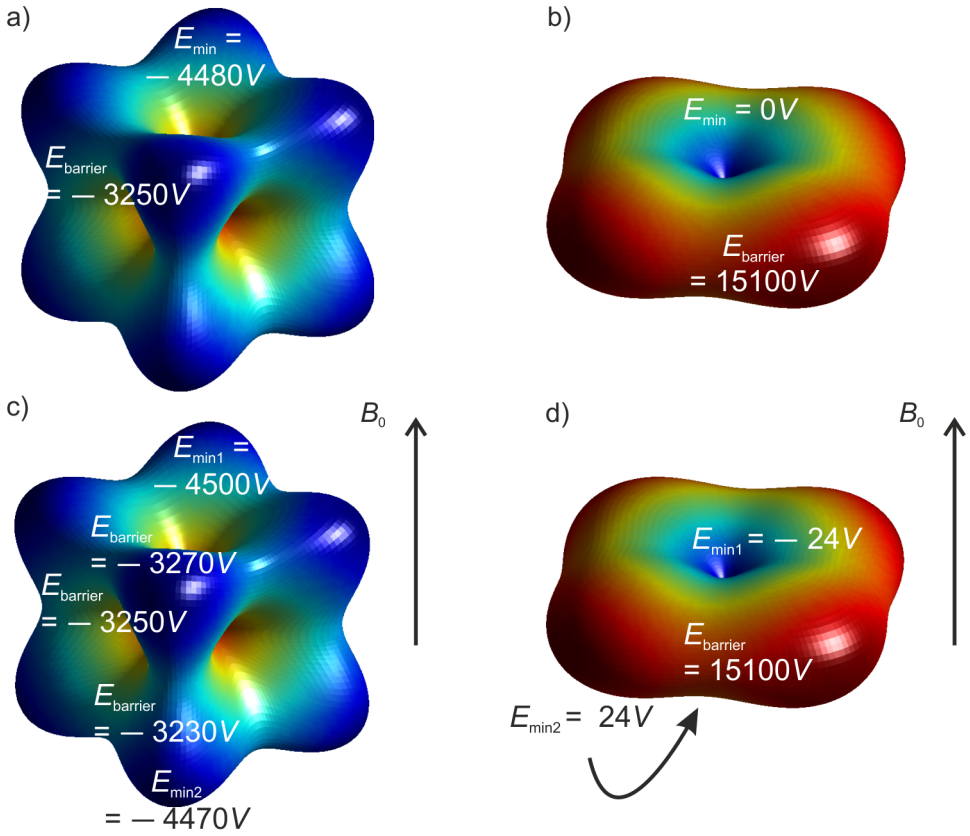

Figure 6.1. Energy surfaces for a single MNP – coloured from blue at the minimum energies to red at the maximum energies (different colour ranges are used for each of a)-d)). The surface colour at any point represents the energy when the magnetisation of the particle points in that direction. The energies at the global minima (and local minima when the low-energy 'easy-axes' are not all degenerate) are shown. The energies of the lowest energy barriers separating these minima are also given. All energies are given in multiples of the volume, V, to 3sf (in Joules). a) $m = 1$, $B_0 = 0$ μT, b) $m = 1.4$, $B_0 = 0$ μT, c) $m = 1$, $B_0 = 50$ μT, d) $m = 1.4$ $B_0 = 50$ μT. $K_1 = -1.3 \times 10^4$ Jm^{-3}, $K_2 = -4 \times 10^3$ Jm^{-3}.

μ_0 is the permeability of free space and D_X and D_Z are demagnetisation factors along the x- and z-axes, given by [263]:

$$D_Z = \frac{1}{1-m^2} + \frac{m \ln\left(-1 + 2m\left(m + \sqrt{m^2-1}\right)\right)}{2\left(m^2-1\right)^{\frac{3}{2}}} \tag{6.7}$$

$$D_X = \frac{1}{2}\left(1 - D_Z\right) \tag{6.8}$$

and m is the ratio of the particle dimensions $\frac{\rho_z}{\rho_x}$ where ρ_i is the particle's radius along the i-axis. Fig 6.1b) shows the energy surface arising from an ellipsoid particle with cubic crystal anisotropy.

Total Anisotropy

The interaction of the applied field with the magnetisation of the MNP also induces an anisotropy given by Equation (6.4). Overall the energy surface is determined by the sum of these three terms, Equations (6.4), (6.5) and (6.6):

$$E = V\left[K_1\left(\frac{1}{4}\sin^2\theta\sin^2 2\phi + \cos^2\theta\right)\sin^2\theta + \frac{K_2}{16}\left(\sin^2 2\phi\sin^2 2\theta\sin^2\theta\right)\right. \tag{6.9}$$

$$\left. + \frac{1}{2}\left(D_X - D_Z\right)M_S^2\mu_0\sin^2\theta' - M_S B_0\cos\theta''\right] \tag{6.10}$$

where the primes indicate that the z-axes of the interactions need not coincide. Stress anisotropies are likely to be much smaller than the crystal, shape and field anisotropies, for magnetite nanoparticles in an isotropically viscous solution, and so this contribution is neglected. Additionally, as we are interested in RPs far from the MNPs we also neglect any surface effects at the edge of a single domain. There is an overall linear dependence on particle volume and therefore it is helpful to compare the magnitude of the three interaction terms. The energy due to field anisotropy at ≈ 50 μT is generally smaller than the crystal anisotropy and unless the MNP is almost exactly spherical this is also much smaller than anisotropy due to shape.

In order to investigate whether any superparamagnetic particles can become blocked by a 50 μT field let us consider the case where all axes are aligned, that is θ and ϕ are the same for each interaction, and compare the energy surfaces for zero-field and Earth-field when $m = 1$ and $m = 1.4$, Fig 6.1. For the spherical particle in Fig 6.1a) there are eight degenerate easy-axes (dark blue) *i.e.* eight global minima. Applying a field in Fig 6.1c) stabilises the four minima aligned with the field ('up') and destabilises those opposed ('down'), there are now four global minima. Fig 6.1b) and d) represent an ellipsoid particle and have two and one global minima respectively.

The perfectly spherical particle in zero-field, Fig 6.1a) has an energy barrier (given as a multiple of the particle volume, V) of $E_A \approx 1230V$ J and $\zeta = 3$. Hence, to have a Néel time of less than 1 μs (and hence exhibit superparamagnetism over the course of a typical RP reaction) the particle must have a radius of $\rho \leq 25.5$ nm at room temperature. For an ellipsoid particle with $m = 1.4$ in zero-field the long-axis radius is $\rho_z \leq 9.6$ nm for SPM character.

A spherical particle ($\rho = 25$ nm) with a 50 μT field applied along its z-axis results in four minima in the direction of the field and four secondary minima remain in the opposite direction, Fig 6.1c). The difference in energy between the two sets of minima is $\approx 30V$ J.

Using the Boltzmann distribution between 'up' (magnetisation aligned with the field) and 'down' (magnetisation aligned against the field) predicts 62% of the SPM will have the magnetic moment in one of the four 'with-field' minima. It is useful to consider the different barrier crossing between the two sets of degenerate minima. The barrier to a transition of the moment from 'down' to 'up' is $E_A \approx 1220V$ J and now $\zeta = 1$ which gives $\tau_N \approx 0.24$ s. The reverse has $E_A \approx 1250V$ J giving $\tau_N \approx 0.38$ s. That is, the applied field locks the magnetic moment in both directions for a time longer than a typical RP reaction. It has very little effect on the energies themselves but significantly acts to reduce the symmetry of the system $\zeta = 3 \rightarrow \zeta = 1$. The hopping time around a set of four equivalent minima (either the 'up' or 'down' set) is $\tau_N \approx 17$ μs ($\zeta = 2$) and within each set there is equal probability of any direction (that is any one of the four degenerate local minima) being populated. Thus, there is a distribution of MNP-field directions because the magnetic moment of the SPM particle does not directly align with the applied field but instead lies along one of four degenerate directions about 45°away from the field.

If the static field is applied directly along one of the eight low-energy directions the degeneracy of the minima is lifted, but even the direction that opposes the applied field remains as a local minimum. The energy difference between the 'minimum-minimum' (*i.e.* the global minimum) and 'maximum-minimum' (the local minimum opposing the field) is only $\approx 50V$ J and the former has a population of just 69%.

The cut-off volume for a non-spherical particle to become SSD is even smaller than in the case of a perfect sphere. Not only is the energy change to the barriers very small but also the statistical factor is not reduced by the application of a field, therefore the interaction with an Earth-strength field will not be strong enough to change the MNP characteristics.

An applied field of Earth-strength is not sufficiently strong to absolutely define the easy-axis of a SPM particle. It can change the dynamics of the magnetic moment fluctuation, and may cause some overpopulation in its general direction. However, it is not reasonable to imagine a system which is characteristically superparamagnetic until an Earth-strength field is applied, at which point it becomes stable-single domain with magnetic moment directly aligned with the applied field. In short, it seems unlikely that magnification of the an Earth-strength field could be achieved by a SPM MNP.

6.2.2 Stable Single Domain Nano-particles

We consider now the stable single domain particles. Such particles have a constant magnetisation in a fixed direction within the particle. However, a strong interaction with the applied field will cause the particle to physically rotate, bringing its moment into alignment with the field. Once again, for this effect to be significant the energy of interaction must be greater than thermal energy and large enough to overcome any resistive force. We assume for simplicity a non-viscous solution and that the nanoparticle is completely free to rotate. Using a simple Boltzmann model; to get $> 95\%$ of particles in the low energy configuration, that is aligned with the field, we require the energy of the interaction to be $E = M_S B_0 V \geq 3k_{\mathrm{B}}T$, corresponding to $V \geq 5 \times 10^{-22}$ m^3 which for a spherical MNP requires a radius, $\rho \geq 50$ nm. Particles with $\rho = 50$ nm are used hereafter. For simplicity we consider only perfectly spherical particles and assume that they are perfectly aligned with the static field they experience.[1]

As long as our RP is sufficiently far from the MNP we can treat the latter's magnetic field like that of a point dipole. At a point (r, θ) in the x, z-plane the components of the field from the MNP along its x-, y- and z-axes (sometimes called the 'local frame') are given by [26]:

$$\begin{aligned} B_x &= \frac{\mu_{env}\mu_{sat}}{4\pi r^3} 3\mathrm{sin}\theta\mathrm{cos}\theta \\ B_y &= 0 \\ B_z &= \frac{\mu_{env}\mu_{sat}}{4\pi r^3} \left(3\mathrm{cos}^2\theta - 1\right) \end{aligned} \tag{6.11}$$

where μ_{env} is the permeability of the environment, taken to be that of water for a general solution phase RP and the dipole is aligned with the z-axis. As the applied field changes direction it causes the MNP to rotate and a RP at fixed orientation with respect to the centre of the MNP will experience a varying total field strength. This is equivalent to moving along the familiar isotropic MARY (Magnetically Altered Reaction Yield) curve [62].

6.3 Magnetite-Radical Pair System

In order to see any kind of direction-dependence in the singlet yield arising from the changing field strength of a rotating MNP the RP must have a fixed orientation relative to the particle on the timescale of radical recombination. We initially suggest two possible arrangements, Fig

[1] To estimate the field alignment we compared only the $\theta = \frac{\pi}{2}$ orientation which does not interact with the field and the most favourable orientation. Of course in reality a continous range of intermediate orientations is populated.

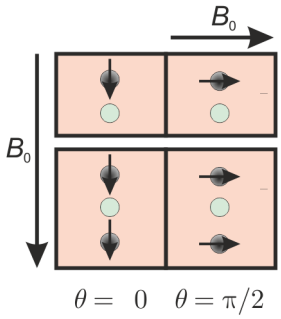

Figure 6.2. Possible arrangements of MNPs (black dots with arrows showing the direction of their moment) and RPs (green dots). In the one-MNP case (upper) θ is the angle between the applied field (parallel to the magnetisation of the MNP) and the MNP–RP position vector. In the two-MNP case (lower) θ is the angle between the applied field and the inter-MNP axis.

6.2.

For the one-MNP system, Fig 6.2 upper, the calculation is relatively straightforward and the MNP moment is assumed to line up precisely with the applied field. Equation (6.11) is then used to calculate the field experienced by a RP due to the MNP, B^{MNP}. The total field, B^T, at this position is then given by:

$$B^T = \sqrt{(B_x^{\mathrm{MNP}})^2 + (B_z^{\mathrm{MNP}} + B_0)^2} \tag{6.12}$$

This is then used in the singlet yield calculation, recalculating B^T for each orientation. The resulting yields for a simple one-nucleus RP are shown in Fig 6.3a). The maximum dependence

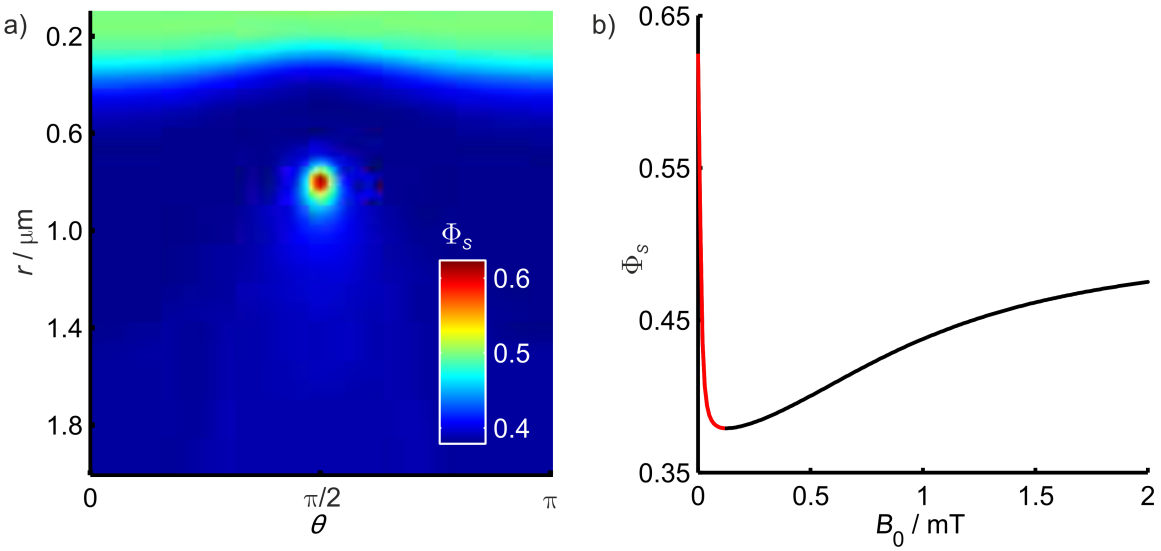

Figure 6.3. Singlet yield as a function of θ the angle between the magnetisation of the MNP and the MNP- RP position vector, and r, the separation. $a = 1$ mT, $k = 1 \times 10^6$ s^{-1}, $B_0 = 50$ μT, ρ, radius of MNP, $= 50$ nm, $\mu_{env} = 1.26 \times 10^{-6}$ m kg s^{-2}A^{-2}. a) 1-MNP system, b) Reference MARY curve for the same RP system on which the steepest part of the curve is highlighted.

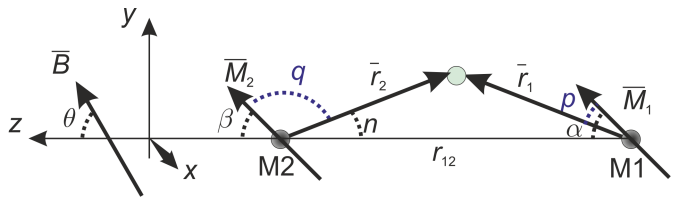

Figure 6.4. Scheme showing the vectors and angles required to calculate the fields from two MNPs that are not necessarily aligned with the applied field. $\overline{B}$ is the applied field vector, M1 and M2 are the MNPs with magnetisation vectors $\overline{M}_1$ and $\overline{M}_2$ respectively. r_{12} describes the inter-MNP separation and $\overline{r}_1$ and $\overline{r}_2$ are the RP position vectors with respect to M1 and M2 respectively.

on θ occurs when the RP is about 0.8 μm from the centre of the MNP, at this separation the total field at $\theta = 0$ *i.e.* when the contribution from the MNP and B_0 align is approximately equal to the field at the minimum of the MARY curve Fig 6.3b). When $\theta = \frac{\pi}{2}$ the x-component of the MNP field is zero, the two contributions along the z-axis are antiparallel and at this separation they almost perfectly cancel thus returning the singlet yield characteristic of zero-field. Thus as θ is varied the entirety of the steepest part of the RP MARY curve is traversed and the maximum directional change in singlet yield is observed. By tuning the separation between MNP and RP it is possible to move over the steepest part of a MARY curve in the course of the MNP rotation. The singlet yield at very small separations goes to 0.5 at all angles as the field strength due to the MNP varies only over the flat high field region of the MARY curve.

It is important to note that the one-nucleus RP used in Fig 6.3 and for subsequent calculations, though very convenient, is rather artificial and gives an extreme low-field effect. More realistic systems often have many nuclei on each radical which reduces the gradient of the low-field effect quite significantly and would therefore lead to a much smaller anisotropic yield from the MNP-RP system than is predicted in Fig 6.3a). However, it is not necessary to use the low-field end of the MARY spectrum, and should the higher field limit show a more promising slope this region could be selected simply by arranging the MNP and RP closer together.

6.3.1 Two MNPs

For a system of two (or more) MNPs it is necessary to account for the weak interaction of the MNPs with each other, this perturbs their equilibrium orientation so that they no longer lie exactly parallel to the applied field.

In this case, and if more MNPs were to be added, the applied field and MNP z-axis are no longer aligned. In order to add together the components of the field it is necessary to define them on the same axes and we now no longer readily know the x-axes of the magnetic moments

from the MNPs. When $\phi = 0$ the x direction can be worked out by adding $\frac{\pi}{2}$ to the $z-$direction, however this becomes more complicated when $\phi \neq 0$ and when the RP does not sit directly on the inter-MNP axis. We choose, therefore, to derive a general method of dealing with this problem which is described below.

1. Vectors defining the position of the RP with respect to each MNP are defined as $\overline{r}_1$ and $\overline{r}_2$, Fig 6.4. The separations between each MNP and the RPs are given by $r_i = |\overline{r}_i|$, and the position vectors are then normalised.

2. The applied field direction is written as a unit vector, $\overline{B} = [\sin\theta\sin\phi, \sin\theta\cos\phi, \cos\theta]$ and B_0 defines the magnitude.

3. The directions of the MNP moments are calculated iteratively to account for inter-MNP interactions, noting that the lowest energy arrangement will have the magnetic moment of each MNP directed along the net field it experiences.

   (a) Each MNP initially has a moment aligned with the applied field. $\overline{M}_1 = \overline{M}_2 = \overline{B}$ and $\alpha = \beta = \theta$.

   (b) The field from M1 at M2 is:

$$B_{x1}^{\mathrm{MNP1}} = \frac{\mu_{env}\mu_{sat}}{4\pi r_{12}^3}\left(3\cos\left(2\pi - \alpha\right)\sin\left(2\pi - \alpha\right)\right) \tag{6.13}$$

$$B_{z1}^{\mathrm{MNP1}} = \frac{\mu_{env}\mu_{sat}}{4\pi r_{12}^3}\left(3\cos^2\left(2\pi - \alpha\right) - 1\right) \tag{6.14}$$

   where B_{z1}^{MNP1} is perpendicular to $\overline{M}_1$ and B_{x1}^{MNP1} is at an angle of $\frac{\pi}{2}$ to $\overline{M}_1$ (clockwise).

   (c) The total field experienced by M1 in the laboratory frame (LF) directions are:

$$B_{2x} = 0 \tag{6.15}$$

$$B_{2y} = B_{0x} + B_{x1}^{\mathrm{MNP1}}\sin\left(\frac{\pi}{2} + \alpha\right) + B_{z1}^{\mathrm{MNP1}}\sin\left(\alpha\right) \tag{6.16}$$

$$B_{2z} = B_{0z} + B_{x1}^{\mathrm{MNP1}}\cos\left(\frac{\pi}{2} + \alpha\right) + B_{z1}^{\mathrm{MNP1}}\cos\left(\alpha\right) \tag{6.17}$$

   (d) The angle that the resultant field makes with the z-axis is then:

$$\beta = \tan^{-1}\left(\frac{B_{2y}}{B_{2z}}\right) \tag{6.18}$$

   As we know the signs of B_{2y} and B_{2z} it is possible to correct the angle returned by

taking $\tan^{-1}$ to ensure it is in the appropriate quadrant.

(e) The moment of M2 is then aligned at this angle and the field at M1 due to M2 and the applied field is calculated as above (though noting that the angle from M2 to M1 is $(\pi - \beta)$). A new α is returned.

(f) The new α and β are compared to the old. They are recalculated until no further adjustment is made. This is assumed to be the equilbrium direction of the two MNP magnetic moments

4. The magnetic moments from each MNP can now be defined by the unit direction vectors: $\overline{M}_1 = [\sin\alpha\sin\phi, \sin\alpha\cos\phi, \cos\alpha]$ and $\overline{M}_2 = [\sin\beta\sin\phi, \sin\beta\cos\phi, \cos\beta]$.

5. The angles between the moment vectors of the MNPs and position vectors of the RP can be found using the dot product:

$$p = \cos^{-1}\left(\overline{r}_1 \cdot \overline{M}_1\right) \tag{6.19}$$

$$q = \cos^{-1}\left(\overline{r}_2 \cdot \overline{M}_2\right) \tag{6.20}$$

6. The vector describing the x-axis for each dipole-radical field is found using the triple cross product rule:

$$\overline{x}_1 = \overline{M}_1 \times \left(\overline{r}_1 \times \overline{M}_1\right) = \overline{r}_1 - \overline{M}_1\left(\overline{M}_1 \cdot \overline{r}_1\right) \tag{6.21}$$

$$\overline{x}_2 = \overline{r}_2 - \overline{M}_2\left(\overline{M}_2 \cdot \overline{r}_2\right) \tag{6.22}$$

As long as the sense of the product is constant this will automatically account for whether the $\overline{r}_i$ is clockwise of anticlockwise of $\overline{M}_i$ and the angles p and q can be used directly.

7. The field from each MNP at the RP site along its own x- and z-axes is calculated:

$$B_{x1}^{\mathrm{MNP1}} = \frac{\mu_{env}\mu_{sat}}{4\pi r_1^3} 3\cos p \sin p \tag{6.23}$$

$$B_{z1}^{\mathrm{MNP1}} = \frac{\mu_{env}\mu_{sat}}{4\pi r_1^3}\left(3\cos^2 p - 1\right) \tag{6.24}$$

$$B_{x2}^{\mathrm{MNP2}} = \frac{\mu_{env}\mu_{sat}}{4\pi r_2^3} 3\cos q \sin q \tag{6.25}$$

$$B_{z2}^{\mathrm{MNP2}} = \frac{\mu_{env}\mu_{sat}}{4\pi r_2^3}\left(3\cos^2 q - 1\right) \tag{6.26}$$

8. The projections of the field from each MNP on each of the LF axes is extracted by scaling

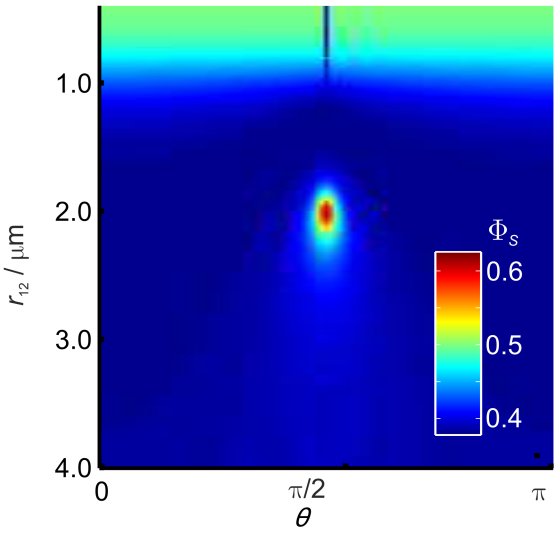

Figure 6.5. Singlet yield as a function of θ the angle between the inter-MNP axis and the applied field direction, and r_{12}, the inter-MNP separation (Fig 6.4). The RP is always exactly half-way between the MNPs. $a = 1$ mT, $k = 1 \times 10^6$ s^{-1}, $B_0 = 50$ μT, $\rho = 50$ nm, $\mu_{env} = 1.26 \times 10^{-6}$ mkgs^{-2}A^{-2}.

the appropriate element of the vector by the field strength:

$$B_x = B_{x1}^{\mathrm{MNP1}}\overline{x}_1[1] + B_{z1}^{\mathrm{MNP1}}\overline{z}_1[1] + B_{x2}^{\mathrm{MNP2}}\overline{x}_2[1] + B_{z2}^{\mathrm{MNP2}}\overline{z}_2[1] + B_0\overline{B}[1] \quad (6.27)$$

$$B_y = B_{x1}^{\mathrm{MNP1}}\overline{x}_1[2] + B_{z1}^{\mathrm{MNP1}}\overline{z}_1[2] + B_{x2}^{\mathrm{MNP2}}\overline{x}_2[2] + B_{z2}^{\mathrm{MNP2}}\overline{z}_2[2] + B_0\overline{B}[2] \quad (6.28)$$

$$B_z = B_{x1}^{\mathrm{MNP1}}\overline{x}_1[3] + B_{z1}^{\mathrm{MNP1}}\overline{z}_1[3] + B_{x2}^{\mathrm{MNP2}}\overline{x}_2[3] + B_{z2}^{\mathrm{MNP2}}\overline{z}_2[3] + B_0\overline{B}[3] \quad (6.29)$$

9. The total field is then given by:

$$B = \sqrt{B_x^2 + B_y^2 + B_z^2} \quad (6.30)$$

10. These fields are then used as normal in the RP simulation.

The simplest two-MNP scheme is that shown in Fig 6.2(lower), where the RP sits on the inter-MNP axis exactly halfway between the two MNPs which are slowly moved further apart. This is equivalent to setting $n = 0$ and $|r_1| = |r_2|$ in Fig 6.4 and varying r_{12}. For a simple one-nucleus RP the singlet yield as a function of r_{12} and θ is shown in Fig 6.5. Like in the one-MNP case (Fig 6.3) it is possible to achieve a very anisotropic singlet yield when the separation between RP and MNPs is such that the steepest part of the MARY curve is sampled as the MNPs rotate.

However, RPs that are far from the optimum distance from the MNPs while showing the same 'shape' anisotropic response, have a much reduced angle-dependence in the singlet yield.

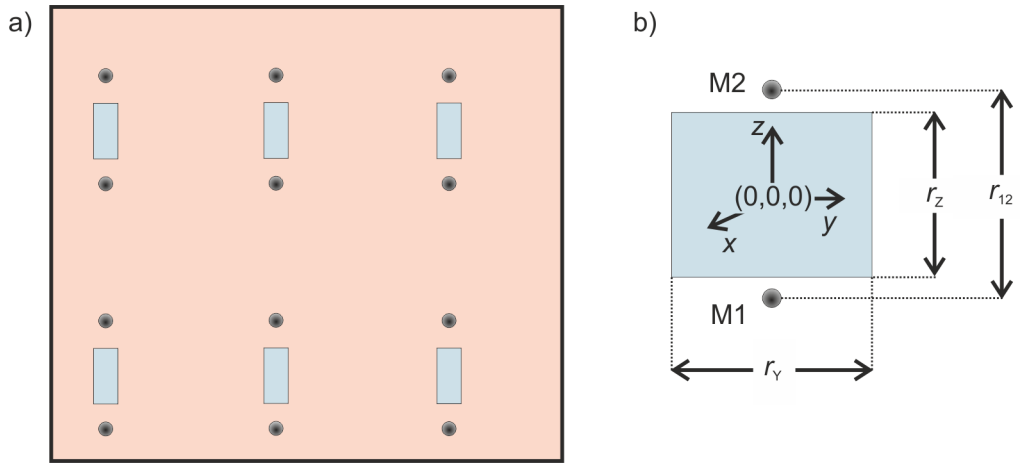

Figure 6.6. a) Suggested array of two-MNP RP arrangements. MNPs are represented by black dots and the RP solution is shown in blue. b) 2D schematic of a single two-MNP system with RPs in a pool of dimensions $\{r_X, r_Y, r_Z\}$ (r_X is the depth and is not shown).

An ensemble of RPs which are distributed across a range of separations will show a smaller anisotropic response overall. Additionally if the RPs are distributed evenly around the MNPs the anisotropic effect will average to zero across the ensemble.

In order to minimise the contribution of the RP reactions far away from MNPs (those on the tail of Figs 6.3a) and 6.5) and to ensure that the RPs are not evenly distributed around the RPs, we consider an extended system with pools of RP solution between MNPs as shown in Fig 6.6a). The maximum difference in singlet yield, $\Delta\Phi_S^{\mathrm{MAX}} = \max(\Phi_S) - \min(\Phi_S)$, as a function of the RP position in the pool is shown in Fig 6.7a). There is a clear radius of optimum directional sensitivity around each MNP at a distance comparable to that in the one-MNP case, Fig 6.3. However, the angles at which the maximum and minimum yields are achieved are not the same at all RP positions as is illustrated in Fig 6.7b). Taking an average the ensemble of positions gives Fig 6.7c) which has a rather small overall anisotropy. The total anisotropy is improved if the pool is made thinner as this restricts the RPs to sitting as closely as possible on the inter-MNP axis and thus showing directional responses of the same shape. Further enhancement would be achieved by limiting the length of the pool to just the region around $0.8-1$ μm from the MNPs where the yield anisotropy is at a maximum. Fig 6.7d) shows the average singlet yield from the region between $y = \pm 0.2$ μm and $z = \pm 0.2$ μm, shown with a white box on Fig 6.7a), clearly a much larger anisotropy is achieved from this region alone.

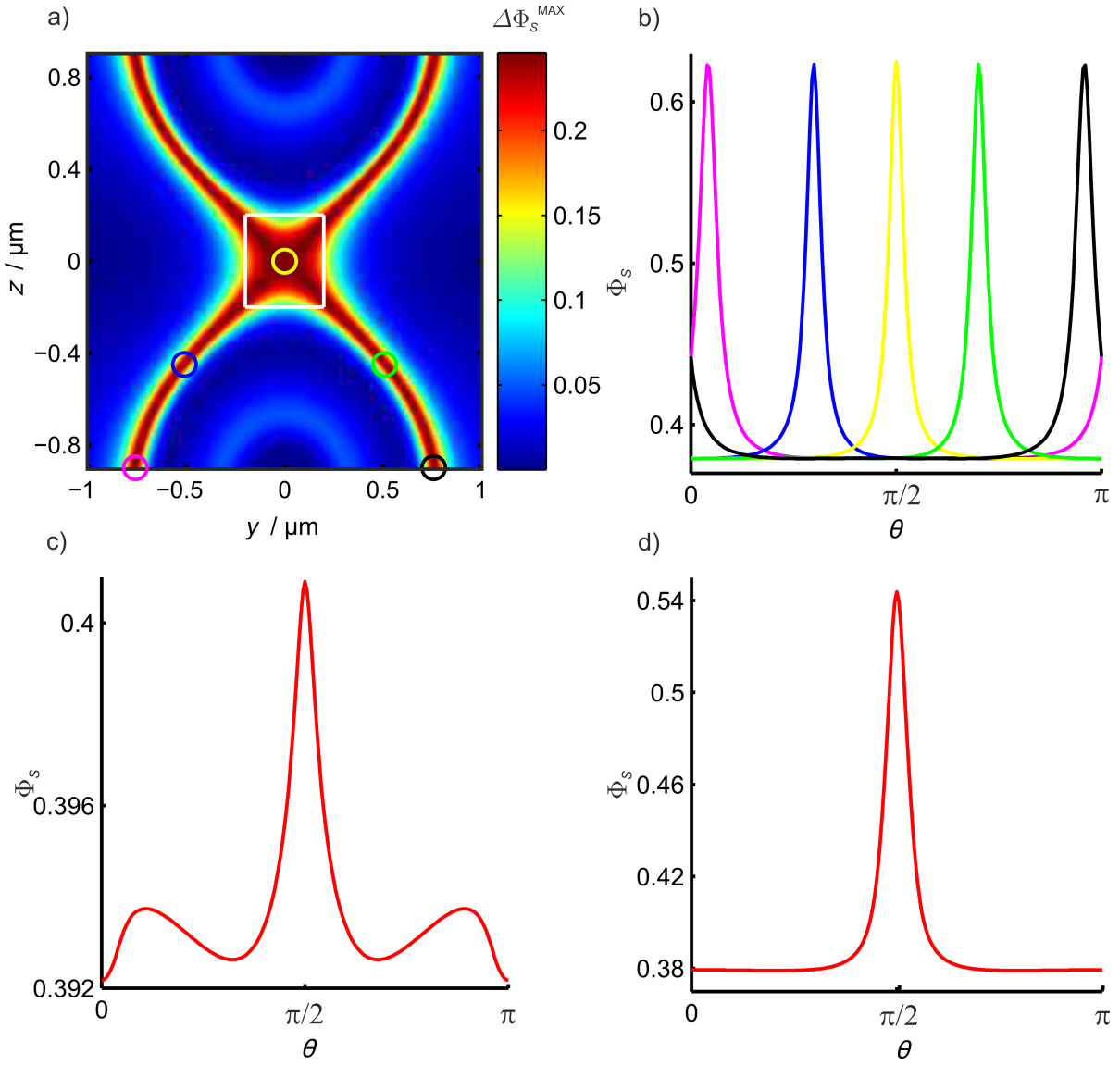

Figure 6.7. a) Maximum singlet yield anisotropy ($\Delta\Phi_S^{\mathrm{MAX}} = \max(\Phi_S) - \min(\Phi_S)$) at each position in the pool of Fig 6.6b). Five positions are highlighted and b) shows the angle-dependence of the singlet yield at these positions. c) The average singlet yield across the ensemble as a function of θ, d) The average singlet yield from the positions within the white box shown in a) . The pool is assumed to have no depth, $r_{\mathrm{X}} = 0$ μm, $r_{\mathrm{Y}} = 2$ μm, $r_{\mathrm{Z}} = 1.8$ μm. $r_{12} = 2$ μm, $B_0 = 50$ μT, $\rho = 50$ nm and $\mu_{env} = 1.26 \times 10^{-6}$ m kg s^{-2}A^{-2}. The RP has a single nucleus with $a = 1$ mT and $k = 1 \times 10^6$ s^{-1}.

6.3.2 Relaxation

Rotational motion is likely to induce relaxation in any RP reaction, independent of the presence of MNPs, by modulating the anisotropic HFI. Additionally, in the presence of a MNP translational motion across the field gradient of the MNP is likely to induce relaxation. An estimate of the magnitude of the field change is given by:

$$\Delta B = |B(r - \mathrm{d}r) - B(r)| \tag{6.31}$$

where

$$\langle \mathrm{d}r \rangle = \sqrt{2Dt} = \sqrt{\frac{k_\mathrm{B}Tt}{3\pi\eta d}} \tag{6.32}$$

using the Stokes-Einstein relation. The viscosity of water is $\eta = 8.9 \times 10^{-4}$ Pa s^{-1}, $T = 300$ K, the RP lifetime is $t = \frac{1}{k} = 1$ μs and estimating a small organic molecule as having radius $d \approx 0.3$ nm gives $\langle \mathrm{d}r \rangle \approx 30$ nm. The field from the MNP is largest at $\theta = 0$ and a RP will see the largest change in field strength if the RP moves directly towards the MNP. Using $r = 0.8$ μm gives $\Delta B \approx 12$ μT, such a small change is unlikely to induce significant relaxation on the timescale of the reaction. Of course for RPs closer to the MNPs the change in field will be larger, but those RPs show a smaller yield anisotropy anyway so additional relaxation will make little difference.

6.4 Conclusion

This chapter began by considering the magnetic properties required of magnetite nanoparticles in order to show a significant response to an Earth-strength field. We showed that it is unlikely that individual particles small enough to be superparamagnetic would show much response to a 50 μT static field and therefore considered only stable-single-domain particles for the remainder of the investigation.

We have suggested a system which could potentially convert the often strong magnetic-field strength dependence of an isotropic RP reaction yield into an anisotropic response. This was achieved using the orientation-dependence of the magnetic field from nanoparticles of magnetite to vary the total field strength (from MNP and the applied static field) experienced by a RP. We assumed that a single-domain MNP is free to rotate in the applied field and aligns its moment along the net field it experiences, arising from the static field and any other nearby MNPs. When the magnetic moment of the MNP is pointing directly at the RP, the RP experiences a field of the same sign from both the MNP and the static field, $B = B_0 + B^\mathrm{MNP}$. When the magnetic moment of the MNP is directed perpendicular to the RP position, the RP experiences fields of opposite sign from the MNP and static field, $B = B_0 - \frac{B^\mathrm{MNP}}{2}$ (at this position the field from the magnetite is half that when directed at the RP). By tuning the separation of the MNP and RP it is possible to achieve limiting total field strengths which coincide with regions of maximum and minimum singlet yield on the MARY curve. Thus as the static field is rotated the steepest

part of a MARY curve is sampled and a large anisotropy is seen in the reaction yield.

A simple one-nucleus case has been considered, but any RP with a significant MFE should display a pronounced angle-dependence in its yield when at a suitable separation from a MNP. A practical implementation of such a system is hard to imagine and we have suggested a possible 2-MNP system, of well defined MNP-RP geometries that would constrain the distribution of RP positions and might possibly be suitable for scaling up to an array of such systems. In practice it would probably be very difficult to make such a system with suitable resolution.

There are of course other possible mechanisms by which magnetite could enhance the anisotropy of the radical pair mechanism. If we were willing to sacrifice rotational disorder it may be possible to achieve amplification of the 'normal' anisotropic HFI-induced directional reaction yield simply by having the total field experienced by the RP larger than the applied field alone. This combined with the orientationally varying total field strengths might lead to useful anisotropy enhancements and it would be interesting to investigate RP reactions of this sort.

Finally we indulge in some slightly more far-fetched speculation. One might imagine combining the polarised triplets of Chapter 3 with the strong fields accessible in the vicinity of MNPs. Assuming the initial field aligns along the intersystem-crossing z-axis an initial T_0 state will be isolated from $T_\pm$ and can evolve only into the singlet and back. If there is sufficient mixing due to HFIs, and a reasonably slow rate constant, the singlet yield at high field and $\theta = 0$ will be 0.5. When the strong applied field is perpendicular to the original z-axis the initial T_0 state in this eigenbasis is a combination of T_+^x, T_-^x and the coherences between them (Subsection 3.3.2). As these states are energetically isolated from the singlet there is almost no singlet-triplet interconversion and the singlet yield will be 0. Potentially this system could return an anisotropic singlet yield varying from 0 to 0.5 *i.e.* a 100% change in singlet yield across from $\theta = 0$ to $\theta = \frac{\pi}{2}$. In this case the large static field significantly outweighs any anisotropic HFIs and there will be little fine structure in the yield anisotropy arising from these interactions. It is difficult to imagine a suitable system which might be expected to show these effects in practice, but if one could be found the anisotropy of the yield could be dramatic.

Chapter 7

Long-Lived States in Multi-Spin Systems

7.1 Introduction

The majority of this thesis is concerned with the effects of weak magnetic fields on chemical reactions. In this chapter however, the *Spinach* library, introduced at the end of Chapter 2 and described in full in Ref [95], has been applied to the investigation of long-lived states in nuclear magnetic resonance (NMR) spectroscopy.

The most famous nuclear equivalent of the electronic spin states at the heart of radical pair (RP) spin dynamics are found in ortho- and para- hydrogen. Hydrogen with spin-$\frac{1}{2}$ behaves, apart from the smaller gyromagnetic ratio, identically to an electron, and a pair of ^{1}H nuclei are able to form a singlet (S) and three triplet (T_x, T_y and T_z) spin states when their angular momenta are combined, these are para and ortho forms of molecular hydrogen respectively [260]. Transitions between the two forms are spin-forbidden and occur very slowly unless a catalyst is present.[1]

Potentially such spin-state isolation could be present for any pair of spin-$\frac{1}{2}$ nuclei. With molecular hydrogen as the obvious exception, it is rare to find isolated two-spin systems and for realistic molecules it is necessary to suppress all asymmetric interactions, *i.e.* those which are not the same on both nuclei, to maintain a long-lived state [264, 265]. Only in the last decade has the phenomenon of long-lived singlet states really begun to attract significant interest from

[1] A catalyst, depending on the type, can act to change the magnetic environment of one end of the molecule, thus allowing the two nuclear spins to precess at different rates and change the relative phase between them - this is a nuclear analogue of the RPM.

the perspective of NMR. The first experimental observation of a long-lived singlet state was seen by Carravetta and Levitt in 2004 in 2,3-dibromothiophene [266]. Since then many molecules have been shown to exhibit long-lived singlet states and have found application in, for example, polarisation storage [267–270], measurements of slow diffusion [271], and to obtain molecular structural information [272].

Similar long-lived states have been analysed [273, 274], and observed [269, 270, 275] in three- and four- spin systems but larger spin systems have not been systematically treated. Following a brief overview of dipolar relaxation and the relaxation-resistant singlet state already mentioned, this chapter presents the results of a systematic search for long-lived states across a range of spin-$\frac{1}{2}$ coupling topologies for 4-8 spins and for some real molecule examples. The main results of this analysis have been reported in Ref [97].

7.1.1 Dipole-dipole Relaxation

For conventional liquid-state NMR, nuclear relaxation arises from random fluctuations in the nuclear spin interactions due to molecular motion [276], of which the dominant contribution usually comes from modulation of the dipolar interactions between nuclear spins.[2]

Through-space dipole-dipole relaxation arises from time-dependent fluctuations in the local magnetic field experienced by one spin due to the magnetic moment of the other [66]. The dipolar coupling is described for a pair of point-dipoles by the Hamiltonian (reproduced from Section 1.3.3 for two nuclei):

$$\hat{H}_{\mathrm{D}} = \frac{\mu_0 \gamma_n^2}{4\pi\hbar^2 r^3}\left[\hat{I}_A \cdot \hat{I}_B - \frac{3}{r^2}(\hat{I}_A \cdot \vec{r})(\hat{I}_B \cdot \vec{r})\right] \tag{7.1}$$

where $\hat{I}_i$ is a vector of the nuclear spin operators, γ_n is the nuclear gyromagnetic ratio, r is the inter-nuclear separation and $\vec{r}$ is a unit vector in the spin-spin direction. From Equation (7.1) it is evident that both random rotational motion at fixed distance (*i.e.* changing the relative orientation of $\vec{r}$ with the applied field) and modulation of the internuclear distance will result in random fluctuations in the local magnetic field and thus nuclear relaxation.

The dipolar interaction operator of Equation (7.1) is clearly symmetric with respect to the permutation of the two spins (operators acting on different spins by definition must commute)

[2]This is directly analogous to the modulation of anisotropic hyperfine interactions (HFIs) between electrons and nuclei discussed in the previous chapter.

thus similarly the permutation operator $\hat{\mathcal{P}}$ and the dipolar Hamiltonian must commute [264]:

$$\left[\hat{\mathcal{P}}, \hat{H}_{\mathrm{D}}\right] = 0 \tag{7.2}$$

Given this symmetry the dipolar coupling operator cannot change the spin state of the pair of spins it couples between states of different symmetry.

For solution-state NMR, Bloch-Redfield-Wangsness (BRW) theory is usually considered an adequate model of spin-relaxation, the master equation of which was derived in Chapter 2. For two equivalent nuclei subject to just a Zeeman interaction and time-dependent dipolar interactions the master equation is given by:

$$\begin{aligned}\frac{\mathrm{d}\hat{\rho}(t)}{\mathrm{d}t} = &-\mathrm{i}\hat{\hat{H}}_0\hat{\rho}(t) - \left[\int_0^\infty \left\langle \hat{\hat{H}}_{\mathrm{D}}(t)\mathrm{e}^{\mathrm{i}\left(\omega_A\hat{\hat{I}}_{A_z}+\omega_B\hat{\hat{I}}_{B_z}\right)\tau}\hat{\hat{H}}_{\mathrm{D}}(t+\tau)\mathrm{e}^{-\mathrm{i}\left(\omega_A\hat{\hat{I}}_{A_z}+\omega_B\hat{\hat{I}}_{B_z}\right)\tau}\right\rangle \mathrm{d}\tau\right] \\ &\times\left(\hat{\rho}(t)-\hat{\rho}_{eq}\right)\end{aligned} \tag{7.3}$$

where the $\langle\cdots\rangle$ indicates an ensemble average, and ω_i is the Zeeman resonance frequency of nucleus i. Like any other spin operator the dipolar Hamiltonian may be written as a sum over the irreducible spherical tensors (ISTs) with time-dependent coefficients given by the Wigner functions. Assuming isotropic rotational diffusion the correlation functions of the Wigner functions are well-known, allowing convenient evaluation of Equation (7.3). Modulation of internuclear distance cannot be treated in this way, but for fairly rigid molecules contributions of this kind are not likely to be significant. Herein we are concerned only with the effect of rotational motion on dipole-dipole interactions.

7.1.2 Singlet State

Before considering more complicated multi-spin systems it is worthwhile briefly reviewing the original two-spin singlet. The singlet state is antisymmetric with respect to permutation of electrons:

$$\mathcal{P}\left(|\alpha\beta\rangle - |\beta\alpha\rangle\right) = \left(|\beta\alpha\rangle - |\alpha\beta\rangle\right) = -\left(|\alpha\beta\rangle - |\beta\alpha\rangle\right) \tag{7.4}$$

and the triplet states are symmetric:

$$\mathcal{P}\left|\alpha\alpha\right\rangle = +\left|\alpha\alpha\right\rangle \tag{7.5}$$

$$\mathcal{P}\left(\left|\beta\alpha\right\rangle + \left|\alpha\beta\right\rangle\right) = \left(\left|\beta\alpha\right\rangle + \left|\alpha\beta\right\rangle\right) = +\left(\left|\beta\alpha\right\rangle + \left|\alpha\beta\right\rangle\right) \tag{7.6}$$

$$\mathcal{P}\left|\beta\beta\right\rangle = +\left|\beta\beta\right\rangle \tag{7.7}$$

A full analytical treatment of the relaxation matrix elements arising from isotropic rotational modulation of two dipolar coupled spins may be found in Ref [264]. In this work it is shown that in the commonly used bases built from $\alpha\beta$ product operators there are no states which are obviously resistant to dipole-dipole relaxation, however in the ST (singlet-triplet) product basis the relaxation superoperator is block diagonal (Equation 31 from Ref [264]). Using the symbolic processing procedure of Ref [108], and making use of the extreme narrowing condition for convenience, the dipole-dipole relaxation operator can be derived analytically. The form is identical to that for modulation of anisotropic HFI though χ, the relaxation rate constant, now contains the dipolar coupling information. The resulting relaxation superoperator is, as was found in Ref [264], block diagonal with respect to populations and coherences. The reduced superoperator just considering the population states $\{SS, T_+T_+, T_0T_0, T_-T_-\}$ is shown below:

$$\begin{pmatrix} 0 & 0 & 0 & 0 \\ 0 & -\frac{3\chi}{20} & \frac{\chi}{20} & \frac{\chi}{10} \\ 0 & \frac{\chi}{20} & -\frac{\chi}{10} & \frac{\chi}{20} \\ 0 & \frac{\chi}{10} & \frac{\chi}{20} & -\frac{3\chi}{20} \end{pmatrix} \tag{7.8}$$

which if we define $W_1 = \frac{\chi}{20}$ and $W_2 = \frac{\chi}{10}$ reproduces the population block of Equation 31 from Ref [264]. There is no connection between the singlet and triplet states (or between spin-state populations and coherences). The triplet states are relaxed between themselves, the singlet-triplet coherences are eroded (dephasing) and the singlet state is unaffected.

A similar conclusion can be reached by considering the symmetry of the dipolar operator and the states of interest. [264, 274] The dipolar relaxation superoperator:

$$\hat{\hat{R}} = \int_0^\infty \left\langle \hat{\hat{H}}_{\mathrm{D}}(t)\mathrm{e}^{\mathrm{i}\tau\left(\omega_A\hat{I}_{A_z}+\omega_B\hat{I}_{B_z}\right)}\hat{\hat{H}}_{\mathrm{D}}(t+\tau)\mathrm{e}^{-\mathrm{i}\tau\left(\omega_A\hat{I}_{A_z}+\omega_B\hat{I}_{B_z}\right)}\right\rangle \mathrm{d}\tau \tag{7.9}$$

from Equation (7.3) inherits the permutation symmetry of the dipolar superoperator when the two nuclei are subject to equivalent Zeeman interactions, $\omega_A = \omega_B = \omega$. In this case

the singlet and triplet levels are eigenstates of the total angular momentum along the z-axis, $\hat{\hat{H}}_0 = \omega(\hat{\hat{I}}_{A_z} + \hat{\hat{I}}_{B_z})$ and swapping the spins leaves them in the same magnetic environment as they started. Hence it follows that:

$$\left[\hat{\hat{\mathcal{P}}}, \hat{\hat{R}}\right] = 0 \tag{7.10}$$

Therefore the matrix elements of $\hat{\hat{R}}$ can only be non-zero between states of the same parity, *i.e.* both symmetric, both antisymmetric or both a mixture under the permutation of the two nuclei.

The singlet and triplet spin states of the pair cannot be interconverted by dipole-dipole relaxation and while the triplets can be relaxed between sub-levels the singlet state is dynamically isolated [264].

The non-relaxing subspace of a two-spin system therefore comprises the singlet state, for which the projection operator is $\hat{Q}_S$ and the ubiquitous identity operator, $\hat{\mathbb{1}}$. Any linearly independent states may be chosen as the basis of the null space and the projector for the mixture of triplets, is just $\hat{\mathbb{1}} - \hat{Q}_S$. The projector for the difference state between singlet and triplet is defined as:

$$\hat{Q}_{TS} = \hat{Q}_S - \hat{Q}_{T_+} - \hat{Q}_{T_0} - \hat{Q}_{T_-} \tag{7.11}$$

where $\hat{Q}_i$ is the projection operator of state i.

All simulations were carried out in Liouville space and using the normalised IST basis. They are related to the spin-$\frac{1}{2}$ spin operators according to:

$$\hat{T}_{0,0} = \frac{1}{\sqrt{2}}\hat{\mathbb{1}} \tag{7.12}$$

$$\hat{T}_{1,+1} = -\hat{S}_+ \tag{7.13}$$

$$\hat{T}_{1,0} = \sqrt{2}\hat{S}_z \tag{7.14}$$

$$\hat{T}_{1,-1} = \hat{S}_- \tag{7.15}$$

It proved more convenient to define the singlet, triplet and difference states in a normalised vector form. In the above basis the singlet is defined as:

$$S = \frac{1}{4}\hat{\mathbb{1}} - \hat{S}_z^A\hat{S}_z^B - \frac{1}{2}\left(\hat{S}_+^A\hat{S}_-^B + \hat{S}_-^A\hat{S}_+^B\right) \tag{7.16}$$

$$= \frac{1}{2}\left(\hat{T}_{0,0}\hat{T}_{0,0} + \hat{T}_{1,+1}\hat{T}_{1,-1} - \hat{T}_{1,0}\hat{T}_{1,0} + \hat{T}_{1,-1}\hat{T}_{1,+1}\right) \tag{7.17}$$

Thus, the four vectors of interest for the two-spin system each have at most four non-zero elements in the vector and working in the $\left\{\hat{T}_{0,0}\hat{T}_{0,0},\ \hat{T}_{1,+1}\hat{T}_{1,-1},\ \hat{T}_{1,0}\hat{T}_{1,0},\ \hat{T}_{1,-1}\hat{T}_{1,+1}\right\}$ reduced basis:

$$1 = \begin{pmatrix} 1 \\ 0 \\ 0 \\ 0 \end{pmatrix},\ P_S = \frac{1}{2}\begin{pmatrix} 1 \\ 1 \\ -1 \\ 1 \end{pmatrix},\ P_T = \frac{1}{\sqrt{12}}\begin{pmatrix} 3 \\ -1 \\ 1 \\ -1 \end{pmatrix},\ P_{ST} = \frac{1}{\sqrt{3}}\begin{pmatrix} 0 \\ 1 \\ -1 \\ 1 \end{pmatrix} \tag{7.18}$$

by taking combinations of these vectors it is possible to define the following relationships:

$$1 = \frac{1}{2}\left(P_S + \sqrt{3}P_T\right) \tag{7.19}$$

$$P_{ST} = \frac{1}{\sqrt{3}}\left(2P_S - 1\right) = \frac{1}{2}\left(\sqrt{3}P_S - P_T\right) \tag{7.20}$$

The difference state P_{ST} was convenient to work with when inspecting the eigenvectors of long-lived states as it has no contribution from the unit operator. Also, P_{ST} and 1 form an orthonormal basis as does the pair P_S and P_T. However, it is most important that the basis vectors are linearly independent and although for the more complicated systems encountered later it is possible to form an orthonormal set of null space vectors this is at the cost of describing the states in terms of complicated linear combinations. Instead the states will be listed, where possible, in the simplest form which preserves linear independence. For simplicity, the normalisation factors will henceforth be omitted.

7.1.3 Applications and Uses of Long-lived States

Before embarking on the full treatment of multi-spin systems it is interesting to briefly outline some of the many (and wide-ranging) applications of long-lived states used to date.

Polarisation Storage

One of the major limitations to NMR spectroscopy is the inherent insensitivity arising from the tiny population differences from Boltzmann distributions across spin energy levels even at low temperature. Many hyperpolarisation techniques have been developed to enhance the population differences, increasing polarisation and thus enhancing NMR signals [277, 278]. One method is dynamic nuclear polarisation (DNP) by which magnetisation is transferred from a more polarised species (normally an electron) to the spin of interest. In many examples of DNP the sample

must be shuttled between the polarisation equipment and the spectrometer, relaxation during this time incurs losses in the magnetisation gain if the sample is not moved rapidly [269]. Methods for storing polarisation as singlet polarisation [270], with its much greater resistance to relaxation, extends the time frame over which polarisation can be used. Although a singlet state between equivalent spins is not visible by NMR (any transitions incur a change of spin state and are hence forbidden) pulse sequences are available to transfer polarisation to a more usable form [270]. Alternatively removing the equivalency of the two spins, either by turning off factors suppressing inequivalency or by chemical reaction can also make use of the polarisation available from a singlet state. This underlies the use of direct hydrogenation of molecules to gain from the polarisation associated with para-H_2 when the hydrogenating mixture is enriched with this component, for example para-hydrogen induced polarisation (PHIP) and para-hydrogen and synthesis allow dramatically enhanced nuclear alignment (PASADENA) [278].

Diffusion Studies

NMR has long been used in the study of molecular translational diffusion coefficients. Based upon a spin-echo experiment [279], a pulsed field gradient (PFG) is used to encode molecular position via the phase accumulated under the pulse. A 180° pulse flips the magnetisation, and a second identical PFG then causes the spins to rephase. If the molecule has not moved it experiences an identical field on either side of the 180° pulse and is perfectly rephased, forming the maximum echo. If it has undergone some diffusion it experiences a different field strength in the second half of the experiment and rephasing is imperfect - the echo is attenuated. It is possible to separate the diffusive dephasing from T_2 type dephasing and thus provide a measure of the diffusion coefficient [280]. This technique is limited by the timescale of relaxation, that is, if the diffusion is much slower than T_2 relaxation effects then the effects of diffusion are swamped and can no longer be isolated. This is often true of large biomolecules and highly viscous solutions. In order to study such molecules it is necessary to extend the relaxation times of the spin states, this can be achieved using long-lived states to encode polarisation and phase during the diffusion time [271, 281–283].

Structural Information

Apart from the obvious advantages to structure determination incurred by enhanced NMR signals from hyperpolarisation, the relaxation properties of the long-lived states themselves can

be used to determine local structure. For example, singlet states across diastereotopic CH_2 of amino acids have been used to retrieve information about molecular conformations [272]. As an over simplified overview: the coherent evolution of the singlet state is dominated by asymmetric out-of-pair interactions with neighbouring groups, thus the lifetime of a singlet state gives a measure of the dipolar coupling differences between the singlet protons and spins on the adjacent group. This information can be understood in terms of the relative orientation of the singlet protons and the main body of the residue, that is, the torsional angle.

Chemical shift anisotropy (CSA) arises from the electronic shielding of a nucleus from the external field by a neighbouring group with a non-symmetric distribution of electrons, for example from ring currents of aromatic systems that lead to different amounts of shielding for a nucleus above/below the plane of the ring compared to one in the plane. The combination of shielding fields from all neighbouring groups can be described by a single tensor, the CSA tensor, on each nucleus, directly analogous to the anisotropic g-tensors observed in electron paramagnetic resonance (EPR) and in the RPM. As the molecule tumbles the nuclei experience varying net fields and this random fluctuation of local fields incurs nuclear relaxation. Long-lived states are not, in general, immune to CSA-relaxation and the relaxation constants of long-lived states can be used to determine the relative orientations of the chemical shift anisotropy tensors of the two spins involved [284], when other factors, such as coherent evolution, are suppressed.

Magnetic Resonance Imaging

Like NMR, magnetic resonance imaging (MRI) suffers from the weak polarisation of spin states under Boltzmann considerations alone and signal enhancement from hyperpolarisation is an area of much interest [285]. Polarisation storage through the use of long-lived states, as aforementioned, increases the time period over which polarisation transfer from hyperpolarising agents to the sample region can be conducted. A singlet state on the spins-$\frac{1}{2}$ of ^{15}N-nitrous oxide has been shown to have a lifetime of $\approx$ 26 minutes. As N_2O is soluble in blood the long lifetime might be expected to allow transport of the hyperpolarising agent to remote regions while still maintaining some nuclear order which is potentially of great value to medical imaging [286].

Furthermore it has been shown in Ref [268] that long-lived singlet states can be stored across equivalent nuclei. Singlets states on equivalent nuclei cannot be detected directly but a reaction pathway which removes the spin equivalence will allow the polarisation to be observed. Long-lived states on equivalent spins of metabolically active substrates allow a means by which to

observe the metabolic pathway along which the substrate reacts - only when the equivalency of the nuclei is lost, *i.e.* reaction, does the associated polarisation become detectable [268]. The enhancement will appear only in the product molecule, and only in the location of reaction.

Quantum Memory

Quantum information processing (QIP) and quantum computation (QC) are severely limited by dephasing processes which slowly return states to equilibrium [287]. States which resist such relaxation are vital for the construction of quantum memory modules [288]. One long-lived state allows only one piece of saved information however spin systems with multiple relaxation-resistant states may be populated in any single long-lived state or any linear combination of them [289]. Thus a system with two or more populatable long-lived states (that is not the trivial unit operator) could have, in principle, infinite different linear combinations and correspondingly infinite memory capacity if the linear combinations could be selectively populated and addressed/read-out. Of course in practice this would probably be very difficult in which case having multiple linearly independent long-lived states may prove more useful. These are just the kind of systems investigated in this chapter.

7.2 Invariance Under the Liouvillian

In order for a state, $\hat{\rho}$, to be long-lived it must not evolve over time under the system Liouvillian, $\hat{\hat{L}}$, that is, it must be invariant under $\hat{\hat{L}}$ [97]:

$$\exp\left\{-\mathrm{i}\hat{\hat{L}}t\right\}\hat{\rho} = \hat{\rho} \tag{7.21}$$

Writing the propagator as the result of a Taylor expansion gives:

$$\begin{aligned} \left(\sum_{n=0}^{\infty}\frac{(-\mathrm{i}t)^n}{n!}\hat{\hat{L}}\right)\hat{\rho} &= \hat{\rho} \\ \hat{\rho} + \left(\sum_{n=1}^{\infty}\frac{(-\mathrm{i}t)^n}{n!}\hat{\hat{L}}\right)\hat{\rho} &= \hat{\rho} \\ \Rightarrow \left(\sum_{n=1}^{\infty}\frac{(-\mathrm{i}t)^n}{n!}\hat{\hat{L}}\right)\hat{\rho} &= 0 \end{aligned} \tag{7.22}$$

where $\hat{\hat{L}} = \hat{\hat{H}} + \mathrm{i}\hat{\hat{R}}$ and $\hat{\hat{H}}$ is the Hamiltonian superoperator. Equation (7.22) can be only be satisfied at all times if:

$$\hat{\hat{L}}\hat{\rho} = 0 \tag{7.23}$$

The diagonalised Liouvillian acting on its own eigenbasis may be written in matrix form as:

$$\begin{pmatrix} \lambda_1^L & 0 & \cdots & \\ 0 & \lambda_2^L & & \\ \vdots & & \ddots & \\ & & & \lambda_n^L \end{pmatrix} \begin{pmatrix} \rho_1^L \\ \rho_2^L \\ \vdots \\ \rho_n^L \end{pmatrix} = \begin{pmatrix} \lambda_1^L \rho_1^L \\ \lambda_2^L \rho_2^L \\ \vdots \\ \lambda_n^L \rho_n^L \end{pmatrix} \tag{7.24}$$

where λ_i^L and ρ_i^L are the eigenvalues and eigenvectors of $\hat{\hat{L}}$ respectively. Inspection of Equation (7.24) clearly shows that the requirement of Equation (7.23) is only satisfied for eigenvectors of the Liouvillian with zero eigenvalues. The set of states with zero eigenvalues is called the null-space of the superoperator, and this is the subspace of states, K, which do not evolve under the system Liouvillian. This may be formally defined as:

$$\hat{\hat{L}} \colon K \to \{0\} \tag{7.25}$$

and K is the null space of the superoperator $\hat{\hat{L}}$.

Therefore, finding states which are invariant under $\hat{\hat{L}}$ is equivalent to finding the null space of the superoperator [274]. In practice this is readily achieved. The Liouvillian is built, diagonalised and the eigenvalues inspected [290]. Strictly, the null space is defined only by those eigenvectors with exactly zero eigenvalues, however as we are interested in long-lived states rather than *infinitely* long-lived states the criterion is relaxed for the remainder of this chapter and we consider all states which have eigenvalues significantly smaller than the system average.

A Quick Test

To find the full subspace of long-lived states it is necessary to diagonalise the full Liouvillian. However, a quick test for the long-lived character of a state is provided by Equation (7.23). A state suspected of being long-lived is operated on by the Liouvillian, or just the relaxation superoperator when the coherent evolution is not considered. If the resulting vector is zero (or all elements are nearly zero) the state is long-lived and if the resulting vector is far from being all

zeros the state is not long-lived. For states returning small but non-zero vectors this test gives no measure of the size of the relaxation rate, whereas the absolute magnitude of the eigenvalue of a state can be considered as a measure of the rate (relaxation rate if $\hat{\hat{H}} = 0$) constant of the state evolution.

7.2.1 Suppression of Coherent Evolution

For a system to be truly long-lived it must be invariant under the full system Liouvillian, as just outlined. Thus it must resist relaxation through incoherent processes and remain unaffected by coherent evolution, that is, under the Hamiltonian superoperator term in the Liouvillian. For equivalent nuclei the two spins evolve under identical interactions and therefore cannot change the relative phase between them, they remain as a singlet. Remove the equivalency however and the two spins are evolving under different interactions and there can be coherent evolution between the singlet spin state and its rapidly relaxing triplet counterpart (and back).[3]

Considered from the symmetry argument perspective. It is often the case that $\hat{\hat{H}}$ breaks the inversion symmetry of the spin-pair either through different shielding of the two spins, and hence non-equivalent Larmor precession frequencies, or by out-of-pair couplings (scalar and dipolar can be equally destructive) to different nuclei. In either of these cases permuting the spins does not leave them in the same environment they started in, and inversion symmetry is lost.

Fortunately, suppressing the coherent evolution of long-lived states has been the focus of much research in recent years and there are several well-developed techniques to control such evolution, and these approaches are briefly outlined below.

Field-Shuttling

Differences in chemical shift between inequivalent sites causes evolution between the singlet and triplet states (via singlet-triplet zero-quantum coherences).[4] The most intuitive method to suppress such evolution is to remove the sample from the high field environment, where differences in chemical shift lead to large differences in Larmor frequency, to low field [264]. This has been achieved in practice by physically removing the sample from the spectrometer, following the preparation pulses, to an area of low-field. After a suitable period the sample is

[3] In analogy with the coherent evolution of RPs, the out-of-pair asymmetric couplings may be considered like different hyperfine interactions on the two electrons, and different Larmor frequencies as the different g-values of the electrons.

[4] This is entirely analogous to evolution, in the RPM, between the singlet and triplet electron states driven by different g-values of the two electrons.

returned to high-field for the detection sequence [266].

Spin-Locking

An alternative method for suppressing coherent evolution due to chemical shift differences lies in the application of a radio-frequency (RF) field perpendicular to the static field and with frequency usually corresponding to the mean chemical shift. A resonant (or almost resonant) RF field is symmetric with respect to the two spins and if this symmetric interaction is strong enough to outweigh the asymmetric Zeeman interaction then the nuclei have been made effectively equivalent. It has been shown in Ref [265, 291] that the long-lived singlet state is well isolated from the rapidly relaxing triplet states when the nutation frequency (the amplitude of the RF field in frequency units) arising from the RF-field is larger than the difference in chemical shift frequencies of the two sites. As long as this condition is met spin-locking is possible, even if the RF-field is a long way off resonance [292].

Decoupling

Often the two spins of interest in a long-lived singlet state are subject to asymmetric scalar out-of-pair couplings to other spins. The Hamiltonian for such coupling interactions does not commute with the dipole-dipole operator under which the spins are invariant, because the out-of-pair coupling removes the inversion symmetry of the two spins. Thus couplings will induce evolution between the singlet and triplet states.[5] It has been shown in Ref [290] that a strong scalar coupling between the spins of the long-lived state gives some stabilisation of the state with respect to external coupling. In addition, it is possible to effectively decouple spins by application of an appropriate pulse sequence [60, 284].

7.2.2 Incoherent Processes

The focus of most of the discussion thus far has been concerned with states that are immune to dipole-dipole relaxation. The previous section, in outlining a selection of approaches from the a vast toolbox of NMR techniques available, has shown that control of the coherent evolution of long-lived states is well-developed. It is the incoherent, relaxation processes which are least understood and which are of interest for most of the results presented hereafter. Unless otherwise stated, for the remainder of this chapter we concern ouselves only with invariance under the

[5] This is analogous to hyperfine-driven coherent evolution of the spin-states in the RPM.

relaxation superoperator.

7.3 Relaxation in *Spinach*

The results which follow were computed using the *Spinach* library of codes that was introduced in the Chapter 2 [95]. The method of generating relaxation superoperators, as outlined in Chapter 2, for low-field relaxation in the extreme narrowing limit arising from modulation of HFIs was not used for the high-field NMR application in which we are interested predominantly in dipole-dipole couplings. Instead, a later implementation by Kuprov that makes up the relaxation module of the *Spinach* library was utilised. This formulation of Redfield theory avoids diagonalisation of the static Hamiltonian, which is extremely costly for large matrices, by instead performing a numerical integration of the integral in Equation (7.3) [109]. As we go on to diagonalise the resulting relaxation superoperator, diagonalisation is still the limiting factor for the size of spin-system that can be considered. For more general spin-dynamics applications the numerical, diagonalisation-free implementation gives a large speed-up. The *Spinach* relaxation module is capable of including any anisotropic interactions as sources of relaxation, it includes all cross-correlations and dynamic frequency shifts if requested though these are usually small and have been neglected in the simulations that follow. Although the isotropic rotational diffusion approximation is used for the operators generated in this chapter, *Spinach* is capable of using arbitrary user-specified correlation functions.

7.4 Spin System Survey

In the simulations presented below the dipolar interactions were calculated directly from coordinates specified from the geometries of the model systems. CSAs were not considered for the model systems and the coherent part of the Liouvillian was neglected. All interaction tensors were fed into the relaxation theory module of the *Spinach* library, the resulting relaxation superoperator was diagonalised and the eigenvectors corresponding to small eigenvalues were inspected.

For linearly independent states sharing a common eigenvalue any linear combination of those states will have the same eigenvalue. In the terms of our analysis this means that any linear combination of states in the null-space is itself a state belonging to the null space and correspondingly has a near zero-eigenvalue. Inconveniently, in many the cases the eigenvectors of the

null space as revealed by diagonalisation of the relaxation superoperator,[6] were not instantly recognisable as localised singlets, singlet-triplet differences or anything else commonly encountered, instead being, in most cases, linear combinations of such states. It was thus necessary to take linear combinations of the null space eigenstates in an attempt to discover meaningful states, though this was at the expense of orthogonality. In many cases this proved extremely challenging as the state-lists of large systems are long and many states were populated and to different degrees. However, it was possible with some algebra to find suitable linear combinations which simplified the states to something meaningful.

7.4.1 Strongly Interacting Systems

The search for long-lived states was begun by extension of the two-spin strongly dipolar-coupled singlet system to strongly dipolar-coupled systems of more spins. A nearest neighbour separation of 1 Å was chosen for convenience. In this work we use the term 'strongly coupled' to refer to the relative strength of the dipolar couplings in the system with no reference to any scalar couplings or chemical shift differences that may be present. This returns a dipolar coupling of $D \approx 120$ kHz for two ^{1}H and as 1 Å is just shorter than a typical aliphatic C-H bond length this provides an upper bound on the dipolar interactions likely to be encountered in organic molecules. All pair-wise dipolar interactions were included in the relaxation superoperator and the coupling constants and dipolar axes were calculated directly from the geometry of the spin system by the *Spinach* core. These values were then used for calculation of $\hat{\hat{R}}$.

Spin-systems with three to six spins were investigated in a variety of geometries. The results of the survey are shown in Figure 7.1. The system geometries are shown, along with the point group to which they belong, grouped according to the number of long-lived states they possess. Note we have relaxed the null space requirement such that eigenvalues that not identically zero, but are distinct from the majority are included. For absolute eigenvalues sorted in descending order there is a smooth decrease in magnitude until the set of the long-lived states at which point there is a sharp drop in the size of the absolute eigenvalue. It should be noted that all systems have one long-lived state, the unit operator ($\hat{\mathbb{1}}$), that commutes with every operator and hence is invariant under any Liouvillian. This state is not very interesting and will not be further discussed, though it may always be taken in combination with the two-spin singlet-triplet difference state to yield a pure singlet.

[6] Calculated numerically using MATLABs eig.m function for small systems and eigs.m for larger systems where the full diagonalisation went beyond the memory limit.

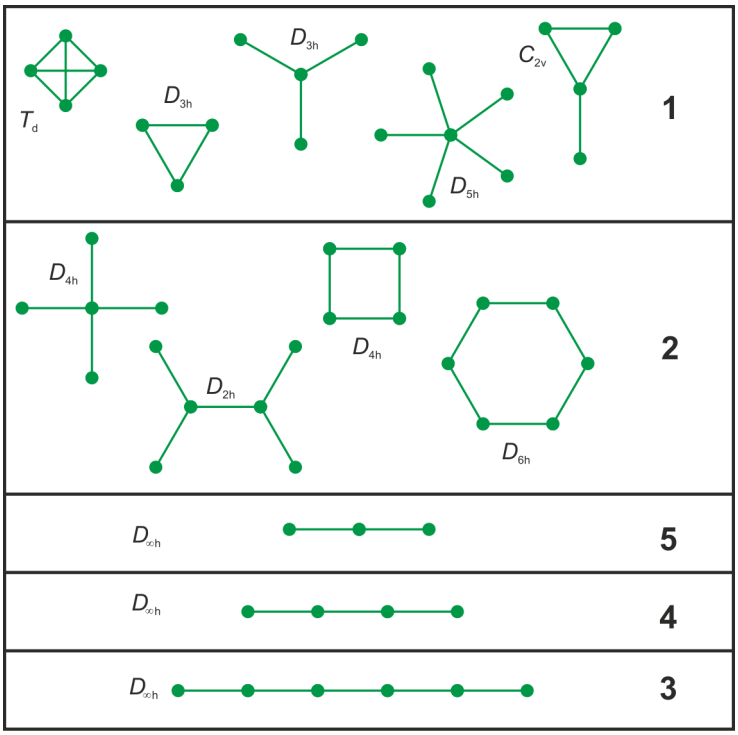

Figure 7.1. Strongly dipolar coupled spin-systems grouped according to null-space size *i.e.* number of long-lived states. Nodes represent spin positions and solid lines a separation of 1 Å($D \approx 120$ kHz). All pair-wise dipolar interactions were included in the simulation.

Inspection of the three-spin systems reveals the same result as was calculated by different methods in Refs [273] and [274]. For isotropic rotational diffusion only a linear arrangement of spins-$\frac{1}{2}$ can result in a long-lived state (besides $\hat{\mathbb{1}}$). Furthermore, and consistent with Ref [273], the long-lived states associated with this topology have a singlet across the terminal spins, there are four non-trivial long-lived states because the terminal singlet may be combined with each of $\{\hat{\mathbb{1}},\ T_{1,+1},\ T_{1,0},\ T_{1,-1}\}$ $\left(\propto \left\{\hat{\mathbb{1}}, \hat{S}_+, \hat{S}_z, \hat{S}_-\right\}\right)$ on the central spin.

For larger systems only coupling topologies that have a centre of inversion show any long-lived states at all, as would be expected for a dipolar relaxation superoperator which inherits the symmetry with respect to permutation across pairs of coupled spins of its Hamiltonian precursor. Perhaps surprisingly, the long-lived states are not formed from combinations of singlets across the most strongly coupled pairs, *i.e.* those with minimum separation, but instead from the symmetric combinations of products of singlets across the spins interchanged by the inversion symmetry. For example, the D_{4h} system with numbering shown in Fig 7.2, has just one non-trivial long-lived state which has the form:

$$P_{ST}^{\{1,3\}} + P_{ST}^{\{2,4\}} + \sqrt{3} P_{ST}^{\{1,3\}} P_{ST}^{\{2,4\}} \tag{7.26}$$

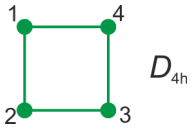

Figure 7.2 Strongly coupled four spin-$\frac{1}{2}$ system of D_{4h} point group with spin numbering.

which may be expanded according to Equation (7.20) and taken in combination with $\hat{\mathbb{1}}$ to yield the more readily recognised $P_S^{\{1,3\}}P_S^{\{2,4\}}$ – singlets across the diagonal of the square, *i.e.* across the weakest coupled spins. These are the spins related by inversion through the centre of the strongly coupled network. The same state, *i.e.* singlets across the inversion related spins, is also present in the null space of the linear four-spin topology, along with the unit operator and two further mixed states. There is no possible linear combination of the null space vectors which gives an isolated singlet across any pair of spins in the system, a fact which may be verified by substitution of the state into Equation (7.23).

7.4.2 Both Strongly and Weakly Interacting Systems

Multi-spin systems are known to have a long-lived state when a localised singlet interacts only weakly with neighbouring spins. Analogously to the linear three-spin system one might envisage four states arising from a localised singlet interacting weakly with another isolated spin:

$$P_S^{\{1,2\}}\hat{\mathbb{1}} \tag{7.27}$$

$$P_S^{\{1,2\}}T_{1,+1} \tag{7.28}$$

$$P_S^{\{1,2\}}T_{1,0} \tag{7.29}$$

$$P_S^{\{1,2\}}T_{1,-1} \tag{7.30}$$

where $T_{1,i}$ are the ISTs (directly proportional to the single spin operators). Indeed, a stretched isosceles triangles returns just such a null space. However, in practice if a system had a truly isolated spin it would be immune to dipolar interactions anyway. More interesting is the possibility of sets of strongly coupled pairs of spins which are strongly dipolar coupled within a pair ($D \approx$ 120 kHz) but weakly coupled between pairs ($D \approx 120$ Hz). Such systems were modelled in the current section with basic spin separations of 1 Å and 10 Å for strong and weak interactions respectively. The results of this analysis are shown in Fig 7.3.

When the null space is not too large the states deriving from singlet states across distinct pairs of spins are listed. From direct inspection of the output eigenvectors this description is less

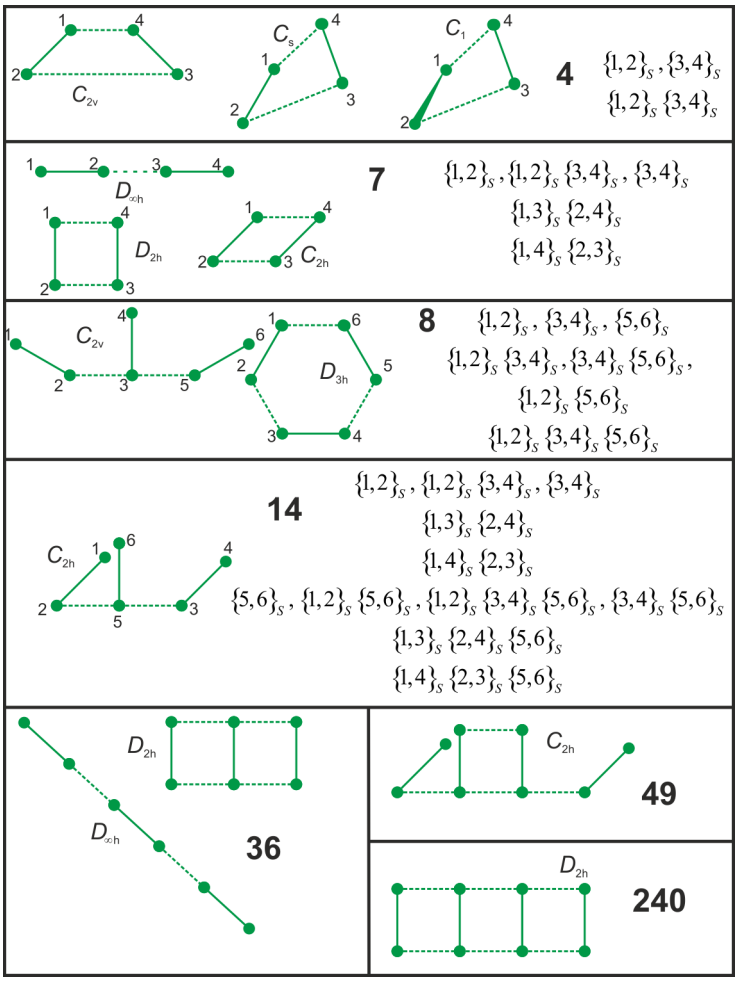

Figure 7.3. Multi-spin systems with both strong ($D \approx 120$ kHz represented by solid lines) and weak ($D \approx 120$ Hz represented by dashed lines) dipolar couplings, grouped according to null-space size, n. When $n < 20$ the constituent states of each group based upon singlet states, P_S (Equation (7.18)), across pairs of spins $\{i, j\}$ are given. Nodes represent spin positions. All pair-wise dipolar interactions were included.

intuitive than the singlet-triplet difference states but is much more useful and it should be noted that an isolated singlet-triplet mixed state is related to a pure singlet by simple addition of a unit operator and the linear combination of singlet-triplet difference states encountered across the weakly coupled spins may be related to products of localised singlets by:

$$P_S^{\{ab\}\{cd\}} = \frac{1}{4}\left(\hat{\mathbb{1}} + \sqrt{3}P_{ST}^{\{ab\}} + \sqrt{3}P_{ST}^{\{cd\}} + 3P_{ST}^{\{ab\}\{cd\}}\right) \tag{7.31}$$

where the numerical factors are included to account for vector normalisation. In the figures the short-hand $\{ab\}$ is used for a singlet across spins a and b. In most cases, such state-lists, along with the unit operator, can completely define the null space basis in terms of linearly independent states.

However, for the four-spin C_{2h} parallelogram there is an additional long-lived state not built

from localised P_{ST} states. The seventh state is the sum of all sixteen states which are direct product permutations of $\{\hat{\mathbb{1}},\ T_{1,+1},\ T_{1,0},\ T_{1,-1}\}$. It is difficult to imagine how this state could be useful.

Inspection of the results in Fig 7.3 reveals that spin systems which have strongly coupled pairs of spins related to each other by a centre of inversion have the largest null spaces. The *pairs of pairs* need not be related by a centre of inversion which coincides with that of the whole system if there is one, but one which reflects the local symmetry of pair of pairs. Given that a dipolar operator can couple only two spins directly, it is natural that most long-lived states will be based on two-spin singlets and products of two-spin singlets.

Consider, for example, the $C_{2\mathrm{h}}$ six-spin system that has fourteen long-lived states despite not having an overall centre of inversion. The states listed can be understood as direct-product type combinations of the null space of the four-spin $C_{2\mathrm{h}}$ parallelogram with the null space of a simple two-spin system.

$$\left\{\begin{array}{c} \hat{\mathbb{1}} \\ \{1,2\}_S \\ \{3,4\}_S \\ \{1,2\}_S\{3,4\}_S \\ \{1,3\}_S\{2,4\}_S \\ \{1,4\}_S\{2,3\}_S \end{array}\right\} \otimes \left\{\begin{array}{c} \hat{\mathbb{1}} \\ \{5,6\}_S \end{array}\right\} \tag{7.32}$$

where $\{ab\}_S$ indicates a singlet state across spins a and b and the set is completed by the two states that arise from the $\{\hat{\mathbb{1}},\ T_{1,+1},\ T_{1,0},\ T_{1,-1}\}$ mixed state on the parallelogram with either $\{5,6\}_S$ or $\hat{\mathbb{1}}$ on the other spin-pair.

For systems, such as the $D_{2\mathrm{h}}$ six-spin rectangular system in which there are three pairs of inversion-related strongly-coupled pairs one might expect 42 states by direct addition of the three sets of fourteen states available from twinning each parallelogram with the remaining two spins for which there are three permutations, though in fact taking such permutations returns some states repeatedly. In reality we observed only 36 states. The states arising from taking all three permutations of parallelogram and pairs return the expected products of the five singlet derived states across four-spins and singlet/$\hat{\mathbb{1}}$ on the two-spins, keeping only one incidence of each state of course. All three two-spin singlets arise as the product of P_S with $\hat{\mathbb{1}}_4$ but of course the three permutations of $\hat{\mathbb{1}}_4 \otimes \hat{\mathbb{1}}_2$ give some states multiple times and thus only one occurrence

is contributed to the total. In addition there are some more complicated mixed states which could not be simplified.

If the weakly coupled spin-pairs are brought closer together the long-lived states become increasingly perturbed and tend smoothly to the strong coupling limiting case of Fig 7.1 which has matching symmetry.

Clearly increasing the number of inversion-related pairs increases the number of long-lived states more dramatically than simply adding more pairs of spins in any orientation. Equally increasing the spin-system size by introducing pairs of spins seems more realistic than adding completely isolated spins. Therefore, having established some symmetry rules for maximising the number of long-lived states it is fruitful to consider some real molecules which might be expected to show such states in reality. The next section is concerned with null-space analysis of some commercially available molecules.

7.5 Real Molecule Examples

7.5.1 Experimentally Observed Four-Spin Long-Lived States

Ref [293] reports the observation of long-lived states in three molecules with four spin-$\frac{1}{2}$ systems. The molecules are 4-aminobenzoic acid, **1**, 4-hydroxybenzoic acid, **2**, and citric acid, **3**, for which the structures and their measured T_{LLS}, that is long-lived state lifetime, are summarised in Fig 7.4. The identities of the long-lived states are not known however. In this work the authors suggest that the long-lived state may be an isolated singlet on one of the pairs of spins with minimum separation though this is called into question by the asymmetric scalar couplings of the 'singlet spins' to external nuclei. Later work by the same authors in Ref [290] reveals that relatively strong inter-pair scalar coupling can give some immunity to the coherent evolution of a singlet incurred by asymmetric scalar coupling of the pair to external spins,[7] thus supporting the hypothesis that the long-lived state is a localised singlet.

Our analysis of systems with similar symmetry, $D_{2\mathrm{h}}$ in the case of 4-aminobenzoic acid and 4-hydroxybenzoic acid and probably C_1 in the case of citric acid (unless the H-bonding between the two carboxylic acid groups holds the structure extremely rigidly), Fig 7.3, reveals that in both cases there is a localised singlet across either pair of strongly coupled spins which might indeed be responsible for the experimentally observed long-lived character. However, in both cases there is also a product singlet state across both localised singlets and for the two aromatic

[7] Analogous to the suppression of evolution of the RP by strong exchange or dipolar coupling.

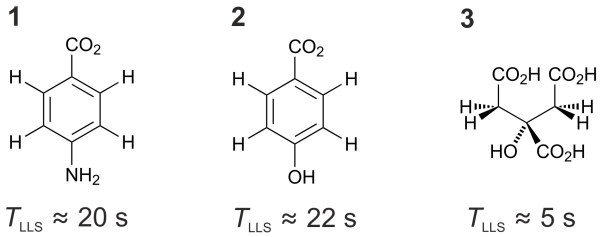

Figure 7.4. Molecules with four-spin systems that have been shown experimentally to exhibit a long-lived state. **1** 4-aminobenzoic acid, **2** 4-hydroxybenzoic acid and **3** citric acid. For each molecule the measured lifetime of this state, T_{LLS}, is shown.

molecules products of singlet pairs across any permutation of the four spins may be populated. Which state is populated in the experiments will depend on the pulse sequence used.

7.5.2 Three Real Molecule Examples

In order to maximise the number of long-lived states in a real molecule we require:

- Strongly-coupled pairs of spins
- Inversion symmetry, independent of molecular symmetry, between pairs of strongly-coupled spins
- Molecular rigidity so that the symmetry between pairs is not significantly broken by molecular motion
- Small CSA of the spins of interest (being immune to dipolar relaxation does not provide immunity to CSA relaxation)
- Weak scalar (and dipolar) coupling to external spins

Most of the above criteria have been met by the molecules in the previous section in which long-lived states have been observed. However we present here a further three example molecules, bicyclopropylidene, naphthalenetetrone and p-benzoquinone (Fig 7.5), that are expected to show multiple long-lived states.

In the following simulations the dipolar interactions were calculated directly from crystal structure geometry coordinates. The crystal structure geometries were input and thus the CSA tensors and scalar couplings were estimated using the DFT GIAO B3LYP/EPR-II method in Gaussian 03 [294]. The Gaussian output files can be found in the molecules folder of the *Spinach*

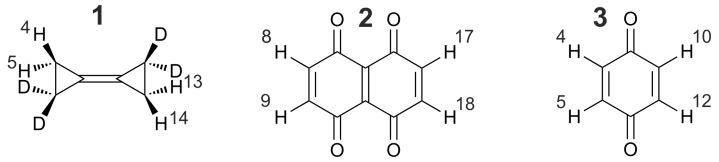

Figure 7.5. Example molecules expected to show long-lived states. **1** bicylopropylidene, **2** naphthalenetetrone and **3** p-benzoquinone. Numbering shown is consistent with the Gaussian output files available in the molecules folder of the *Spinach* library. The relevant data pertaining to these simulations are reproduced in the subsequent tables.

Table 7.1. Atomic parameters for bicyclopropylidene calculated with Gaussian 03 (using B3LYP functional and EPR-II basis. NMR properties were computed using the GIAO method). Atom numbering is as in the Gaussian output file and Fig 7.5 molecule **1**. Crystal structure from Ref [295]

Atom	**Atomic coordinates / Å**	**Chemical shift tensor / ppm**
4	$\begin{pmatrix}1.878000 & -0.332000 & 1.779200\end{pmatrix}$	$\begin{pmatrix}31.9666 & -0.8605 & 0.6082\\ -5.0811 & 37.6188 & -6.4210\\ 5.3750 & -7.1735 & 36.9629\end{pmatrix}$
5	$\begin{pmatrix}2.430600 & 0.651700 & 0.690600\end{pmatrix}$	$\begin{pmatrix}41.2897 & 1.4425 & -3.2160\\ 6.0879 & 31.6434 & -2.2064\\ -7.5668 & -1.6927 & 33.3079\end{pmatrix}$
13	$\begin{pmatrix}-0.604000 & -2.226700 & -1.186600\end{pmatrix}$	$\begin{pmatrix}30.4288 & 2.6108 & -0.2093\\ -0.6744 & 44.6410 & -0.3937\\ -0.1147 & -5.8230 & 31.3936\end{pmatrix}$
14	$\begin{pmatrix}-0.051500 & -1.243000 & -2.274700\end{pmatrix}$	$\begin{pmatrix}34.0984 & -1.2143 & -6.1301\\ 1.6543 & 30.6556 & -2.8968\\ -6.5945 & 2.7798 & 41.9037\end{pmatrix}$

library but the relevant data for these simulations are summarised for each molecule in Tables 7.1 to 7.6.[8]

Dipole-dipole Relaxation Only

In order to consider dipolar relaxation only, the CSA tensors were averaged to their isotropic components. By comparison of the geometries of the example molecules with the spin systems surveyed earlier one would probably expect each molecule to have a null space of seven states. The ten smallest eigenvalues (from a total of 256) resulting from diagonalisation of the dipole-dipole relaxation superoperator of each molecule are given in Table 7.7. Inspection of these ten eigenvalues allows clear definition of the null space eigenvectors, those with eigenvalues more

[8]It should be noted that *Spinach* reads the Gaussian output files directly and thus the file for bicyclopropylidene-d_4 as used here was 'artificially deuterated' by replacing the unwanted ^{1}H spins with spin-0 nuclei which *Spinach* ignores.

Table 7.2. Scalar coupling parameters for bicyclopropylidene, in Hz, calculated by Gaussian 03 (using B3LYP/EPR-II with GIAO). Atom numbering is as in the Gaussian output file and Fig 7.5 molecule **1**.

Atom	**4**	**5**	**13**
5	-16.5886		
13	2.14004	2.60914	
14	2.56393	2.15407	-16.225

than 100 times smaller than the average. As expected each molecule returns six non-trivial long-lived states (and the unit operator) when considering dipolar relaxation alone. The nature of the states is essentially identical to those observed for the D_{2h} rectangle of Fig 7.3, though the closer proximity between the pairs in the real molecules leads to some additional perturbation of the states and they are slightly less well-defined than in the artificial example, and accordingly the small eigenvalues are slightly larger. They are slightly further along the road to the strongly coupled limiting case (just one long-lived state (Fig 7.1) than the idealised example – this is particularly true of p-benzoquinone as it has the smallest separation between the spins). However, as can clearly be seen in Table 7.7, there are still seven states with eigenvalues at least 100 times smaller than the average.

Table 7.3. Atomic parameters for naphthalenetetrone calculated with Gaussian 03 (using B3LYP functional and EPR-II basis. NMR properties were computed using the GIAO method). Atom numbering is as in the Gaussian output file and Fig 7.5 molecule **2**. Crystal structure from Ref [296]

Atom	**Atomic coordinates / Å**	**Chemical shift tensor / ppm**
8	$\begin{pmatrix}1.033300 & -3.199200 & -1.104100\end{pmatrix}$	$\begin{pmatrix}31.7033 & 3.6987 & -0.5024\\ 3.5559 & 23.5725 & -1.9032\\ 0.1729 & -1.2690 & 28.5119\end{pmatrix}$
9	$\begin{pmatrix}2.756400 & -1.665700 & -1.491800\end{pmatrix}$	$\begin{pmatrix}25.3357 & 4.4757 & 2.3360\\ 4.3285 & 30.2041 & -1.4728\\ 0.8655 & -1.3147 & 27.5992\end{pmatrix}$
17	$\begin{pmatrix}-2.756400 & 1.665700 & 1.491800\end{pmatrix}$	$\begin{pmatrix}25.3357 & 4.4757 & 2.3360\\ 4.3285 & 30.2041 & -1.4728\\ 0.8655 & -1.3147 & 27.5992\end{pmatrix}$
18	$\begin{pmatrix}-1.033300 & 3.199200 & 1.104100\end{pmatrix}$	$\begin{pmatrix}31.7033 & 3.6987 & -0.5024\\ 3.5559 & 23.5725 & -1.9032\\ 0.1728 & -1.2690 & 28.5119\end{pmatrix}$

Table 7.4. Scalar coupling parameters for naphthalenetetrone, in Hz, calculated by Gaussian03 (using B3LYP/EPR-II with GIAO). Atom numbering is as in the Gaussian output file and Fig 7.5 molecule **2**.

Atom	**8**	**9**	**17**
9	9.25793		
17	-0.293323	-0.383734	
18	-0.401759	-0.293323	9.25793

Dipole-dipole and CSA evolution

As has been mentioned previously long-lived states are only invariant under operators with which they commute. Thus, though dipole-dipole relaxation is usually the dominant mechanism in liquid-state NMR, the long-lived states identified here are not necessarily immune to other modes of relaxation. Modulation of chemical shift anisotropies is one such mechanism and in order to improve the realism of our system the contributions to relaxation from rotational modulation of CSA were also included. As the frequency difference incurred through CSA depends linearly on the applied field strength a moderate field of 1.0 T was used in the simulation. The ten smallest eigenvalues for this case are shown in Table 7.7 for each molecule. At this field there remain six long-lived states, (the same singlet based states as previously) and the values are largely unchanged. As would be expected increasing the field increases the eigenvalues.

Table 7.5. Atomic parameters for p-benzoquinone calculated with Gaussian 03 (using B3LYP functional and EPR-II basis. NMR properties were computed using the GIAO method). Atom numbering is as in the Gaussian output file and Fig 7.5 molecule **3**. Crystal structure from Ref [297]

Atom	**Atomic coordinates / Å**	**Chemical shift tensor / ppm**
4	$\begin{pmatrix}0.848400 & -0.311900 & 2.313900\end{pmatrix}$	$\begin{pmatrix}24.7672 & 1.1127 & -0.5008\\ 0.8491 & 28.8392 & 2.1272\\ -0.4283 & 2.9854 & 23.5466\end{pmatrix}$
5	$\begin{pmatrix}0.351600 & -2.222000 & 1.090200\end{pmatrix}$	$\begin{pmatrix}24.6358 & 1.0725 & 0.5672\\ 1.4291 & 25.7714 & 3.7926\\ 0.5845 & 2.9719 & 25.8630\end{pmatrix}$
10	$\begin{pmatrix}-0.351600 & 2.222000 & -1.090200\end{pmatrix}$	$\begin{pmatrix}24.6358 & 1.0725 & 0.5672\\ 1.4291 & 25.7714 & 3.7926\\ 0.5845 & 2.9719 & 25.8630\end{pmatrix}$
12	$\begin{pmatrix}-0.848400 & 0.311900 & -2.313900\end{pmatrix}$	$\begin{pmatrix}24.7672 & 1.1127 & -0.5008\\ 0.8491 & 28.8392 & 2.1272\\ -0.4283 & 2.9854 & 23.5466\end{pmatrix}$

Table 7.6. Scalar coupling parameters for p-benzoquinone, in Hz, calculated by Gaussian03 (using B3LYP/EPR-II with GIAO). Atom numbering is as in the Gaussian output file and Fig 7.5 molecule **3**.

Atom	**4**	**5**	**10**
5	13.1280		
10	2.20162	-0.52824	
12	-0.578260	2.20162	13.1280

Coherent Evolution

We have thus far ignored the coherent evolution part of the Liouvillian, *i.e.* $\hat{\hat{H}}$, assuming that the well-developed methods of coherent control render it uninteresting. For completeness here however we switch on the coherent evolution again, and hence scalar couplings and Zeeman interactions are allowed to contribute, though as we are dealing here with chemically equivalent nuclei there are still no differences in isotropic chemical shifts. This time the full Liouvillian, $\hat{\hat{L}} = \hat{\hat{H}} + \mathrm{i}\hat{\hat{R}}$, is diagonalised and its null space inspected.

The final column of Table 7.7 shows the ten smallest eigenvalues of a system with dipole-dipole and CSA relaxation and coherent evolution in a 1.0 T static field. Bicyclopropylidene, which has the largest out-of-pair scalar couplings and the largest CSA, suffers the largest reduction in its null space size as there remains only one state which has a significantly smaller eigenvalue than the average, and even this is not clearly distinguishable from the next largest. For this molecule the clear differentiation between null space eigenvalues and the rest is no longer present.

Naphthalenetetrone and p-benzoquinone however appear far more promising. Even under uncontrolled coherent evolution there is one extremely long lived state (eigenvalue $< 10^{-10}$ s^{-1}) aside from the unit operator. This state is the product singlet state across the inversion related spins of the full four-spin system, using the numbering of Fig 7.5, for naphthalenetetrone the state is:

$$P_S^{\{8,18\}} P_S^{\{9,17\}} \tag{7.33}$$

and for p-benzoquinone it is:

$$P_S^{\{4,12\}} P_S^{\{5,10\}} \tag{7.34}$$

Even when the field is increased to 10 T this particular state retains an eigenvalue of less than 10^{-10} s^{-1}. In a weaker field, for example 0.1 T, the four other singlet-based states also show long-

lived character. As coherent evolution can be suppressed, to a large extent, in NMR experiments the full relaxation operator null space states (column two of Table 7.7) is likely to be the most useful.

7.6 Conclusions

In the work presented in this chapter we implemented a null space analysis of the relaxation superoperator on a range of different multi-spin systems with a range of system geometries. It has been shown that there are long-lived states available even in strongly dipolar coupled

Table 7.7. Ten smallest absolute eigenvalues (in s^{-1}) for dipolar relaxation only, dipolar and CSA relaxation and under the full Liouvillian for the three example molecules of Fig 7.5, in a 1.0 T static magnetic field. The identically zero eigenvalue always belongs to the identity operator. A 10^{-10} s isotropic rotational correlation time was used in all cases.

Molecule	Dipolar relaxation	Dipolar and CSA relaxation	Total Liouvillian
1	0	0	0
	0.0000	0.0009	0.0684
	0.0015	0.0024	0.1271
	0.0038	0.0046	0.7623
	0.0057	0.0064	2.3863
	0.0057	0.0065	2.8843
	0.0087	0.0093	3.4775
	1.8803	1.8695	3.9168
	1.8803	1.8695	3.1968
	1.8803	1.8809	5.6113
2	0	0	0
	0.0000	0.0000	0.0000
	0.0001	0.0003	0.0643
	0.0003	0.0004	0.0644
	0.0004	0.0005	0.1581
	0.0004	0.0005	0.2967
	0.0006	0.0009	0.2988
	0.1710	0.1683	0.3294
	0.1710	0.1683	0.3778
	0.1710	0.1683	0.4549
3	0	0	0
	0.0000	0.0000	0.0000
	0.0032	0.0033	0.0648
	0.0038	0.0038	0.0946
	0.0084	0.0085	0.1612
	0.0084	0.0085	0.3264
	0.0088	0.0088	0.3382
	0.1669	0.1644	0.3904
	0.1669	0.1644	0.4158
	0.1669	0.1669	0.5289

systems when the system has a centre of inversion. For systems which comprise several strongly coupled pairs of spins with weak inter-pair dipolar coupling many long-lived states are available. The number of long-lived states is maximised by having strongly coupled pairs related by a centre of inversion, which need not be coincident with the centre of inversion (if there is one) of the whole system.

We have examined three real molecules for long-lived states under dipole-dipole relaxation only, dipole-dipole and CSA relaxation and finally under the full relaxation superoperator and coherent evolution. In the former two limits, all three molecules exhibit the seven long-lived states typical of their symmetry. Additionally, both naphthalenetetrone and p-benzoquinone return two extremely long-lived states even under coherent evolution. The long-lived state, aside from the identity operator, is formed from the product of singlets across the inversion related spins of the full system.

Of course it would be of practical interest to try and identify more precisely the nature of the long-lived states that have thus far been observed [293]. They are most likely to be localised singlet states, in which case the extremely long-lived state, the product of singlets across the inversion centre of the whole system, of naphthalenetetrone and p-benzoquinone might provide an even more dramatic lifetime enhancement if the state can be populated in the first instance. It would be interesting to apply the same procedure used here to the systematic study of states immune to other forms of relaxation, for example CSA, as obviously states found in the null space of two or more relaxation superoperators would be extremely useful.

From a practical perspective the next steps will be to investigate if it is possible to drive a system into the product of singlet states experimentally but such a challenge is beyond the scope of this work. Having established a straightforward method of examining molecules for long-lived states this could be applied to any molecule with a spin system small enough to be computable, and should be used to screen real molecules for suitability before beginning experiments.

Bibliography

[1] U. E. Steiner and T. Ulrich. Magnetic-field effects in chemical-kinetics and related phenomena. *Chem. Rev.*, 89(1), 51–147, 1989

[2] P. Atkins and T. Lambert. Effect of a magnetic-field on chemical-reaction. *Annu. Rep. Prog. Chem. Sect. A-Physical & inorganic chemistry*, 72, 67–88, 1975

[3] R. Kaptein and L. J. Oosterhoff. Chemically induced dynamic nuclear polarization III (anomalous multiplets of radical coupling and disproportionation products). *Chem. Phys. Lett.*, 4(4), 214–216, 1969

[4] G. L. Closs. Mechanism explaining nuclear spin polarizations in radical combination reactions. *J. Am. Chem. Soc.*, 91(16), 4552–4554, 1969

[5] W. Gerlach and O. Stern. Das magnetische Moment des Silberatoms. *Z. Phys. A Hadron. Nuc.*, 9, 353–355, 1922

[6] W. Gerlach and O. Stern. Der experimentelle Nachweis der Richtungsquantelung im Magnetfeld. *Z. Phys. A Hadron. Nuc.*, 9, 349–352, 1922

[7] W. Pauli. Zur Frage der theoretischen Deutung der Satelliten einiger Spektrallinien und ihrer Beeinflussung durch magnetische Felder. *Naturwissenschaften*, 12, 741–743, 1924

[8] W. Pauli. Zur Quantenmechanik des magnetischen Elektrons. *Z. Phys. A Hadron. Nuc.*, 43, 601–623, 1927

[9] P. A. M. Dirac. The quantum theory of the electron. *Proc. R. Soc. Lon. A Mat.*, 117(778), 610–624, 1928

[10] P. W. Atkins and R. S. Friedman. *Molecular quantum mechanics.* Oxford University Press, 1997

[11] D. M. Brink and G. R. Satchler. *Angular momentum.* Clarendon, 1993

[12] D. A. Varshalovich, A. N. Moskalev and V. K. Khersonskii. *Quantum theory of angular momentum.* World Scientific, 1988

[13] S. Bhatnagar, R. Mathur and R. N. Kapur. The effects of magnetic field on certain chemical reactions. *Philosophical Mag. Series 7*, 8, 457–573, 1925

[14] K. McLauchlan and U. Steiner. The spin-correlated radical pair as a reaction intermediate. *Mol. Phys.*, 73(2), 241–263, 1991

[15] C. T. Rodgers and P. J. Hore. Chemical magnetoreception in birds: The radical pair mechanism. *Proc. Natl. Acad. Sci. USA*, 106(2), 353–360, 2009

[16] A. B. Rovinsky and A. M. Zhabotinsky. Mechanism and mathematical-model of the oscillating bromate-ferroin-bromalonic acid reaction. *J. Phys. Chem*, 88(25), 6081–6084, 1984

[17] N. J. Turro, V. Ramamurthy and J. Scaiano. *Modern molecular photochemistry of organic molecules.* University science books, 2010

[18] M. Tanaka, T. Yago, Y. Sakaguchi, T. Takamasu and M. Wakasa. Magnetic field effects on hydrogen abstraction of thiobenzophenone as a probe of microviscosity. *J. Phys. Chem B*, 115(9), 1936–1943, 2011

[19] C. Timmel, U. Till, B. Brocklehurst, K. McLauchlan and P. Hore. Effects of weak magnetic fields on free radical recombination reactions. *Mol. Phys.*, 95(1), 71–89, 1998

[20] R. Prabhakar, P. E. M. Siegbahn, B. F. Minaev and H. Ågren. Activation of triplet dioxygen by glucose oxidase: Spin-orbit coupling in the superoxide ion. *J. Phys. Chem B*, 106(14), 3742–3750, 2002

[21] O. Efimova and P. J. Hore. Role of exchange and dipolar interactions in the radical pair model of the avian magnetic compass. *Biophys. J.*, 94(5), 1565–1574, 2008

[22] H. Cao, K. Miyata, T. Tamura, Y. Fujiwara, A. Katsuki, C.-H. Tung and Y. Tanimoto. Effects of high magnetic field on the intramolecular exciplex fluorescence of chain-linked phenanthrene and dimethylaniline. *J. Phys. Chem A*, 101(4), 407–411, 1997

[23] K. B. Henbest, P. Kukura, C. T. Rodgers, P. J. Hore and C. R. Timmel. Radio frequency magnetic field effects on a radical recombination reaction: A diagnostic test for the radical pair mechanism. *J. Am. Chem. Soc.*, 126(26), 8102–8103, 2004

[24] C. T. Rodgers, S. A. Norman, K. B. Henbest, C. R. Timmel and P. J. Hore. Determination of radical re-encounter probability distributions from magnetic field effects on reaction yields. *J. Am. Chem. Soc.*, 129(21), 6746–6755, 2007

[25] A. Carrington and A. D. McLachlan. *Introduction to magnetic resonance*. Harper and Row, 1969

[26] P. J. Hore. *Nuclear magnetic resonance*. Oxford University Press, 1995

[27] H. R. Ward. Chemically induced dynamic nuclear polarization (CIDNP). I. Phenomenon, examples, and applications. *Acc. Chem. Res*, 5(1), 18–24, 1972

[28] P. J. Hore, C. G. Joslin and K. A. McLauchlan. The role of chemically-induced dynamic electron polarization (CIDEP) in chemistry. *Chem. Soc. Rev.*, 8, 29–61, 1979

[29] R. G. Lawler. Chemically induced dynamic nuclear polarization (CIDNP). II. Radical-pair model. *Acc. Chem. Res*, 5(1), 25–33, 1972

[30] S. K. Wong, D. A. Hutchinson and J. K. S. Wan. Chemically induced dynamic electron polarization. II. A general theory for radicals produced by photochemical reactions of excited triplet carbonyl compounds. *J. Chem. Phys.*, 58(3), 985–989, 1973

[31] K. A. McLauchlan and D. G. Stevens. The electron spin polarized (CIDEP) spectra of isopropyl radicals. A test of radical pair mechanism theory. *J. Magn. Reson. (1969)*, 63(3), 473 – 483, 1985

[32] C. Blaettler, F. Jent and H. Paul. A novel radical-triplet pair mechanism for chemically induced electron polarization (CIDEP) of free radicals in solution. *Chem. Phys. Lett.*, 166(4), 375 – 380, 1990

[33] H. G. Kuettner, H. L. Selzle and E. W. Schlag. Radiationless transitions in the presence of a weak magnetic field: Glyoxal. *Chem. Phys. Lett.*, 48, 207 – 211, 1977

[34] P. P. Parui, D. N. Nath and M. Chowdhury. Determination of interfacial dielectric constant of AOT-based reverse micelle by probing magnetic field effect on pyrene-DMA exciplex luminescence. *Chem. Phys. Lett.*, 396(4-6), 329 – 334, 2004

[35] H. Werner, H. Staerk and A. Weller. Solvent, isotope and magnetic-field effects in geminate recombination of radical ion-pairs. *J. Chem. Phys.*, 68(5), 2419–2426, 1978

[36] A. Weller, H. Staerk and R. Treichel. Magnetic-field effects on geminate radical-pair recombination. *Faraday Discuss. Chem. Soc.*, 78, 271–278, 1984

[37] K. Maeda, K. B. Henbest, F. Cintolesi, I. Kuprov, C. T. Rodgers, P. A. Liddell, D. Gust, C. R. Timmel and P. J. Hore. Chemical compass model of avian magnetoreception. *Nature*, 453(7193), 387–390, 2008

[38] S. J. Kubarev and E. A. Pshenichnov. The effect of high frequency magnetic fields on the recombination of radicals. *Chem. Phys. Lett.*, 28(1), 66 – 67, 1974

[39] S. Batchelor, K. McLauchlan and I. Shkrob. Reaction yield detected magnetic-resonance in exciplex systems .1. B_0 and B_1 spectra. *Mol. Phys.*, 75(3), 501–529, 1992

[40] C. R. Timmel and P. J. Hore. Oscillating magnetic field effects on the yields of radical pair reactions. *Chem. Phys. Lett.*, 257(3-4), 401 – 408, 1996

[41] N. J. Turro and B. Kraeutler. Magnetic field and magnetic isotope effects in organic photochemical reactions. A novel probe of reaction mechanisms and a method for enrichment of magnetic isotopes. *Acc. Chem. Res*, 13(10), 369–377, 1980

[42] N. J. Turro, D. R. Anderson, M.-F. Chow, C.-J. Chung and B. Kraeutler. Magnetic and micellar effects on photoreactions. 2. Magnetic isotope effects on quantum yields and magnetic field effects on separation efficiency. Correlation of carbon-13 enrichment parameters with quantum yield measurements. *J. Am. Chem. Soc.*, 103(13), 3892–3896, 1981

[43] A. Hoff. Magnetic-interactions between photosynthetic reactants. *Photochem. Photobiol.*, 43(6), 727–745, 1986

[44] A. Angerhofer and R. Bittl. Radicals and radical pairs in photosynthesis. *Photochem. Photobiol.*, 63(1), 11–38, 1996

[45] R. A. Goldstein and S. G. Boxer. Effects of nuclear-spin polarization on reaction dynamics in photosynthetic bacterial reaction centers. *Biophys. J.*, 51(6), 937–946, 1987

[46] W. Wiltschko and R. Wiltschko. Magnetic orientation and magnetoreception in birds and other animals. *J. Comp. Physiol. A: Neuroethology, Sensory, Neural, and Behavioral Physiology*, 191, 675–693, 2005

[47] J. L. Kirschvink. Birds, bees and magnetism - A new look at the old problem of magnetoreception. *Trends Neurosci.*, 5(5), 160–167, 1982

[48] S. M. Reppert, R. J. Gegear and C. Merlin. Navigational mechanisms of migrating monarch butterflies. *Trends Neurosci.*, 33(9), 399 – 406, 2010

[49] K. J. Lohmann and C. M. F. Lohmann. Orientation and open-sea navigation in sea turtles. *J. Exp. Biol*, 199(1), 73–81, 1996

[50] H. Cadiou and P. A. McNaughton. Avian magnetite-based magnetoreception: a physiologist's perspective. *J. R. Soc. Interface*, 7, S193–S205, 2010

[51] K. Schulten, C. E. Swenberg and A. Weller. Biomagnetic sensory mechanism based on magnetic-field modulated coherent electron-spin motion. *Z. Phys. Chem. Frankfurt*, 111(1), 1–5, 1978

[52] Y. Liu, R. Edge, K. Henbest, C. Timmel, P. Hore and P. Gast. Magnetic field effect on singlet oxygen production in a biochemical system. *Chem. Comm.*, 2, 174–176, 2005

[53] M. Ahmad, P. Galland, T. Ritz, R. Wiltschko and W. Wiltschko. Magnetic intensity affects cryptochrome-dependent responses in *Arabidopsis thaliana*. *PLANTA*, 225(3), 615–624, 2007

[54] S.-R. Harris, K. B. Henbest, K. Maeda, J. R. Pannell, C. R. Timmel, P. J. Hore and H. Okamoto. Effect of magnetic fields on cryptochrome-dependent responses in *Arabidopsis thaliana*. *J. R. Soc. Interface*, 6(41), 1193–1205, 2009

[55] A. Buchachenko, D. Kouznetsov, S. Arkhangelsky, M. Orlova and A. Markarian. Spin biochemistry - Magnetic Mg-24 Mg-25 Mg-26 isotope effect in mitochondrial ADP phosphorylation. *Cell Biochem. Biophys.*, 43(2), 243–251, 2005

[56] A. L. Buchachenko, D. A. Kuznetsov, N. N. Breslavskaya, L. N. Shchegoleva and S. E. Arkhangelsky. Calcium induced ATP synthesis: Isotope effect, magnetic parameters and mechanism. *Chem. Phys. Lett.*, 505(4-6), 130–134, 2011

[57] A. L. Buchachenko, N. N. Lukzen and J. B. Pedersen. On the magnetic field and isotope effects in enzymatic phosphorylation. *Chem. Phys. Lett.*, 434(1-3), 139–143, 2007

[58] A. L. Buchachenko and D. A. Kuznetsov. Magnetic field affects enzymatic ATP synthesis. *J. Am. Chem. Soc.*, 130(39), 12868–12869, 2008

[59] P. Hore, J. Jones and S. Wimperis. *NMR: The toolkit.* Oxford University Press, 2000

[60] R. Ernst, G. Bodenhausen and A. Wokaun. *Principles of nuclear magnetic resonance in one and two dimensions.* Clarendon Press, 1987

[61] V. A. Bagryansky, V. I. Borovkov and Y. N. Molin. Quantum beats in radical pairs. *Russ. Chem. Rev.*, 76(6), 535–549, 2007

[62] U. Till, C. R. Timmel, B. Brocklehurst and P. J. Hore. The influence of very small magnetic fields on radical recombination reactions in the limit of slow recombination. *Chem. Phys. Lett.*, 298(1-3), 7–14, 1998

[63] I. Kuprov. Spin dynamics. Lecture Course, 2009

[64] O. Efimova and P. J. Hore. Evaluation of nuclear quadrupole interactions as a source of magnetic anisotropy in the radical pair model of the avian magnetic compass. *Mol. Phys.*, 107(7), 665–671, 2009

[65] P. Zeeman. On the influence of magnetism on the nature of the light emitted by a substance. *Philosophical Mag.*, 43, 226–239, 1897

[66] M. Levitt. *Spin dynamics.* Wiley, 2001

[67] S. M. Blinder. The hyperfine interaction Hamiltonian. *J. Mol. Spectrosc.*, 5, 17–23, 1960

[68] C. Herring and M. Flicker. Asymptotic exchange coupling of two hydrogen atoms. *Phys. Rev.*, 134(2A), A362–A366, 1964

[69] P. Atkins and J. De Paula. *Atkins' Physical Chemistry.* Oxford University Press, 8th edition, 2006

[70] J. B. Pedersen. High field CIDNP. General analytic results. *J. Chem. Phys.*, 67, 4097–4102, 1977

[71] G. J. Bowden and M. J. Prandolini. Complete solution for two-coupled spin-1/2 nuclei evolving under chemical shift and dipolar interaction. *J. Math. Chem.*, 16, 1–7, 1994

[72] M. Justinek, G. Grampp, S. Landgraf, P. J. Hore and N. N. Lukzen. Electron self-exchange kinetics determined by MARY spectroscopy: Theory and experiment. *J. Am. Chem. Soc.*, 126(17), 5635–5646, 2004

[73] J. B. Pedersen and J. H. Freed. Theory of chemically induced dynamic electron polarization. I. *J. Chem. Phys.*, 58(7), 2746–2762, 1973

[74] Matlab 2009a. The MathWorks Inc., 2009. Natick, MA, USA

[75] R. Haberkorn. Density matrix description of spin-selective radical pair reactions. *Mol. Phys.*, 32(5), 1491–1493, 1976

[76] I. K. Kominis. Quantum zeno effect explains magnetic-sensitive radical-ion-pair reactions. *Phys. Rev. E*, 80(5), 056115, 2009

[77] I. K. Kominis. Quantum zeno effect explains magnetic-sensitive radical-ion-pair reactions - *erratum*. *Phys. Rev. E*, 81(2), 029901, 2010

[78] I. K. Kominis. Radical-ion-pair reactions are the biochemical equivalent of the optical double-slit experiment. *Phys. Rev. E*, 83(5, Part 2), 056118, 2011

[79] J. A. Jones and P. J. Hore. Spin-selective reactions of radical pairs act as quantum measurements. *Chem. Phys. Lett.*, 488(1-3), 90–93, 2010

[80] A. I. Shushin. Effect of state-selective reactive decay on the evolution of quantum systems. *J. Chem. Phys.*, 133(4), 7, 2010

[81] K. L. Ivanov, M. V. Petrova, N. N. Lukzen and K. Maeda. Consistent treatment of spin-selective recombination of a radical pair confirms the Haberkorn approach. *J. Phys. Chem A*, 114(35), 9447–9455, 2010

[82] J. Jones, K. Maeda and P. Hore. Reaction operators for spin-selective chemical reactions of radical pairs. *Chem. Phys. Lett.*, 507(4-6), 269 – 273, 2011

[83] I. K. Kominis. Comment on 'spin-selective reactions of radical pairs act as quantum measurements' (chem. phys. lett. 488 (2010) 90-93). *Chem. Phys. Lett.*, 508(1-3), 182 – 183, 2011

[84] J. Jones, K. Maeda, U. Steiner and P. Hore. Reply to comment on 'Spin-selective reactions of radical pairs act as quantum measurements'. *Chem. Phys. Lett.*, 508(1-3), 184 – 185, 2011

[85] M. Tiersch. Open quantum system approach to decide on the recombination mechanism in radical pair reactions. In *Spin Chemistry Meeting 2011*. 2011

[86] J. Kowalewski and L. Maeler. *Nuclear spin relaxation in liquids: Theory, experiments and applications.* Taylor and Francis, 2006

[87] H.-P. Breuer and F. Petruccione. *The theory of open quantum systems.* Oxford University Press, Oxford ; New York, 2002

[88] E. M. Gauger, E. Rieper, J. J. L. Morton, S. C. Benjamin and V. Vedral. Sustained quantum coherence and entanglement in the avian compass. *Phys. Rev. Lett.*, 106(4), 040503–040506, 2011

[89] S. Gao. Lindblad approach to quantum dynamics of open systems. *Phys. Rev. B*, 57(8), 4509–4517, 1998

[90] A. G. Redfield. On the theory of relaxation processes. *IBM J. Res. Dev.*, 1(1), 19–31, 1957

[91] R. K. Wangsness and F. Bloch. The dynamical theory of nuclear induction. *Phys. Rev.*, 89(4), 728–739, 1953

[92] M. Goldman. Formal theory of spin-lattice relaxation. *J. Magn. Reson.*, 149(2), 160–187, 2001

[93] N. Wagner-Rundell. *Electron spin relaxation effects on radical recombinations reactions in weak magnetic fields.* DPhil thesis, University of Oxford, 2008

[94] H. J. Hogben, P. J. Hore and I. Kuprov. Strategies for state space restriction in densely coupled spin systems with applications to spin chemistry. *J. Chem. Phys.*, 132(17), 174101, 2010

[95] H. J. Hogben, M. Krzystyniak, G. T. P. Charnock, P. J. Hore and I. Kuprov. Spinach - a software library for simulation of spin dynamics in large spin systems. *J. Magn. Reson.*, 208(2), 179–194, 2011

[96] H. J. Hogben, O. Efimova, N. Wagner-Rundell, C. R. Timmel and P. J. Hore. Possible involvement of superoxide and dioxygen with cryptochrome in avian magnetoreception: Origin of Zeeman resonances observed by in vivo EPR spectroscopy. *Chem. Phys. Lett.*, 480(1-3), 118–122, 2009

[97] H. Hogben, P. Hore and I. Kuprov. Multiple decoherence-free states in multi-spin systems. *J. Magn. Reson.*, 211(2), 217 – 220, 2011

[98] I. Kuprov, N. Wagner-Rundell and P. J. Hore. Polynomially scaling spin dynamics simulation algorithm based on adaptive state-space restriction. *J. Magn. Reson.*, 189(2), 241–250, 2007

[99] I. Kuprov. Polynomially scaling spin dynamics II: Further state-space compression using Krylov subspace techniques and zero track elimination. *J. Magn. Reson.*, 195(1), 45–51, 2008

[100] C. T. Rodgers. *Effects of periodic magnetic fields on radical recombination reactions.* Part II thesis, University of Oxford, 2003

[101] N. N. Lukzen. Personal Communication, 2009

[102] A. A. Karabanov, I. Kuprov, G. T. P. Charnock, A. van der Drift, L. Edwards and W. Koeckenberger. On the accuracy of the state space restriction approximation for spin dynamics simulations. *J. Chem. Phys.*, 135, 084106, 2011

[103] L. Edwards and I. Kuprov. Personal Communication, 2011

[104] M. Hochbruck and C. Lubich. On krylov subspace approximations to the matrix exponential operator. *SIAM J. Numer. Anal.*, 34(5), 1911–1925, 1997

[105] N. Biggs. *Algebraic graph theory.* Cambridge University Press, 1974

[106] V. A. Bagryansky, O. M. Usov, V. I. Borovkov, T. V. Kobzeva and Y. N. Molin. Quantum beats in recombination of spin-correlated radical ion pairs with equivalent protons. *Chem. Phys.*, 255(2-3), 237 – 245, 2000

[107] J. H. Freed. Generalized cumulant expansions and spin-relaxation theory. *J. Chem. Phys.*, 49(1), 376–392, 1968

[108] I. Kuprov, N. Wagner-Rundell and P. J. Hore. Bloch-Redfield-Wangsness theory engine implementation using symbolic processing software. *J. Magn. Reson.*, 184(2), 196–206, 2007

[109] I. Kuprov. Diagonalization-free implementation of spin relaxation theory for large spin systems. *J. Magn. Reson.*, 209(1), 31–38, 2011

[110] J. L. Sudmeier, S. E. Anderson and J. S. Frye. Calculation of nuclear spin relaxation times. *Concept. Magnetic. Res.*, 2(4), 197–212, 1990

[111] Mathematica 7. Wolfram Research, Inc., 2010. Champaign, Illinois

[112] M. Bak, J. T. Rasmussen and N. C. Nielsen. SIMPSON: A general simulation program for solid-state NMR spectroscopy. *J. Magn. Reson.*, 147(2), 296 – 330, 2000

[113] M. Veshtort and R. G. Griffin. SPINEVOLUTION: A powerful tool for the simulation of solid and liquid state NMR experiments. *J. Magn. Reson.*, 178(2), 248 – 282, 2006

[114] A. Jerschow. MathNMR: Spin and spatial tensor manipulations in Mathematica. *J. Magn. Reson.*, 176(1), 7 – 14, 2005

[115] J. M. Dust and D. R. Arnold. Substituent effects on benzyl radical ESR hyperfine coupling constants. The $\sigma_\alpha\cdot$ scale based upon spin delocalization. *J. Am. Chem. Soc.*, 105(5), 1221–1227, 1983

[116] M. V. Fedin, H. Yashiro, P. A. Purtov, E. G. Bagryanskaya and M. D. E. Forbes. Theoretical and experimental studies of chemically induced electron-nuclear polarization in low magnetic fields. *Mol. Phys.*, 100(8), 1171–1180, 2002

[117] A. L. Buchachenko, D. A. Kouznetsov, M. A. Orlova and A. A. Markarian. Magnetic isotope effect of magnesium in phosphoglycerate kinase phosphorylation. *Proc. Natl. Acad. Sci. USA*, 102(31), 10793–10796, 2005

[118] D. Hornikova, P. Herman, J. Mejsnar, J. Vecer and J. Zurmanova. Creatine kinase structural changes induced by substrates. *Biochim. Biophys. Acta: Proteins & Proteomics*, 1794(2), 270 – 274, 2009

[119] J. Cai, G. G. Guerreschi and H. J. Briegel. Quantum control and entanglement in a chemical compass. *Phys. Rev. Lett.*, 104(22), 220502, 2010

[120] G. Jaeger. *Quantum entanglement, information, and the foundations of quantum mechanics*. Springer, 2009

[121] S. C. Benjamin. Entanglement tutorial. In *Quantum measurement and chemical spin dynamics*. 2010

[122] D. Bouwmeester, J. Pan, K. Mattle, M. Eibl, H. Weinfurter and A. Zeilinger. Experimental quantum teleportation. *Nature*, 390(6660), 575–579, 1997

[123] S. Hill and W. K. Wootters. Entanglement of a pair of quantum bits. *Phys. Rev. Lett.*, 78(26), 5022–5025, 1997

[124] W. K. Wootters. Entanglement of formation of an arbitrary state of two qubits. *Phys. Rev. Lett.*, 80(10), 2245–2248, 1998

[125] G. E. Katsoprinakis, A. T. Dellis and I. K. Kominis. Coherent triplet excitation suppresses the heading error of the avian compass. *New J. Phys.*, 12, 085016, 2010

[126] J. H. Van der Waals and M. S. de Groot. Magnetic interactions related to phosporescence. In *The triplet state*. 1967

[127] H. F. Hameka. Spin-orbit coupling in organic molecules. In *The triplet state*. 1967

[128] C. A. Hutchinson Jr. Magnetic resonance sprectra of organic molecules in triplet states in single crystals. In *The triple state*. 1967

[129] P. B. Ayscough, editor. *Electron spin resonance vol 5*. The Chemical Society, 1979

[130] P. W. Atkins and G. T. Evans. Electron spin polarization in a rotating triplet. *Mol. Phys.*, 27, 1633–1644, 1974

[131] P. J. Hore. The triplet mechanism of chemically induced dynamic electorn polarization. A vector model. *Chem. Phys. Lett.*, 69, 563–566, 1980

[132] T. Yago, J.-U. Weidner, G. Link, T.-S. Lin and G. Kothe. Quantum oscillations in photo-excited triplet states in an external magnetic field. *Chem. Phys. Lett.*, 438(4-6), 351–357, 2007

[133] G. Kothe, T. Yago, J.-U. Weidner, G. Link, M. Lukaschek and T.-S. Lin. Quantum oscillations and polarization of nuclear spins in photoexcited triplet states. *J. Phys. Chem B*, 114(45), 14755–14762, 2010

[134] U. Steiner. Spin-selective depopulation of triplet sublevels in rapidly rotating triplet exciplexes detected by a heavy-atom-induced magnetic field effect. *Chem. Phys. Lett.*, 74, 108–112, 1980

[135] M. J. M. Leask. A physicochemical mechanism for magnetic field detection by migratory birds and homing pigeons. *Nature*, 267, 144–145, 1977

[136] C. T. Rodgers. *Magnetic Field Effects in Chemical Systems.* DPhil thesis, University of Oxford, 2007

[137] S. Salzmann, M. R. Silva-Junior, W. Thiel and C. M. Marian. Influence of hte LOV domain on low-lying excited states of flavin: A combined quantum-mechanics/molecular-mechanics investigation. *J. Phys. Chem B*, 113, 15610–15618, 2009

[138] W. Wiltschko and R. Wiltschko. Magnetoreception in birds: Two receptors for two different tasks. *J. Ornithol.*, 148, S61–S76, 2007

[139] W. Wiltschko and R. Wiltschko. Magneticcompass of European robins. *Science*, 176(4030), 62–64, 1972

[140] R. J. Gegear, L. E. Foley, A. Casselman and S. M. Reppert. Animal cryptochromes mediate magnetoreception by an unconventional photochemical mechanism. *Nature*, 463(7282), 804–808, 2010

[141] R. Muheim, N. Edgar, K. Sloan and J. Phillips. Magnetic compass orientation in C57BL/6J mice. *Learning & Behavior*, 34, 366–373, 2006

[142] F. J. Diego-Rasilla, R. M. Luengo and J. B. Phillips. Magnetic compass mediates nocturnal homing by the alpine newt, *Triturus alpestris. Behav. Ecol. Sociobiol.*, 58, 361–365, 2005

[143] J. L. Gould, J. L. Kirschvink and K. S. Deffeyes. Bees have magnetic remanence. *Science*, 201(4360), 1026–1028, 1978

[144] R. Blakemore. Magnetotactic bacteria. *Science*, 190(4212), 377–379, 1975

[145] U. Homberg. In search of the sky compass in the insect brain. *Naturwissenschaften*, 91, 199–208, 2004

[146] R. Wiltschko and W. Wiltschko. Avian navigation: From historical to modern concepts. *Animal Behaviour*, 65(2), 257 – 272, 2003

[147] H. G. Wallraff. Avian olfactory navigation: its empirical foundation and conceptual state. *Animal Behaviour*, 67(2), 189 – 204, 2004

[148] W. W. Cochran, H. Mouritsen and M. Wikelski. Migrating songbirds recalibrate their magnetic compass daily from twilight cues. *Science*, 304(5669), 405–408, 2004

[149] R. Muheim, J. B. Phillips and S. Åkesson. Polarized light cues underlie compass calibration in migratory songbirds. *Science*, 313(5788), 837–839, 2006

[150] A. J. Kalmijn. Electric and magnetic field detection in elasmobranch fishes. *Science*, 218(4575), 916–918, 1982

[151] M. G. Paulin. Electroreception and the compass sense of sharks. *J. Theor. Biol.*, 174(3), 325 – 339, 1995

[152] M. J. Freake, R. Muheim and J. B. Phillips. Magnetic maps in animals: A theory comes of age? *The Quarterly Review of Biology*, 81(4), 327–347, 2006

[153] R. Wiltschko and W. Wiltschko. Magnetoreception. *BioEssays*, 28(2), 157–168, 2006

[154] R. Wiltschko, S. Denzau, D. Gehring, P. Thalau and W. Wiltschko. Magnetic orientation of migratory robins, *Erithacus rubecula*, under long-wavelength light. *J. Exp. Biol*, 214, 3096–9101, 2011

[155] I. A. Solov'yov and W. Greiner. Theoretical analysis of an iron mineral-based magnetoreceptor model in birds. *Biophys. J.*, 93(5), 1493–1509, 2007

[156] J. L. Kirschvink, M. M. Walker, S. B. Chang, A. E. Dizon and K. A. Peterson. Chains of single-domain magnetite particles in chinook salmon, *Oncorhynchus tshawytscha*. *J. Comp. Physiol. A: Neuroethology, Sensory, Neural, and Behavioral Physiology*, 157, 375–381, 1985

[157] G. Falkenberg, G. Fleissner, K. Schuchardt, M. Kuehbacher, P. Thalau, H. Mouritsen, D. Heyes, G. Wellenreuther and G. Fleissner. Avian magnetorrection: Elaborate iron mineral containing dendrites in the upper beak seem to be a common feature of birds. *PloS One*, 5, e9231, 2010

[158] T. Ritz, S. Adem and K. Schulten. A model for photoreceptor-based magnetoreception in birds. *Biophys. J.*, 78(2), 707–718, 2000

[159] T. Biskup, E. Schleicher, A. Okafuji, G. Link, K. Hitomi, E. D. Getzoff and S. Weber. Direct observation of a photoinduced radical pair in a cryptochrome blue-light photoreceptor. *Angew. Chem. Intl. Ed.*, 48(2), 404–407, 2009

[160] J. C. S. Lau, N. Wagner-Rundell, C. T. Rodgers, N. J. B. Green and P. J. Hore. Effects of disorder and motion in a radical pair magnetoreceptor. *J. R. Soc. Interface*, 7, S257–S264, 2010

[161] I. A. Solov'yov, H. Mouritsen and K. Schulten. Acuity of a cryptochrome and vision-based magnetoreception system in birds. *Biophys. J.*, 99(1), 40–49, 2010

[162] J. Lau. Personal Communication, 2010

[163] H.-P. Lipp, A. L. Vyssotski, D. P. Wolfer, S. Renaudineau, M. Savini, G. Tröster and G. Dell'Omo. Pigeon homing along highways and exits. *Curr. Biol.*, 14(14), 1239 – 1249, 2004

[164] K. P. Able. Comparison of vanishing bearings, orientation directions and ringing recoveries of spring migrant white-throated sparrows (*Zonotrichia albicollis*). *J. Ornithol.*, 131, 317–323, 1990

[165] W. Wiltschko and R. Wiltschko. Migratory orientation of European robins is affected by the wavelength of light as well as by a magnetic pulse. *J. Comp. Physiol. A: Neuroethology, Sensory, Neural, and Behavioral Physiology*, 177, 363–369, 1995

[166] S. T. Emlen and J. T. Emlen. A technique for recording migratory orientation of captive birds. *The Auk*, 83(3), 361–367, 1966

[167] R. S. Coe, M. Prevot and P. Camps. New evidence for extraodinarily rapid change of the geomagnetic-field during a reversal. *Nature*, 374(6524), 687–692, 1995

[168] J. L. Kirschvink, M. M. Walker and C. E. Diebel. Magnetite-based magnetoreception. *Curr. Opin. Neurobiol.*, 11(4), 462–467, 2001

[169] R. Wiltschko, K. Stapput, P. Thalau and W. Wiltschko. Directional orientation of birds by the magnetic field under different light conditions. *J. R. Soc. Interface*, 7, S163–S177, 2010

[170] W. Wiltschko and R. Wiltschko. Light-dependent magnetoreception in birds: the behaviour of European robins, *Erithacus rubecula*, under monochromatic light of various wavelengths and intensities. *J. Exp. Biol*, 204(19), 3295–3302, 2001

[171] W. Wiltschko, U. Munro, H. Ford and R. Wiltschko. Red-light disrupts magnetic orientation of migratory birds. *Nature*, 364(6437), 525–527, 1993

[172] W. Wiltschko, A. Möller, M. Gesson, C. Noll and R. Wiltschko. Light-dependent magnetoreception in birds: Analysis of the behaviour under red light after pre-exposure to red light. *J. Exp. Biol*, 207(7), 1193–1202, 2004

[173] R. A. Holland. Differential effects of magnetic pulses on the orientation of naturally migrating birds. *J. R. Soc. Interface*, 7(52), 1617–1625, 2010

[174] C. Mora, M. Davison, J. Wild and M. Walker. Magnetoreception and its trigeminal mediation in the homing pigeon. *Nature*, 432(7016), 508–511, 2004

[175] D. A. Keays. A majority of iron rich cells in the feather follicle, olfactory epithelium and subcutaneous tissue of *Columbia livia* are negative for neuronal markers, are nucleated and share a similar ultrastructure. In *RIN 11. Orientation and navigation. Birds, humans and other animals.* 2011

[176] H. Mouritsen, G. Feenders, M. Liedvogel, K. Wada, E. D. Jarvis and M. E. Raichle. Night-vision brain area in migratory songbirds. *Proc. Natl. Acad. Sci. USA*, 102(23), 8339–8344, 2005

[177] M. Zapka, D. Heyers, C. M. Hein, S. Engels, N. L. Schneider, J. Hans, S. Weiler, D. Dreyer, D. Kishkinev, J. M. Wild and H. Mouritsen. Visual but not trigeminal mediation of magnetic compass information in a migratory bird. *Nature*, 461(7268), 1274–1278, 2009

[178] D. Heyers, M. Manns, H. Luksch, O. Guentuerkuen and H. Mouritsen. A visual pathway links brain structures active during magnetic compass orientation in migratory birds. *PLoS One*, 2(9), e937, 2007

[179] W. Wiltschko, K. Stapput, P. Thalau and R. Wiltschko. Avian magnetic compass: Fast adjustment to intensities outside the normal functional window. *Naturwissenschaften*, 93(6), 300–304, 2006

[180] T. Ritz, R. Wiltschko, P. J. Hore, C. T. Rodgers, K. Stapput, P. Thalau, C. R. Timmel and W. Wiltschko. Magnetic compass of birds is based on a molecule with optimal directional sensitivity. *Biophys. J.*, 96(8), 3451–3457, 2009

[181] N. Keary, T. Rudolph, J. Voss, P. Thalau, R. Wiltschko, W. Wiltschko and H. Bischof. Oscillating magnetic field disrupts magnetic orientation in zebra finches, *Taeniopygia guttata*. *Front. Zool.*, 6, 25, 2009

[182] P. Thalau, T. Ritz, K. Stapput, R. Wiltschko and W. Wiltschko. Magnetic compass orientation of migratory birds in the presence of a 1.315 MHz oscillating field. *Naturwissenschaften*, 92, 86–90, 2005

[183] M. Vácha, T. Půžová and M. Kvíčalová. Radio frequency magnetic fields disrupt magnetoreception in american cockroach. *J. Exp. Biol*, 212(21), 3473–3477, 2009

[184] J. Phillips. Use of magnetic compass cures by epigeic rodents. In *RIN 11. Orientation and navigation. Birds, humans and other animals*. 2011

[185] J. R. Woodward, C. R. Timmel, K. A. McLauchlan and P. J. Hore. Radio frequency magnetic field effects on electron-hole recombination. *Phys. Rev. Lett.*, 87(7), 077602, 2001

[186] C. T. Rodgers, K. B. Henbest, P. Kukura, C. R. Timmel and P. J. Hore. Low-field optically detected EPR spectroscopy of transient photoinduced radical pairs. *J. Phys. Chem A*, 109(23), 5035–5041, 2005

[187] M. Edn, Y. K. Lee and M. H. Levitt. Efficient simulation of periodic problems in NMR. Application to decoupling and rotational resonance. *J. Magn. Reson., Series A*, 120(1), 56 – 71, 1996

[188] M. Hohwy, H. Bildsoe, H. J. Jakobsen and N. C. Nielsen. Efficient spectral simulations in NMR of rotating solids. The γ-COMPUTE algorithm. *J. Magn. Reson.*, 136(1), 6–14, 1999

[189] I. A. Solov'yov and K. Schulten. Magnetoreception through cryptochrome may involve superoxide. *Biophys. J.*, 96(12), 4804–4813, 2009

[190] V. Balland, M. Byrdin, A. P. M. Eker, M. Ahmad and K. Brettel. What makes the difference between a cryptochrome and DNA photolyase? A spectroelectrochemical comparison of the flavin redox transitions. *J. Am. Chem. Soc.*, 131(2), 426–427, 2009

[191] W. H. Koppenol, D. M. Stanbury and P. L. Bounds. Electrode potentials of partially reduced oxygen species, from dioxygen to water. *Free Radical Bio. Med.*, 49(3), 317 – 322, 2010

[192] F. Mueller. *The chemistry and biochemistry of flavoenzymes*. CRC Press Inc, 1991

[193] J. C. Arents, M. A. Perez, J. Hendriks and K. J. Hellingwerf. On the midpoint potential of the FAD chromophore in a BLUF-domain containing photoreceptor protein. *FEBS Lett.*, 585(1), 167 – 172, 2011

[194] N. Hoang, E. Schleicher, S. Kacprzak, J.-P. Bouly, M. Picot, W. Wu, A. Berndt, E. Wolf, R. Bittl and M. Ahmad. Human and *Drosophila* cryptochromes are light activated by flavin photoreduction in living cells. *PloS Biology*, 6, e160, 2008

[195] J.-P. Bouly, E. Schleicher, M. Dionisio-Sese, F. Vandenbussche, D. V. D. Straeten, N. Bakrim, S. Meier, A. Batschauer, P. Galland, R. Bittl and M. Ahmad. Cryptochrome blue light photoreceptors are activated through interconversion of flavin redox states. *J. Biol. Chem.*, 282, 9381–9391, 2007

[196] M. Tinkham and M. W. P. Strandberg. Theory of the fine structure of the molecular oxygen ground state. *Phys. Rev.*, 97(4), 937–951, 1955

[197] E. Schleicher, R. Wenzel, M. Ahmad, A. Batschauer, L.-O. Essen, K. Hitomi, E. Getzoff, R. Bittl, S. Weber and A. Okafuji. The electronic state of flavoproteins: Investigations with proton electron-nuclear double resonance. *App. Magn. Reson.*, 37, 339–352, 2010

[198] K. P. Huber and G. Herzberg. *Molecular apectra and molecular structure Vol. 4*. Molecular Spectra and Molecular Structure. Van Nostrand Reinhold, New York, 2008

[199] G. Herzberg. *Spectra of diatomic molecules*. Molecular spectra and molecular structure. Van Nostrand, 1950

[200] T. Y. Karogodina, I. G. Dranov, S. V. Sergeeva, D. V. Stass and U. E. Steiner. Kinetic magnetic-field effect involving the small biologically relevant inorganic radicals NO and $O_2^{\bullet -}$. *ChemPhysChem*, 12(9), 1714–1728, 2011

[201] T. Karogodina, S. Sergeeva, D. Stass and U. Steiner. Magnetic field effect on recombination of nitric oxide and superoxide anion in high magnetic field. *Doklady Physical Chemistry*, 436, 5–7, 2011. ISSN 0012-5016

[202] H. R. Zeller, R. T. Shuey and W. Känzig. The molecular character of the $O_2^{\bullet -}$ -center in alkali halides. *J. Phys. Colloques*, 28(C4), 81–88, 1967

[203] M. C. R. Symons, G. W. Eastland and L. R. Denny. Effect of solvation on the electron spin resonance spectrum of the superoxide ion. *J. Chem. Soc. Faraday Trans. 1*, 76, 1868–1874, 1980

[204] J. Guy, S. McGorray, X. Qi, J. Fitzsimmons, A. Mancuso and N. Rao. Conjugated deferoxamine reduces blood-brain barrier disruption in experimental optic neuritis. *Ophthalmic Res.*, 26, 310–323, 1994

[205] S. Belia, F. Santilli, S. Beccafico, L. De Feudis, C. Morabito, G. Dav, G. Fan and M. A. Mariggi. Oxidative-induced membrane damage in diabetes lymphocytes: Effects on intracellular Ca^{2+} homeostasis. *Free Radical Res.*, 43(2), 138–148, 2009

[206] C. M. Wong, A. K. Cheema, L. Zhang and Y. J. Suzuki. Protein carbonylation as a novel mechanism in redox signaling. *Circulation Research*, 102(3), 310–318, 2008

[207] M. Hinata, I. Matsuoka, T. Iwamoto, Y. Watanabe and J. Kimura. Mechanism of Na^{+}/Ca^{2+} exchanger activation by hydrogen peroxide in guinea-pig ventricular myocytes. *J. Pharmacol. Sci.*, 103(3), 283–292, 2007

[208] J. Vsquez-Vivar, A. Denicola, R. Radi and O. Augusto. Peroxynitrite-mediated decarboxylation of pyruvate to both carbon dioxide and carbon dioxide radical anion. *Chem. Res. Toxicol.*, 10(7), 786–794, 1997

[209] R. Edge, A. El-Agamey, E. J. Land, S. Navaratnam and T. G. Truscott. Studies of carotenoid one-electron reduction radicals. *Arch. Biochem. Biophys*, 458(2), 104 – 110, 2007

[210] M. G. Bonini, S. Miyamoto, P. D. Mascio and O. Augusto. Production of the carbonate radical anion during xanthine oxidase turnover in the presence of bicarbonate. *J. Biol. Chem.*, 279(50), 51836–51843, 2004

[211] G. Lassmann, M. Kolberg, G. Bleifuss, A. Graslund, B.-M. Sjoberg and W. Lubitz. Protein thiyl radicals in disordered systems: A comparative EPR study at low temperature. *Phys. Chem. Chem. Phys.*, 5, 2442–2453, 2003

[212] I. A. Shkrob. The structure of the hydrated electron. part 1. Magnetic resonance of internally trapping water anions: A density functional theory study. *J. Phys. Chem A*, 111(24), 5223–5231, 2007

[213] I. A. Shkrob, W. J. Glover, R. E. Larsen and B. J. Schwartz. The structure of the hydrated electron. part 2. A mixed quantum/classical molecular dynamics embedded cluster density

functional theory: Single-excitation configuration interaction study. *J. Phys. Chem A*, 111(24), 5232–5243, 2007

[214] A. V. Veselov and R. W. Fessenden. Medium effects on the ESR spectrum of the hydrated electron. *J. Phys. Chem*, 97(14), 3497–3499, 1993

[215] C. M. R. Clancy and M. D. E. Forbes. Time-resolved electron paramagnetic resonance study of photoionization of tyrosine anion in aqueous solution. *Photochem. Photobiol.*, 69(1), 16–21, 1999

[216] R. A. Edwards, G. Jickling and R. J. Turner. The light-induced reactions of tryptophan with halocompounds. *Photochem. Photobiol.*, 75(4), 362–368, 2002

[217] C. W. M. Kay, R. Feicht, K. Schulz, P. Sadewater, A. Sancar, A. Bacher, K. Moebius, G. Richter and S. Weber. EPR, ENDOR and TRIPLE resonance spectroscopy on the neutral flavin radical in *Escherichia coli* DNA photolyase. *Biochemistry*, 38, 16740–16748, 1999

[218] S. Weber, K. Moebius, G. Richter and C. W. M. Kay. The electronic structure of the flavin co-factor in DNA photolyase. *J. Am. Chem. Soc*, 123, 3790–3798, 2001

[219] M. Liedvogel and H. Mouritsen. Cryptochromes-a potential magnetoreceptor: What do we know and what do we want to know? *J. R. Soc. Interface*, 7(Suppl. 2), S147–S162, 2010

[220] M. Liedvogel, K. Maeda, K. Henbest, E. Schleicher, T. Simon, C. R. Timmel, P. J. Hore and H. Mouritsen. Chemical magnetoreception: Bird cryptochrome 1a is excited by blue light and forms long-lived radical-pairs. *PLoS One*, 2(10), e1106, 2007

[221] A. Moller, S. Sagasser, W. Wiltschko and B. Schierwater. Retinal cryptochrome in a migratory passerine bird: A possible transducer for the avian magnetic compass. *Naturwissenschaften*, 91(12), 585–588, 2004

[222] H. Mouritsen, U. Janssen-Bienhold, M. Liedvogel, G. Feenders, J. Stalleicken, P. Dirks and R. Weiler. Cryptochromes and neuronal-activity markers colocalize in the retina of migratory birds during magnetic orientation. *Proc. Natl. Acad. Sci. USA*, 101(39), 14294–14299, 2004

[223] C. Niessner, S. Denzau, J. C. Gross, L. Peichl, H.-J. Bischof, G. Fleissner, W. Wiltschko and R. Wiltschko. Avian ultraviolet/violet cones identified as probable magnetoreceptors. *PLoS One*, 6(5), e20091, 2011

[224] K. B. Henbest, K. Maeda, P. J. Hore, M. Joshi, A. Bacher, R. Bittl, S. Weber, C. R. Timmel and E. Schleicher. Magnetic-field effect on the photoactivation reaction of *Escherichia coli* DNA photolyase. *Proc. Natl. Acad. Sci. USA*, 105(38), 14395–14399, 2008

[225] K. Maeda, A. J. Robinson, K. B. Henbest, H. J. Hogben, T. Biskup, M. Ahmad, , E. Schleicher, S. Weber, C. R. Timmel and P. J. Hore. Magnetically sensitive light-induced reactions in cryptochrome are consistent with its role as a magnetoreceptor. Submitted

[226] R. Sinha and D. Hader. UV-induced DNA damage and repair: A review. *Photoch. Photobio. Sci.*, 1(4), 225–236, 2002

[227] A. Sancar. Structure and function of DNA photolyase and cryptochrome blue-light photoreceptors. *Chem. Rev.*, 103(6), 2203–2237, 2003

[228] R. R. Rustandi and M. S. Jorns. Photoinduced spin-polarized radical-pair formation in a DNA photolyase substrate complex at low-temperature. *Biochemistry*, 34(7), 2284–2288, 1995

[229] K. Brettel and M. Byrdin. Reaction mechanisms of DNA photolyase. *Curr. Opin. Biol.*, 20(6), 693–701, 2010

[230] A. MacFarlane and R. Stanley. Cis-syn thymidine dimer repair by DNA photolyase in real time. *Biochemistry*, 42(28), 8558–8568, 2003

[231] K. Kume, M. Zylka, S. Sriram, L. Shearman, D. Weaver, X. Jin, E. Maywood, M. Hastings and S. Reppert. mCRY1 and mCRY2 are essential components of the negative limb of the circadian clock feedback loop. *Cell*, 98(2), 193–205, 1999

[232] C. Lin and T. Todo. The cryptochromes. *Genome Biol.*, 6(5), 220, 2005

[233] C. A. Brautigam, B. S. Smith, Z. Ma, M. Palnitkar, D. R. Tomchick, M. Machius and J. Deisenhofer. Structure of the photolyase-like domain of cryptochrome 1 from *Arabidopsis thaliana*. *Proc. Natl. Acad. Sci. USA*, 101(33), 12142–12147, 2004

[234] H. Park, S. Kim, A. Sancar and J. Deisenhofer. Crystal-structure of DNA photolyase from *Escherichia coli*. *Science*, 268(5219), 1866–1872, 1995

[235] T. Klar, R. Pokorny, J. Moldt, A. Batschauer and L.-O. Essen. Cryptochrome 3 from *Arabidopsis thaliana*: Structural and functional analysis of its complex with a folate light antenna. *J. Mol. Biol.*, 366(3), 954 – 964, 2007

[236] K. Hitomi, L. DiTacchio, A. S. Arvai, J. Yamamoto, S.-T. Kim, T. Todo, J. A. Tainer, S. Iwai, S. Panda and E. D. Getzoff. Functional motifs in the (6-4) photolyase crystal structure make a comparative framework for DNA repair photolyases and clock cryptochromes. *Proc. Natl. Acad. Sci. USA*, 106(17), 6962–6967, 2009

[237] H. Yang, Y. Wu, R. Tang, D. Liu, Y. Liu and A. R. Cashmore. The C termini of *Arabidopsis* cryptochromes mediate a constitutive light response. *Cell*, 103(5), 815 – 827, 2000

[238] S. Weber, C. Kay, H. Mogling, K. Mobius, K. Hitomi and T. Todo. Photoactivation of the flavin cofactor in *Xenopus laevis* (6-4) photolyase: Observation of a transient tyrosyl radical by time-resolved electron paramagnetic resonance. *Proc. Natl. Acad. Sci. USA*, 99(3), 1319–1322, 2002

[239] Y. Gindt, E. Vollenbroek, K. Westphal, H. Sackett, A. Sancar and G. Babcock. Origin of the transient electron paramagnetic resonance signals in DNA photolyase. *Biochemistry*, 38(13), 3857–3866, 1999

[240] B. Giovani, M. Byrdin, M. Ahmad and K. Brettel. Light-induced electron transfer in a cryptochrome blue-light photoreceptor. *Nat. Struct. Biol.*, 10(6), 489–490, 2003

[241] S. Weber, T. Biskup, A. Okafuji, A. R. Marino, T. Berthold, G. Link, K. Hitomi, E. D. Getzoff, E. Schleicher and J. R. Norris, Jr. Origin of light-induced spin-correlated radical pairs in cryptochrome. *J. Phys. Chem B*, 114(45), 14745–14754, 2010

[242] T. Biskup. Personal Communication, 2011

[243] A. Robinson. *Magnetic field effects on biological systems.* DPhil thesis, University of Oxford, 2010

[244] K. Maeda. Personal Communication, 2011

[245] C. Aubert, M. Vos, P. Mathis, A. Eker and K. Brettel. Intraprotein radical transfer during photoactivation of DNA photolyase. *Nature*, 405(6786), 586–590, 2000

[246] F. Lendzian, M. Sahlin, F. MacMillan, R. Bittl, R. Fiege, S. Potsch, B. M. Sjoberg, A. Graslund, W. Lubitz and G. Lassmann. Electronic structure of neutral tryptophan radicals in ribonucleotide reductase studied by EPR and ENDOR spectroscopy. *J. Am. Chem. Soc.*, 118(34), 8111–8120, 1996

[247] A. Weller, F. Nolting and H. Staerk. A quantitative interpretation of the magnetic field effect on hyperfine-coupling-induced triplet fromation from radical ion pairs. *Chem. Phys. Lett.*, 96(1), 24 – 27, 1983

[248] T. Suzuki, T. Miura, K. Maeda and T. Arai. Spin dynamics of the radical pair in a low magnetic field studied by the transient absorption detected magnetic field effect on the reaction yield and switched external magnetic field. *J. Phys. Chem A*, 109(44), 9911–9918, 2005

[249] T. Fukuju, H. Yashiro, K. Maeda, H. Murai and T. Azumi. Singlet-born SCRP observed in the photolysis of tetraphenylhydrazine in an SDS micelle: Time dependence of the population of the spin states. *J. Phys. Chem A*, 101(42), 7783–7786, 1997

[250] M. V. Fedin, P. A. Purtov and E. G. Bagryanskaya. Anisotropic hyperfine interaction-induced spin relaxation in a low magnetic field. *Chem. Phys. Lett.*, 339(5-6), 395 – 404, 2001

[251] A. I. Shushin. The effect of the spin exchange interaction on SNP and RYDMR spectra of geminate radical pairs. *Chem. Phys. Lett.*, 181(2-3), 274–278, 1991

[252] M. Byrdin, A. Lukacs, V. Thiagarajan, A. P. M. Eker, K. Brettel and M. H. Vos. Quantum yield measurements of short-lived photoactivation intermediates in DNA photolyase: Toward a detailed understanding of the triple tryptophan electron transfer chain. *J. Phys. Chem A*, 114(9), 3207–3214, 2010

[253] D. M. Popovic, A. Zmiric, S. D. Zaric and E. W. Knapp. Energetics of radical transfer in DNA photolyase. *J. Am. Chem. Soc.*, 124(14), 3775–3782, 2002

[254] A. Lukacs, A. P. M. Eker, M. Byrdin, K. Brettel and M. H. Vos. Electron hopping through the 15 angstrom triple tryptophan molecular wire in DNA photolyase occurs within 30 ps. *J. Am. Chem. Soc*, 130(44), 14394–14395, 2008

[255] V. Binhi. Do naturally occurring magnetic nanoparticles in the human body mediate increased risk of childhood leukaemia with EMF exposure? *Int. J. Radiat. Biol.*, 84(7), 569–579, 2008

[256] N. G. Chalkias, P. Kahawong and E. P. Giannelis. Activity increase of horseradish peroxidase in the presence of magnetic particles. *J. Am. Chem. Soc*, 130(10), 2910–2911, 2008

[257] A. E. Cohen. Nanomagnetic control of intersystem crossing. *J. Phys. Chem. A*, 113(41), 11084–11092, 2009

[258] N. Yang and A. E. Cohen. Optical imaging through scattering media via magnetically modulated fluorescence. *Opt. Express*, 18(25), 25461–25467, 2010

[259] J. Cai. Quantum probe and design for a chemical compass with magnetic nanostructures. *Phys. Rev. Lett.*, 106(10), 100501, 2011

[260] N. N. Greenwood and A. Earnshaw. *Chemistry of the elements*. Butterworth-Heinemann, Oxford, 2nd ed. edition, 1997

[261] S. Blundell. *Magnetism in condensed matter*. Oxford University Press, Oxford, 2001

[262] Y. Gossuin, P. Gillis, A. Hocq, Q. L. Vuong and A. Roch. Magnetic resonance relaxation properties of superparamagnetic particles. *Wiley Interdiscip Rev Nanomed Nanobiotechnol.*, 1(3), 299–310, 2009

[263] J. A. Osborn. Demagnetizing factors of the general ellipsoid. *Phys. Rev.*, 67(11-1), 351–357, 1945

[264] M. Carravetta and M. H. Levitt. Theory of long-lived nuclear spin states in solution nuclear magnetic resonance. I. Singlet states in low magnetic field. *J. Chem. Phys.*, 122(21), 214505, 2005

[265] G. Pileio and M. H. Levitt. Theory of long-lived nuclear spin states in solution nuclear magnetic resonance. II. Singlet spin locking. *J. Chem. Phys.*, 130(21), 214501, 2009

[266] M. Carravetta, O. G. Johannessen and M. H. Levitt. Beyond the T_1 limit: singlet nuclear spin states in low magnetic fields. *Phys. Rev. Lett.*, 92(15), 153003, 2004

[267] P. R. Vasos, A. Comment, R. Sarkar, P. Ahuja, S. Jannin, J. P. Ansermet, J. A. Konter, P. Hautle, B. van den Brandt and G. Bodenhausen. Long-lived states to sustain hyperpolarized magnetization. *Proc. Natl. Acad. Sci. USA*, 106(44), 18469–18473, 2009

[268] W. S. Warren, E. Jenista, R. T. Branca and X. Chen. Increasing hyperpolarized spin lifetimes through true singlet eigenstates. *Science*, 323(5922), 1711–1714, 2009

[269] P. Ahuja, R. Sarkar, S. Jannin, P. R. Vasos and G. Bodenhausen. Proton hyperpolarisation preserved in long-lived states. *Chem. Comm.*, 46(43), 8192–8194, 2010

[270] G. Pileio, M. Carravetta and M. H. Levitt. Storage of nuclear magnetization as long-lived singlet order in low magnetic field. *Proc. Natl. Acad. Sci. USA*, 107(40), 17135–17139, 2010

[271] P. Ahuja, R. Sarkar, P. R. Vasos and G. Bodenhausen. Diffusion coefficients of biomolecules using long-lived spin states. *J. Am. Chem. Soc.*, 131(22), 7498–7499, 2009

[272] M. C. D. Tayler, S. Marie, A. Ganesan and M. H. Levitt. Determination of molecular torsion angles using nuclear singlet relaxation. *J. Am. Chem. Soc.*, 132(24), 8225–8227, 2010

[273] A. K. Grant and E. Vinogradov. Long-lived states in solution NMR: Theoretical examples in three- and four-spin systems. *J. Magn. Reson.*, 193(2), 177–190, 2008

[274] A. A. Karabanov, C. Bretschneider and W. Koeckenberger. Symmetries of the master equation and long-lived states of nuclear spins. *J. Chem. Phys.*, 131(20), 20415, 2009

[275] P. Ahuja, R. Sarkar, P. R. Vasos and G. Bodenhausen. Long-lived states in multiple-spin systems. *ChemPhysChem*, 10(13), 2217–2220, 2009

[276] N. Bloembergen, E. M. Purcell and R. V. Pound. Relaxation effects in nuclear magnetic resonance absorption. *Phys. Rev.*, 73(7), 679–712, 1948

[277] T. Maly, G. T. Debelouchina, V. S. Bajaj, K.-N. Hu, C.-G. Joo, M. L. MakJurkauskas, J. R. Sirigiri, P. C. A. van der Wel, J. Herzfeld, R. J. Temkin and R. G. Griffin. Dynamic nuclear polarization at high magnetic fields. *J. Chem. Phys.*, 128(5), 052211, 2008

[278] J. Natterer and J. Bargon. Parahydrogen induced polarization. *Proc. Nuc. Mag. Res. Sp.*, 31(4), 293 – 315, 1997

[279] E. L. Hahn. Spin echoes. *Phys. Rev.*, 80(4), 580–594, 1950

[280] Y. Cohen, L. Avram and L. Frish. Diffusion NMR spectroscopy in supramolecular and combinatorial chemistry: An old parameter - New insights. *Angew. Chem. Intl. Ed.*, 44(4), 520–554, 2005

[281] S. Cavadini, J. Dittmer, S. Antonijevic and G. Bodenhausen. Slow diffusion by singlet state NMR spectroscopy. *J. Am. Chem. Soc.*, 127(45), 15744–15748, 2005

[282] S. Cavadini and P. R. Vasos. Singlet states open the way to longer time-scales in the measurement of diffusion by NMR spectroscopy. *Concept. Magnetic. Res. Part A*, 32A(1), 68–78, 2008

[283] R. Sarkar, P. R. Vasos and G. Bodenhausen. Singlet-state exchange NMR spectroscopy for the study of very slow dynamic processes. *J. Am. Chem. Soc.*, 129(2), 328–334, 2007

[284] P. Ahuja, R. Sarkar, P. R. Vasos and G. Bodenhausen. Molecular properties determined from the relaxation of long-lived spin states. *J. Chem. Phys.*, 127(13), 134112, 2007

[285] A. Viale and S. Aime. Current concepts on hyperpolarized molecules in MRI. *Curr. Opin. Chem. Biol.*, 14(1), 90 – 96, 2010

[286] G. Pileio, M. Carravetta, E. Hughes and M. H. Levitt. The long-lived nuclear singlet state of N-15-nitrous oxide in solution. *J. Am. Chem. Soc.*, 130(38), 12582–12583, 2008

[287] T. Yu and J. H. Eberly. Sudden death of entanglement. *Science*, 323(5914), 598–601, 2009

[288] G. Hétet, J. J. Longdell, A. L. Alexander, P. K. Lam and M. J. Sellars. Electro-optic quantum memory for light using two-level atoms. *Phys. Rev. Lett.*, 100(2), 023601, 2008

[289] S. S. Roy and T. S. Mahesh. Initialization of NMR quantum registers using long-lived singlet states. *Phys. Rev. A*, 82(5), 052302, 2010

[290] G. Pileio and M. H. Levitt. J-stabilization of singlet states in the solution NMR of multiple-spin systems. *J. Magn. Reson.*, 187(1), 141–145, 2007

[291] M. Carravetta and M. H. Levitt. Long-lived nuclear spin states in high-field solution NMR. *J. Am. Chem. Soc.*, 126(20), 6228–6229, 2004

[292] K. Gopalakrishnan and G. Bodenhausen. Lifetimes of the singlet-states under coherent off-resonance irradiation in NMR spectroscopy. *J. Magn. Reson.*, 182(2), 254 – 259, 2006

[293] G. Pilelo, M. Concistre, M. Carravetta and M. H. Levitt. Long-lived nuclear spin states in the solution NMR of four-spin systems. *J. Magn. Reson.*, 182(2), 353–357, 2006

[294] M. J. Frisch, G. W. Trucks, H. B. Schlegel, G. E. Scuseria, M. A. Robb, J. R. Cheeseman, J. A. Montgomery, Jr., T. Vreven, K. N. Kudin, J. C. Burant, J. M. Millam, S. S. Iyengar, J. Tomasi, V. Barone, B. Mennucci, M. Cossi, G. Scalmani, N. Rega, G. A. Petersson, H. Nakatsuji, M. Hada, M. Ehara, K. Toyota, R. Fukuda, J. Hasegawa, M. Ishida, T. Nakajima, Y. Honda, O. Kitao, H. Nakai, M. Klene, X. Li, J. E. Knox, H. P. Hratchian, J. B. Cross, C. Adamo, J. Jaramillo, R. Gomperts, R. E. Stratmann, O. Yazyev, A. J. Austin, R. Cammi, C. Pomelli, J. W. Ochterski, P. Y. Ayala, K. Morokuma, G. A. Voth, P. Salvador, J. J. Dannenberg, V. G. Zakrzewski, S. Dapprich, A. D. Daniels, M. C. Strain, O. Farkas, D. K. Malick, A. D. Rabuck, K. Raghavachari, J. B. Foresman, J. V. Ortiz, Q. Cui, A. G. Baboul, S. Clifford, J. Cioslowski, B. B. Stefanov, G. Liu, A. Liashenko, P. Piskorz, I. Komaromi, R. L. Martin, D. J. Fox, T. Keith, M. A. Al-Laham, C. Y. Peng, A. Nanayakkara, M. Challacombe, P. M. W. Gill, B. Johnson, W. Chen, M. W. Wong, C. Gonzalez, and J. A. Pople. Gaussian 03. Pittsburgh PA, 2003

[295] M. Traetteberg, A. Simon, E. M. Peters and A. Demeijere. Bonding properties of bicyclopropylidene - gas-phase electron-diffraction study and X-ray crystal structure analysis. *J. Mol. Struct.*, 118(3-4), 333–343, 1984

[296] F. Herbstein and M. Kapon. 1,4,5,8-Naphthalenetetrone. *Acta Crystallog. Sect. B-Structural Science*, 38, 3123–3125, 1982

[297] J. Trotter. Rho-benzoquinone - mean-plane fourier. *Acta Crystallog.*, 14(5), 553, 1961

Appendix

Manuscript for submission to *Proc. Natl. Acad. Sci. USA* 2011.

Magnetically sensitive light-induced reactions in cryptochrome are consistent with its proposed role as a magnetoreceptor

Kiminori Maeda[a,1], Alexander J. Robinson[a,1], Kevin B. Henbest[a], Hannah J. Hogben[b], Till Biskup[b], Margaret Ahmad[c], Erik Schleicher[d], Stefan Weber[d], Christiane R. Timmel[a,2], & P. J. Hore[b,2]

[a]Department of Chemistry, University of Oxford, Centre for Advanced Electron Spin Resonance, Inorganic Chemistry Laboratory, Oxford, UK.

[b]Department of Chemistry, University of Oxford, Physical & Theoretical Chemistry Laboratory, Oxford, UK.

[c]Université Paris VI, 4 Place Jussieu, 75005 Paris, France and Pennsylvania State University, Media, Pennsylvania 19063, USA.

[d]Institute of Physical Chemistry, Albert-Ludwigs-Universitt Freiburg, 79104 Freiburg, Germany.

[1]These authors contributed equally to this work.

[2]To whom correspondence may be addressed.

E-mail: peter.hore@chem.ox.ac.uk or christiane.timmel@chem.ox.ac.uk

Keywords:

- magnetoreception
- radical pair mechanism
- magnetic compass
- migratory birds
- quantum biology

Among the biological phenomena that fall within the emerging field of 'quantum biology' is the suggestion that magnetically sensitive chemical reactions are responsible for the magnetic compass of migratory birds. It has been proposed that transient radical pairs are formed by photo-induced electron transfer reactions in cryptochrome proteins and that their coherent spin dynamics are influenced by the geomagnetic field leading to changes in the quantum yield of the signalling state of the protein. Despite a variety of supporting evidence, it is still not clear whether cryptochromes have the properties required to respond to magnetic interactions orders of magnitude weaker than the thermal energy, k_BT. Here we demonstrate that the kinetics and quantum yields of photo-induced flavin–tryptophan radical pairs in cryptochrome are indeed magnetically sensitive. The mechanistic origin of the magnetic field effect is clarified, its dependence on the strength of the magnetic field measured, and the rates of relevant spin-dependent, spin-independent and spin-decoherence processes determined. We argue that cryptochrome is fit for purpose as a chemical magnetoreceptor.

Originally identified in plants (1), and subsequently found in organisms ranging from bacteria to insects and mammals, cryptochromes are blue-light photoreceptor proteins with a variety of functions including entrainment of circadian rhythms and, in plants, light-dependent regulation of growth and development (reviewed in Ref. (2)). They have high sequence-homology and structural similarity to their evolutionary ancestors, the DNA photolyases (3, 4) and all members of the cryptochrome/photolyase family contain the redox-active cofactor flavin adenine dinucleotide (FAD). Cryptochromes were proposed as potential magnetoreceptors by Ritz *et al.* in 2000 in an attempt to explain the mechanism by which migratory birds are able to sense the direction of the Earth's magnetic field for the purpose of navigation (5). Based on an earlier suggestion by Schulten (6), and drawing on the known magnetic sensitivity of radical pair reactions *in vitro* (reviewed in Ref. (7)), this idea has gained considerable support. Eleven years after the original suggestion, cryptochrome remains the only candidate radical pair magnetoreceptor.

Photoreduction of the fully oxidised state of FAD in most proteins of the cryptochrome/photolyase family appears to be mediated by electron transfer along a conserved triad of tryptophan (Trp) residues to give a flavosemiquinone radical, $FAD^{\bullet-}$ or $FADH^{\bullet}$, together with a radical derived from the terminal residue of the Trp-triad (8, 9). At least in plants, where the photo-active functions of cryptochromes are best understood, the flavosemiquinone form of the protein is thought to be the signalling state (10, 11). If the quantum yield of this state were dependent on the direction of the Earth's magnetic field, then in principle cryptochrome could act as a compass sensor. The evidence accumulated over the last 11 years in support of the cryptochrome hypothesis has been reviewed in Refs (12, 13). Hitherto, cryptochrome photochemistry has not been shown to be magnetically sensitive.

Cryptochromes have also attracted attention as potential mediators of biological effects of extremely low frequency (ELF) electromagnetic fields. Five observations are pertinent here. (a) Epidemiology suggests a link between small increased risks of childhood leukaemia and long-term exposure to 50/60 Hz ELF fields stronger than 0.4 μT (14, 15). (b) Disruption of circadian timing has been associated with susceptibility to cancer (16). (c) Cryptochromes are key components in the transcriptional regulation of mammalian circadian clocks (although there is no evidence that they function as photoreceptors or for the involvement of radicals) (2). (d) The radical pair mechanism is currently the only physically plausible mechanism by which magnetic interactions that are orders of magnitude weaker than k_BT can affect chemical reactions (7, 17). (e) Of the various radical pair systems considered as possible mediators of biological magnetic

field effects, cryptochromes are the most likely candidates given their known (photo-)chemical and physical properties (18).

In the following, we demonstrate that photo-induced radical pairs in a cryptochrome (Cry-1 from the plant *Arabidopsis thaliana*, *At*Cry) *are* sensitive *in vitro* to weak applied magnetic fields. Comparing the behavior of *At*Cry with that of *Escherichia coli* photolyase (*Ec*PL), we determine the reaction steps responsible for the magnetic field effect, elucidate what appears to be the principal spin-decoherence mechanism, obtain estimates of the rates of these processes, and provide evidence that radical pairs in cryptochromes could have the properties required to respond to Earth-strength (~50 μT) fields at physiological temperatures.

RESULTS

Magnetic field effect on radical pair kinetics. The photochemistry of *At*Cry and *Ec*PL has been studied using flash photolysis transient absorption spectroscopy. Figs 1A and C show difference spectra obtained from *At*Cry and *Ec*PL containing the flavin chromophore in its fully oxidized state, in (liquid) water-glycerol mixtures in the absence of an applied magnetic field. The two sets of spectra are broadly similar, showing depletion of the FAD ground state at 450 nm and formation of FAD and Trp radicals, visible as overlapping bands at wavelengths below 420 nm and above 500 nm. The principal differences between the two proteins are the relatively rapid (~10 μs) attenuation of the signal below 420 nm for *At*Cry and the change in the shape of the signal in the range 500–650 nm for *Ec*PL (also ~10 μs).

The spectra of *Ec*PL in Fig. 1C and those obtained at higher temperatures and lower glycerol contents are consistent with rapid (<< 1 μs) formation, by photo-induced electron transfer, of a [$FAD^{\bullet-}$ $TrpH^{\bullet+}$] radical pair followed by deprotonation of the $TrpH^{\bullet+}$ radical (~10 μs) to give the neutral $Trp^{\bullet}$ radical (19). Simultaneously, the ground state band at 450 nm recovers with a ~10 μs component via electron–hole recombination of [$FAD^{\bullet-}$ $TrpH^{\bullet+}$] to regenerate the FAD and TrpH ground states. Henceforth we refer to the sequentially formed radical pairs, [$FAD^{\bullet-}$ $TrpH^{\bullet+}$] and [$FAD^{\bullet-}$ $Trp^{\bullet}$] in *Ec*PL, as RP1 and RP2 respectively.

The situation is a little more complex for *At*Cry. The spectra in Fig. 1A are consistent with the rapid initial formation and slower recombination of [$FAD^{\bullet-}$ $TrpH^{\bullet+}$] (RP1) and the subsequent formation of a secondary radical pair (RP2), the identity of which is less clear than for *Ec*PL. The tryptophanyl radical in *At*Cry either rapidly deprotonates (< 1 μs) or exists in an equilibrium of the $TrpH^{\bullet+}$ and $Trp^{\bullet}$ forms; both possibilities are consistent with the data. The absorption decay observed below 420 nm indicates either protonation of $FAD^{\bullet-}$ to give the neutral $FADH^{\bullet}$ radical or the disappearance of a tyrosyl radical formed very rapidly (< 1 μs) by electron transfer from a nearby tyrosine residue: $TrpH^{\bullet+}$ + Tyr → TrpH + $Tyr^{\bullet+}$. Protonation of $FAD^{\bullet-}$ in an algal cryptochrome has been observed on the same timescale as the spectral changes in Fig. 1A (20); the marked drop in absorption below 420 nm (time constant, ~2 μs) was found to be accompanied by a smaller rise between 500 and 600 nm. The latter is not seen here probably because it is obscured by the recombination of RP1 which appears to be faster in *At*Cry than in the algal protein. Formation of tyrosyl radicals has been reported in *At*Cry (21), but on a much slower (~1 ms) timescale than the changes in Fig. 1A which, if due to a tyrosyl radical, would have to be assigned to its reduction by an unknown electron donor following its formation at an unprecedentedly fast rate. We therefore conclude that RP2 in *At*Cry is most likely to be formed from RP1 by $FAD^{\bullet-}$ protonation. We stress that the identity of RP2 in *At*Cry is not crucial for the interpretation of the magnetic field effects reported below. In the light of previous work (21, 22), the Trp radicals are presumed to come from the terminal residue of the Trp-triad, i.e. Trp-324 in *At*Cry and Trp-306 in *Ec*PL.

Figs 1B and D show the changes in the transient absorption spectra of *At*Cry and *Ec*PL, respectively, resulting from the application of a 28 mT magnetic field. Broadly similar to one another, and mirroring the shapes of Figs 1A and C respectively, these action spectra show that

the applied field reduces the transient yields of both FAD and Trp radicals and enhances the recovery of the FAD ground state. The difference between the 2–5 μs and 6–9 μs data below 400 nm in Fig. 1B is consistent with the $FAD^{\bullet-} \rightarrow FADH^{\bullet}$ protonation reaction (19).
Insight into the origin of the magnetic sensitivity is provided by the transient absorption kinetics. Typical time profiles are shown in Fig. 2, recorded for *At*Cry and *Ec*PL at a wavelength where $FAD^{\bullet-}$, $FADH^{\bullet}$, $TrpH^{\bullet+}$ and $Trp^{\bullet}$ radicals all have significant absorptions. Fig. 2A shows a rapid (1.2 μs) initial drop in absorption resulting from the recombination of RP1 and its transformation into RP2, followed by a much slower (>100 μs) decay arising from the recombination of RP2 and any other processes that return these radicals to their diamagnetic precursors. *Ec*PL exhibits a similar biphasic behavior (Fig. 2C, time constants 2.5 μs and >100 μs) with the faster component again attributable to RP1 recombination and RP1 → RP2 conversion ($TrpH^{\bullet+}$ deprotonation). As seen in Figs 2B and D, the effect of the magnetic field is predominantly on the initial fast phase (i.e. during the lifetime of RP1) and leads to a 10–20% suppression of the yield of RP2.

Photochemical reaction mechanism. The magnetic responses of both *At*Cry and *Ec*PL are consistent with the reaction schemes in Fig. 3. RP1 interconverts coherently between singlet and triplet states under the influence of magnetic interactions internal to the radicals (electron-nuclear hyperfine couplings) and Zeeman interactions with the external magnetic field. Only the singlet state of RP1 can revert to the ground state (FAD + TrpH) by electron–hole recombination, the corresponding reaction of the triplet state being spin-forbidden. Simultaneously, one of the constituents of RP1 changes its protonation state to give RP2, a process that is not subject to spin-selection rules and which singlet and triplet undergo at equal rates. The applied magnetic field alters the time-dependent probability that RP1 is singlet or triplet and so changes the fractions of radical pairs that proceed along the two competing pathways. The non-equilibrium state of the spin system allows magnetic interactions much weaker than k_BT to alter the reaction yields. As indicated by the transient absorption data (Figs 1 and 2), the RP1 reactions occur on a ~10 μs timescale, i.e. slow enough to allow time for a ~50 μT magnetic field to modify the singlet–triplet interconversion and fast enough to compete with spin-decoherence, which has been shown by time-resolved EPR to occur in ~10 μs (9). Experimental evidence that RP1 is formed in a *singlet* state from the photo-excited singlet state of the FAD cofactor (^{1}FAD*) is discussed in the Supplementary Information.

Kinetic regulation of magnetic responses. The changes in the photochemical kinetics of *At*Cry and *Ec*PL reported above are produced by applied magnetic fields some 500 times stronger than the Earth's field. To shed light on the conditions under which cryptochrome might be sensitive to much weaker fields, we have sought to clarify some of the factors that determine the amplitude of the responses at 28 mT.
A 28 mT magnetic field elicits 10–20% changes in the yield of RP2 in both *At*Cry and *Ec*PL (Fig. 2), substantially larger than the 3–4% effects previously reported for *Ec*PL in a solution with a lower glycerol content (19). A possible explanation for this difference can be found in the earlier observation (23) that the deprotonation rate (k_f) of the terminal $TrpH^{\bullet+}$ radical in *Ec*PL decreases with increasing concentration of glycerol, an effect attributed to release of the proton to the solvent. Changes in k_f alter the competition between the k_b and k_f reactions (Fig. 3) and so have the potential to tune the magnetic field effect. As shown in Fig. 4 for *Ec*PL, both the lifetime of RP1 (determined by the k_b and k_f steps, Fig. 3) and the magnetic field effect on the quantum yield of RP2 increase with increasing glycerol concentration and decreasing temperature, with an approximately linear correlation between the two quantities. We comment on the origin of this effect in the Supplementary Information.

Magnetic-field dependence of radical yields. Effects of magnetic fields substantially weaker than 28 mT have been explored for *At*Cry and *Ec*PL; the results are shown in Fig. 5. The fractional change in the yield of RP2 (as measured at 510 nm) is given for magnetic fields down to ~1 mT. The changes are roughly three times stronger for *At*Cry than for *Ec*PL but otherwise rather similar. Above 5 mT, both proteins show typical radical pair behavior (7): a monotonic increase in the magnitude of the effect, leveling off in both cases at magnetic fields stronger than ~25 mT. The comparatively large asymptotic magnetic field effects (>20% for *At*Cry and >8% for *Ec*PL) observed here are assumed to arise from the relatively long lifetime of the protein-bound radicals and the restrictions placed on their dynamics by the protein environment.

The width of such field-profiles is often characterized by the parameter $B_{1/2}$, the magnetic field at which the effect reaches half its limiting size at high field. Using hyperfine coupling data for $FAD^{\bullet-}$ and $TrpH^{\bullet+}$, the Weller equation (24) gives an estimate for $B_{1/2}$ of ~3 mT for RP1 (see Supplementary Information). The observed values of $B_{1/2}$ (Fig. 5) are substantially larger: around 10–12 mT for both proteins. Discrepancies of this kind occur quite commonly for radical pair reactions and have often been attributed to electron spin decoherence within the radical pair (see below) (25, 26). Also visible in Fig. 5 are indications that for both proteins the phase of the magnetic response inverts for magnetic fields weaker than 2–3 mT. We return to this point below.

Reversible electron transfer in the Trp-triad. The theoretical basis of the radical pair mechanism is sufficiently developed that quantitative interpretation of experimental data has become fairly routine especially when, as here, the separation and relative orientation of the two radicals are constrained. Even though the data in Fig. 5 exhibit little structure, successful numerical simulations may supply insights into the decoherence mechanism(s) responsible for the larger than expected $B_{1/2}$ values.

Reversible electron transfer between the distal and intermediate residues of the Trp triad has the potential to increase the observed $B_{1/2}$. Denoting the proximal, intermediate and distal tryptophans as W_A, W_B and W_C, the electron transport chain may be written:

$$^1\mathrm{FAD}^*\,W_A W_B W_C \longrightarrow \mathrm{FAD}^{\bullet-}\,W_A^{\bullet+}\,W_B W_C \longrightarrow \underbrace{\mathrm{FAD}^{\bullet-}\,W_A W_B^{\bullet+}\,W_C}_{\mathrm{RP0}} \underset{k'_{ET}}{\overset{k_{ET}}{\rightleftharpoons}} \underbrace{\mathrm{FAD}^{\bullet-}\,W_A W_B W_C^{\bullet+}}_{\mathrm{RP1}}$$

where k_{ET} and k'_{ET} are the rate constants for interconversion of RP1 and the intermediate radical pair comprising $FAD^{\bullet-}$ and $W_B^{\bullet+}$, which we shall call RP0. The limited evidence available suggests that the Trp radical is mostly localized on W_C (i.e. $k_{ET} >> k'_{ET}$) and that k'_{ET} may be fast enough to allow reversible electron hopping from and to W_B during the lifetime of RP1 (27-29). Using centre-to-centre FAD-Trp separations calculated (30) from the X-ray structure of *At*Cry (31) (1.32 nm for RP0 and 1.90 nm for RP1), the inter-radical electron exchange interactions have been estimated (30) as $|J_{RP0}| \approx 10^3$ mT and $|J_{RP1}| \approx 10^{-1}$ mT. Since $|J_{RP0}|$ greatly exceeds $|J_{RP1}|$, the hyperfine interactions and the magnetic field strength, electron hopping would cause strong modulation of the exchange interaction resulting in rapid relaxation of singlet–triplet coherences in RP1 (26). The time required for such decoherence is on the order of $(J_{RP0})^{-1}$, i.e. ~10 ps. Therefore, if k_{ET} is not much larger than 10^{11} s^{-1}, every time RP1 is converted into RP0 there would be significant decoherence before the electron jumped back. Under these conditions, the singlet–triplet dephasing (STD) rate, k_{STD}, should be close to k'_{ET}.
Standard techniques of quantum spin dynamics (7) were employed to simulate the magnetic field effects shown in Fig. 5, using the reaction scheme in Fig. 3. Just two (field-independent) variable parameters were used for each protein: k_b and k_{STD}. The rate constant for the RP1 → RP2 reaction was fixed ($k_f = 2.5 \times 10^5$ s^{-1}) by noting that the magnetic field effect for *Ec*PL at 28 mT (~8%, Fig. 5B) corresponds to a RP1 lifetime of ~4 μs (Fig. 4B). The same value was used for *At*Cry. In the simulations, all coherent superpositions of a singlet state and a triplet state of RP1 were

damped exponentially with the rate constant k_{STD}, and hyperfine couplings were calculated using density functional theory. The red lines in Figs 5A and B are the best-fit simulations, with the optimum parameter values: *At*Cry, $k_b = 4.9 \times 10^5\ s^{-1}$, $k_{STD} = 1.1 \times 10^7\ s^{-1}$; *Ec*PL, $k_b = 1.2 \times 10^5\ s^{-1}$, $k_{STD} = 2.7 \times 10^7\ s^{-1}$. These numbers are plausible: (a) A magnetic field effect as large as ~20% requires effective competition between the two reaction pathways, implying $k_b \approx k_f$. (b) RP1 lifetimes with respect to recombination to the ground state (i.e. k_b^{-1}) of ~2 μs (*At*Cry) and ~8 μs (*Ec*PL) are compatible with the observed transient absorption kinetics. (c) As shown in Fig. 5, the width of the field-dependence is sensitive to the value of k_{STD}; an increase in $B_{1/2}$ from ~3 mT to 10–12 mT requires k_{STD} to be substantially larger than k_b and k_f. (d) The value of k_{STD} for *Ec*PL agrees very well with the estimate of k'_{ET} by Popović *et al*. ($3.2 \times 10^7\ s^{-1}$) (27) but less well with that of Krapf *et al*. ($1.2 \times 10^4\ s^{-1}$) (29). Simulations in which spin relaxation was omitted (Supplementary Fig. 10), or included by means of other models, were uniformly unsuccessful in accounting for the data shown in Fig. 5 (see Supplementary Information for details). Additional simulations, also described in the Supplementary Information, suggest a rationale for the larger magnetic field effect for *At*Cry compared to *Ec*PL (Fig. 5) and for the correlation shown in Fig. 4.

Sensitivity to weaker magnetic fields. We have shown that the effects of magnetic fields stronger than ~5 mT are consistent with singlet–triplet interconversion induced by hyperfine and Zeeman interactions together with singlet–triplet dephasing brought about by electron hopping. In the light of this, we return to the sign change in the magnetic field effect for both proteins below 2–3 mT (Fig. 5). Such phase inversions have been well documented both theoretically and experimentally in other reaction systems (17, 32, 33) and are usually referred to as 'low field effects' (LFE). Numerical simulations of model radical pairs (17) show that when spin relaxation and radical recombination reactions are sufficiently slow, the LFE can be much larger than the ~1% effects seen at ~1 mT in Fig. 5, even in much weaker magnetic fields. The best-fit simulations predict LFEs for both proteins with approximately the correct positions and amplitudes. The other simulations in Fig. 5 indicate that as k_{STD} is reduced the initial slope increases causing the maximum LFE to shift to progressively lower fields. Thus the effect of a 50 μT magnetic field on the yield of RP2 could be significantly larger than implied by the best-fit simulations in Fig. 5 if singlet–triplet dephasing (and any other significant decoherence mechanisms) were sufficiently slow.

DISCUSSION

The cryptochrome hypothesis of radical-pair magnetoreception was proposed 11 years ago. We present here the first direct evidence that cryptochromes can exhibit the magnetically sensitive photochemistry that is the essential prerequisite for a magnetic compass sensor. Magnetic field effects on the quantum yields of radicals produced in *At*Cry in viscous solution of about +1% in a ~1 mT magnetic field, and about –25% in a ~30 mT field, have been detected. The change in phase observed for fields weaker than 2–3 mT is the signature of the low field effect which, under appropriate conditions, could permit significant responses to Earth-strength magnetic fields.

High glycerol concentrations and reduced temperatures have been used here in an attempt to mimic the optimal *in vivo* conditions that might have evolved in a cryptochrome-based magnetoreceptor. One can only speculate about the environment of an avian cryptochrome in a magnetoreceptor cell, but it seems most likely that the proteins must be both immobilized and aligned in order to show the anisotropic magnetic responses essential for a compass detection mechanism (5). Restricted molecular motion and slow spin-decoherence—also essential for a significant magnetic response—were achieved here by varying the temperature and the solvent, but could come about in different and probably more efficient ways *in vivo*, for example by tethering to membrane proteins or cytoskeletal filaments (34), binding to signaling partners (35-

37) and/or cofactors (e.g. ATP (31, 38)), dimerization (39), etc. It does not seem unreasonable to conjecture that under optimum conditions *in vivo*, the effect of a ~50 μT magnetic field could be substantially larger than observed in the present study. Simulations suggest that the low field effect can, under the right conditions, be as large as 10–20% (17). Too little is known about light-dependent cryptochrome signalling in general, and magnetoreception in particular, to say whether this would be large enough to form the basis of a viable magnetoreceptor.

It is evident from our results that a significant magnetic field effect from a cryptochrome-based radical pair requires kinetic competition on a 1–10 μs timescale, between spin-selective electron–hole recombination, and spin-independent formation of the signalling state. If these processes were much faster than 1 μs there would be insufficient time for the geomagnetic field to influence the spin dynamics; if they were much slower, the effect would almost certainly be attenuated by spin-decoherence (12). It seems unlikely, however, that the conformational changes needed to generate the signalling state (probably rearrangement of the C-terminal domain (40)) could be as fast as 10 μs. Our results show that formation of a secondary species (RP2) from the magnetically sensitive radical pair RP1, [$FAD^{\bullet-}$ $TrpH^{\bullet+}$], avoids the need for an abnormally rapid protein rearrangement or exceptionally slow spin-decoherence. Protonation of the $FAD^{\bullet-}$ radical (as may occur in *At*Cry) or deprotonation of the $TrpH^{\bullet+}$ radical (as occurs in *Ec*PL (19, 23)) allows the magnetic field effect on RP1 to be 'stored' in the form of a changed quantum yield of the much longer lived state RP2, from which the signalling state can subsequently be generated. The fact that there is no need for the reactions of RP2 to be magnetically sensitive means that its lifetime can greatly exceed its spin-decoherence time without ill effect.

There are now two members of the cryptochrome/photolyase family that show magnetic responses. Given the very different biological functions of *Ec*PL (DNA repair) and *At*Cry (regulation of growth and development, entrainment of circadian rhythms) and the fact that neither bacteria nor plants appear to have specialised magnetoreceptors, we suggest that magnetic sensitivity is a general feature of this protein family and that the results described here may be extrapolated to bird cryptochromes (and possibly even human cryptochromes).

MATERIALS AND METHODS

Protein preparation. The expression and purification of *Ec*PL (as a mutant that does not bind the methenyltetrahydrofolate cofactor) are described elsewhere (19, 41). To ensure the FAD cofactor was in its fully oxidised state, the protein was pre-treated with potassium ferricyanide as described previously (19). Glycerol was added to ~130 μM protein samples in 50 mM HEPES buffer at pH 7.0 with 100 mM KCl to obtain solutions containing 20–50% glycerol (v/v). Unlike our previous study of *Ec*PL (19), potassium ferricyanide was not added to the samples to re-oxidise photoreduced flavin.

*At*Cry (full length cryptochrome-1) was expressed in Sf21 cells using a recombinant baculovirus expression vector system and purified by Ni-NTA affinity chromatography. Glycerol was added to ~150 μM protein samples in Tris/HCl buffer at pH 7.5 with 500 mM NaCl and 250 mM imidazole to obtain solutions containing 20–60% glycerol (v/v).

Transient absorption spectroscopy. Protein samples (~250 μL) were cooled in a cryostat (Oxford Instruments, Optistat CF) with the temperature controlled to within 0.1 K. The sample was held in a quartz cuvette (Hellma 104.002 QS; 10 mm path length, internal dimensions 2 × 10 × 45 mm) at the centre of the cryostat. Magnetic field pulses of ~4 ms duration, synchronised with the laser flash, were generated using home-built Helmholtz coils. The maximum magnetic field at the position of the sample was 29 mT. Samples were not shielded from the Earth's magnetic field. Radical pairs in *Ec*PL and *At*Cry were generated by flash photolysis using a dye laser (Sirah Cobra) pumped by a Nd:YAG laser (Continuum Surelite 1). The laser dye was Coumarin 460 (Exciton Inc.) in analytical grade methanol (Fisher Scientific). The Nd:YAG laser

produced 5 ns pulses with energy ~100 mJ and repetition rate 1 Hz, tuned by means of a Q-switch delay to produce 5–7 mJ, 460 nm pulses (FWHM 37 nm) from the dye laser. Probe light from a 300 W xenon arc lamp (Oriel) was passed through a water filter to cut out infrared components and through long-pass filters to remove unwanted wavelengths and thence to the sample in a direction orthogonal to the pump pulses. Pump and probe beams were controlled by mechanical shutters to obtain a 0.05 Hz repetition rate to reduce photodegradation of the light-sensitive samples. Probe light was collected using a monochromator (Oriel 77250), fed into a photomultiplier tube (Hamamatsu R928) and from there to an oscilloscope (Iwatsu-LeCroy Waverunner LT342L). Data were transferred to a personal computer and analysed using IGOR PRO (Wavemetrics, Inc.) software.

Spin dynamics simulations. The magnetic field-dependence of radical pair reaction yields (Fig. 5) was calculated from the equation of motion of the radical pair spin density operator in Liouville space including coherent spin dynamics, decoherence processes, and chemical reactivity by means of appropriate superoperators. Singlet–triplet dephasing was introduced as proposed by Shushin (26). Further details are given in the Supplementary Information.

Acknowledgements. We thank S. M. Lea, J. Lillington and A. Bowen for discussions and N. Baker and P. Stehle for technical assistance. P.J.H. and C.R.T. were supported by the EMF Biological Research Trust, DARPA (QuBE: N66001-10-1-4061) and the EPSRC. S.W. and E.S. were funded by DfG grant WE2376/4-1.

Author contributions
K.M., A.J.R. and K.B.H. gathered and analysed the data. H.J.H. simulated the magnetic field effects with advice from K.M. and T.B. E.S., S.W. and M.A. expressed the proteins. K.M., A.J.R., K.B.H., H.J.H., T.B., E.S., S.W., C.R.T. and P.J.H. discussed the data, their interpretation and presentation. C.R.T. and P.J.H. conceived and designed the study. C.R.T. coordinated the experiments. P.J.H. wrote the manuscript.
Conflict of interest statement: The authors declare no conflict of interest.

Additional information: This article contains supporting information online at ...

References

1. Ahmad M, Cashmore AR (1993) *HY4* gene of *A. thaliana* encodes a protein with characteristics of a blue-light photoreceptor. *Nature* 366:162-166.
2. Chaves I, *et al.* (2011) The cryptochromes: Blue light photoreceptors in plants and animals. *Annu. Rev. Plant Biol.* 62:335-364.
3. Weber S (2005) Light-driven enzymatic catalysis of DNA repair: A review of recent biophysical studies on photolyase. *Biochim. Biophys. Acta* 1707:1-23.
4. Sancar A (2008) Structure and function of photolyase and *in vivo* enzymology: 50th anniversary. *J. Biol. Chem.* 283:32153-32157.
5. Ritz T, Adem S, Schulten K (2000) A model for photoreceptor-based magnetoreception in birds. *Biophys. J.* 78:707-718.
6. Schulten K, Swenberg CE, Weller A (1978) A biomagnetic sensory mechanism based on magnetic field modulated coherent electron spin motion. *Z. Phys. Chem. NF* 111:1-5.
7. Rodgers CT (2009) Magnetic field effects in chemical systems. *Pure Appl. Chem.* 81:19-43.
8. Gindt YM, *et al.* (1999) Origin of the transient electron paramagnetic resonance signals in DNA photolyase. *Biochemistry* 38:3857-3866.
9. Biskup T, *et al.* (2009) Direct observation of a photoinduced radical-pair intermediate in a cryptochrome DASH blue-light photoreceptor. *Angew. Chem. Int. Ed.* 48:404-407.
10. Banerjee R, *et al.* (2007) The signaling state of *Arabidopsis* cryptochrome 2 contains flavin semiquinone. *J. Biol. Chem.* 282:14916-14922.
11. Bouly JP, *et al.* (2007) Cryptochrome blue light photoreceptors are activated through interconversion of flavin redox states. *J. Biol. Chem.* 282:9383-9391.
12. Rodgers CT, Hore PJ (2009) Chemical magnetoreception in birds: A radical pair mechanism. *Proc. Natl. Acad. Sci. USA* 106:353-360.
13. Liedvogel M, Mouritsen H (2010) Cryptochromes—a potential magnetoreceptor: What do we know and what do we want to know? *J. Roy. Soc. Interface* 7:S147-S162.
14. Ahlbom A, *et al.* (2000) A pooled analysis of magnetic fields and childhood leukaemia. *Brit. J. Cancer* 83:692-698.
15. Greenland S, *et al.* (2000) A pooled analysis of magnetic fields, wire codes, and childhood leukemia. *Epidemiology* 11:624-634.
16. Reddy AB, Wong GKY, O'Neill J, Maywood ES, Hastings MH (2005) Circadian clocks: Neural and peripheral pacemakers that impact upon the cell division cycle. *Mutat. Res.* 574:76-91.
17. Timmel CR, Till U, Brocklehurst B, McLauchlan KA, Hore PJ (1998) Effects of weak magnetic fields on free radical recombination reactions. *Mol. Phys.* 95:71-89.
18. Lagroye I, Percherancier Y, Juutilainen J, Poulletier De Gannes F, Veyret B (doi: 10.1016/j.pbiomolbio.2011.09.003) ELF magnetic fields: Animal studies, mechanisms of action. *Prog. Biophys. Mol. Biol.*
19. Henbest KB, *et al.* (2008) Magnetic-field effect on the photoactivation reaction of *Escherichia coli* DNA photolyase. *Proc. Natl. Acad. Sci. USA* 105:14395-14399.
20. Langenbacher T, Immeln D, Dick B, Kottke T (2009) Microsecond light-induced proton transfer to flavin in the blue light sensor plant cryptochrome. *J. Am. Chem. Soc.* 131:14274-14280.
21. Giovani B, Byrdin M, Ahmad M, Brettel K (2003) Light-induced electron transfer in a cryptochrome blue-light photoreceptor. *Nature Struct. Biol.* 10:489-490.
22. Li YF, Heelis PF, Sancar A (1991) Active-site of DNA photolyase - tryptophan-306 is the intrinsic hydrogen-atom donor essential for flavin radical photoreduction and DNA-repair *in vitro*. *Biochemistry* 30:6322-6329.

23. Byrdin M, *et al.* (2004) Intraprotein electron transfer and proton dynamics during photoactivation of DNA photolyase from *E. coli*: Review and new insights from an "inverse" deuterium isotope effect. *Biochim. Biophys. Acta* 1655:64-70.
24. Weller A, Nolting F, Staerk H (1983) A quantitative interpretation of the magnetic-field effect on hyperfine-coupling-induced triplet formation from radical ion-pairs. *Chem. Phys. Lett.* 96:24-27.
25. Miura T, Maeda K, Arai T (2006) The spin mixing process of a radical pair in low magnetic field observed by transient absorption detected nanosecond pulsed magnetic field effect. *J. Phys. Chem. A* 110:4151-4156.
26. Shushin AI (1991) The effect of the spin exchange interaction on SNP and RYDMR spectra of geminate radical pairs. *Chem. Phys. Lett.* 181:274-278.
27. Popović DM, Zmiric A, Zaric SD, Knapp EW (2002) Energetics of radical transfer in DNA photolyase. *J. Am. Chem. Soc.* 124:3775-3782.
28. Woiczikowski PB, Steinbrecher T, Kubar T, Elstner M (2011) Nonadiabatic QM/MM simulations of fast charge transfer in *Escherichia coli* DNA photolyase. *J. Phys. Chem. B* 115:9846-9863.
29. Krapf S, Koslowski T, Steinbrecher T (2010) The thermodynamics of charge transfer in DNA photolyase: Using thermodynamic integration calculations to analyse the kinetics of electron transfer reactions. *Phys. Chem. Chem. Phys.* 12:9516-9525.
30. Efimova O, Hore PJ (2008) Role of exchange and dipolar interactions in the radical pair model of the avian magnetic compass. *Biophys. J.* 94:1565-1574.
31. Brautigam CA, *et al.* (2004) Structure of the photolyase-like domain of cryptochrome 1 from *Arabidopsis thaliana*. *Proc. Natl. Acad. Sci. USA* 101:12142-12147.
32. Eveson RW, Timmel CR, Brocklehurst B, Hore PJ, McLauchlan KA (2000) The effects of weak magnetic fields on radical recombination reactions in micelles. *Int. J. Radiat. Biol.* 76:1509-1522.
33. Brocklehurst B (1976) Spin correlation in geminate recombination of radical ions in hydrocarbons. 1. Theory of magnetic-field effect. *J. Chem. Soc. Faraday Trans. II* 72:1869-1884.
34. Kirschvink JL, Winklhofer M, Walker MM (2010) Biophysics of magnetic orientation: Strengthening the interface between theory and experimental design. *J. R. Soc. Interface* 7:S179-S191.
35. Zuo Z, Liu H, Liu B, Liu X, Lin C (2011) Blue light-dependent interaction of CRY2 with SPA1 regulates COP1 activity and floral initiation in *Arabidopsis*. *Curr. Biol.* 21:841-847.
36. Liu B, Liu H, Zhong D, Lin C (2010) Searching for a photocycle of the cryptochrome photoreceptors. *Curr. Opin. Plant Biol.* 13:578-586.
37. Partch CL, Sancar A (2005) Photochemistry and photobiology of cryptochrome blue-light photopigments: The search for a photocycle. *Photochem. Photobiol.* 81:1291-1304.
38. Bouly J, *et al.* (2003) Novel ATP-binding and autophosphorylation activity associated with *Arabidopsis* and human cryptochrome-1. *Eur. J. Biochem.* 270:2921-2928.
39. Sang Y, *et al.* (2005) N-terminal domain-mediated homodimerization is required for photoreceptor activity of *Arabidopsis* cryptochrome 1. *Plant Cell* 17:1569-1584.
40. Kondoh M, *et al.* (2011) Light-induced conformational changes in full-length *Arabidopsis thaliana* cryptochrome. *J. Mol. Biol.* 413:128-137.
41. Schleicher E, *et al.* (2005) Light-induced reactions of *Escherichia coli* DNA photolyase monitored by Fourier transform infrared spectroscopy. *FEBS J.* 272:1855-1866.

Figures

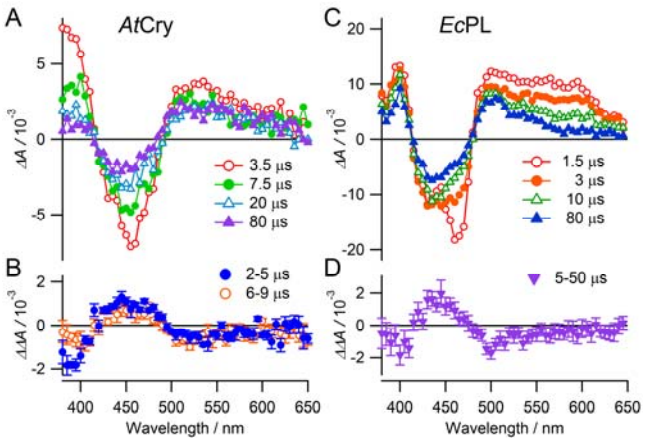

Fig. 1. Transient absorption spectra and magnetic field action spectra of *At*Cry and *Ec*PL. Transient absorption spectra, $\Delta A(0)$, of (A) *At*Cry and (C) *Ec*PL. $\Delta A(0)$ is the difference between signals recorded with and without a 460 nm, 5 ns pump light pulse in the absence of an applied magnetic field. The spectra were integrated over 1 µs periods centered at the indicated times after the pump pulse. Each spectrum is the average of two transients. The laser repetition rate was kept low (0.05 Hz) to minimize protein photodegradation. The 1.5 µs signal in (C) at 460 nm is distorted by a transient effect of the laser pulse on the photomultiplier detector. Experimental conditions: *At*Cry, 250 K, 60% (v/v) glycerol solution; *Ec*PL, 250 K, 50% (v/v) glycerol solution. (B) and (D) Magnetic field action spectra of *At*Cry and *Ec*PL respectively, recorded under the same conditions as (A) and (C), presented as $\Delta\Delta A = \Delta A(28\ \text{mT}) - \Delta A(0)$. Two transients were recorded with the magnetic field and two without. At each wavelength the double-difference kinetic time profiles were smoothed with a 2 µs boxcar function and the mean and standard deviation calculated over the indicated time intervals. At each wavelength the mean ± standard deviation is plotted. The minor differences between the data shown in (C) and (D) and the data reported by Henbest *et al*. (19) are attributed to the different experimental conditions of the latter: 278 K, 20% (v/v) glycerol, 5 mM potassium ferricyanide.

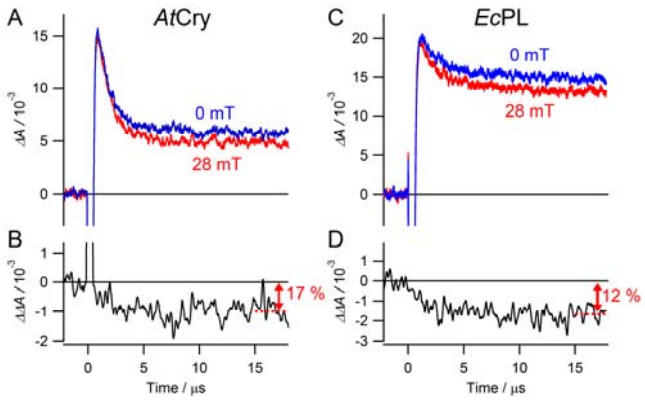

Fig. 2. Magnetic field effects on the photochemical kinetics of *At*Cry and *Ec*PL. Transient absorption kinetic time profiles of (A) *At*Cry and (C) *Ec*PL both recorded at 510 nm with and without a 28 mT applied magnetic field. (B) and (D) Differences between the two signals shown in (A) and in (C) respectively: $\Delta\Delta A = \Delta A(28\text{ mT}) - \Delta A(0)$. 200 ns boxcar smoothing was used to produce (B) and (D); no smoothing was used for (A) and (C). Experimental conditions: *At*Cry, 270 K in 60% (v/v) glycerol solution; *Ec*PL, 250 K in 50% (v/v) glycerol solution. Similar traces for both proteins were observed at temperatures between 240 K and 275 K and glycerol contents between 25% and 65% (Supplementary Figs 1-6).

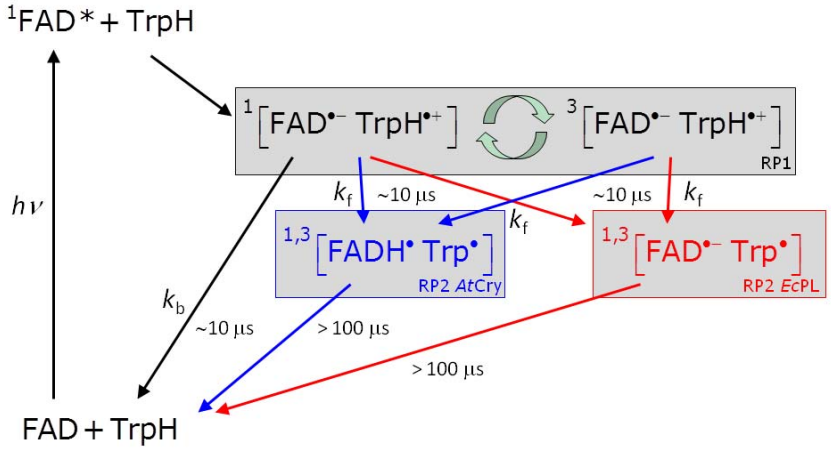

Fig. 3. Proposed photochemical reaction schemes for *At*Cry and *Ec*PL. The black arrows and species are common to both proteins; the blue and red features refer to *At*Cry and *Ec*PL respectively. k_b and k_f are first-order rate constants for electron–hole recombination of RP1 and formation of RP2 from RP1, respectively. Although RP2 in *At*Cry is here drawn as [$FADH^{\bullet}$ $Trp^{\bullet}$], the protonation state of the Trp radical is not certain. The green arrows indicate the coherent, magnetic field-dependent interconversion of the singlet and triplet states of RP1.

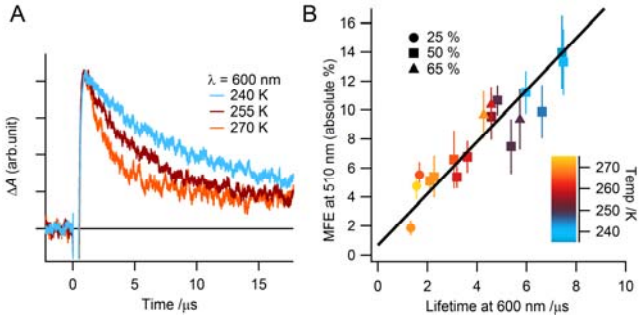

Fig. 4. Correlation between the magnetic field effect on the yield of RP2 and the lifetime of RP1 in *Ec*PL. (A) Transient absorption kinetic time profiles of *Ec*PL in 50% (v/v) glycerol solution in the absence of an applied magnetic field at the temperatures indicated. Recorded at 600 nm, these signals reflect the kinetics of the reactions: $TrpH^{\bullet+} \rightarrow Trp^{\bullet} + H^{+}$ and $^{1}[FAD^{\bullet-}\ TrpH^{\bullet+}] \rightarrow FAD + TrpH$ (Fig. 3). Lifetimes were extracted from such data by fitting to a monoexponential decay with a constant offset. (B) Effect of a 28 mT magnetic field on the yield of RP2 (recorded at 510 nm) plotted against the lifetime of RP1 (measured at 600 nm) over a range of temperatures and glycerol concentrations, as indicated. The vertical axis is the absolute value of the fractional magnetic field effect (MFE): $|\Delta A(28\ \text{mT}) - \Delta A(0)|/\Delta A(0)$. The data plotted here are given in Supplementary Table 1.

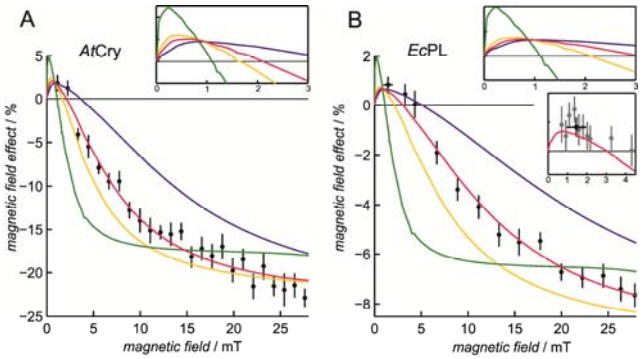

Fig. 5. Magnetic field-dependence of the yield of RP2 in *At*Cry and *Ec*PL. The percentage change in the yield of RP2 (measured at 510 nm) as a function of the strength of the applied magnetic field for (A) *At*Cry and (B) *Ec*PL. Experimental conditions: (A) *At*Cry, 60% glycerol, 270 K; (B) *Ec*PL, 50% glycerol, 260 K. The red lines are the best-fit simulations obtained using the singlet–triplet dephasing model described in the text, with $k_f = 2.5 \times 10^5$ s^{-1} and (A) $k_b = 4.9 \times 10^5$ s^{-1}, $k_{STD} = 1.1 \times 10^7$ s^{-1}; (B) $k_b = 1.2 \times 10^5$ s^{-1}, $k_{STD} = 2.7 \times 10^7$ s^{-1}. The other lines are simulations with the same values of k_f and k_b but (A) k_{STD} / s^{-1} = 0 (green), 5×10^6 (yellow), 5×10^7 (blue); (B) k_{STD} / s^{-1} = 0 (green), 1×10^7 (yellow), 1×10^8 (blue). The two larger insets show expanded views of the simulations in the low field region. The irregularities visible in some of these curves arise from energy-level anti-crossings. The smaller inset in (B) shows, on an expanded scale, the best-fit simulation together with 8 measurements in the range 0.7–2.2 mT that were averaged to obtain the (black) point plotted at B = 1.5 mT in this inset and in the main panel. The error bars associated with this data point represent ±one standard deviation of the 8 measurements. Each data point in the main panels is the average of (A) 10 and (B) 40 (>3 mT) or 80 (<3 mT) transients. At each applied magnetic field strength B, the double-difference kinetic time profiles $\Delta A(B) - \Delta A(0)$ were smoothed with (A) 5 μs and (B) 0.5 μs boxcar functions. The mean ± standard deviation (calculated over the time intervals: (A) 2–170 μs and (B) 7–15 μs is plotted for each datum.

Following the submission of my corrected thesis to my internal examiner in December 2011 two papers were accepted for publication which incorporated material drawn from my thesis.

- The contents of Chapter 3 formed the basis of:

H. J. Hogben, T. Biskup and P. J. Hore. Entanglement and Sources of Magnetic Anisotropy in Radical Pair-Based Avian Magnetoreceptors. Phys. Rev. Lett., 2012, 109 (22), 220501. © 2012 American Physical Society. Available at http://link.aps.org/doi/10.1103/PhysRevLett.109.220501

- The contents of Chapter 5 was the basis of a small part of:

K. Maeda, A. J. Robinson, K. B. Henbest, H. J. Hogben, T. Biskup, M. Ahmad, E. Schleicher, S. Weber, C. R. Timmel and P. J. Hore. Magnetically sensitive light-induced reactions in cryptochrome are consistent with its role as a magnetoreceptor, Proc. Natl. Acad. Sci. USA, 2012, 109 (13), 4774-4779. © 2012 the authors. Available at http://dx.doi.org/10.1073/pnas.1118959109.